



**TOGETHER**  
*for a sustainable future*

## OCCASION

This publication has been made available to the public on the occasion of the 50<sup>th</sup> anniversary of the United Nations Industrial Development Organisation.



**TOGETHER**  
*for a sustainable future*

## DISCLAIMER

This document has been produced without formal United Nations editing. The designations employed and the presentation of the material in this document do not imply the expression of any opinion whatsoever on the part of the Secretariat of the United Nations Industrial Development Organization (UNIDO) concerning the legal status of any country, territory, city or area or of its authorities, or concerning the delimitation of its frontiers or boundaries, or its economic system or degree of development. Designations such as “developed”, “industrialized” and “developing” are intended for statistical convenience and do not necessarily express a judgment about the stage reached by a particular country or area in the development process. Mention of firm names or commercial products does not constitute an endorsement by UNIDO.

## FAIR USE POLICY

Any part of this publication may be quoted and referenced for educational and research purposes without additional permission from UNIDO. However, those who make use of quoting and referencing this publication are requested to follow the Fair Use Policy of giving due credit to UNIDO.

## CONTACT

Please contact [publications@unido.org](mailto:publications@unido.org) for further information concerning UNIDO publications.

For more information about UNIDO, please visit us at [www.unido.org](http://www.unido.org)

22642

Organized by :



international center for  
science and high  
technology



united nations  
industrial development  
organizations



RISTEK  
ministry of research  
and technology  
republic of indonesia



indonesian institute  
of sciences

Proceedings

# Regional Workshop on Lasers and Optoelectronics

P3FT-LIPI, Puspiptek Serpong, Indonesia  
June 25<sup>th</sup> - July 6<sup>th</sup> 2001

supported by :



PUSPIPTEK

PCplus  
TABLOO COMPUTER

GAMMA  
MAJALAH BERITA MINGGUAN

Organized by :



international center for  
science and high  
technology

**Proceedings**

# **Regional Workshop on Lasers and Optoelectronics**

**P3FT-LIPI, Puspiptek Serpong, Indonesia  
June 25<sup>th</sup> - July 6<sup>th</sup> 2001**



united nations  
industrial development  
organizations



**RISTEK**  
ministry of research  
and technology  
republic of indonesia



indonesian institute  
of sciences

supported by :



**PUSPIPTEK**

**PCplus**  
TABLOO COMPUTER

**GAMMA**  
MAJALAH BERITA MINGGUAN

## Table of Contents

Page No

Conference Committee .....	iii
List of Lectures .....	iv
List of Participants .....	vi
Workshop Report by the Chairman .....	ix
Speech by ICS-UNIDO Representative .....	x
Keynote Speech: "Research, Development and Applications of Lasers and Optoelectronics in Indonesia" .. Anung Kusnowo	I
Keynote Speech: "Information In the Speed Of Light, the Indonesian Perspective" .....	IX
Jonathan L. Parapak	
Theory of Laser .....	1
Heinz P. Weber	
Diode Pumped Solid State Laser Systems .....	24
H.P. Weber, W. Lüthy	
Polishing of Diamond Layers .....	36
H.P. Weber, S. Gloor, and W. Lüthy	
Temperature Monitoring with Fluorescing Dyes .....	47
Heinz P. Weber, Valerio Romano	
Pulsed Optoacoustic Spectroscopy and Imaging .....	55
Kornel Köstly, martin Frenz, Heinz P. Weber	
Laser as Medical Instrument for Surgery .....	65
H.P. Weber, M. Frenz, and H. Pratisto	
Dye-enhanced articular Cartilage Soldering .....	84
H.P. Weber, B.J. Züger, B. Ott, Th. Schaffner, P. Mainil-varlet, and M. Frenz	
Fibre Bragg Gratings for Telecommunication and Sensing .....	98
Prabakaran Poopalan	
Telecommunications Optically .....	114
Prabakaran Poopalan	
Laser Application in the Life Extension of Engineering Components .....	142
Nazmul Alam	
Integrated Optics .....	167
John E. Batubara	
Laser Application for Pollution Monitoring/LIDAR .....	193
Mego Pinandito	
Processing Technology of Semiconductor Laser .....	213
DR. Sekartedjo	
	221

Interferometry by Holography and Speckle .....	250
Ichiro Yamaguchi	
Holography and Digital Holography .....	265
Ichiro Yamaguchi	
Laser-induced Shock Wave Plasma Spectroscopy .....	301
K. Kagawa and H. Kurniawan	
Laser Application in Medicine .....	
Hamdani Zain	
Hologram As Protection in Security Packaging .....	
Thomas Edi, Sunarto	324

## Conference Committee

Dr. Achiar Oemry (Chairman)  
Dr. Masbah R. T. Siregar (Co-Chairman)  
Dr. Neni Sintawardani (Co-chairman)  
Dr. Diah Intani (Secretary)  
Dra. Dwi Bayuwati, M.Eng. (Treasurer)  
Hadiyanto, B.Sc.Hon  
Ir. Muchiar, M. Eng.Sc  
Isnaeni, S.Si.  
Dr. Ashadi Salim  
Ir. T. Budi Waluyo, M.Eng.  
Dr. Titin Kathrina  
Dra. Edi Tri Astuti, M.Eng.  
Dra. M. M. Suliyanti  
Ir. Erfan Y. Febrianto  
Drs. Farid W. M, M.Eng.Sc.  
Dr. K.A. Zaini Thosin  
Ruchiat S. Husen  
Kusnandar  
Dr. L.T. Handoko  
Suryadi

## List of Lecturers

No.	Name	Affiliation	E-mail/ Ph. / Fax
1.	Dr. Anung Kusnowo, M.Tech.	Indonesian Institute of Sciences Jl. Jend. Gatot Subroto No. 10 Jakarta	Ph. 62 21 5251586
2.	Jonathan L . Parapak, M.Eng.	PT. Broadband Multimedia Tbk. Bulevar Gajah Mada No.2170 Lippo Karawaci Tangerang 15811, Indonesia	Jonathan.parapak @kabelvision.com Ph. 62 21 5577 7788 Fax. 62 21 5577 7460
3.	Prof. Weber P. Heinz, Ph.D.	Dept. Head, University Bern 75 Bell Laboratories Holmdel Institute of Applied Physics Sidlersh 5, CH-3012 Bern Switzerland.	heinz.weber@iap.unibe.ch Ph. 41-31-6318931
4.	Prabakaran Poopalan. Ph.D.	Telekom Malaysia Photonics Research Centre Departmen of Physics University Malaya 50603 Kuala Lumpur, Malaysia.	pbkanes@lycos.com Ph. 603-79686200/ Fax. 603-79547552
5.	Nazmul Alam. Ph.D.	CSIRO – MST 32 Audley st, Woodville, SA 5012 Australia.	nazmul.alam @cmst.csiro.au
6.	Dr. John E. Batubara	Universitas Pelita Harapan UPH Tower, Lippo Karawaci Tangerang 15811, Indonesia	iebatubara@yahoo.com Ph. 62-21-5460901 Fax. 62-21-5460910
7.	Dr. Sekartedjo	Institut Teknologi Sepuluh November Keputih, Sukolilo Surabaya 60111, Indonesia.	sekar@telkom.net Ph.62-031-5931143
8.	Dr. Mego Pinandito	Puslitbang KIM - LIPI Kawasan PUSPIPTEK Serpong, Tangerang 15314 Indonesia.	m.pinandito@hotmail.com Tel. 62-0217560562, ext. 3311, 3064.
9.	Prof. I. Yamaguchi	Head of Optical Engineering Lab, RIKEN Hiroshima 2-1, Wako, Saitama 351-0198, Japan.	ichiyama@postman.riken.go.jp Ph. 81-48-462-1111, Fax. 81-48-462-4653.
10.	Dr. Hendrik Kurniawan	Program Studi Opto-Elektroteknika dan Aplikasi Laser Universitas Indonesia Jl. Salemba Raya No. 4 Jakarta 10430, Indonesia	Ph. 62-21-330 188 Fax. 62-21-391 8'15

11.	Dr. Hamdani Zain	Program Studi Opto-Elektroteknika dan Aplikasi Laser Universitas Indonesia Jl. Salemba Raya No. 4 Jakarta 10430, Indonesia	Ph. 62-21-330 188 Fax. 62-21-391 8115
12.	Ir. Thomas Edi	PT. Pura Barutama Kudus, Indonesia	Thomas_edi@telkom.net Ph. 62 291 432 604 Fax. 62 291 439 253
13.	Şunarto, ST.	PT. Pura Barutama Kudus, Indonesia	sunarto@puragroup.com Tel. 62 291 432 604 Fax. 62 291 439 253



## List of Participants

No.	Name	Affiliation	E-mail/Ph. /Fax
1.	Hairul Mohd Daud Bin Haji Abd Karim, B.Eng. (Hons), AMIEE.	Jabatan Telekom Brunei Jalan Airport Lama Berakas Bandar Seri Begawan Negara Brunei Darussalam	hrul@brunet.bn Fax. 673-2-380 330
2.	Voo Nyuk Yoong, B.Eng (Hons), MSc, AMIEE.	Physics Dept. Faculty of Science Universiti Brunei Darussalam Tungku Link BE1410 Negara Brunei Darussalam.	nyvoo@fos.ubd.edu.bn
3.	Ak. Mohd. Iskandar Bin Pg. Hj. Petra, B.Eng (Hons), M.Sc.	Physics Dept. Faculty of Science Universiti Brunei Darussalam Tungku Link BE1410 Negara Brunei Darussalam.	amipetra@fos.ubd.edu.bn
4.	Khaled Habib, PhD.	Materials Science Lab. Department of Advanced Systems KISR PO. Box 24885, Safat 13109, Kuwait	khaledhabib@usa.net Fax. 965-543-0239
5.	Vu Duc Thinh, Eng.	Lab for Materials & Engineering of Fibre Optics, Institute of Material Science National Center for Natural Science & Technology of Vietnam Hoang Quoc Viet Street, Cau Giay Dist. Hanoi, Vietnam.	huuan@ims.ncst.ac.vn
6.	Hang Seiha	Renewable Office, Technical Energy Dept. Ministry of Industry Mines and Energy No 47, Preah Norodom Blvd. Phnom Penh, Kampuchea	samy@forum.org.kh Ph. 855-23-427851 855-23-213575 Fax. 855-23-725427
7.	Percival F. Almoro, MSc.	National Institute of Physics, University of the Philippines, Diliman, Quezon City 1101, Philippines	val@nip.upd.edu.ph Ph. 928-0296-4344239 Fax. 928-0296- 4344243
8.	Roslan Hashim	School of Physics University Sains Malaysia Penang 11820, Malaysia	roslan@usm.my Fax. 604-657 9150
9.	Mohd. Zubir Mat Jafri	School of Physics, University Sains Malaysia Penang 11820, Malaysia	mjafri@usm.my
10.	Sulaiman Wadi Harun, MSc.	Photonics Research Centre Department of Physics, Faculty of Science University of Malaya 50603 Kuala Lumpur, Malaysia.	wadi72@yahoo.com Ph. 60-3-7968 6200
11.	Nor Shahida Mohd Shah, B.Eng.	Photonics Research Centre Department of Physics, Faculty of Science University of Malaya 50603 Kuala Lumpur, Malaysia	nshahida@hotmail.com Ph. 60-3-7968 6200

12.	Jumril Yunas, Dipl.-Ing.	Puslitbang Telkoma - LIPI Komplek LIPI Jl. Sangkuriang, Bandung 40135, Indonesia	jumril@telkoma.lipi.go.id Ph. 62 22 2504660 Fax. 62 22 2504659
13.	Gandi Sugandi, A.Md.	Puslitbang Telkoma - LIPI Komplek LIPI Jl. Sangkuriang, Bandung 40135, Indonesia	gandi@tekoma.lipi.go.id Ph. 62 22 250 4660 Fax. 62 22 250 4659
14.	Yaya Suleiman, A.Md.	Puslitbang Telkoma - LIPI Komplek LIPI Jl. Sangkuriang, Bandung 40135, Indonesia	Yaya@tekoma.lipi.go.id Ph. 62 22 250 4660 Fax. 62 22 250 4659
15.	Julinda Pangaribuan, S.Si.	Universitas Pelita Harapan UPH Tower, Lippo Karawaci Tangerang, Indonesia	julindapangaribuan@yahoo.com Ph. 62-21-5460901 Fax. 62-21-5460910
16.	Pria Saptono, S.Si.	Lab. Advanced Physics Jurusan Fisika, FMIPA Institut Teknologi Bandung Jl. Ganesha 10, Bandung, Indonesia	saptono@fislan.fi.itb.ac.id
17.	Drs. Imam Rofi'I, MSc.	Jurusan Fisika, FMIPA Universitas Jember, Jl. Kalimantan III/25, Jember 68121 Indonesia	imam@mipa.unej.ac.id
18.	Jojo L. Manalu, S.Si, MT.	Fakultas Kedokteran Universitas Atmajaya Pluit Raya 2, Jakarta 14440, Indonesia	fk@atmajaya.ac.id
19.	Ir. Marhaban Sigalingging	PT. Serviam Abadimurni Ruko Roxy Blok A no. 21-22 Jl. MH Thamrin Kav. 155-159 Lippo Cikarang, Bekasi 17550, Indonesia	serviam@centrin.net.id Ph. 62-21-756 0570 Fax. 62-21-756 0554
20.	Ir. Retno Wigajatri P, MT.	Program Studi Optoelektroteknika dan Aplikasi Laser Universitas Indonesia Jl. Salemba Raya No. 4 Jakarta 10430, Indonesia	Ph. 62-21-756 0570 Fax. 62-21-756 0554
21.	Ir. Munawar Hadi S, MT.	Perum Peruri Jakarta, Indonesia	Munawar@dnet.id Tel 62 0818 938163
22.	Kapten Chb. Drs. Rahardy	Akademi Militer Magelang, Indonesia	
23.	Drs. Harry Purnomo	Puslitbang KIM – LIPI Kawasan PUSPIPTEK Serpong, Tangerang 15314, Indonesia	Tel: 62 21 7560562 Ext. 3065 Fax. 62 21 7560568
24.	Ir. Rietje Wirawan	Puslitbang Fisika Terapan – LIPI Kawasan PUSPIPTEK Serpong, Tangerang 15314, Indonesia	Ph. 62-21-756 0570 Fax. 62-21-756 0554

25.	Rika Suriamah, BE.	Puslitbang Fisika Terapan – LIPI Kawasan PUSPIPTEK Serpong, Tangerang 15314, Indonesia	Ph. 62-21-756 0570 Fax. 62-21-756 0554
26.	Achmad Subhan, S.Si.	Puslitbang Fisika Terapan – LIPI Kawasan PUSPIPTEK Serpong Tangerang 15314, Indonesia	Ph. 62-21-756 0570 Fax. 62-21-756 0554
27.	Isnaeni, S.Si	Puslitbang Fisika Terapan – LIPI Kawasan PUSPIPTEK Serpong, Tangerang 15314, Indonesia	Ph. 62-21-756 0570 Fax. 62-21-756 0554
28.	Ir.Tomi Budi Waluyo, MEng.	Puslitbang Fisika Terapan – LIPI Kawasan PUSPIPTEK Serpong, Tangerang 15314, Indonesia	tomibudiwaluyo @lipi.fisika.net Ph. 62-21-756 0570 Fax. 62-21-756 0554
29.	Suryadi	Puslitbang Fisika Terapan – LIPI Kawasan PUSPIPTEK Serpong, Tangerang 15314, Indonesia	Ph. 62-21-756 0570 Fax. 62-21-756 0554
30.	Kusnandar	Puslitbang Fisika Terapan – LIPI Kawasan PUSPIPTEK Serpong, Tangerang 15314, Indonesia	Ph. 62-21-756 0570 Fax. 62-21-756 0554
31.	Dra. Edi Tri Astuti, MEng.	Puslitbang Fisika Terapan – LIPI Kawasan PUSPIPTEK Serpong, Tangerang 15314, Indonesia	etri_astuti@hotmail.com Ph. 62-21-756 0570 Fax. 62-21-756 0554

# Regional Workshop on Lasers and Optoelectronics

June 25<sup>th</sup> – July 6<sup>th</sup> 2001

Komplek Puspiptek, Serpong, Tangerang, Indonesia

---

## WORKSHOP REPORT

Your Excellency the Minister of State Research and Technology of the Republic of Indonesia,  
Dr. A.S. Hikam

Your Excellency the Ambassador of Italy, Mr. Merola

Representative of ICS-UNIDO in Indonesia

Representative of Unesco in Jakarta, Prof. Stefan Hill

Participants of the Regional Work Shop on Lasers and Optoelectronics

Ladies and Gentlemen

Assalammu'alaikum w.w.

On behalf of the Steering Committee and Organizing Committee, it is pleasure to welcome you to the Regional Workshop on Lasers and Optoelectronics in particular to the participants who have come from far-away countries in this campus of Puspiptek Serpong.

The Regional Workshop on Lasers and Optoelectronics is jointly organized by the ICS-UNIDO, Research and Development Center for Applied Physics (now Research Center for Physics) Indonesian Institute of Sciences, and Deputy Minister for Research Science and Technology, KMNRT.

This workshop has been realized with full support and sponsor from ICS-UNIDO, lectures from developed countries and prominent user in Indonesian and of course researcher and scientist in Indonesia

There are 11 participants from Asian countries, such as Malaysia, Brunei Darussalam, Philippines, Vietnam, Cambodia, and Kuwait, and 22 participants from Indonesia, will participate in the program. It was planed the 5 experts from Swiss, Australia, Malaysia, Philippines, and Japan, and also 6 experts from Indonesia will deliver lectures in the program.

The objective of the program is to introduce the basic principles and applications of laser and optoelectronics, provide the background needed to follow the development of this technology,

and to strengthen the collaboration among the participated countries in the field of laser and optoelectronics.

We hope through the program could be improved better understanding and linked between our countries, especially in the field of lasers and optoelectronics.

In closing, I would like to express our thanks to the ICS-UNIDO for their financial support, and to the office of Minister of State Research and Technology, which gave full support.

I would also like to extent our appreciation and thanks to Unesco, GAMMA, PC PLUS, Gincosan, and Puspiptek, for their financial and in-kind contribution. Our appreciation and thanks are also due to the Chairman of LIPI, the Chairman of the Physical Sopciaety of Indonesia, and the Director of Puspiptek for their support.

We would like also to thanks the lectures, the participants, P.T. Indosat the telecommunication company and P.T., Pirelli the manufacture of fiber optics cable, for their participation in the works shops.

Finally, I wish you success in your deliberation

Thank you very much for your kind attention.

Wassalammu'alaikum w.w.

Achiar Oemry



**INTERNATIONAL CENTRE FOR SCIENCE  
AND HIGH TECHNOLOGY**



*Area Science Park, Building L2, Padriciano 99, 34012 Trieste, Italy*  
*Phone: +39-040-9228-111 Fax: +39-040-9228-122*  
*<http://www.ics.trieste.it/>*

**Regional Workshop**

**“LASERS AND OPTOELECTRONICS”**

**Komp. Puspiptek-Serpong, Tangerang (Indonesia)**  
**25 June -6 July 2001**

**OPENING MESSAGE**

This Workshop is suggested and supported by the International Centre for Science and High Technology - UNIDO, Trieste (Italy) as a starting activity of a long term collaboration plan with the Ministry for Research and Technology. The visit of a high level delegation headed by his Excellency Minister Muhammad A.S. Hikam to the Trieste international institutions in May 2000 and the return visit to H.E. Minister Hikam of a delegation from the same Trieste institutions in March this year were significant occasions for discussions about ways and means of cooperation.

The purpose of this event, which was firmly encouraged and supported by H.E. Minister Hikam, is to expose scientists and technicians to the modern topics of optoelectronics which are interesting research subjects for their application to industrial high technology.

For this reason the joint participation of researchers and experts from industry is the special feature of this activity.

The workshop is expected to stimulate the interest of scientists, technicians and industrial managers on the importance of expanding the research and training activities especially in techniques such as the use of laser based systems for medicine, spectroscopic applications, holography as well as in the main application of fibre optics for communications and sensors.

We are confident that this workshop will enhance the interaction between industry and university so as to allow researchers to be informed on the practical needs of the production world and managers and technicians to be made aware of the most advanced views of science in order to innovate their own systems.

The spirit of the course of the course is to stimulate a wide collaboration of institutions and industries in Indonesia and in our Region. Therefore several Indonesian institutions are active parts of the programme and participation of colleagues from different countries in our region is very much appreciated. We look forward to collaboration in the wide and productive field of optoelectronics and photonics with scientists and industrial partners in our Region. Consistently, an expected output of this meeting is that proposal for further similar activities may be presented by all of you so as to start new stimulating cooperation projects.

It is a pleasure to express thankful thoughts to the main organizing institutions: State Ministry for Research and Technology (RISTEK) and the Indonesian Institute of Sciences (LIPI) and in particular to Dr. A. Hartanto, Dr. A. Oemry, Dr. N. Sintawardani and Dr. D. Intani.

Gallieno Denardo

# RESEARCH, DEVELOPMENT, AND APPLICATION OF LASERS AND OPTOELECTRONICS IN INDONESIA

(keynote speech)

**Dr. Anung Kusnowo, MTech.**  
Dep. of LIPI Chairman for Engineering Sciences  
Indonesian Institute of Sciences (LIPI),  
Jl. Jend Gatot Subroto 10, Jakarta 12710  
E-mail: anung@mss.lipi.go.id

In less than fifty years after Theodore Maiman from Hughes Aircraft U.S.A demonstrated the first working laser, and less than forty years after Charles K. Kao from Standard Telecommunication Laboratories U.K predicted that optical fibre could be used as a new transmission medium, lasers and optical fibres (as well as other optoelectronics components) are now widely used in our lives (either knowingly or unknowingly to the users). Now we are living in an era of optical fibre communication, laser surgery, laser welding, optical sensor, and optical data storage to name a few. Since the last decades of the 20<sup>th</sup> century, lasers and optoelectronics technology has been established, utilized, and developed in many countries of the world, including Asia. Based on this perspective, and thanks to ICS-UNIDO, this workshop is organized for participants from universities, research institutes, and industries from Asian countries. I, hereby, sincerely wellcome all of you.

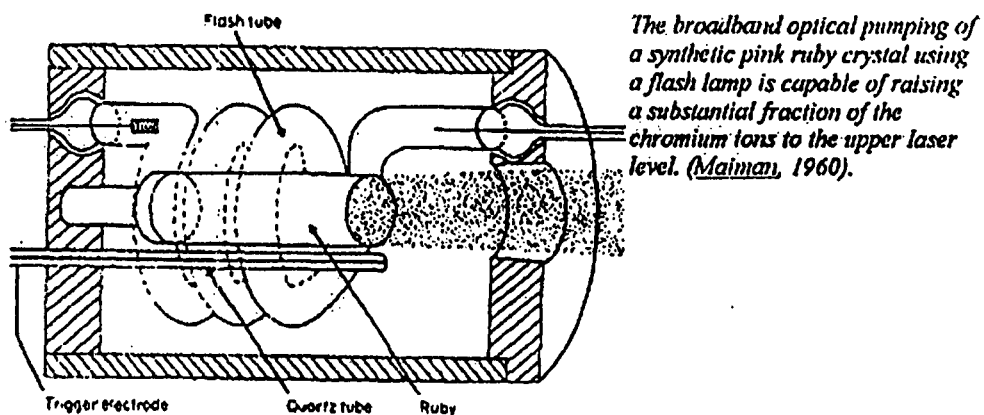


**Figure 1.** Diagram of the first (ruby) laser.  
(source: <http://www.scientificamerican.com>)



In this speech I shall try to describe in brief the R&D activities and applications of lasers and optoelectronics in Indonesia. Like in many other countries, Indonesia also utilizes optical fibre communication system as a part of its telecommunication systems. That's why the organizer is planning to take you, the participants, to PT Pirelli Cables Indonesia to see its optical fibre cabling facilities, and to PT Indosat's submarine optical fibre communication cable station to see, or to listen explanation on, how optical fibre at work. The visit is scheduled on Monday, July 2<sup>nd</sup> 2001. Apart from international experts invited to be lecturers in this workshop, the organizer also asked several prominent persons here to be the lecturers. I shall take this opportunity to describe briefly the activities of their institutions/companies. I shall not, however, intend to give an extensive and complete elaboration about R&D activities and applications of lasers and optoelectronics technology in Indonesia. And, of course, I shall not intend to claim that Indonesia is already very well developed in this fascinating technology (frankly speaking, in some areas we are still behind our neighbouring countries). Nevertheless, I do hope that I could illustrate, especially to overseas participants, our position that could be used as a stepping stone to further strengthen the understanding and collaboration on R&D activities and applications of lasers and optoelectronics technology, especially between the countries participating in this workshop.

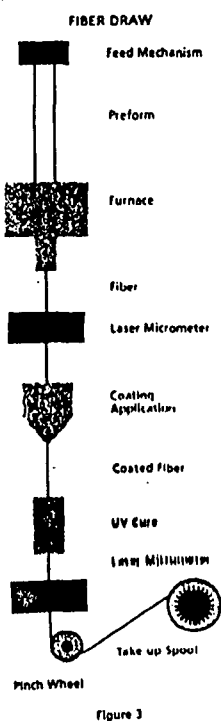


**Figure 2. Optical Fiber Manufacturing.**  
 (source: <http://www.fotec.com>)



**Figure 3. Fiber Preform.**  
 (source: *Laser Focus World*, March 2001)

Let me begin with the Postgraduate Study Program of Opto-Electrotechniques and Laser Application Department, University of Indonesia. The main purposes of this department (established in 1977) is to educate university students to master required knowledge for the applications of lasers and optoelectronics as well as to reach their master and doctoral degrees. There are four study programs that are emphasized in this department, namely: *Optical Communications, Applied Spectroscopy, Instrumentation and Photonic Devices, and Image Processing and Remote Sensing*. Let me focus on the Applied Spectroscopy Laboratory. This laboratory has succeeded in making the first high power nitrogen pulse laser in Indonesia and obtained the first reward in the Second ASEAN Science and Technology week in the Philippines in 1989. This laboratory has also succeeded, in 1992, in making the first carbon-dioxide pulse laser in Indonesia. This laboratory obtains fund from the World Bank to conduct researches in the field of atomic spectroscopy and since 1986 involved in research cooperation with the University of Fukui, Japan. The organizer will take you to visit this department on Thursday, July 5<sup>th</sup> 2001, and you will also have lectures there.

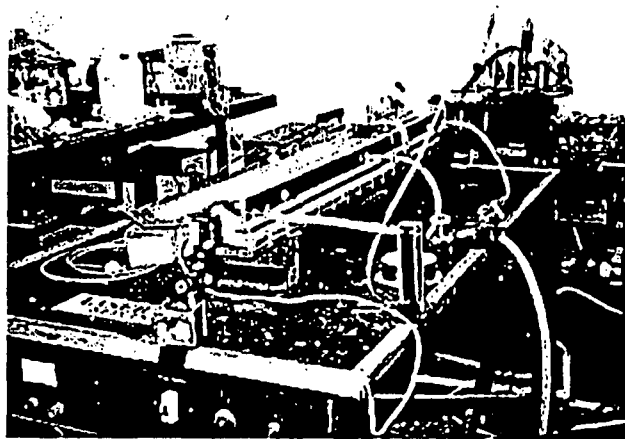


Figure 4. Pulse laser TE N<sub>2</sub>.

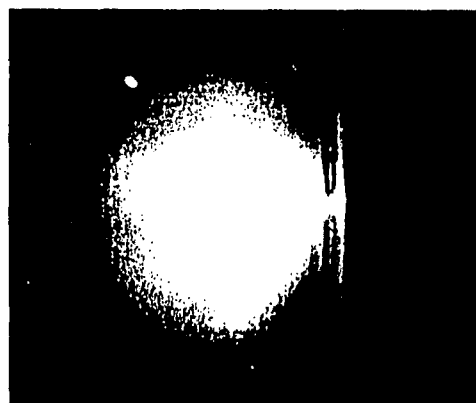
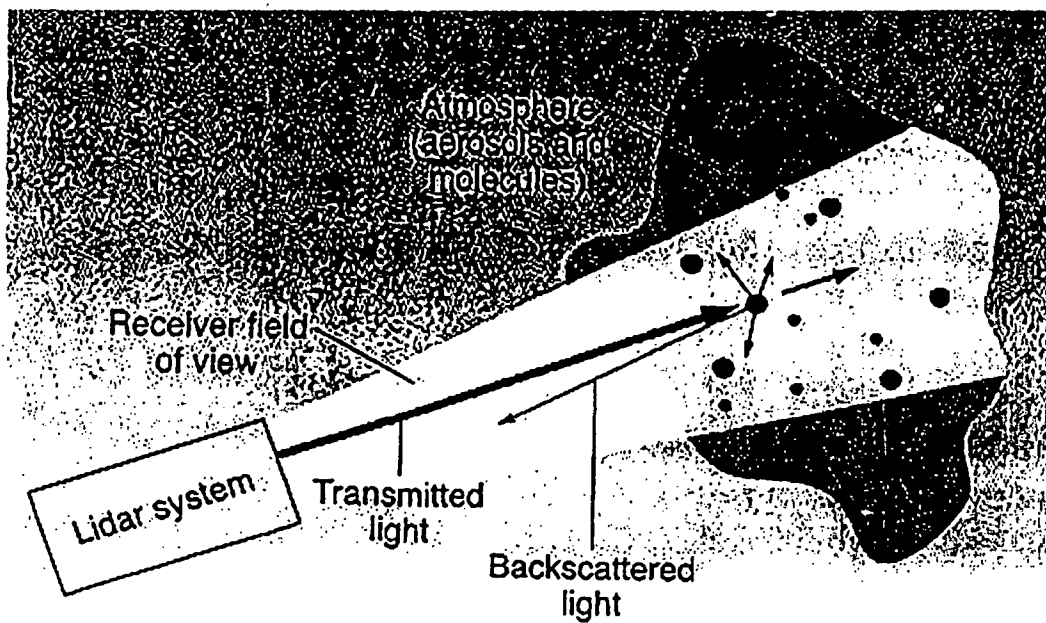


Figure 5. Plasma of Zn generated by TEA CO<sub>2</sub> laser. III

Research, development, and application of LIDAR (Light Detection and Ranging) is one of the activities in R&D Centre for Calibration, Instrumentation, and Metrology – Indonesian Institute of Sciences (RDCKIM – LIPI). In collaboration with NEDO Japan this centre utilize laser systems to measure aerosols and other pollutants in several cities in Indonesia. This centre also has optical workshop to manufacture lenses and other optical components and successful in design and construction of night-vision system for M16/FNC assault rifles. The organizer is planning to take you there on Wednesday, June 27<sup>th</sup> 2001.



**Figure 6. Principle of LIDAR.**  
(source: *Laser Focus World*, March 2001)

Now, let me shift to a private company PT Pura Nusapersada, a division of Pura Group, which is a hologram manufacturer for promotional and security applications. Their promotional holographic material covers wide range of polypropylene, polyester, paper and carton board with customized colours, patterns gauges and widths. These products dedicated to give enhancement to any merchandising medium. The materials, specifically designed to be fully compatible with contemporary printing and packaging technology, are suitable for label, gift wrap, shopping bag, and fancy sticker. To prevent product counterfeiting, PT Pura Nusapersada provides holographic materials to be used as security device. They are available in sticker (laminated using High Refractive Index film), Tear Tape, and Hologram on Aluminum Foil. A lecture about the application of holography at this company is scheduled on Friday, July 6<sup>th</sup> 2001.

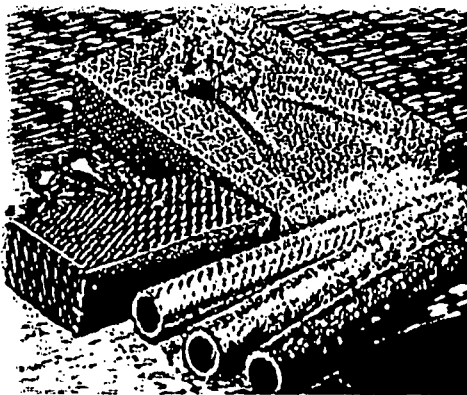


Figure 7. Gift Wrap Hologram.

(source: <http://www.puragroup.com>)



Figure 8. E-beam Hologram.

If you have problems with your skin, you can visit the Jakarta Skin Centre that applies laser technology. Using several types of laser they conduct selective photothermolysis to destroy only the cells that should be destroyed without altering the other normal skin cells. For example, they have an *Nd:YAG laser* to destroy all pigmented lesions like freckles, brown spots, as well as tattoos with various colours. They also use *ruby laser* to destroy brown, blue or black skin diseases. For surgery, such as blepharoplasty (to eliminate baggy eyelids) and circumcision (for child and adult), a *CO<sub>2</sub> laser* is employed. Whilst a relatively low power *He-Ne laser* is used to stimulate skin healing, hair growth, normal pigmentation, preventing skin scarring, etc. You will have a lecture about the application of laser for skin treatments on Friday, July 6<sup>th</sup> 2001.

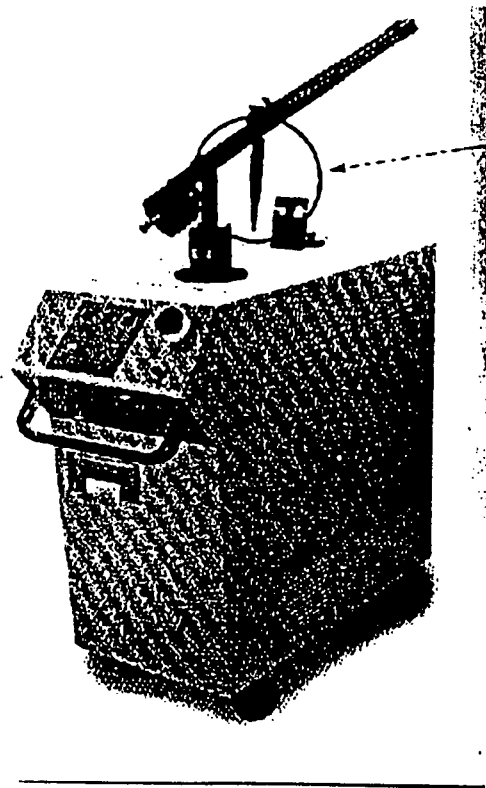


Figure 9. Nd:YAG laser for skin treatment.  
(source: <http://www.skinjsc.com>)

Now, let me talk about the activities at the host of this workshop: the R&D Centre for Applied Physics – Indonesian Institute of Sciences (RDCAP – LIPI). Since 1984 this centre is conducting research, development, and transfer of technology in the applications of lasers and optoelectronics. The activities include the R&D on crystal growing (Si single crystal and III-V compounds for photonic devices), R&D on micro-optic components such as planar microlens, the development of holography and speckle interferometry, R&D on high power lasers such as design and construction of a 500W CO<sub>2</sub> laser, and the development of optical fibre systems such as optical fibre hydrophone. Facilities to support those activities include an LPE (Liquid Phase Epitaxy) System, Photolithography System, Crystal Growing Apparatus, Electronic Speckle Pattern Interferometry System, and optical fibre instrumentation (such as Fusion Splicer, Fibre Polisher, OTDR, Optical Spectrum Analyzer, etc.) as well as various lasers (He-Ne, Nd:YAG, Argon, laser diodes, etc.). A laboratory visit and demonstration is scheduled for you on Tuesday and Wednesday, July 3<sup>rd</sup> – 4<sup>th</sup> 2001.



Figure 10. CO<sub>2</sub> laser.

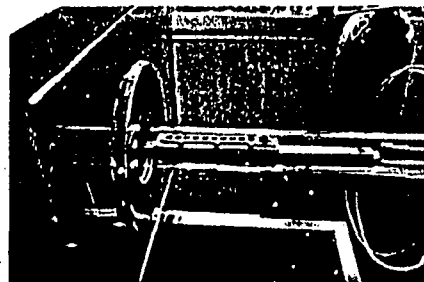


Figure 11. Growth-boat in LPE system

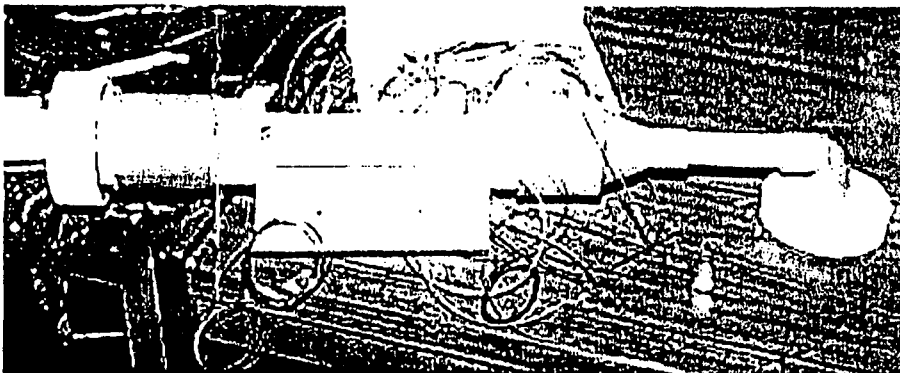


Figure 12. Construction of optical fibre hydrophone.

Of course there are other institutions and companies in Indonesia which are actively doing research, development, and application of lasers and optoelectronics technology. Some lecturers of this workshop come from the **Pelita Harapan University** and **Institute of Technology of Surabaya** (you can ask detailed information directly to them). Other educational institutions include **Department of Physics, Institute Technology of Bandung** and **Gadjah Mada University** in Yogyakarta. In LIPI itself there are other centres involved in this technology, such as the **R&D Centre for Material for Electronic and Telecommunication Components**. Several private companies are being contractors for **PT Telkom** (our telecommunication company), such as **PT Alcatel Indonesia** which responsible to provide optical fibre infrastructures.

Last but not least, let me talk about the measurable output of R&D activities, namely patents and international publications. I must admit that such outputs from institutions in Indonesia are still very low. Yes there are some patents (such as *TROPIC*: Test of Material by Rotation of Mechanics and Optics) and publications (such as in SPIE Proceedings or in IOP/Institute of Physics publications) by some Indonesian researchers/educators; however, in general, we are still poorly performed. So, let me to remind and urge you, in particular my Indonesian fellows, to work harder and to utilize any legal means, such as this workshop, to increase your performance which can be measured by the number of patents and publications (internationally, not locally) you produced.

Finally, I would like to wellcome again all the participants of this workshop. For overseas participants, please enjoy your stay in Indonesia which, unfortunately, still not in its best conditions. I hope that you can benefit from this workshop and disseminate your knowledge to your colleagues back home. I do hope that in the near future we can build a strong cooperation between us. For all the lecturers, please accept my sincere appreciation. We are very grateful that you accepted our invitation to be a lecturer here in this workshop. Furthermore, I would like to thank ICS-UNIDO for the financial support of this workshop (hopefully we will have more cooperation in the future), and to the Organizer who had, and still has to, worked hard for the success of this workshop. Thank you very much.

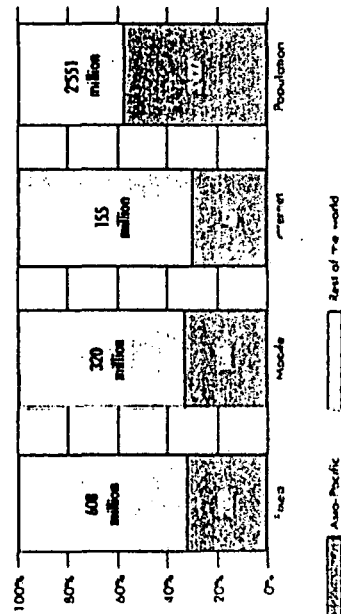
## Information In the Speed of Light, The Indonesian Perspective

By: Jonathan Parapak

### 1. The New World

- New digital economy is expanding globally.
- All business, small or big, will become e-business.
- Internet, multimedia and wireless communications will grow exponentially.
- New business environment - competitive and volatile (liberalized market).
- Cost of bandwidth will drop dramatically and processors capacity will increase 10 times in 5 years.
- Many new players will join the industry

Distribution of fixed and mobile telephone subscribers, Internet users and population in the Asia-Pacific region and the rest of the world (1999)



Source: ITU, 2000

### 2. New Direction of Technological Development in the Asia Region

- Mobile is overtaking fixed line installation.
- Internet is growing exponentially.
- Brick & mortar business is embracing click & mortar-E-commerce.
- The sharp downturn of internet/dot com companies became a valuable lesson for developing easy to understand new business models for a solid operation and a clear path to profitability.
- CAD/CAM-integrated manufacturing will attract "new production centers".
- The cost of computing has declined exponentially.
- Many initiatives are under way to provide fast internet connectivity in the region through optical fiber network/submarine cables and satellites system.
- Cina, India and ASEAN are centers of growth in the coming year.



### 3. The Impact Of ICT Development On The Growth Potential In The Asia's Market

- Creating new employment opportunities e.g. Bali Camp in Indonesia.
- Expanding market reach for SME, such as furniture and handicraft shops, home stays in several cities in Indonesia.
- E-commerce will grow exponentially. Enhancing the efficiency of governments in delivering government services, and reducing corruption.
- Improving and expanding the reach of quality education; access of information and technology.

### 4. Connectivity Issues In The ICT Industry

- Digital divide is a reality within many countries, inter country and inter region.
- Barrier to entries such as monopolistic regulatory environment, over-regulation of tariffs and technology, unlevelled playing field, unclear and inconsistent policies, lack of capital, technical and managerial expertise.
- Unattractive investment climate due to political, economic, and employment policies.
- Uncertain legal frame-work relating to IPR, e-commerce, privacy and security.

### 5. ICT Development - The Indonesian Perspective

- Democratization process is continuing.
- Liberalization of the infocom sector is taking place.
- New law 36/99 went into effect in September 2000.
- National Coordinating Team (TKTI) is chaired by the Vice-President.
- New Presidential Instruction No. 5/2001 on ICT policy framework was issued 24 May 2001.
- New momentum of industry restructuring was achieved last week (elimination of Indosat, Telekom cross-Ownership)
- The establishment of an IRB is seriously considered/planned.
- Private sector's participation is being encouraged.
- By 2005, the Nusantara Infrastructure will reach all Kabupaten (regional district) and 50% of Kecamatan.
- By 2005, internet users will exceed 10 million and may reach 20 million.
- By 2005 cellular phones will exceed 10 million.

### 5. ICT Development: - The Indonesian Perspective

- Infocom/ICT for unity and cohesiveness of the people and empowering the society, alleviation of poverty, enhancement of transparency and efficiency.
- Productive and harmonious cooperation between the public and private sector.
- Expansion of IIR, mainly by the private sector, should be accelerated.
- Acceleration of infocom development by private sector's participation through the improvement of a conducive investment environment.
- Human Resources Development should be a high priority.
- Government-on-line is to be implemented during the next 2-5 years.
- Legal frame work for e-commerce is being established.

### 5. ICT Development - The Indonesian Perspective

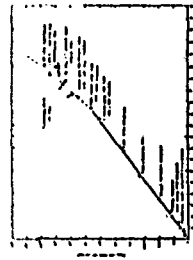
#### Some Major Programmes

- Remove entry barrier into the telecommunications market.
- Strengthen the regulatory regime.
- Remove of restrictions on ICT investment and bureaucratic procedures on investments.
- Adopt minimalist e-commerce law.
- Stimulate R & D on ICT.
- Expedite Human Resources development.
- Facilitate internet access to schools and universities.
- Implement government on-line.
- Develop community telecenters.

### 6. Why are optical fibers are so good ?

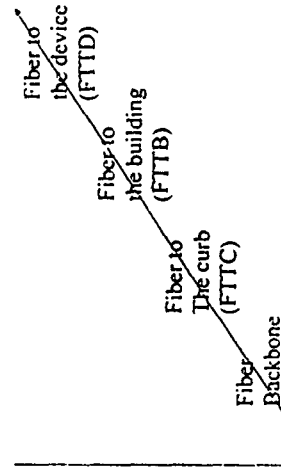
- Frequency of the light beams is in the vicinity of  $2 \cdot 10^{14}$  Hz. Bandwidth needed for voice is only 4 KHz. Thus, the capacity of fiber is  $2 \cdot 10^{14} \text{ Hz} / 4 \cdot 10^3 \text{ Hz} = 50 \cdot 10^9$   
The whole world can be on the phone on a single fiber at the same time !.
- In practice, it has not proven possible to achieve these maximum capacity, although in current links the fiber wins by huge margin over others.

### Bandwidth Evolution

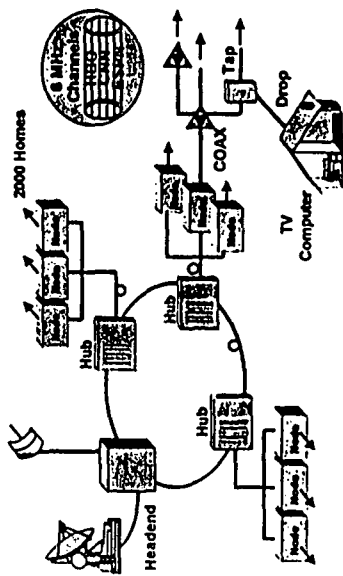


- The communication data rate depicted was drawn in 1995, and already out of date.
- At this moment, technology for 40 Gbit at a single wavelength is available. With the advance of DWDM technology, a single fiber can carry up 160 wavelengths, giving the total of 6.4 Tbit on a single fiber.

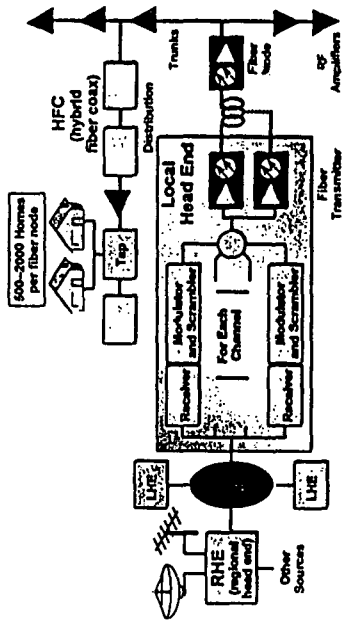
### Network Evolution



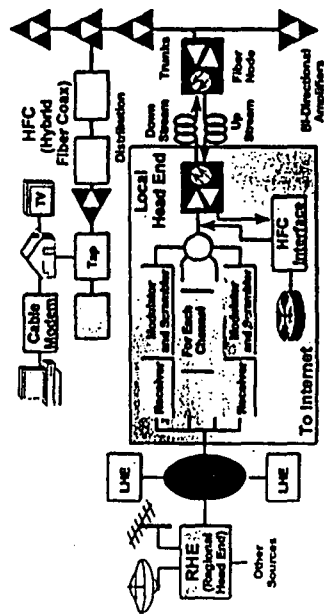
### Fiber Network architecture Hybrid Fiber Coax (HFC)



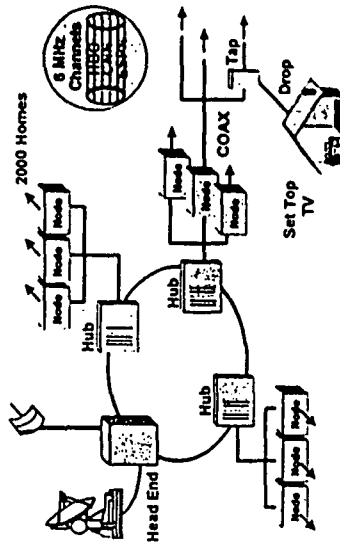
### Cable TV Network Diagram One Way



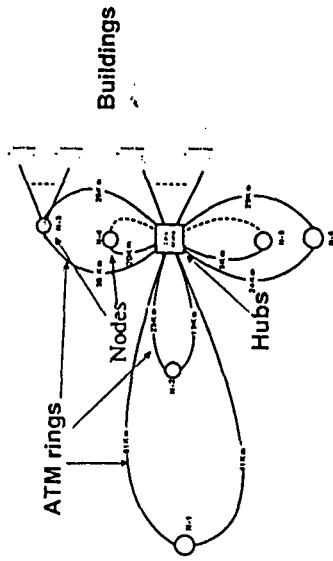
### Cable TV Network Diagram Two Way



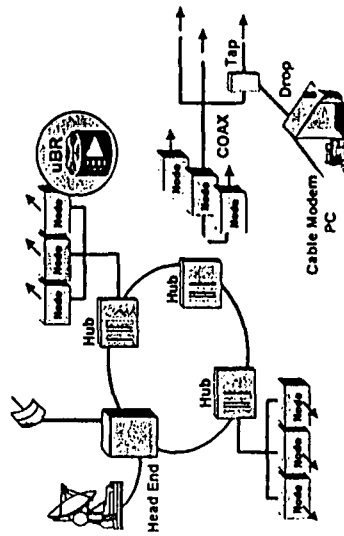
### Head End Network Diagram



Corporate Access Network



Head End Network Diagram



# Theory of Laser

Heinz P. Weber  
Institute of Applied Physics  
University of Bern  
heinz.weber@iap.unibe.ch



## Light Amplification by Stimulated Emission of Radiation

## **Laser principle**

---

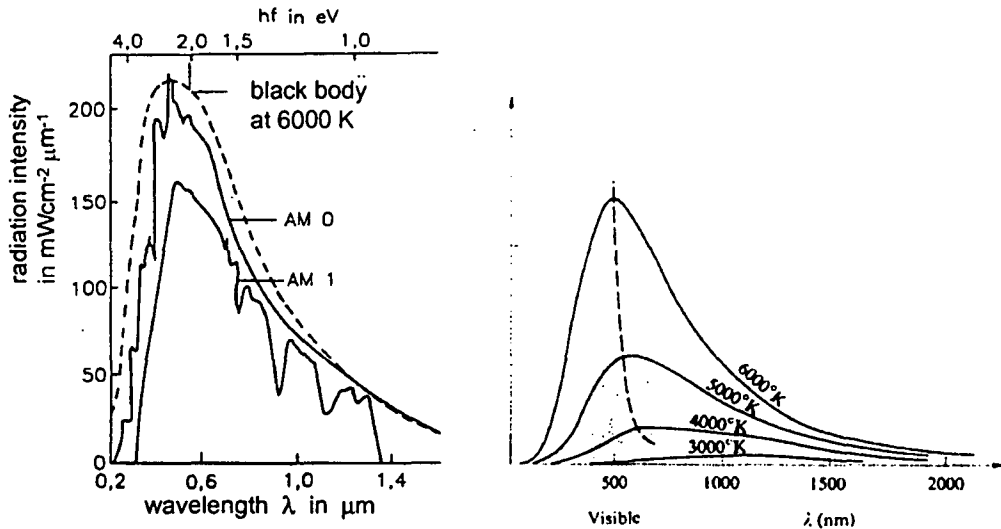
- Properties of lasers
- Absorption, spontaneous and stimulated emission
- Population inversion
- Optical amplification
- Excitation mechanism
- Energy levels with the laser process

## **Properties of laser light**

---

- monochromatic
- small Divergence
- coherence
- high beam intensity
- ultrashort light pulses possible

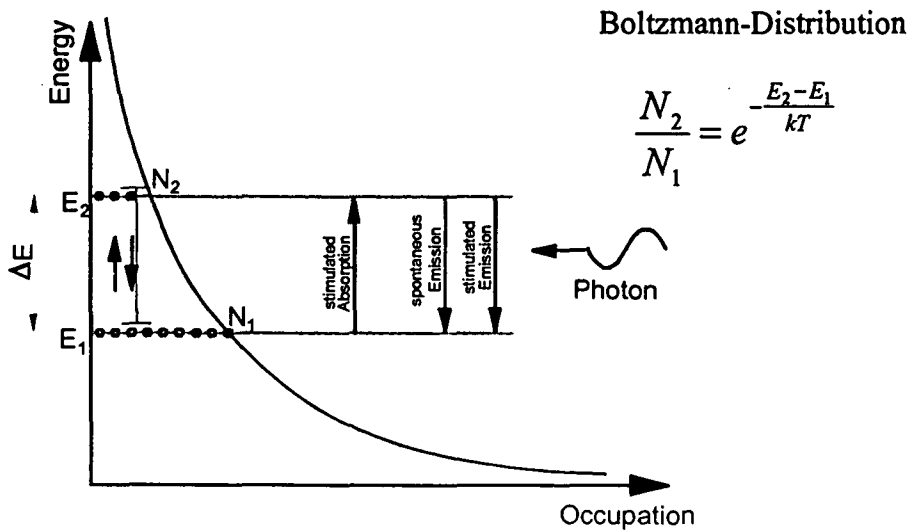
# Planck radiation law



Laser Theory

H.P. Weber

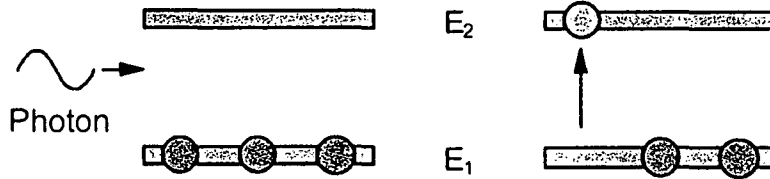
# Thermodynamic equilibrium



Laser Theory

H.P. Weber

## Absorption



$$E_{\text{photon}} = h\nu = E_1 - E_2$$

$$\lambda_{\text{photon}} = \frac{hc}{E_1 - E_2}$$

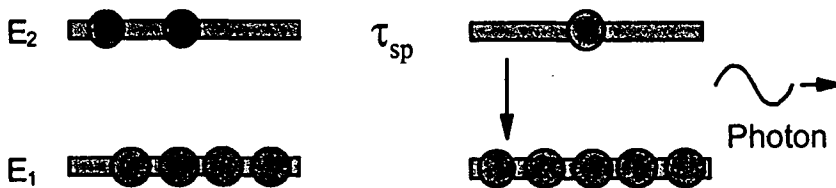
$$dW_{12} = u(\nu) B_{12} dt$$

$B_{12}$  = Einstein-coefficient  
for Absorption

Laser Theory

H.P. Weber

## Spontaneous emission



$$dW_{21}^{\text{sp}} = A_{21} dt$$

$$A_{21} = \frac{1}{\tau_{sp}}$$

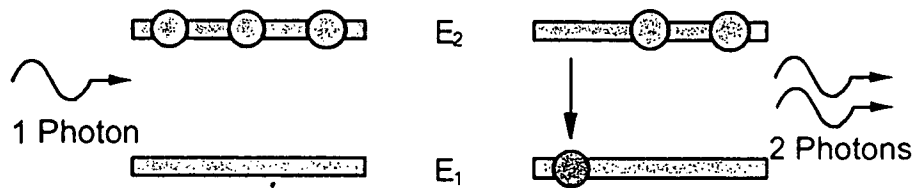
Einstein coefficient  
for spontaneous Emission

Laser Theory

H.P. Weber



## Stimulated emission



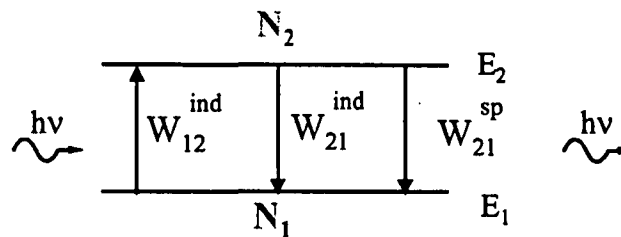
$$dW_{21}^{\text{ind}} = u(\nu) B_{21} dt$$

$B_{21}$  = Einstein coefficient  
for stimulated  
Emission

Laser Theory

H.P. Weber

## Rate equations



Niveau 1:

$$\frac{dN_1}{dt} = -N_1 B_{12} u(\nu) + N_2 B_{21} u(\nu) + N_2 A_{21}$$

Niveau 2:

$$\frac{dN_2}{dt} = N_1 B_{12} u(\nu) - N_2 B_{21} u(\nu) - N_2 A_{21}$$

Laser Theory

H.P. Weber

## Thermodynamic equilibrium

Transition  $1 \leftrightarrow 2 =$  Transition  $2 \leftrightarrow 1$

$$N_2 A_{21} + N_2 B_{21} u(\nu) = N_1 B_{12} u(\nu)$$

 Radiation field

$$u(\nu) = \frac{N_2 A_{21}}{N_1 B_{12} - N_2 B_{21}}$$

$$u(\nu) = \frac{A_{21}}{B_{21}} \cdot \frac{\frac{N_2}{N_1}}{\frac{B_{12}}{B_{21}} \left(1 - \frac{N_2}{N_1}\right)}$$

Laser Theory

H.P. Weber

## Thermodynamic equilibrium

Population densities behave to form a Boltzmann-distribution

$$\frac{N_2}{N_1} = e^{-\frac{E_2 - E_1}{kT}}$$

$$u(\nu) = \frac{A_{21}}{B_{21}} \cdot \frac{e^{-\frac{h\nu}{kT}}}{\frac{B_{12}}{B_{21}} \left(1 - e^{-\frac{h\nu}{kT}}\right)} = \frac{A_{21}}{B_{21}} \cdot \frac{1}{\frac{B_{12}}{B_{21}} \left(e^{\frac{h\nu}{kT}} - 1\right)}$$

Laser Theory

H.P. Weber

## Einstein coefficients

Radiation field follows the thermodynamic Equilibrium of the Planck Radiation formula

$$u(\nu, T) d\nu = \frac{8\pi h \nu^3}{c^3} \cdot \frac{1}{e^{\frac{h\nu}{kT}} - 1} d\nu$$



$$B_{21} = B_{12}$$

$$\frac{A_{21}}{B_{21}} = \frac{8\pi h \nu^3}{c^3}$$

Laser Theory

H.P. Weber

## Spontaneous and stimulated emission

$$\frac{dW_{21}^{ind}}{dW_{21}^{sp}} = \frac{B_{21} u(\nu) dt}{A_{21} dt} = \frac{1}{e^{\frac{h\nu}{kT}} - 1}$$

Ratio of probability for stimulated and spontaneous Emission

1) high Frequencies  $\nu$ :  $h\nu \gg kT$

$$\frac{dW_{21}^{ind}}{dW_{21}^{sp}} = e^{-\frac{h\nu}{kT}} \ll 1$$

2) low Frequencies  $\nu$ :  $h\nu \ll kT$

$$\frac{dW_{21}^{ind}}{dW_{21}^{sp}} = \frac{kT}{h\nu} \gg 1$$

Laser Theory

H.P. Weber

## Population inversion and amplification

The beam intensity  $I_\nu$  at frequency  $\nu$  [ $\text{Wcm}^{-2}$ ] is connected to spectral energy density [ $\text{Ws}\cdot\text{cm}^{-3}$ ] via the velocity of light  $c$  :  $u(\nu) = \frac{I_\nu}{c}$

Gain rate of the beam intensity in propagation direction

$$\frac{dI_\nu}{dx} = \frac{h\nu}{c \cdot \Delta\nu} \cdot B_{21}(N_2 - N_1) \cdot I_\nu$$

$$I_\nu(x) = I_{\nu 0} \cdot e^{\alpha_\nu x} \quad \text{with} \quad \alpha_\nu = \frac{c^2}{8\pi\nu^2 \Delta\nu} \cdot (N_2 - N_1) \cdot \frac{1}{\tau_{sp}} \quad A_{21}$$

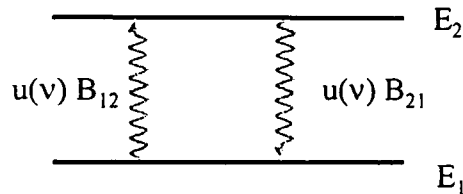
$\alpha_\nu$  = Amplification coefficient in the center of the amplification profile with center frequency  $\nu$  and half width  $\Delta\nu$ .

## Excitation methods

- Optical excitation
- Electrical excitation via gas discharge
- Electrical excitation via carrier injection
- Chemical reactions

## Optical excitation (2-level-system)

$u(\nu)$  = irradiated spectral energy density



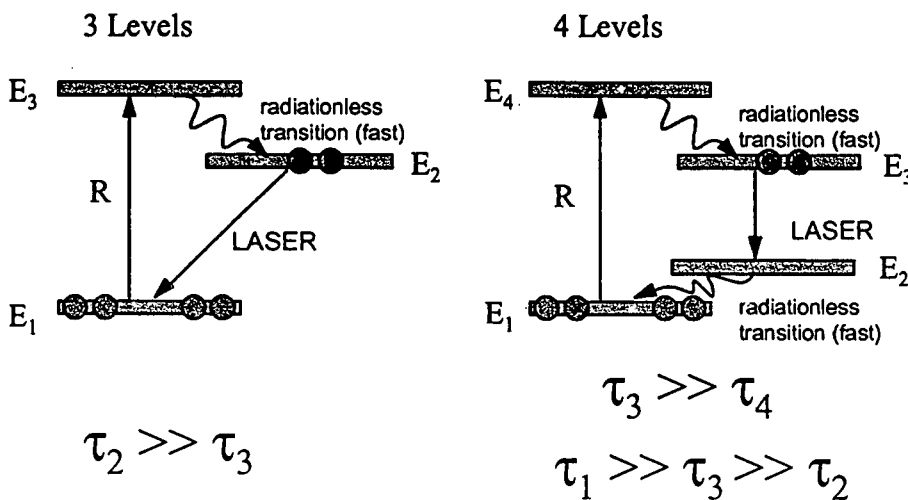
absorption = stimulated emission

With optical excitation in a two-level-system population inversion can not be realized erreicht werden! Optical excitation leads at its best to equal population (= transparent).

Laser Theory

H.P. Weber

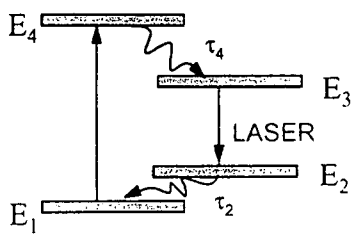
## Laser energy levels



Laser Theory

H.P. Weber

## 4-level-system



Lifetime  $\tau_4$  and  $\tau_2$  small means

⇒ Energy levels 4 and 2 practically empty

$$N_1 = N_1 + N_3 \quad \text{total occupation density}$$

$$\frac{dN_3}{dt} = R \cdot N_1 - A_{32} N_3 - u(\nu) \cdot B_{32} (N_3 - N_2)$$

Density of photon number: 
$$\frac{dn}{dt} = u(\nu) \cdot B_{32} (N_3 - N_2) - \frac{n}{\tau_c}$$

Spectral energy density  $u(\nu)$  is equivalent to density of photon number

$$B_{32} \cdot u(\nu) = B_{32} \cdot n \cdot \frac{h\nu}{\Delta\nu} = B \cdot n$$

Rate equations for 4-level-systems

$$\frac{dN_3}{dt} = R \cdot N_1 - A_{32} N_3 - B \cdot n \cdot (N_3 - N_2) \quad \text{and} \quad \frac{dn}{dt} = B \cdot n \cdot (N_3 - N_2) - \frac{n}{\tau_c}$$

Laser Theory

H.P. Weber

## Population inversion

with  $\Delta N = N_3 - N_2 \approx N_3$  the rate equation reads:

$$\frac{d\Delta N}{dt} = R \cdot N_1 - B \cdot \Delta N \cdot n - \frac{\Delta N}{\tau_3} \quad \text{and} \quad \frac{dn}{dt} = B \cdot \Delta N \cdot n - \frac{n}{\tau_c}$$

This is a system of nonlinearly coupled differential equations.  
Both equations hold the common nonlinear term  $\Delta N n$ .

One can deduce:

- 1.) Critical population inversion at threshold
- 2.) Population inversion in steady state

Laser Theory

H.P. Weber

## Critical inversion

To reach the oscillation condition  $\alpha_v 2L \geq \delta$  a minimum population inversion  $\Delta N_c$  is required.

When the laser oscillates, then the change in density photon number must be  $\geq 0$

$$\frac{dn}{dt} \geq 0 \quad \text{hence} \quad \left( B \cdot \Delta N - \frac{1}{\tau_c} \right) \cdot n \geq 0$$

critical population:  $\Delta N_c = \frac{1}{\tau_c \cdot B}$

critical pump rate:  $R_c \cdot N_1 = \frac{\Delta N}{\tau_3} \approx \frac{N_3}{\tau_3}$

The critical pump rate that leads to the critical population inversion  $\Delta N_c$  at laser threshold, just compensates the decay of the excited atoms via spontaneous emission out of the upper laser level.

## Population inversion at steady state

If the pump rate is increased after reaching the critical inversion, at sufficiently high pump rate a constant density of photon number  $n_0$  is established.

Requirement:  $R = \text{const.} > R_c$ ,  $n(t) = n_0 = \text{const.}$ ,  $dn/dt = 0$

→ for the density of photon number

$$0 = n_0 \cdot \left( B \cdot \Delta N - \frac{1}{\tau_c} \right) \quad n_0 > 0 \text{ folgt: } \Delta N_0 = \frac{1}{\tau_c B}$$

Population inversion at threshold = Population inversion in equilibrium

$$\Delta N_0 = \Delta N_c$$

# Resonators

---

It is the gain medium that delivers the power  
and  
It is the resonator, that determines the quality of the radiation field !

- Properties of optical resonators used for lasers
- Influence of resonator geometry on laser radiation properties
- \* Manipulation of local intensity distribution of laser radiation

# Resonators

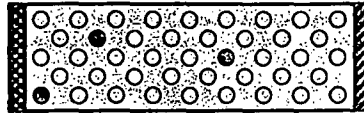
---

- Resonator geometry
- Transverse order modes
- Resonator types
- Stable laser oscillation
- Fabry-Pérot-resonator



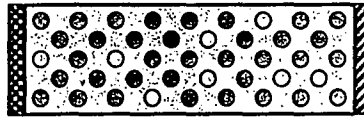
# Laser resonator principle

Original state

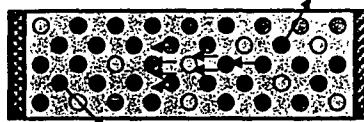


Pump- light

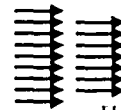
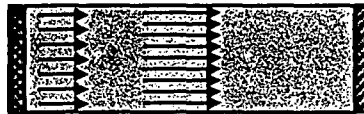
Excitation



stimulated emission



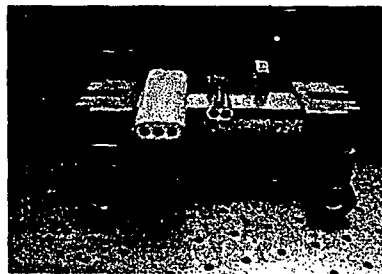
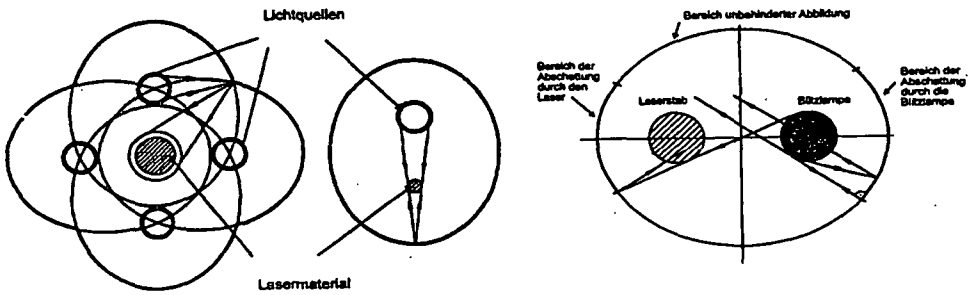
Resonator-oscillation



H.P. Weber

Laser Resonator

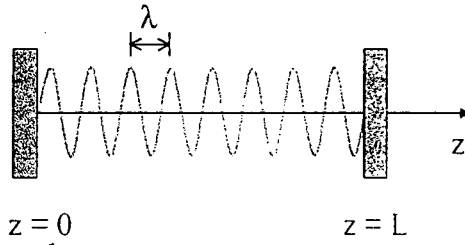
# Laser - excitation



H.P. Weber

Laser Resonators

# Fabry-Pérot-Resonator



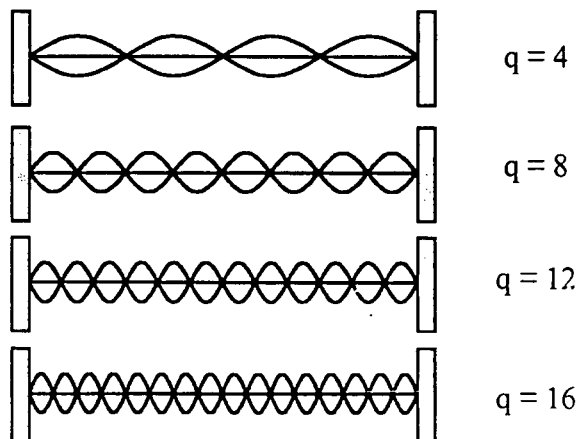
stationary field distribution within the resonators:  
 (linearly polarized wave in x-direction  $E_x(z,t) = E_x(z)$ )

$$E(z) = E_0 \cdot \sin kz = E_0 \cdot \sin \frac{2\pi}{\lambda} \cdot z \quad kL = q\pi \quad q = 0, 1, 2, 3, \dots$$

$q$  = Number of nodes along resonator axis

$$q = \frac{L}{\lambda/2}$$

# Field distribution



axial modes in  
 Fabry-Pérot  
 resonator

## Fabry-Pérot-resonator

$k_q$  = wavevector of standing wave with  $q$  nodes in resonator

→ Oscillating radiation is superposition of individual standing waves with the longitudinal field distributions  $E_q$ :

$$E(z) = \sum_q E_q = \sum_q E_{q0} \cdot \sin k_q z$$

The resonator condition  $kL = q\pi$  however tells what the individual frequencies (or wavelengths) of the individual standing waves are:

The Resonator length  $L$  requires:

$$kL = q\pi \quad \text{and} \quad \nu = \frac{c}{\lambda} = k \cdot \frac{c}{2\pi} \quad \longrightarrow \quad \boxed{\nu_q = q \cdot \frac{c}{2L}}$$

Laser Resonators

H.P. Weber

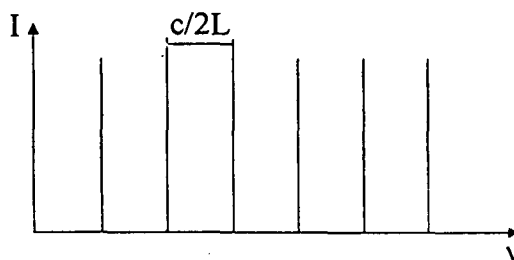
## Resonance condition

Frequency separation between adjacent modes:  $\nu_q - \nu_{q-1} = \nu_{q+1} - \nu_q = c/2L$

Frequency separation  $c/2L$  is named free spectral range of the resonator



**Frequency spacing between mode neighbours depends only on the length of the resonator!**



Frequency spectrum of an ideal resonator

Laser Resonators

H.P. Weber

## Resonance condition

- The longitudinal field distributions of the electrical field in an open resonator can be described by superposition of standing waves
- The length of the resonator is a multiple  $q$  of half the wavelength of a mode
- Frequency separation of adjacent modes depends only on the length of the resonator

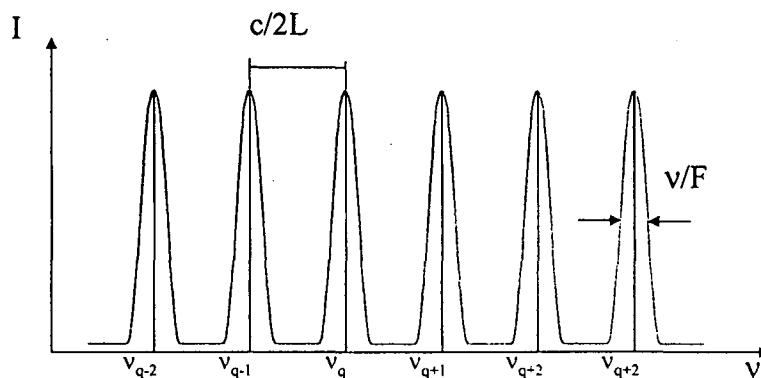
Resonance-wavelength:  $\lambda_q = \frac{2L}{q}$

Free spectral-range:  $\nu_q = \frac{c}{2L}$

Laser Resonators

H.P. Weber

## Real resonator



Laser Resonators

H.P. Weber

## Intensity in passive resonator

Intensity in resonator is a function of frequency

$$I = \frac{I_{\max}}{1 + \left(\frac{2F}{\pi}\right)^2 \cdot \sin^2\left(\frac{\pi\nu}{\nu_q}\right)}$$

$$r = \frac{E_0}{E_r} = \sqrt{\frac{I_0}{I_r}} \quad \text{Mirror reflections}$$

$$F = \frac{\pi\sqrt{r}}{1-r} = \text{Finesse}$$

The Finesse is a measure for the quality of the resonators. The finesse is responsible for the width of the resonance frequency  $\delta\nu = \nu/F$  and the lifetime  $\tau_c$  of the photons within the resonator.

Laser Resonators

H.P. Weber

## Properties of passive resonator

Max. Intensity:  $I = I_{\max}$  für  $\nu = \nu_q$

Min. Intensity:  $I = I_{\min}$  für  $\nu = \frac{2q-1}{2} \cdot \nu_q$

$$I_{\min} = \frac{I_{\max}}{1 + \left(\frac{2F}{\pi}\right)^2}$$

The contrast (difference between  $I_{\max}$  und  $I_{\min}$ ) becomes larger with increasing finesse  $F$  of the resonator.

Halfwidth  $\delta\nu$  of the resonances:  $\delta\nu = \frac{\nu_q}{F}$

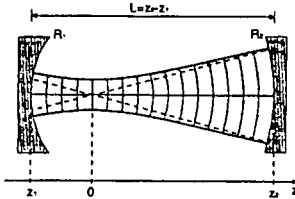
Lifetime of trapping of photons  $\tau_c$ :  $\tau_c = 2\pi \frac{1}{\delta\nu}$

Laser Resonators

H.P. Weber

# Confocal resonator

- How is the transversal field distribution of resonator modes ?
- What are the conditions for stable resonators ?



Gaussian and Hermite-Gaussian distributions are solutions of the wave equation

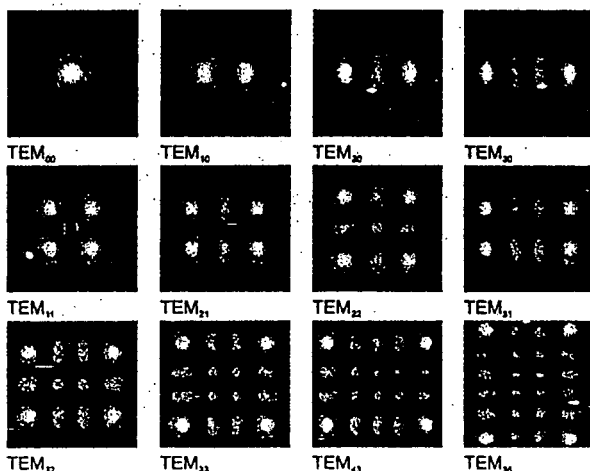
$$E(x, y, z) \approx e^{-\frac{x^2+y^2}{\omega^2(z)}} \cdot e^{-ik \cdot \frac{x^2+y^2}{2R(z)}}$$

$$E(x, y, z) \approx \left(\frac{\omega_0}{\omega}\right) H_1\left(\sqrt{2} \frac{x}{\omega}\right) \cdot H_m\left(\sqrt{2} \frac{y}{\omega}\right) \cdot e^{-\frac{x^2+y^2}{\omega^2(z)}} \cdot e^{\left\{-ik \left(\frac{x^2+y^2}{2R(z)}\right) + i(1+l+m)\Phi\right\}}$$

Laser Resonators

H.P. Weber

# Transverse order modes (Hermite-Gauss)



transverse order  
intensity distribution

$$TEM_{lmq}$$

Hermite-Polynoms:

$$H_0(u) = 1$$

$$H_1(u) = 2u$$

$$H_2(u) = 4u^2 - 2$$

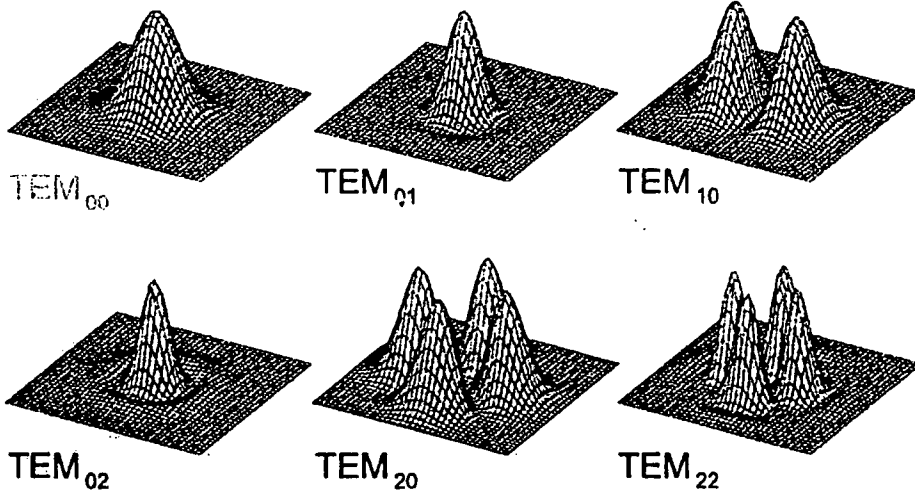
$$H_3(u) = 8u^3 - 12u$$

$$H_4(u) = 16u^4 - 48u^2 + 12$$

Laser Resonators

H.P. Weber

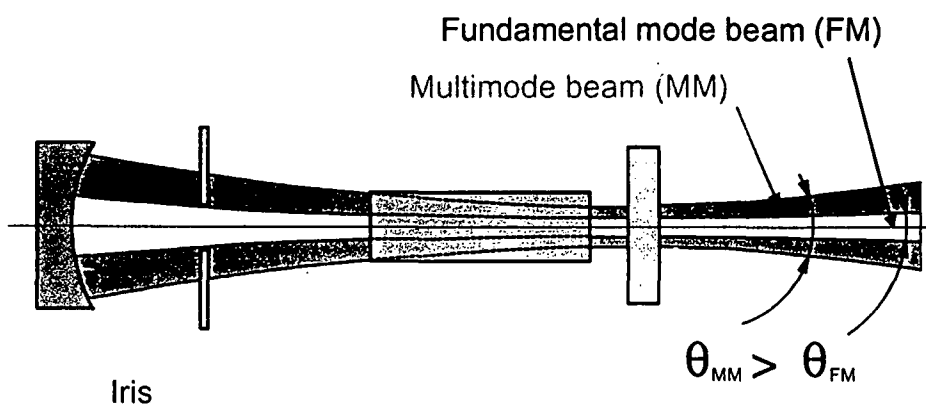
## Transverse order modes (Laguerre-Gauss)



Laser Resonators

H.P. Weber

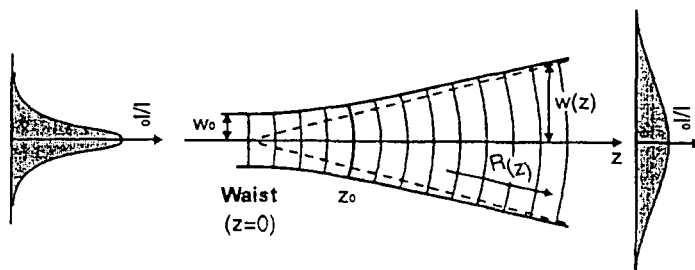
## Mode selection



Laser Resonators

H.P. Weber

## Gauss intensity distribution



$$z_0 = \frac{\pi \omega_0^2}{\lambda} \quad \text{Rayleigh Range}$$

$$\Phi(z) = \tan^{-1} \left( \frac{z}{z_0} \right) \approx \frac{\lambda}{\pi \omega_0}$$

$$R(z) = z \cdot \left[ 1 + \left( \frac{z_0}{z} \right)^2 \right]$$

$$\omega^2(z) = \omega_0^2 \left[ 1 + \left( \frac{z}{z_0} \right)^2 \right]$$

Laser Resonators

H.P. Weber

## Focus diameter

What is the minimum realizable spot size by focusing with a lens of focal length  $f$  ?

$$w_{\min} = f \cdot \Phi \quad \text{lower limit is given by diffraction law}$$

$$w_{\min} = f \cdot \frac{2}{\pi} \cdot \frac{\lambda}{D_L} = \frac{2}{\pi} \cdot \lambda \cdot \frac{f}{D_L} \quad D_L = \text{Diameter of incident beam}$$

$$w_{\min} \approx \lambda \cdot F$$

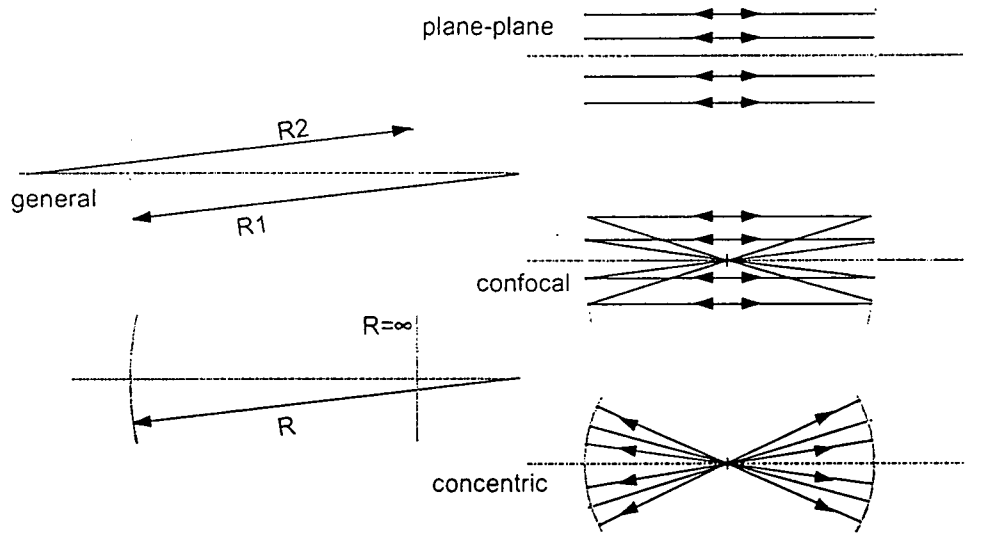
$F = f/D_L$  is ratio between focal length and diameter of incident beam

Laser Resonators

H.P. Weber



# Resonator geometries



Laser Resonators

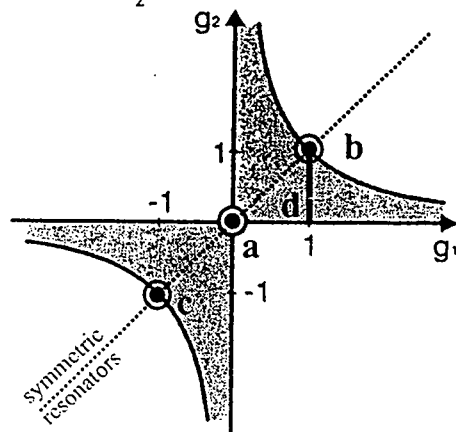
H.P. Weber

# Stability criteria

g-Parameters:  $g_1 = 1 - \frac{L}{R_1}$       $g_2 = 1 - \frac{L}{R_2}$

$0 \leq g_1 \cdot g_2 \leq 1$

- a) confocal ( $R_1 = R_2 = L$ )
- b) plane-plane ( $R_1 = R_2 = \infty$ )
- c) concentric ( $R_1 = R_2 = L/2$ )
- d) semi-spherical ( $R_1 = \infty, R_2 \geq L$ )

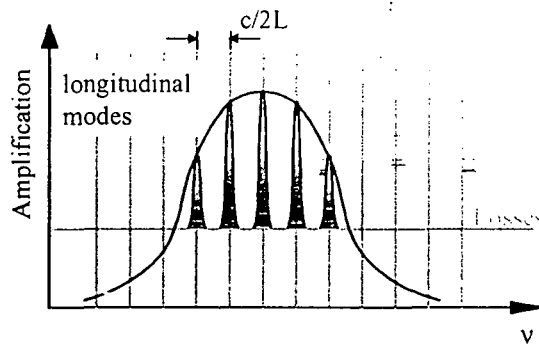


Laser Resonators

H.P. Weber

## Amplification profile

The linewidth broadening leads to modification of amplification  $\alpha_\nu$ . Instead of the natural linewidth  $\Delta\nu = 1/\tau$  the broadened line profile of the transition is essential and has to be taken to calculate the gain  $\alpha(\nu)$ .



Example:

HeNe ( $\lambda = 632 \text{ nm}$ ).

Resonator length  $L = 30 \text{ cm}$

Mode spacing  $\nu = c/2L = 500 \cdot 10^6 \text{ s}^{-1}$

Doppler width  $\nu_D = 3 \cdot 10^9 \text{ s}^{-1}$

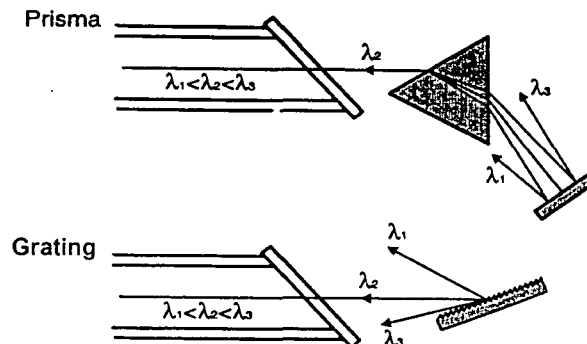
→ 6 longitudinal modes can oscillate

Laser Resonators

H.P. Weber

## Wavelength selection

frequency selective elements:  
Prisma  
Gratings  
Fabry-Pérot-Etalons

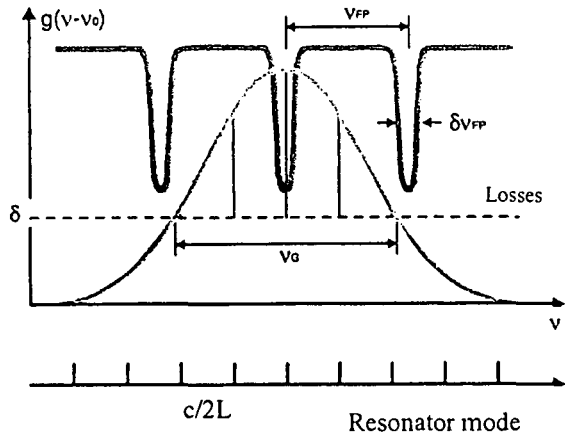


Laser Resonators

H.P. Weber

# Etalon

$$v_G < 2 v_{FP} \quad \delta v_{FP} < v = c/2L$$



Laser Resonators

H.P. Weber

# Coherence

Two waves are at a given point coherent to each other, if at this point the phase difference of the two waves is constant in time.

Time coherence

$$t_{\text{coherence}} \approx \frac{1}{\Delta v}$$

$$l_{\text{coherence}} = c \cdot t_{\text{coherence}}$$

Coherence time

Coherence length

Light source	Coherence time [s]	Coherence length [m]
visible light	$10^{-15}$	$3 \cdot 10^{-7}$
Hg lamp	$10^{-9}$	0.3
HeNe laser	$10^{-2} - 10^{-4}$	$3 \cdot 10^6 - 3 \cdot 10^4$

Coherence is equivalent to Interference capability

Laser Resonators

H.P. Weber



# Diode Pumped Solid State Laser Systems

H.P. Weber, W. Lüthy

Institute for Applied Physics, University of Bern, Sidlerstrasse 5,  
CH-3012 Bern, Switzerland



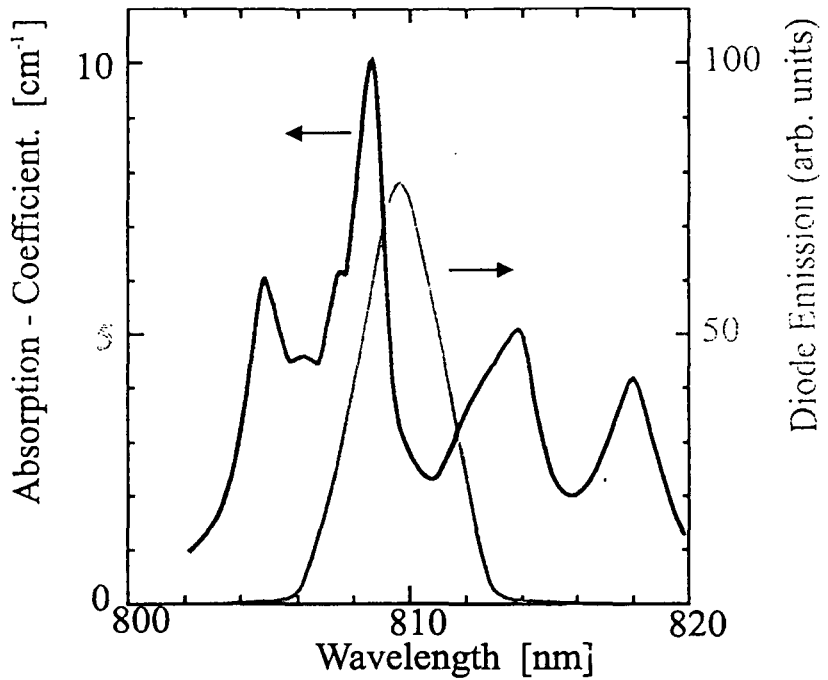
## Motivation for Diode Laser Pumping

- **very efficient**
- **no excess heating**
- **no high voltage**
- **no electrical noise**
- **all solid state**
- **reliable / long lifetime**



# Pump Wavelengths

- Al Ga As  
780 - 870 nm
- In Ga As  
900 - 990 nm



# Dopants and Sensitizers

	Absorption	Emission	Sensitizing
Nd	810 nm	1.06 , 1.33 $\mu\text{m}$	
Er	790 nm    970 nm	1.55 , 2.8 $\mu\text{m}$	
Tm	785 nm	1.9 $\mu\text{m}$	Ho at 2 $\mu\text{m}$
Yb	940 nm	1.02 $\mu\text{m}$	Ho at 2 $\mu\text{m}$ , Er at 2.8 $\mu\text{m}$



# Dopant Concentration

$$\text{Rate} \propto \left(\frac{1}{d}\right)^6$$

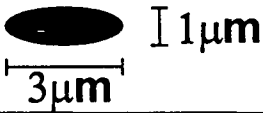
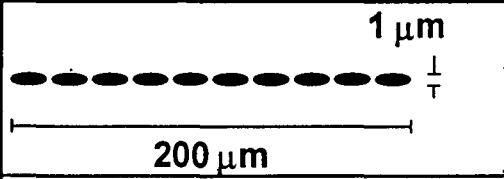
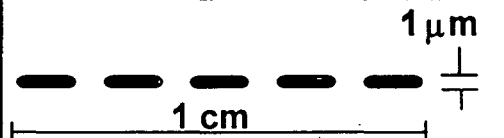
$$\text{Rate} = W \cdot C_1 \cdot C_2$$

## Enhancement by Migration



# Available laser diodes

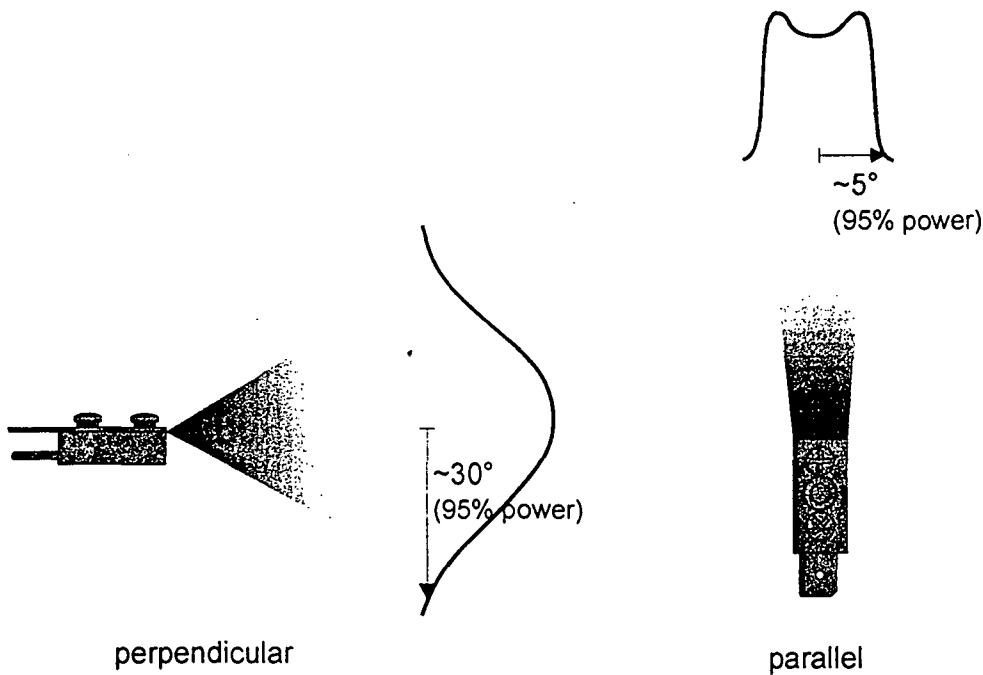
GaAlAs with  $\lambda = 780 \text{ nm} - 870 \text{ nm}$  or InGaAs with  $\lambda = 900 \text{ nm} - 990 \text{ nm}$

	<p>Single stripe (single mode) laser diodes diffraction limited emission, <math>P \approx 0.1 \text{ W}</math>; MOPA <math>\approx 1 \text{ W}</math>.</p>
	<p>Multistripe emitter (phased array) of laser diodes. The phase of adjacent diodes changes by <math>180^\circ</math>. This leads to dual lobed emission. <math>P \approx 1 \text{ W}</math>.</p>
	<p>Array of multistripe emitters (uncoupled phased arrays). Spatially incoherent emission <math>P \approx 10 \text{ W}</math></p>

Consequences: vertical angle  $\approx 40^\circ$  FWHM, horizontal angle  $\approx 10^\circ$  FWHM



# Emission Properties (e.g. Jenoptik 10 W)

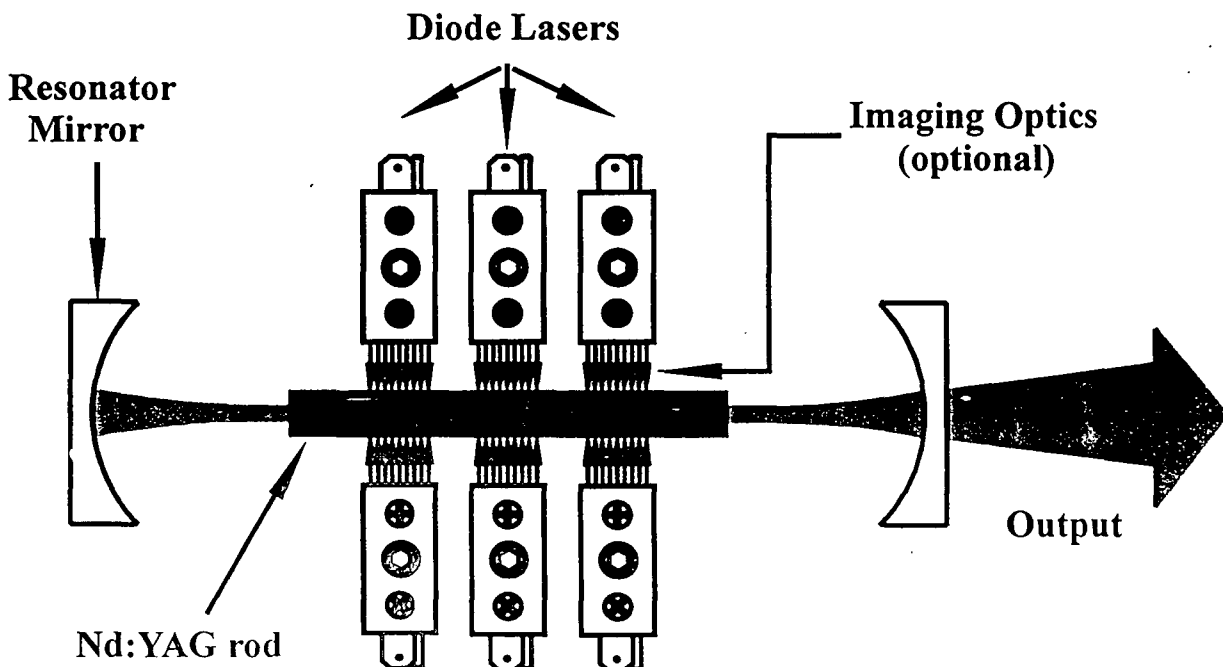


- Perpendicular to junction plane:  
Good beam quality, large divergence  
⇒ fast beamshaping optics required

- Parallel to junction plane:  
Bad beam quality, small divergence  
⇒ beamshaping?

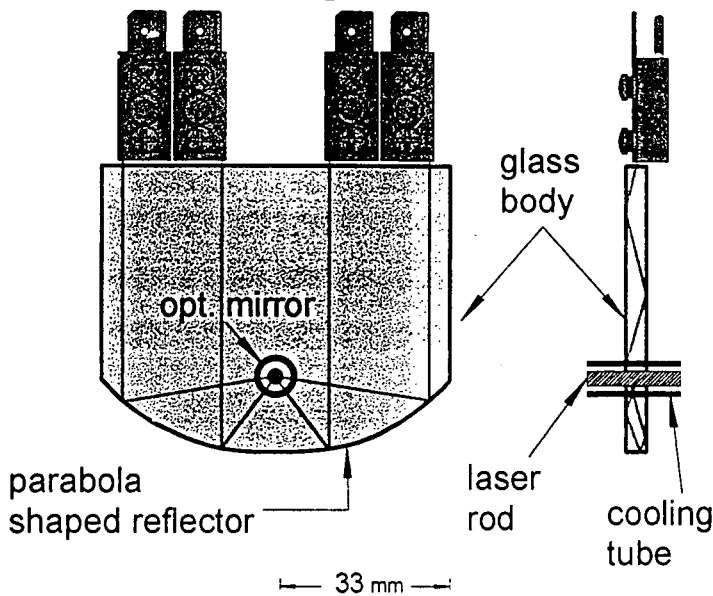


# Transverse Pumping Scheme





## Parabolic glass pump cavity setup

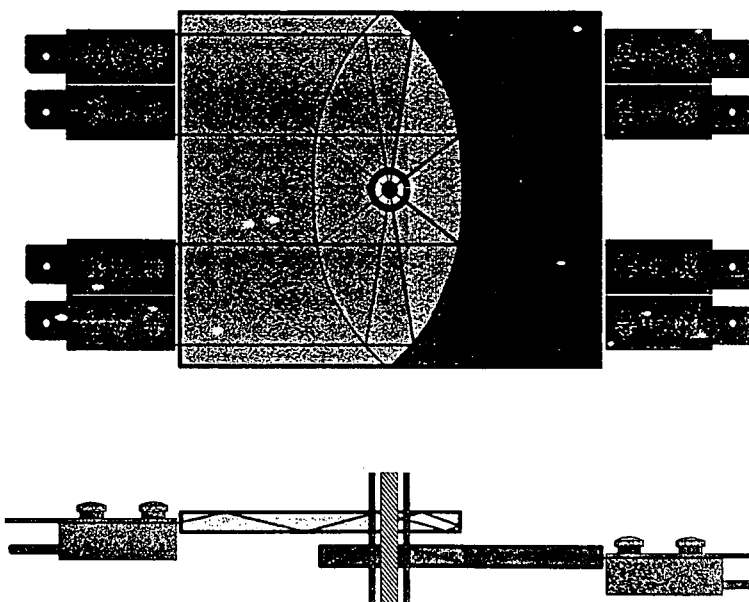


### Properties:

- reduced divergence ( $3.3^\circ$  @ 95%)
- thin cavities possible ( $\leq 4$  mm)
- 4 Diodes per slice (i.e.  $\sim 40 - 60$  W)
- low adjustment requirements ( $\pm 0.5$  mm)
- compact and scalable
- cheap



## Scaling the ParaLas design to high powers

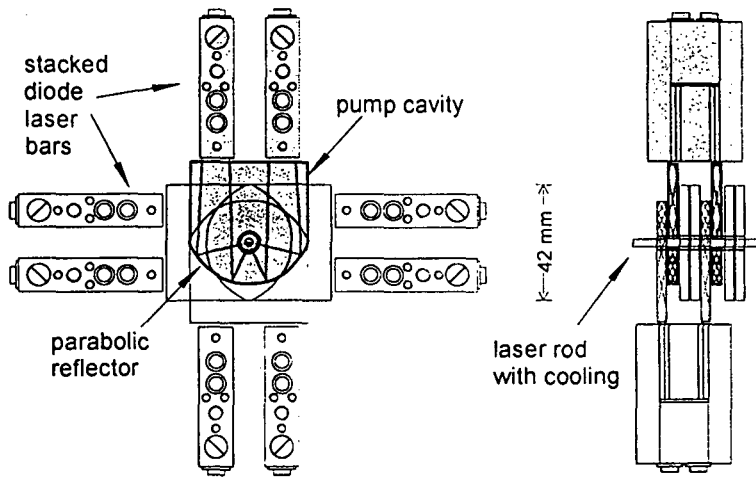


- Rotating the slices with respect to the others i.e.  $90^\circ$  symmetry
- Stacking along the rod axis
- Two parabola slices rotated by  $180^\circ$
- 4 mm thick slices
- Max. Pump power available:  $\sim 90$  W





# Experimental Results



Max. pump power =  
84 W/slice

$$\Rightarrow P_{pump, max} \approx 670 \text{ W}$$

Pumped length =  
26.4 mm

$$\Rightarrow 240 \text{ W/cm}$$

$P_{abs} \approx 60\%$

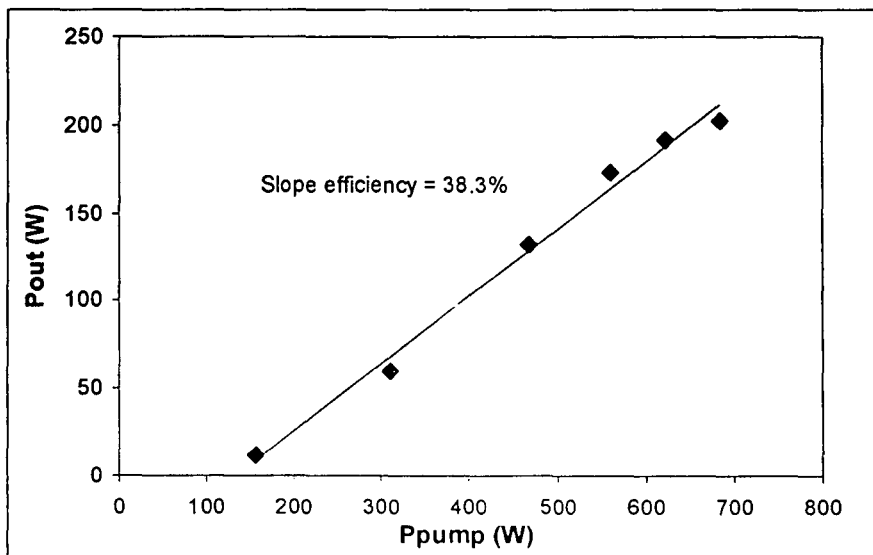
$$\Rightarrow g_0 \approx 0.25 \text{ cm}^{-1}$$

Thermal lens specific  
focal length

$$C_f \approx 18'000 \text{ mm} \cdot \text{W/mm}^2$$



# Performance of scaled diode-pumped Nd:YAG laser



$M^2 \approx 100 - 50$

$M^2 < 20$

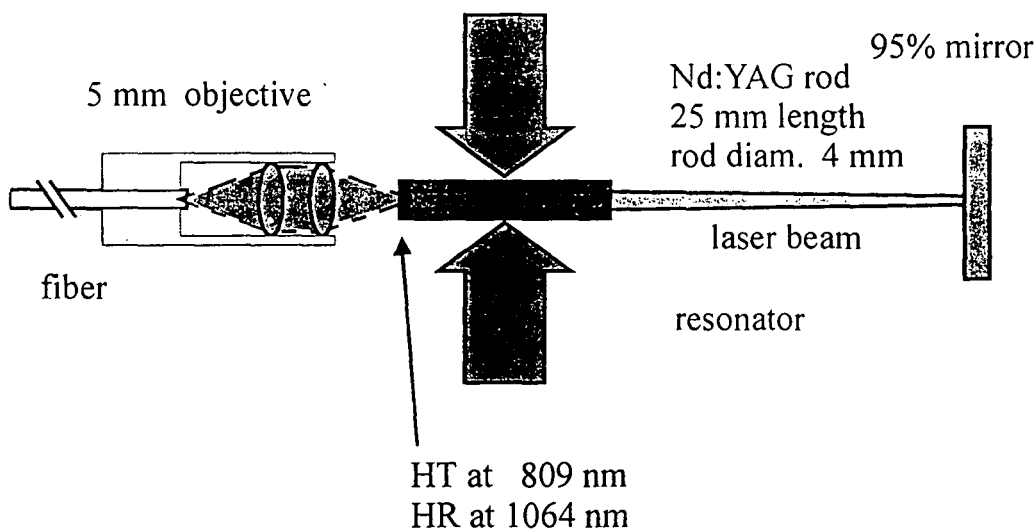
$P_{out} = 103 \text{ W}$   
with an optimized  
resonator



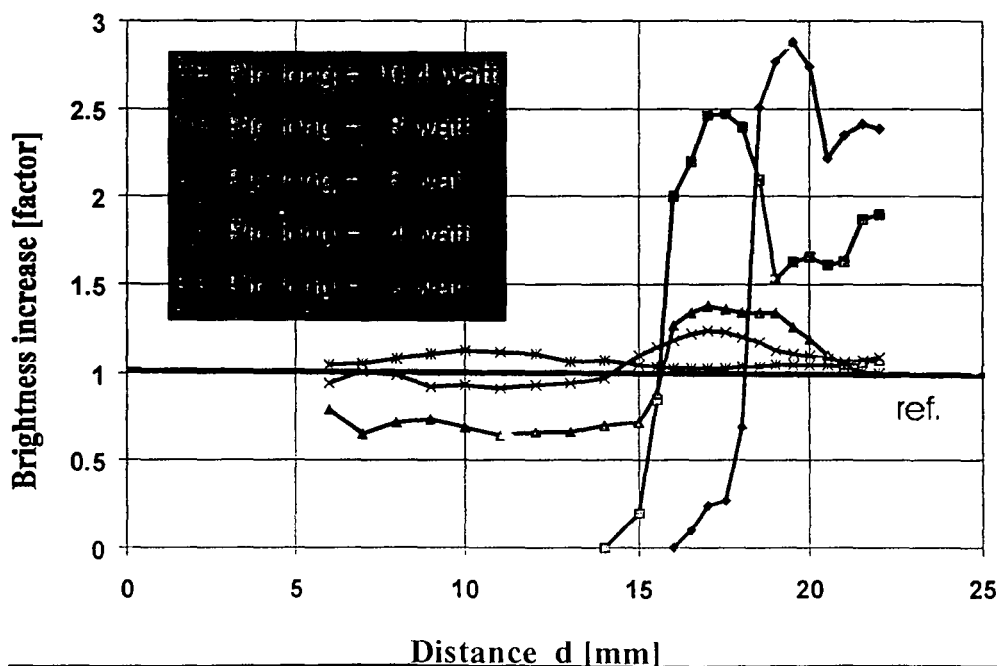
# Additional Longitudinal Pumping

longitudinal  
pumping  
max 13.7 Watt

transversal  
pumping  
140 Watt



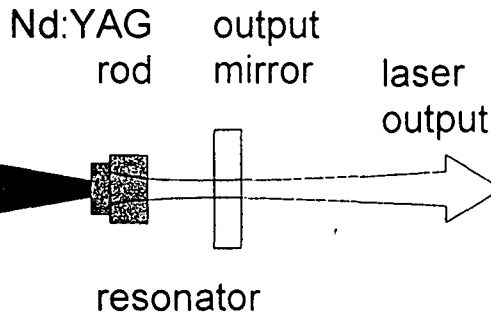
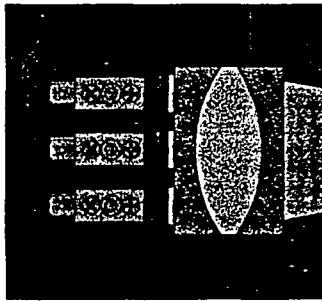
# Brightness increase (d), L = 313mm





# Pump Arrangements

diode laser  
pump source



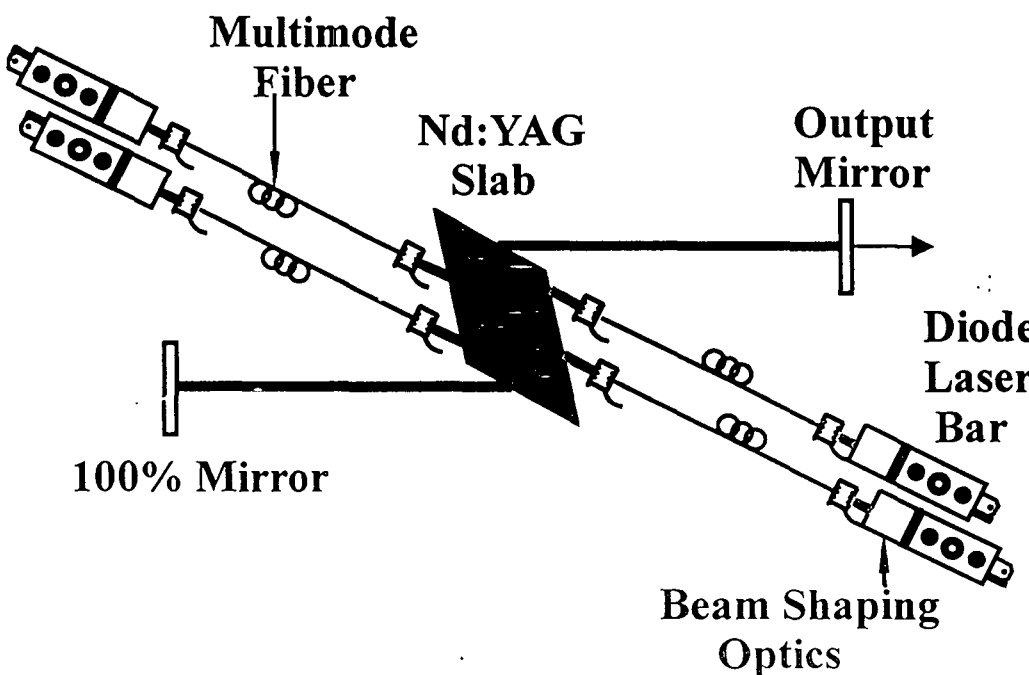
**Longitudinal pumping:**  
**High power cw single end diode pumped Nd:YAG laser**

$$P_{\text{pump}} > 100 \text{ W}$$

$$P_{\text{out}} > 50 \text{ W}$$



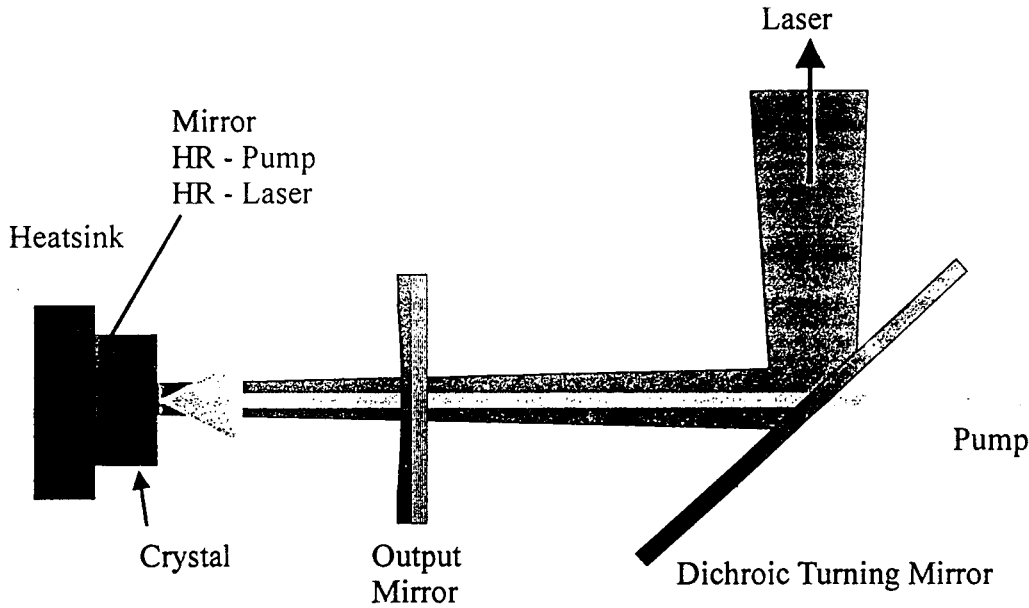
# Longitudinal Pumping Scheme



Scalable  
Compact  
Flexible  
different thermal lens in horiz. and vert. plane



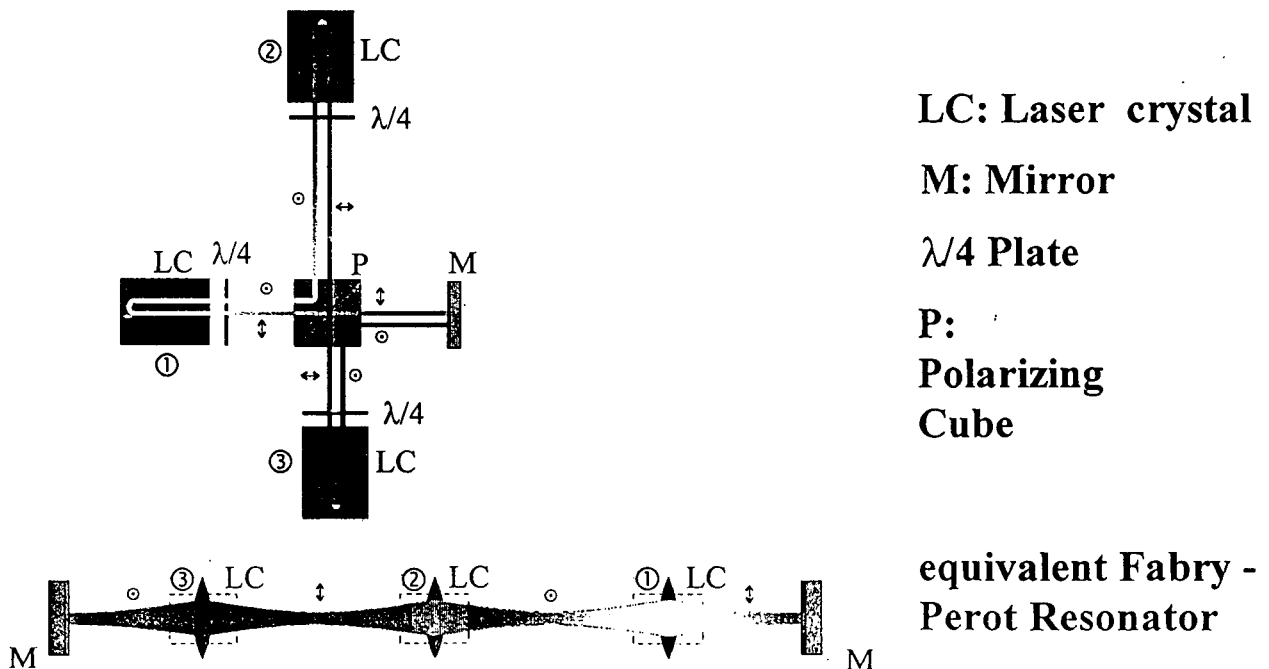
# Active Mirror Mode



Tm: Ho: YAG, P.J. Morris et al. Opt. Comm. 104, 97-101 (1993)

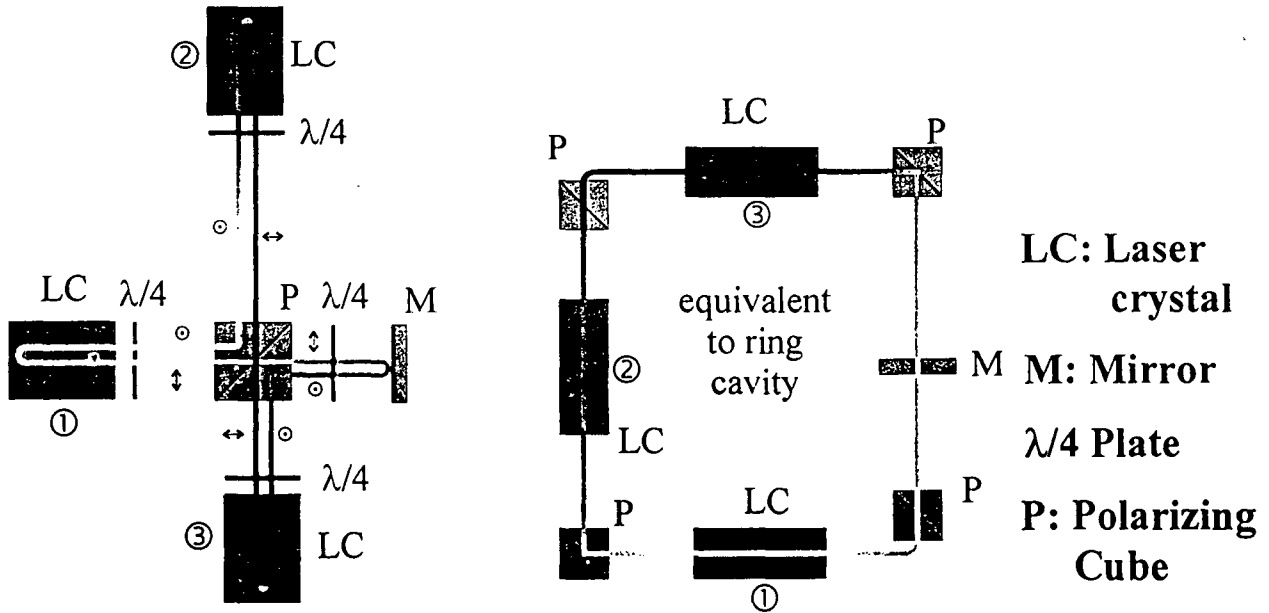


# System with Several Crystals

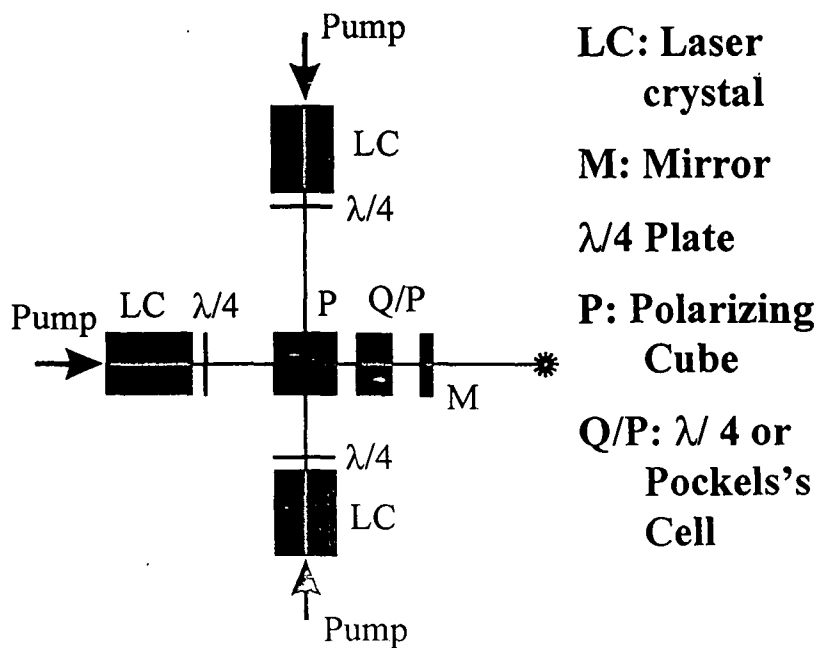
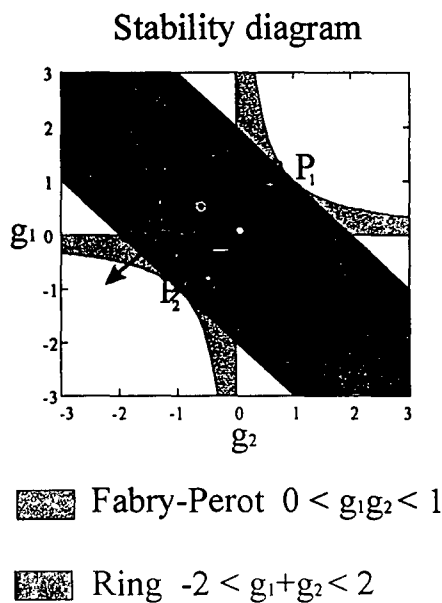




# Modified for Ring Laser Arrangement



# g - Diagram



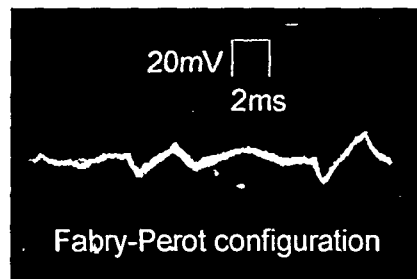
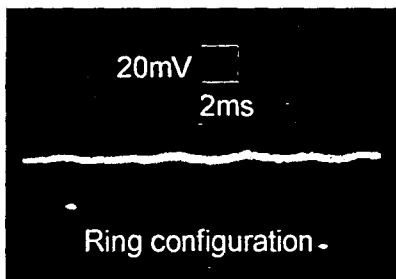


# Performance

## CW (both ring and Fabry-Perot)

slope efficiency: 53%  
 optical efficiency: 37%  
 output power: 9.9 W  
 $M^2$ : 1.0 .. 1.3

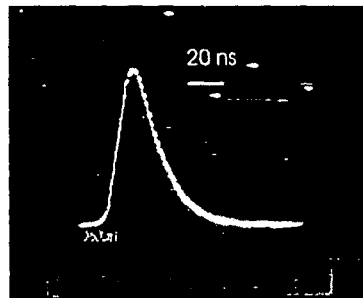
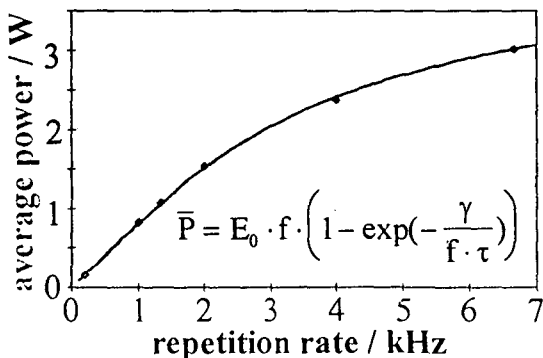
temporal stability near the confocal point



# Configuration Q - Switch

repetition rate /kHz	average power /W	energy per pulse /mJ	pulse duration /ns	peak power /kW
0.2	0.16	0.78	20	39
1.0	0.83	0.83	23	36
1.3	1.08	0.81	23	35
2.0	1.53	0.77	25	31
4.0	2.38	0.60	35	17
6.7	3.02	0.45	40	11

**total  
 pump power:  
 24 W**





# Summary / Outlook

**All Solid State Laser Systems will dominate the Market**

**Monomode Emission      1 W- 50 W :      Fibers**

**Multimode Emission      10 W - 1 kW :      Crystal  
Lasers**

**Applications:      Metal Machining  
                         Medicine  
                         Measurement**



# Polishing of diamond layers

H.P. Weber, S. Gloor, and W. Lüthy

Institute of Applied Physics, University of Bern,  
Sidlerstrasse 5, CH-3012 Bern, Switzerland,  
leinz.weber@iap.unibe.ch

S. Pimenov, and V.I. Konov

General Physics Institute, Vavilow Street 38,  
117942 Moscow, Russia



## Motivation

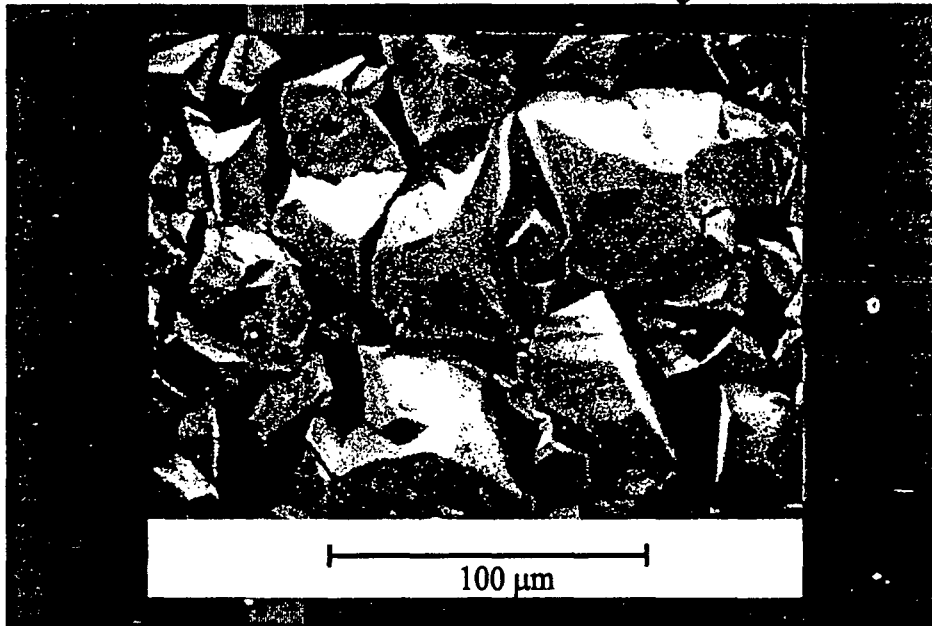
- **Surface hardening**
- **Tribology (0.05 with ruby)**
- **Cooling (4 – 5 Cu)**
- **Electronics**
- **Windows**

**Need for high  
surface quality**





## CVD Diamond Layers

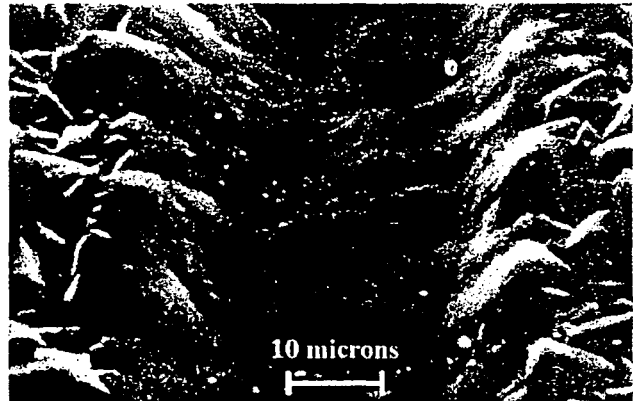
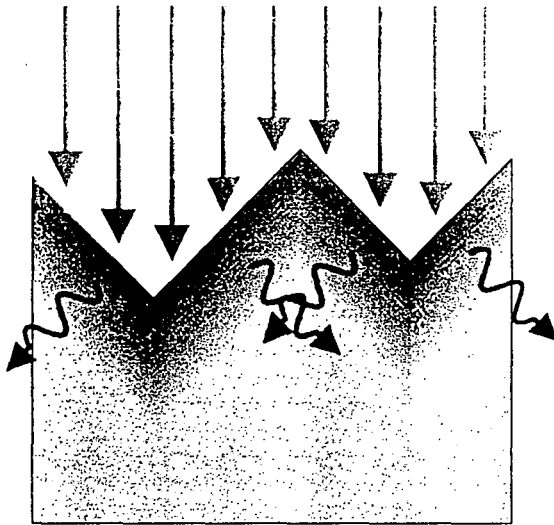


## Polishing

<u>Mechanical Polishing</u>	<u>Laser Polishing</u>
<ul style="list-style-type: none"><li>• High Quality</li><li>• <math>\pm</math> flat surfaces</li><li>• time consuming</li><li>• expensive</li></ul>	<ul style="list-style-type: none"><li>• Quality dependent on grain size</li><li>• arbitrary surfaces</li><li>• rapid process</li><li>• inexpensive</li></ul>



# Polishing Mechanisms: Heat dissipation



Diamond Polishing

Slide

5



# Lasers for Polishing

<p><b>ArF Excimer laser</b> <math>\lambda=193 \text{ nm}</math></p>	<ul style="list-style-type: none"> <li>• strong absorption,</li> <li>• short penetration depth (<math>1.6 \mu\text{m}</math>)</li> <li>• suitable for thin diamond layers</li> </ul>
<p><b>KrF Excimer laser</b> <math>\lambda=248 \text{ nm}</math></p>	<ul style="list-style-type: none"> <li>• absorption due to defects and impurities</li> <li>• Good optical elements available</li> <li>• high resolution etching</li> </ul>
<p><b>Cu-vapor laser</b> <math>\lambda=510 \text{ nm}</math></p>	<ul style="list-style-type: none"> <li>• absorption due to defects and impurities</li> <li>• high beam quality and repetition rate.</li> <li>• suitable for thick windows</li> </ul>

Diamond Polishing

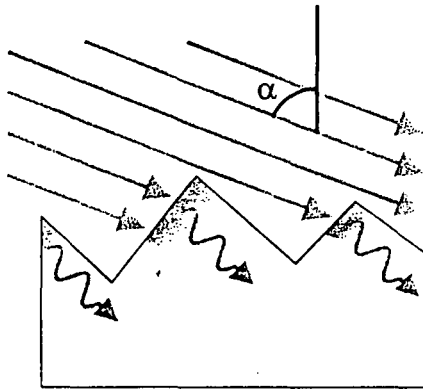
38

Slide

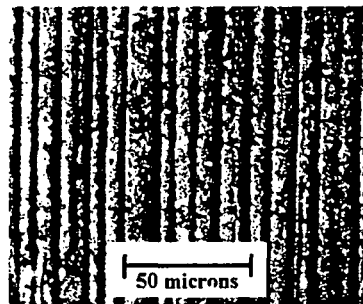
6



# Polishing: Influence of shadow



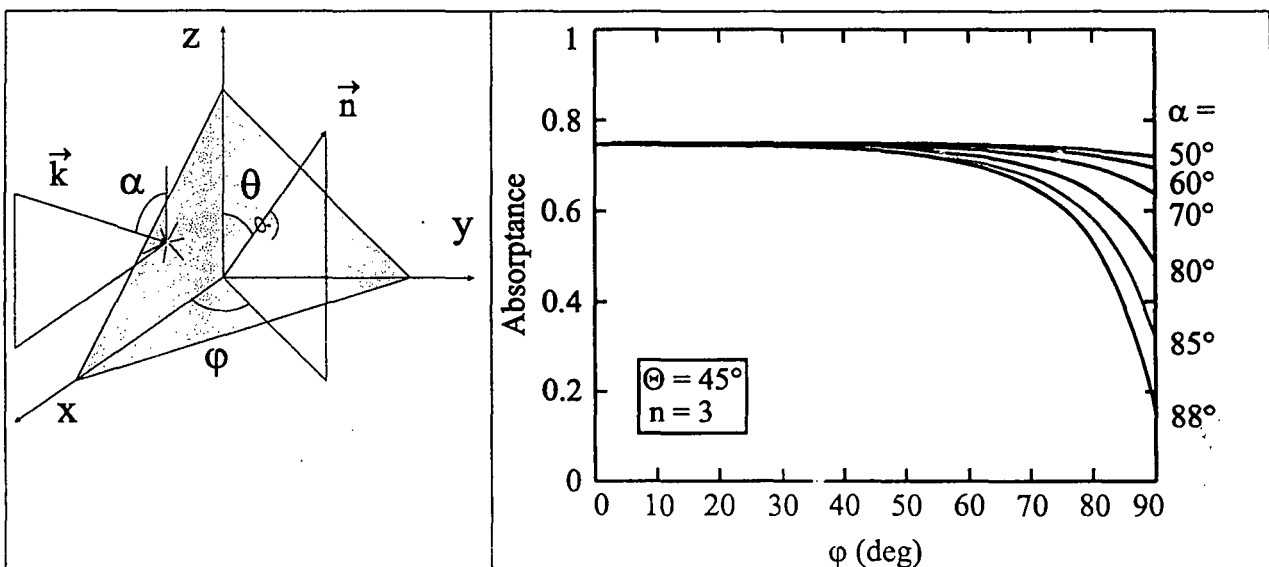
For  $\alpha = 85^\circ \Rightarrow$  Ripples



$\alpha$	$0^\circ$	$73^\circ$	$80^\circ$	$85^\circ$
$R_{\min}$ [ $\mu\text{m}$ ]	0.17	0.12	0.09	0.11

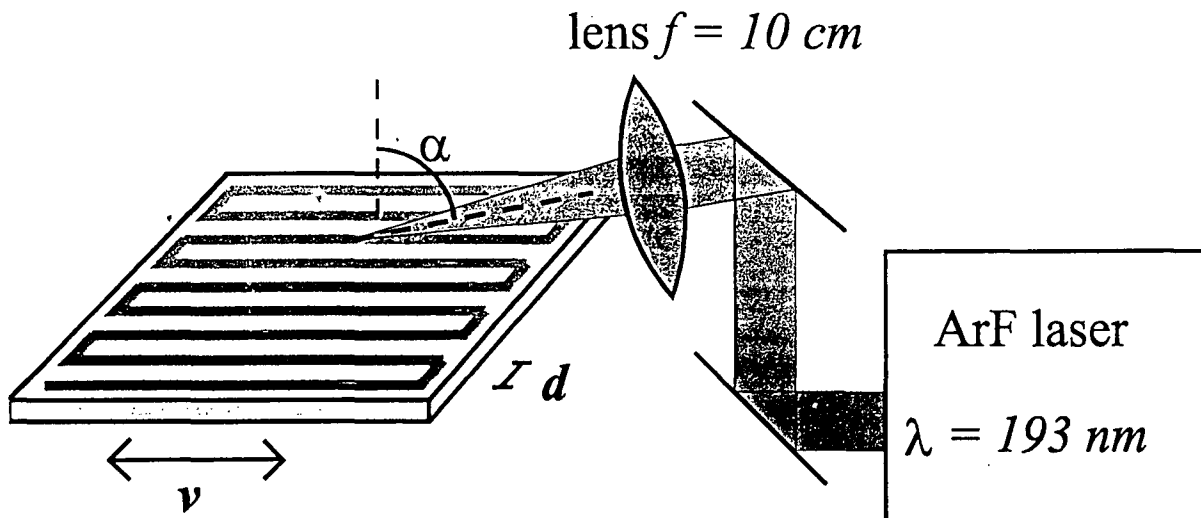


# Origin of Ripples

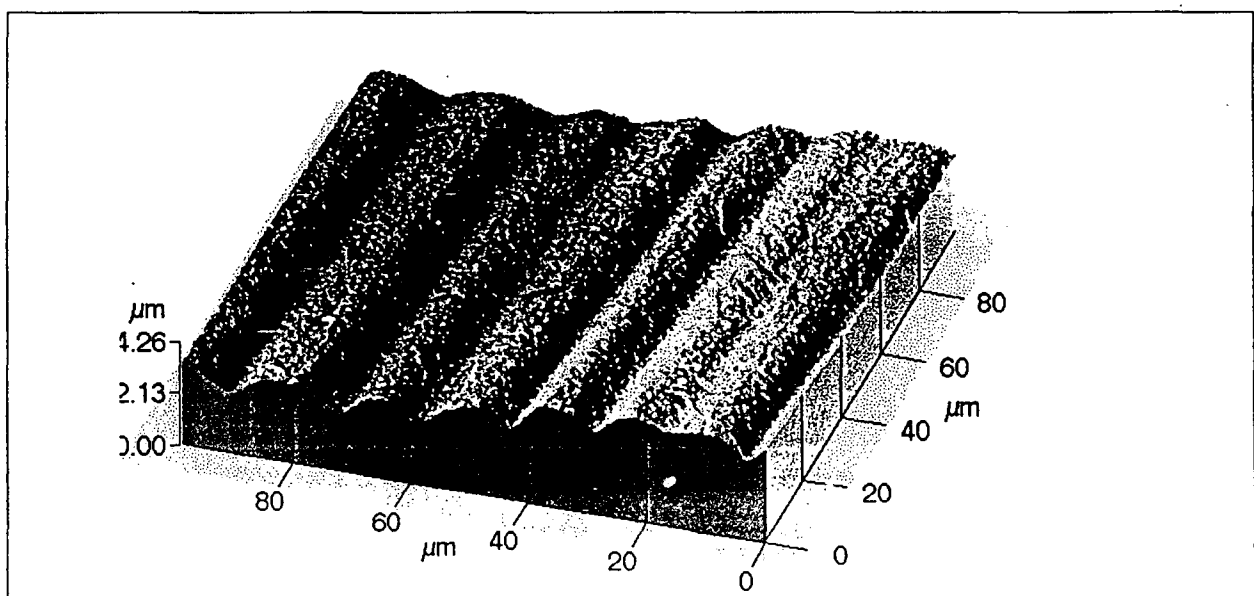




# Experimental Procedure

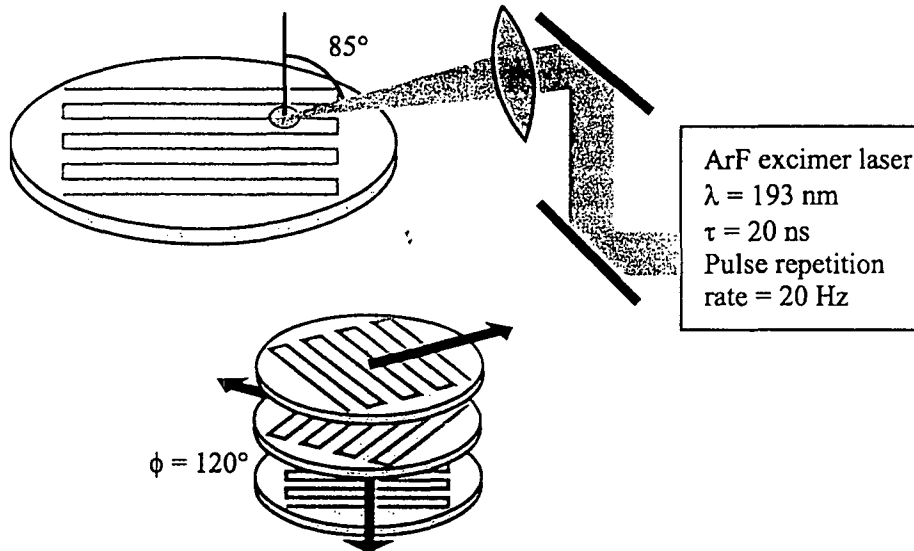


# Grooves

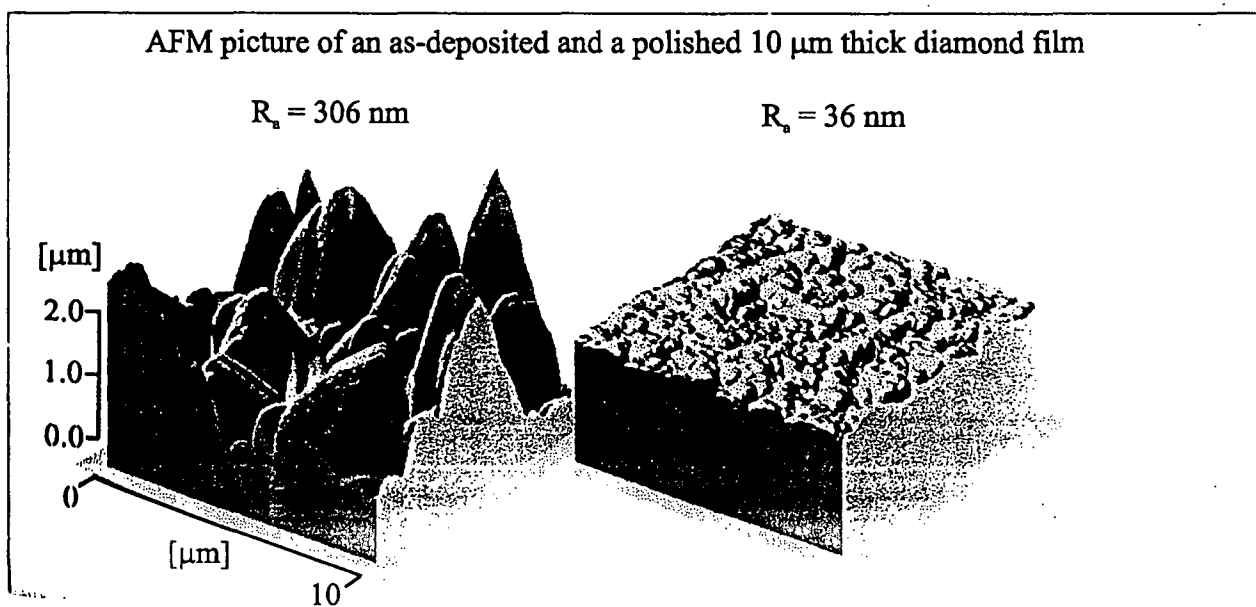




## Polishing of large areas

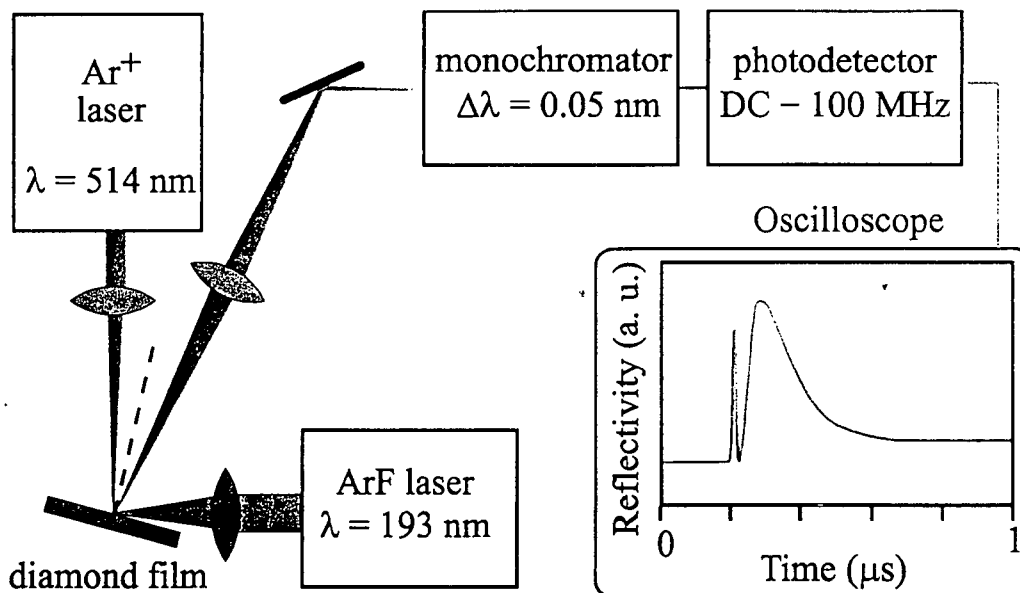


## Results

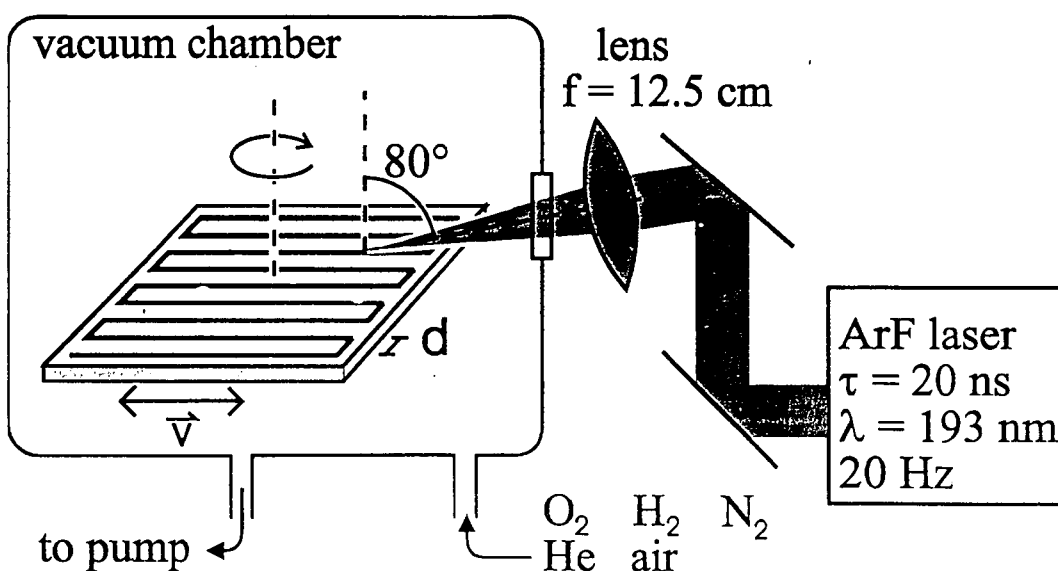




## Surface Melting

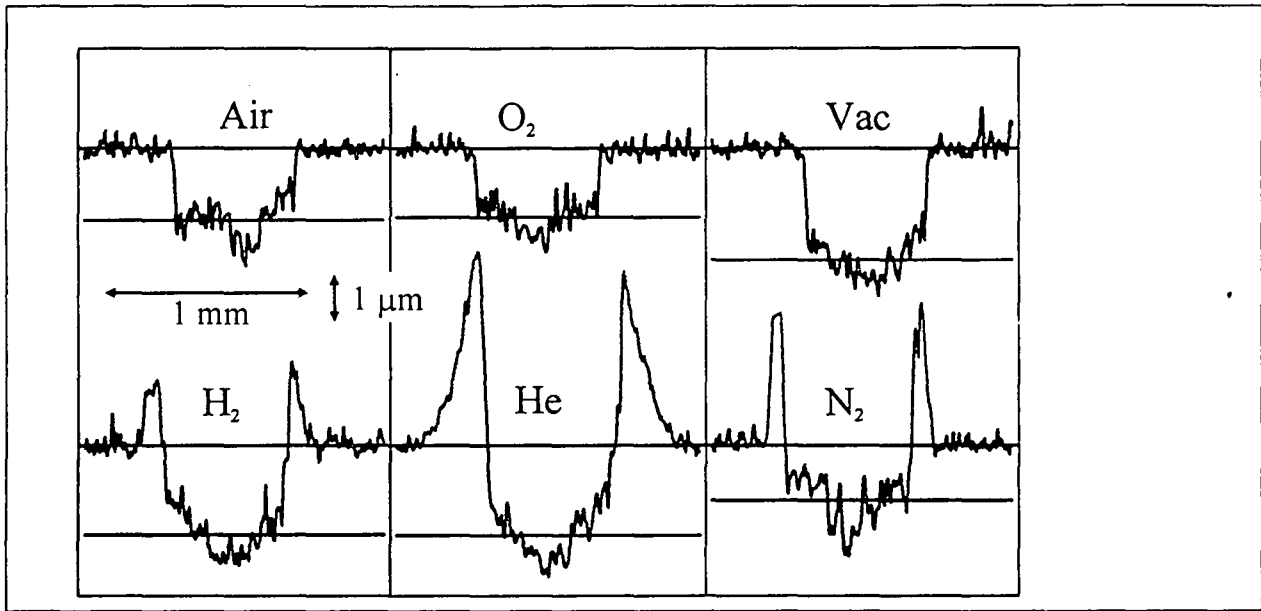


## Influence of the Atmosphere

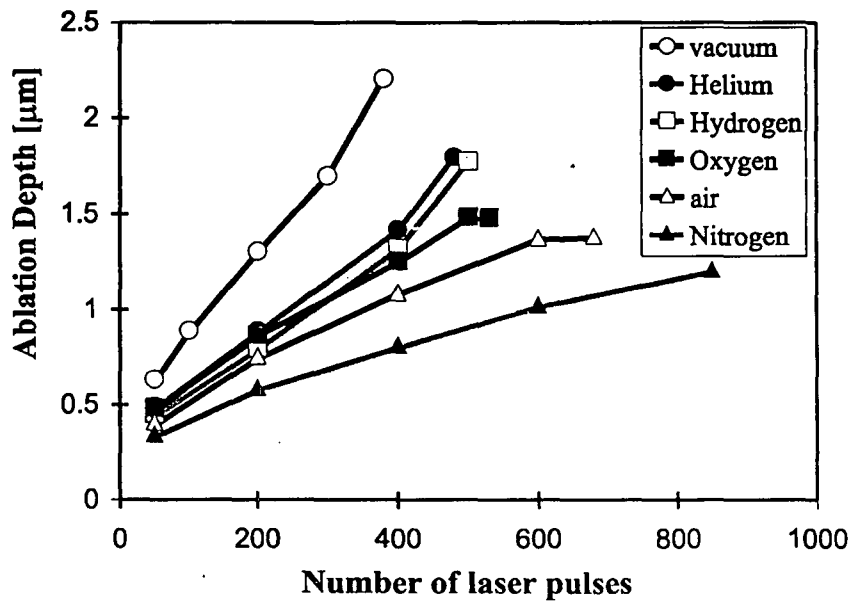




## Drilling of Holes

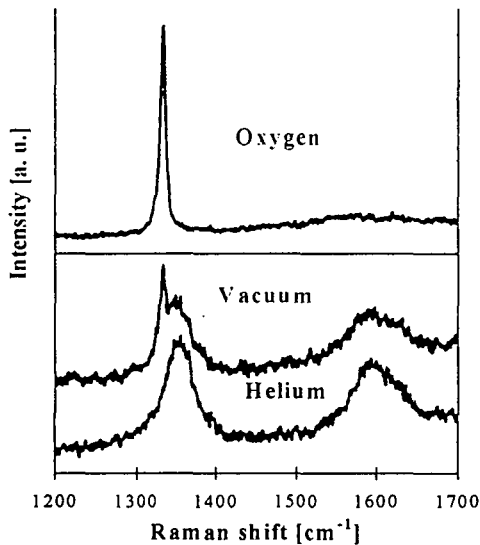


## The Ablation Rate





## Atmospheric Conditions



- Inert gases: lead to deposition of carbon close to the drilled hole.
- Vacuum leads to deposition of carbon far away from the hole.
- Oxygen or air burns the carbon and leads to clean holes.
- Most suitable atmosphere is air.



## Resulting Roughness of Surfaces

	$R_{AFM}$ [nm]	$R_{Profilometer}$ [nm]
as-deposited	412	140
air	66	44
O <sub>2</sub>	54	46
H <sub>2</sub>	69	47
He	130	48
vacuum	57	47

Using an other atmosphere does not lead to better polishing values.  
Therefore air is the most convenient atmosphere





## Quantitative results

- **Mechanical polishing (7-10 $\mu$ m polishing powder)**  
10 h/cm<sup>2</sup> with excellent surface quality

For **Laser** Source ArF Excimer laser,  $\lambda = 193$  nm

500 mJ/pulse, Spot 0.8 · 1 mm<sup>2</sup> with 20 Hz

thin film (small grains <1  $\mu$ m)      20 min/cm<sup>2</sup>

thick film (larger grains  $\approx 10$   $\mu$ m)    3 h/ cm<sup>2</sup>

**Combination** laser – mech.      3 + 3 h = 6 h



## Summary and Outlook

- Laser Polishing can substitute a large part of mechanical polishing.
- Laser polishing can be applied to complicated surfaces.
- For most applications a combination of Laser Polishing and mechanical finish will be most efficient.
- Polishing can be performed in ambient atmosphere.
- Carbon layers can oxydatively be etched away



**Layers: 30  $\mu\text{m}$  thick on polished silicon from  $\text{CH}_4/\text{H}_2$  mixture**

**Substrate temperature: 1050° C, 2-3% methane total pressure 12 kPa**

**2-4  $\text{mm}^2$  with 80% overlap, 1.8 – 20  $\text{J}/\text{cm}^2$**

**Roughness with Profilometer radius 1  $\mu\text{m}$**

**AFM 20 nm**

**Vac 1 Pa, Gas  $10^5$  Pa, 12  $\text{J}/\text{cm}^2$**

**Holes 5.5  $\text{J}/\text{cm}^2$ , Profilometer 5  $\mu\text{m}$**

**Graphite removed with  $\text{O}_2$  at ca. 600°C or in  $\text{H}_2$  Plasma**

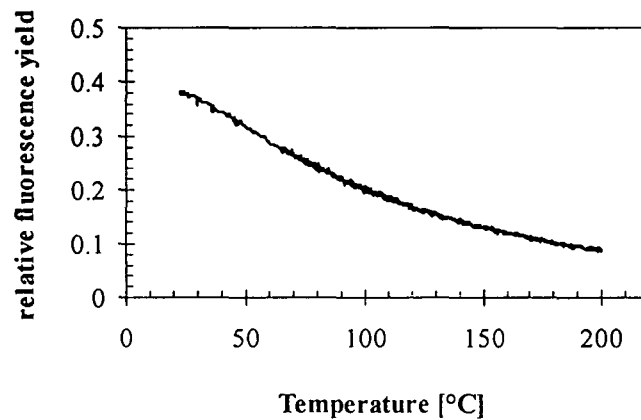


## Temperature Monitoring with Fluorescing Dyes

Heinz P. Weber, Valerio Romano  
Institute of Applied Physics  
University of Berne, Switzerland

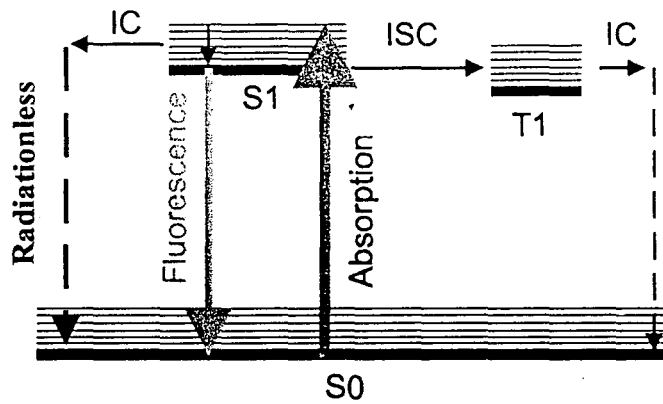


## Fluorescence yield of Rhodamin B



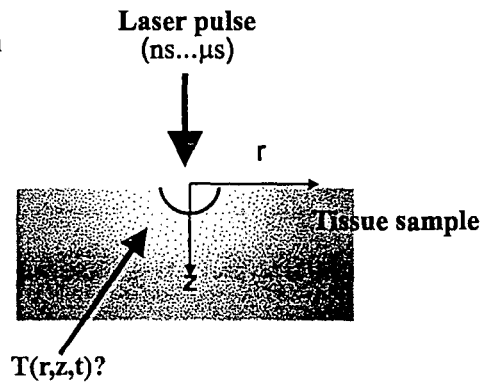


## Energy level diagram



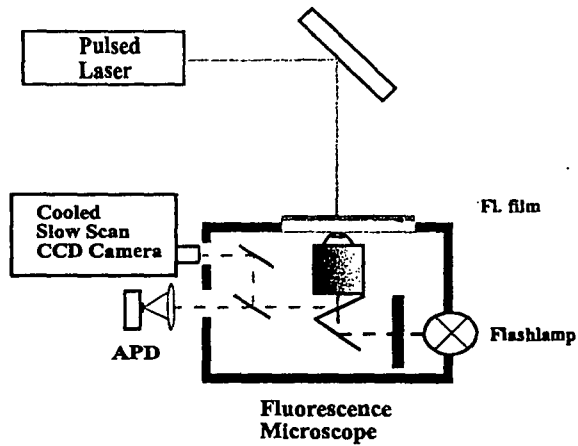
## Goals for measuring $T(r, z, t)$

- microscopical resolution
- rise time 10 nsec
- precision  $< \pm 1^\circ\text{C}$
- range  $20^\circ\text{C} - 150^\circ\text{C}$





## Setup for microscopy

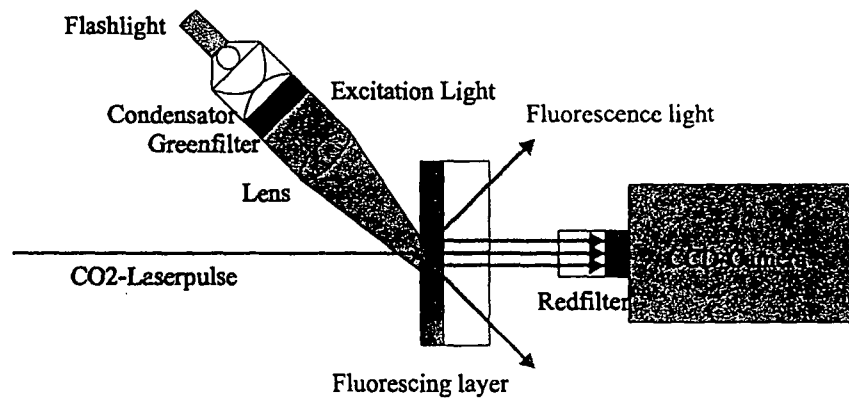


Temperature monitoring

Slide 5



## Experimental Arrangement



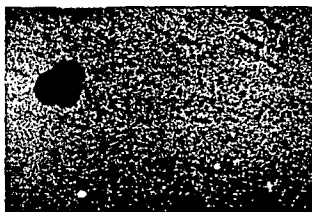
Temperature monitoring

Slide 6

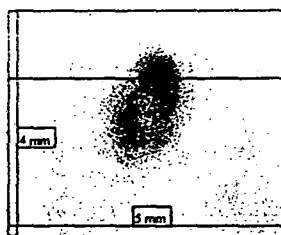


## Measurement sequence

Reference



Signal from  $\Delta T$



Measurement

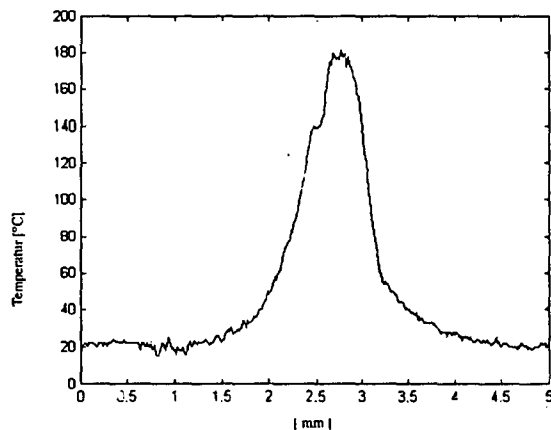


Temperature monitoring

Slide 7



## Evaluated profile (calibrated)

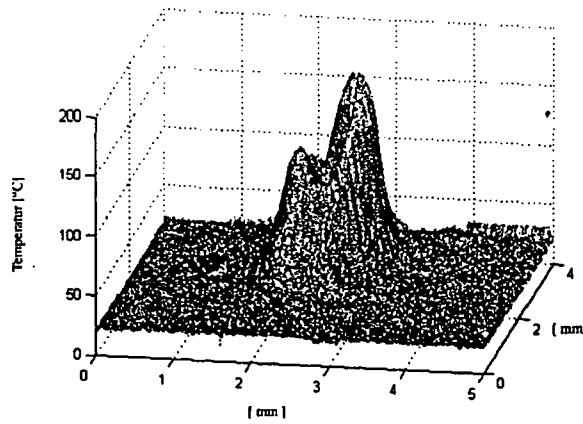


Temperature monitoring

Slide 8



## 3D representation of temp. profile

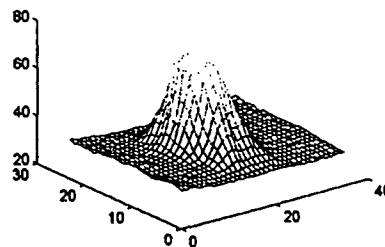
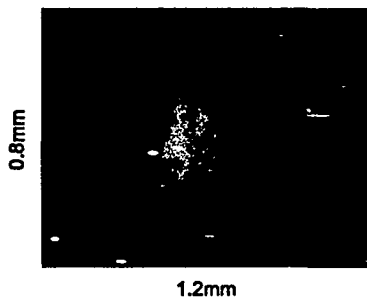


Temperature monitoring

Slide 9



## Fluorescence and evaluated temperature

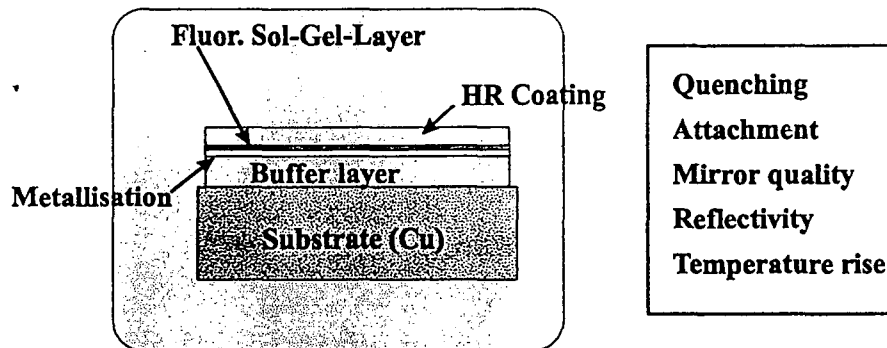


Temperature monitoring

Slide 10



## Composition of laser mirror



Temperature monitoring

Slide 11



## Mirror parameters

- **Quenching** Sol-Gel layer is not in direct contact with substrate
- **Attachment** Al as metallisation
- **Surface quality** OK with up to 7 double layers of coating
- **Reflectivity**
  - 96 % (Al without high reflector)
  - 98 % (Au without high reflector)
  - 99 % (with high reflector)
- **Heating** dimensioning so that  $\Delta T = 20^\circ\text{C}$  for  $I_{\text{max}}$

Temperature monitoring

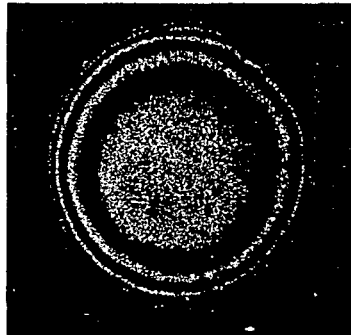
Slide 12





## Coated CO<sub>2</sub> mirror

Planity (Interferogram)



1 Ring: 309 nm

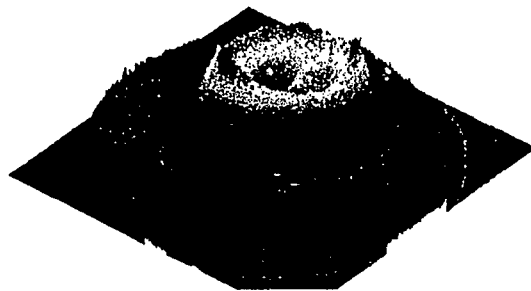
Temperature monitoring

Slide 13



## Profile of CO<sub>2</sub> laser beam

running at 3600W



Temperature monitoring

Slide 14



## Summary

- **temperature distributions with  $\mu\text{m}$  resolution is realized**
- **timeframes with 10 nsec durations can be inspected**
- **temperature range can be adjusted with appropriate dyes**
- **intensity distributions on laser mirrors can be measured**
- **special constructions of mirrors were realized**
  
- **temperature range for measurement can be extended by using other fluorescing species like rare earth doped media**



---

# Pulsed Optoacoustic Spectroscopy and Imaging

Kornel Köstli, Martin Frenz, Heinz P. Weber  
Institute of Applied Physics  
University of Bern, Switzerland

## Contents

---



Principle of optoacoustics

- State of the art / research

Novel pressure measurement technique

Reconstruction of the absorbed energy distribution of absorbed light

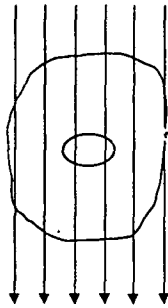
- Principle: Transit time of pressure wave
- Principle: Transformation time frequencies  
into spatial frequencies
- Comparison

## Imaging principles

University of Bern  
Laser Department



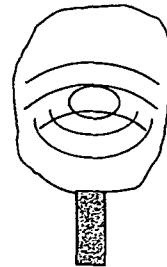
X - rays



Optical tomography



Ultrasound



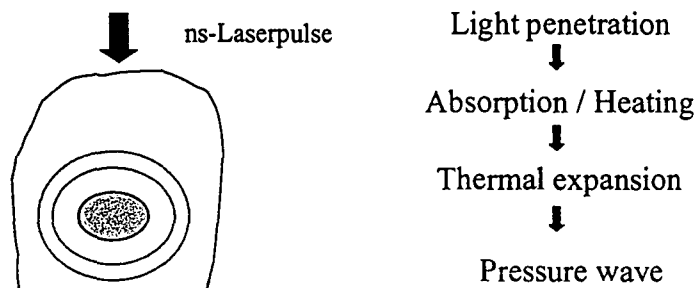
Advantages no scattering  
Disadvantages ionising

contrast, spectra  
limited resolution

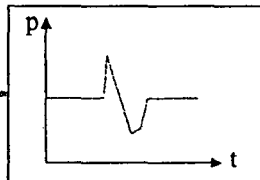
large penetration  
low contrast/  
resolution

## Optoacoustics: Combination of light and ultrasound

University of Bern  
Laser Department



Ultrasound-sensor



Advantages:  
- not ionising  
- high contrast  
- "deep" penetration

## Optoacoustic: Tomographie

University of Bern  
Laser Department



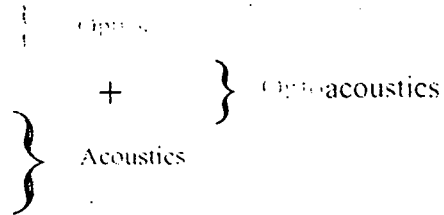
Short laser pulse heats absorbing structures in tissue

Fast temperature rise leads to increase in pressure

Pressure wave propagates in form of highfrequency ultrasound (MHz)

Detection of pressure wave at the surface of tissue

Calculation of initial pressure distribution  
=> Tomography - layers through highly scattering tissue



## Light distribution in scattering medium

University of Bern  
Laser Department



- homogeneous medium:

$$I(z) = I_0 \cdot e^{-\mu \cdot z} \quad I = \text{intensity}$$

- low scattering:

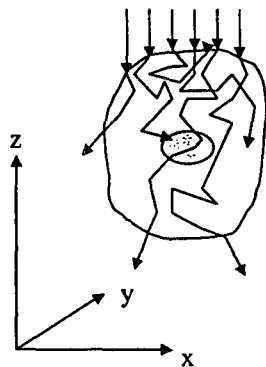
$$\mu = \mu_{total} = \mu_a + \mu_s \quad \begin{array}{l} \mu_a = \text{absorpt. coeff.} \\ \mu_s = \text{scatt. coeff.} \end{array}$$

- high scattering:

$$\mu = \mu_{effektiv} = \sqrt{3\mu_a(\mu_a + (1-g)\mu_s)} \quad g = \text{anisotropy factor}$$

- inhomogeneous medium:

Monte Carlo simulation (numerical)





## Thermo elastic pressure

Short laser pulse heats absorbing structures in tissue:

$$\Delta T(\bar{x}) = \frac{H(\bar{x}) \cdot \mu_a(\bar{x})}{c \cdot \rho}$$

$H = E/A = \text{radiance}$

Volume extension coeff.  $\gamma$ :

$$\gamma \cdot \Delta T = \frac{\Delta V_T}{V}$$

$\mu_a = \text{absorpt. coeff.}$

$c = \text{spez. heatcap.}$

Compressibility  $\chi$ :

$$\chi \cdot \Delta p = -\frac{\Delta V_p}{V}$$

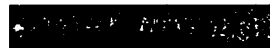
$\rho = \text{density}$

Fast Heating without extension leads to pressure:

$$\Delta V_{total} = \Delta V_p + \Delta V_T = 0$$

$$\Delta p(\bar{x}) = \frac{\gamma}{\chi} \cdot \Delta T(\bar{x}) = \frac{\gamma}{\chi \cdot c \cdot \rho} \cdot H(\bar{x}) \cdot \mu_a(\bar{x})$$

Grüneisencoeff.  $\Gamma = \frac{\gamma}{\chi \cdot c \cdot \rho}$



## Thermo elastic pressure

Numerical example: Soft tissue has similar thermoelastic properties as water:

$$E = 1 \text{ mJ}, r = 1.25 \text{ mm} \rightarrow H = 20 \text{ mJ/cm}^2$$

$$\mu_a = 200 \text{ cm}^{-1}$$

$$\Gamma = 0.11 \text{ at } T = 20^\circ\text{C}$$

$$\rightarrow \Delta T = 1^\circ\text{C} \text{ and } p = 4.4 \text{ bar}$$

➔ Pressure generation without thermal damage

## Pressure expansion

University of Bern  
Laser Department



Basic relations  
of Acoustics:

$$\frac{\partial^2 \phi(\vec{x}, t)}{\partial t^2} - c^2 \Delta \phi(\vec{x}, t) = -\frac{p_0(\vec{x})}{\rho_0} \delta(t)$$

Wave equation with  
perturbation  $p_0(x)$

$$\vec{v}(\vec{x}, t) = \nabla \phi(\vec{x}, t)$$

For velocity potential  
 $\Phi(x)$

$$p(\vec{x}, t) = -\rho_0 \frac{\partial \phi(\vec{x}, t)}{\partial t}$$

Describes pressure  
expansion in a  
acoustically  
homogeneous medium

$\rho_0$  = Density

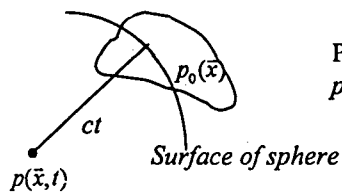
$c = \frac{1}{\sqrt{\rho_0 \cdot \chi}}$  = Velocity of sound

## Pressure expansion

University of Bern  
Laser Department



Solution of wave equation: 
$$p(\vec{x}, t) = \frac{1}{4\pi c} \frac{\partial}{\partial t} \left( \int_{|\vec{x}-\vec{x}'|=ct} \frac{p_0(\vec{x}')}{|\vec{x}-\vec{x}'|} d\sigma \right)$$



Poisson integral over initial pressure distribution  
 $p_0(x)$ , where  $d(p_0(x))/dt=0$

Problem for optoacoustic tomography: "Inverse- Problem"

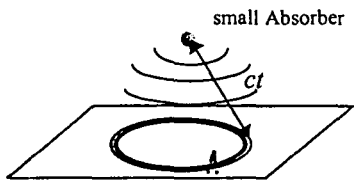
Out of the measurement  $p(\vec{x}, t)$  the initial  
pressure distribution  $p_0(\vec{x})$  has to be found.  
= Calculation of distribution of absorbed light  
Based on twodimensional pressure measurement

# Optoacoustic tomography

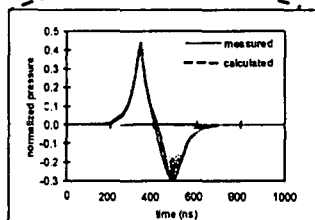
University of Bern  
Laser Department



Pressure propagation:

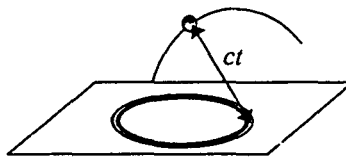


x-y-plane with bipolar pressure signal at time  $t$

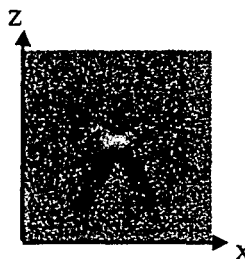


Backward calculation:

Back projection on Spherical surface



From every single Pressure measurement  $p(x,y,t)$

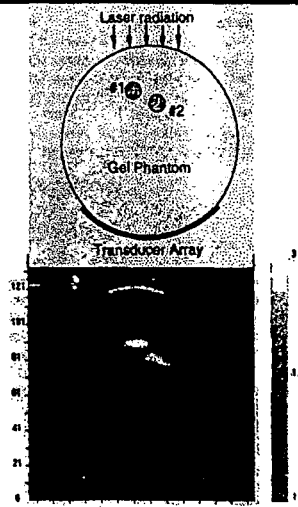
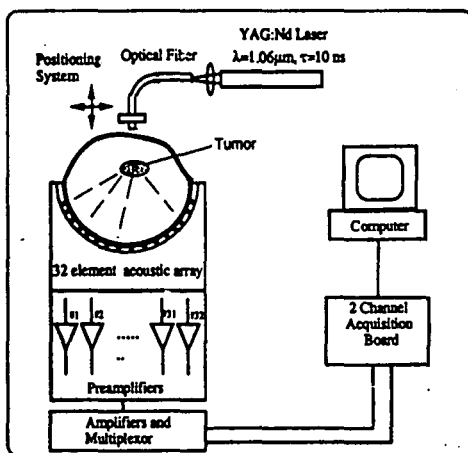


# State of the art

University of Bern  
Laser Department



## Recognition of breast cancer



1998 Oraevsky et al.  
1999 Kruger et al.

Light source: Nd:YAG  
Light source: Microwaves

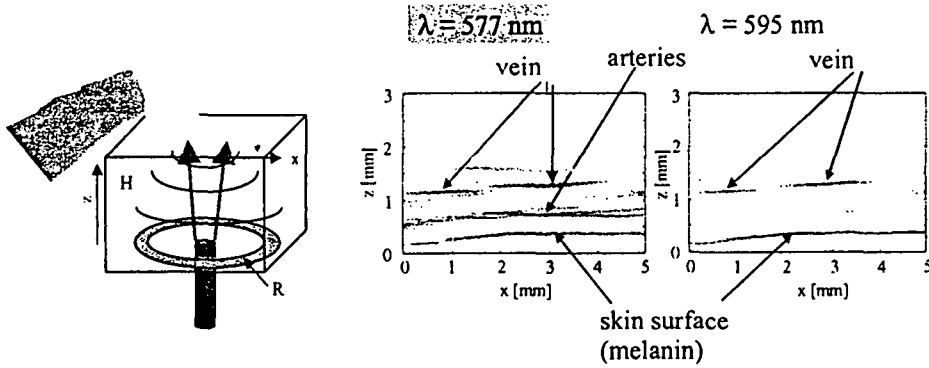


## State of the art

University of Bern  
Laser Department



Visualisation of blood vessels in hand *in-vivo*:



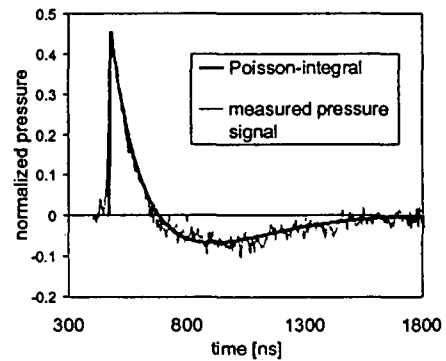
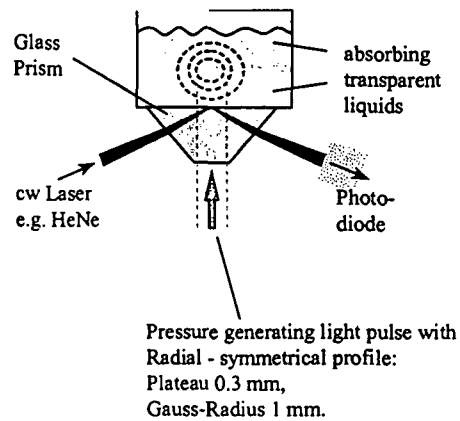
2000, Laser Department, Uni Bern Lightsource: OPO

## Novel optical pressure measurement $p(t)$

University of Bern  
Laser Department



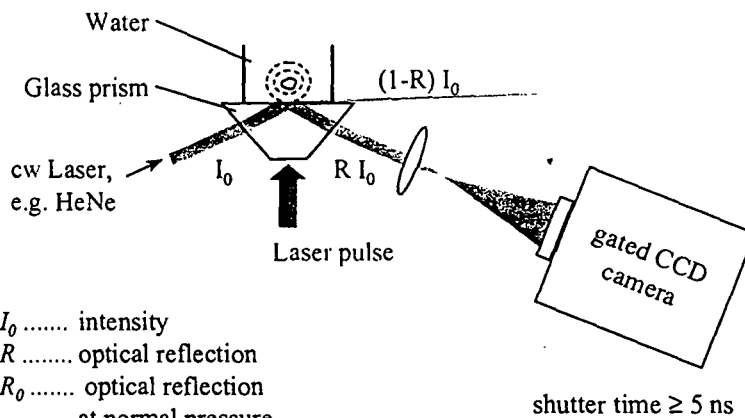
Comparison: Experiment versus  
Poissonintegral (numerical)



$\alpha = 73 \text{ cm}^{-1}$  at  $\lambda = 1880 \text{ nm}$   
 $d(\text{detector-sample}) = 0.7 \text{ mm}$

## Novel pressure measurement $p(x,y)$

University of Bern  
Laser Department



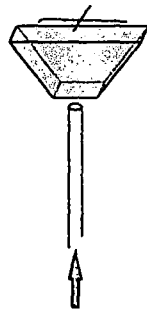
$I_0$  ..... intensity  
 $R$  ..... optical reflection  
 $R_0$  ..... optical reflection  
 at normal pressure  
 $R_0 = 0.5 \dots 0.85$

## Example: pressure measurement $p(x,y)$

University of Bern  
Laser Department



Sample: Two crossed hairs  
in water



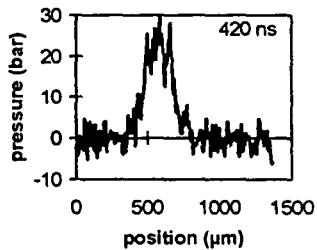
6 ns laser pulse



Shutter time:  
5 ns

420 ns after  
Laser pulse

1 mm



## Optical pressure measurement

University of Bern  
Laser Department



### Advantages

- transparent  
 ➔ Reflection measurement possible
- high resolution  
 ➔ temporal up to 5 ns  
 ➔ and spatial 5 μm  
 (piezo: ~ 100 μm)
- established technique (CCD chip)

### Disadvantages

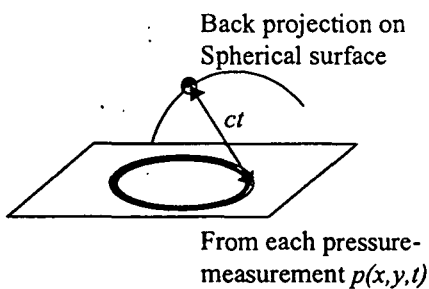
- sensitivity:  
 1 % intensity change / Bar  
 ➔  $p_{\min} = \text{some } 100 \text{ mbar}$
- (piezo-sensor: 33 V/bar  
 ➔  $p_{\min} = \text{some } 1 \text{ mbar}$ )

## Reconstruction of pressure source

University of Bern  
Laser Department



Old reconstruction based on Poissonintegral



New reconstruction based on separation of pressure waves into plane waves

$$p(\vec{x}, t) = \text{Re} \int P(\vec{k}) \cdot e^{i(\vec{k} \cdot \vec{x} - \omega t)} d^3 k$$

and

$$\omega = c \cdot \sqrt{k_x^2 + k_y^2 + k_z^2}$$

(Dispersion relation)



## Summary

Optoacoustic: Novel imaging procedure for medicine

2D-Pressure measurement:

Fast pressure measurement for relection measurement

Novel reconstruction algorithm for tomography:

- Calculation of entire volume in sufficiently short time (5s for  $32^3$  pressure points)
- nearly artefacts
- high spatial resolution (40  $\mu\text{m}$ )

Medical applications Anwendungen:

- on-line feedback for laser surgery (Eye, cartilage, thermotherapy,...)
- image formation (blood circulation in skin and organs in-vivo)
- diagnoses (bloodvalues in-vivo and spatially resolved within the body, cancer recognition)



# Laser as Medical Instrument for Surgery

H.P. Weber, M. Frenz and H. Pratisto

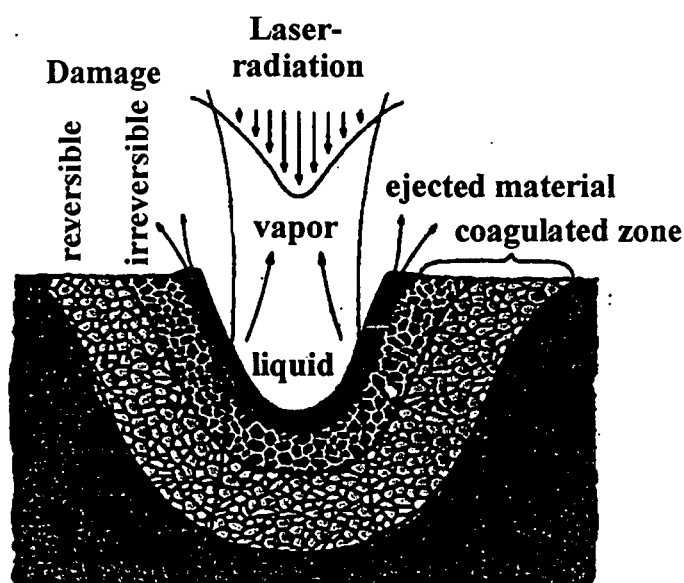
Institute of Applied Physics, University of Bern, Sidlerstrasse 5,  
CH-3012 Bern, Switzerland

Laser in surgery

Slide 0



## Principle of Laser - Cutting



Laser in surgery

65

Slide 1

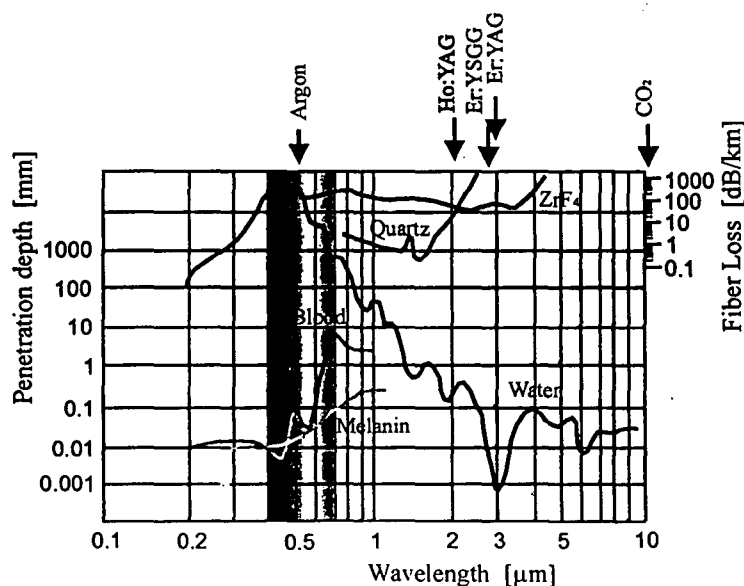


## Why near IR Laser - Radiation

- **High Absorption**  
allows for high precision (10  $\mu\text{m}$  range) and helps for controlled coagulation range
- **Pulsed application**  
duration determines heat dissipation
- **Optical Fibers**  
allows for simplified guiding of radiation to patient  
allows for endoscopic surgery in much simpler setup



## Absorption Spectrum of Water

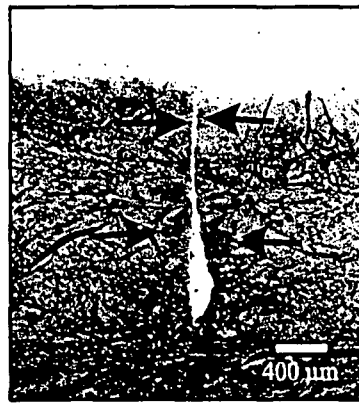
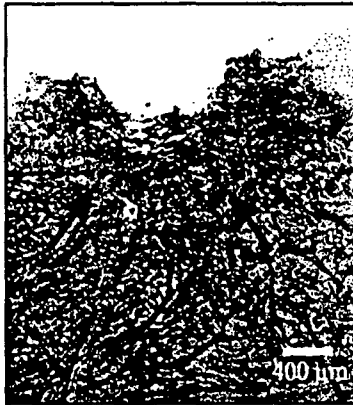




## Comparison Coagulation for Ho and Er

Holmium

Erbium



Tissue: Meniscus

$E = 1 \text{ J}, \tau = 400 \mu\text{s}$

$E = 0.1 \text{ J}, \tau = 400 \mu\text{s}$

10 Pulses



## Surgery within liquid Environment

Reasons:

- Surgeon wants to avoid desiccation
- Surgeon wants sterile environment.  
Rinsing with physiological saltwater is standard

Problems:

- Space between fiber tip and tissue is filled with water  
absorption of  $3 \mu\text{m}$  radiation within  $1 \mu\text{m}$   
( $2 \mu\text{m}$  radiation within  $100 \mu\text{m}$ )



## Solution for transmission of Radiation:

### Formation of "Gas Bubble"

Idea: Optical radiation evaporates water. Water vapor takes much larger volume.

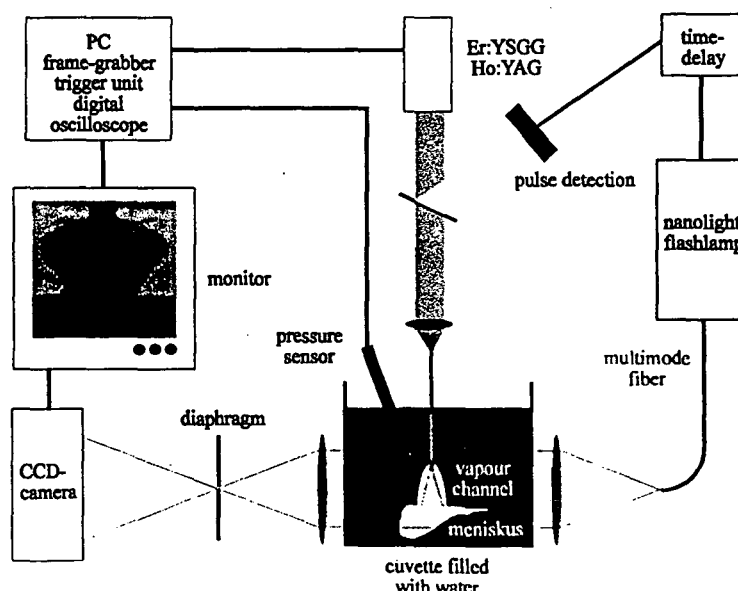
For 1 Torr volume - ratio liquid / vapor is 1000.

Water vapor is narrow band absorber and thus "transparent" for optical radiation.

We shoot ourselves an open channel for our radiation



## Arrangement for Detection of Bubbles

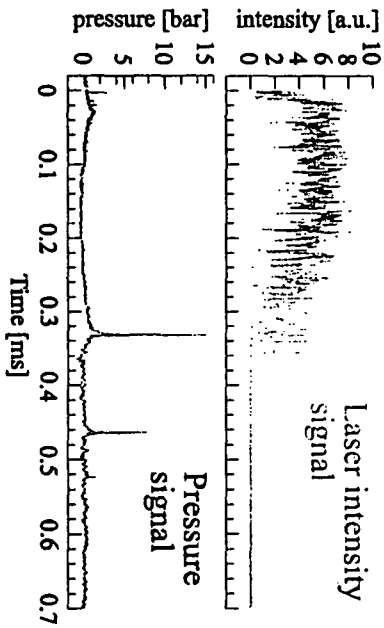
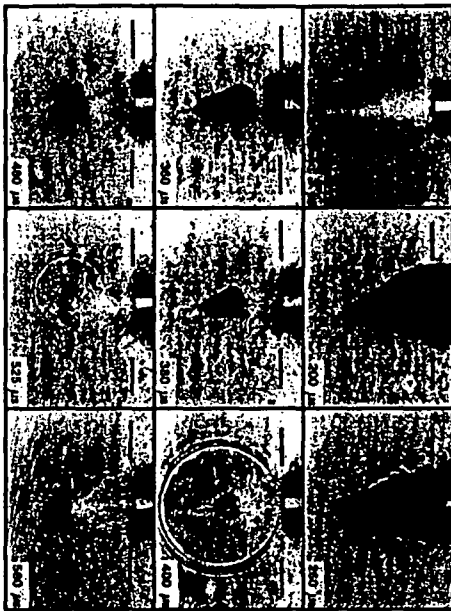




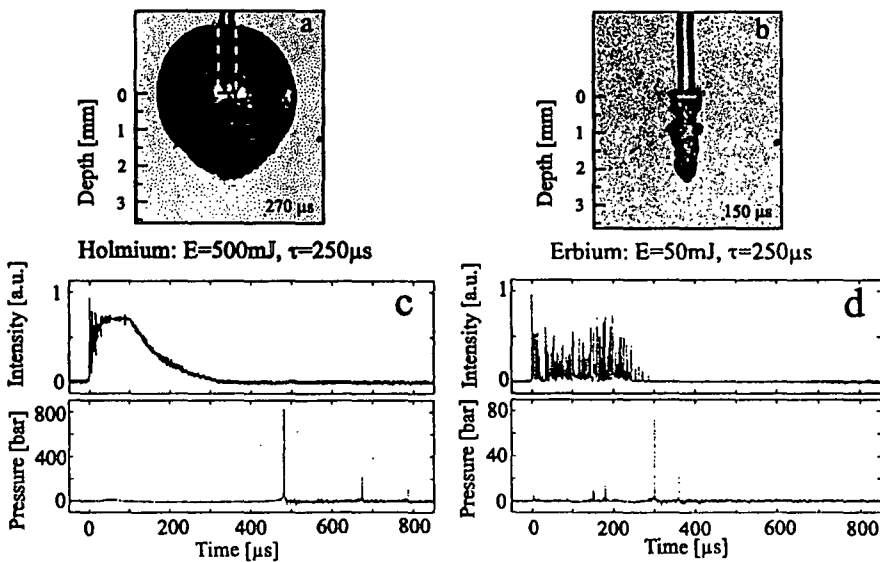


# Bubbles and Pressure Transients of Er in H<sub>2</sub>O

E = 200 mJ fiber Dia = 1.5 mm

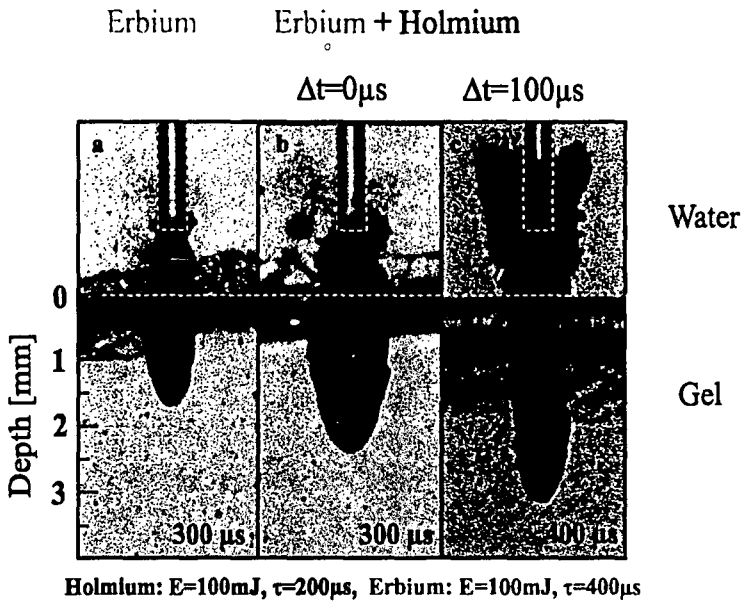


# Holmium - Erbium Bubble

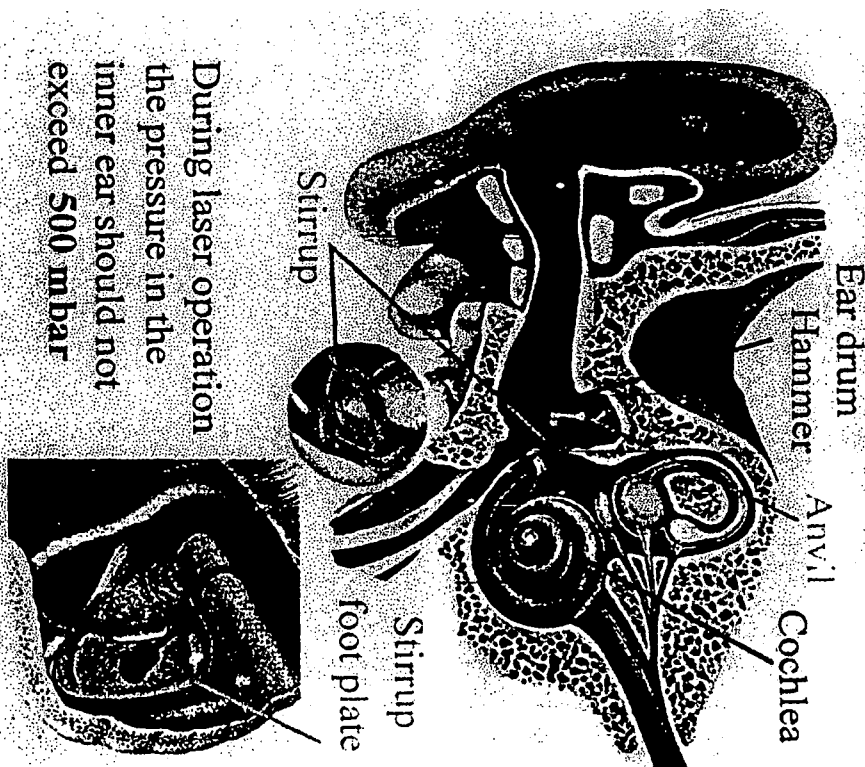


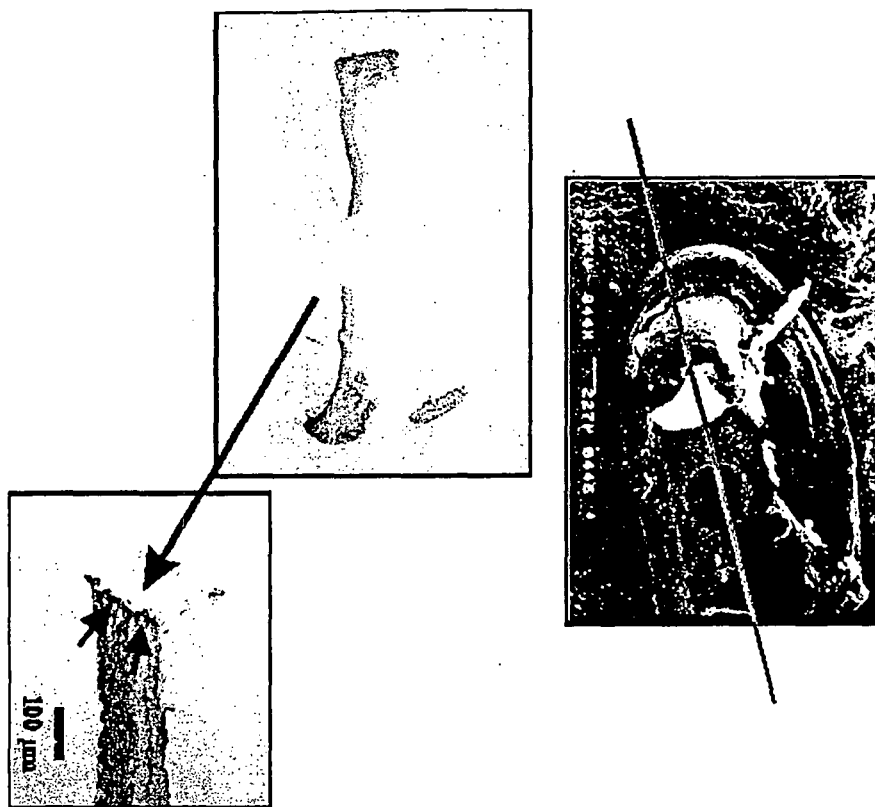


# Impact in Poly-acrylamide-gel



## Schematic of Operation of Ear Laser Stapedotomy





# Fenestration of Foot Plate

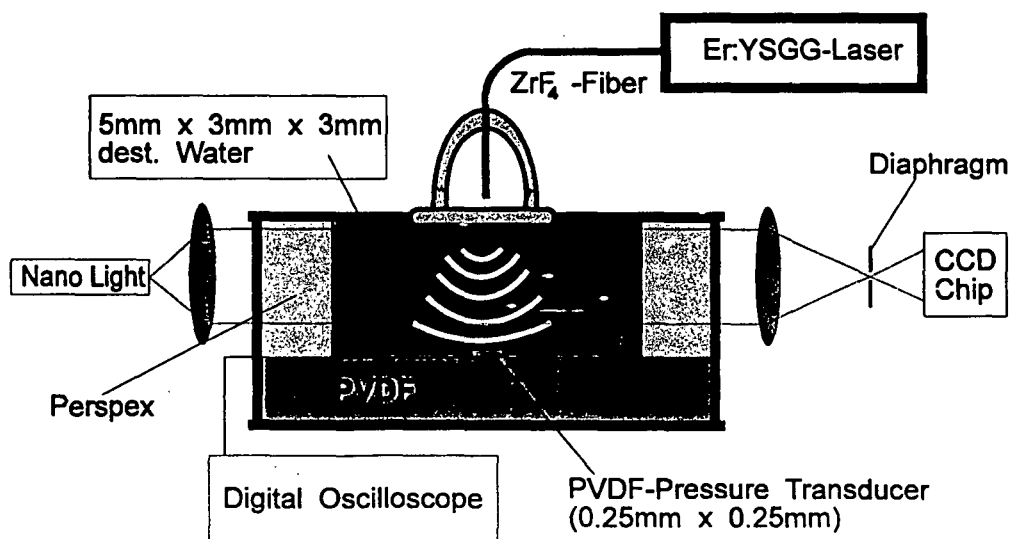
University of Bern  
 Inst of Applied Physics  
 Laser Department



University of Bern  
 Inst of Applied Physics  
 Laser Department

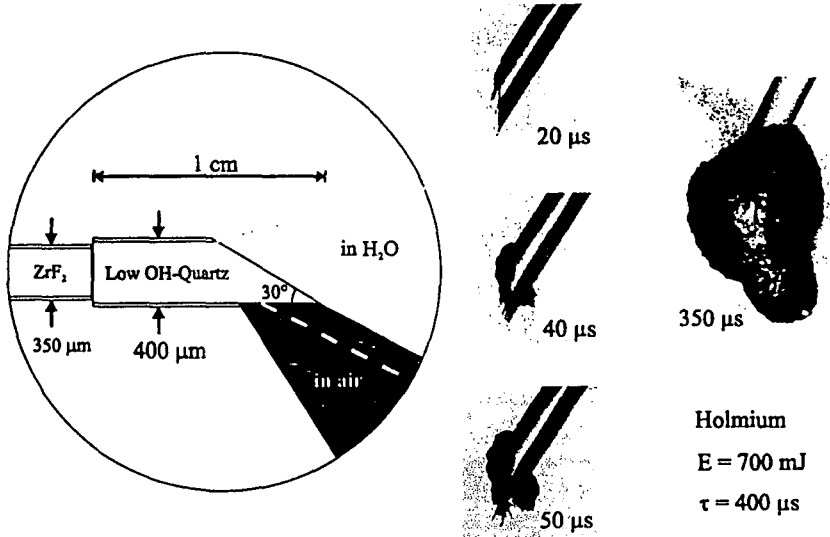


## Simulation of the Inner Ear





## The use of side-firing fibers



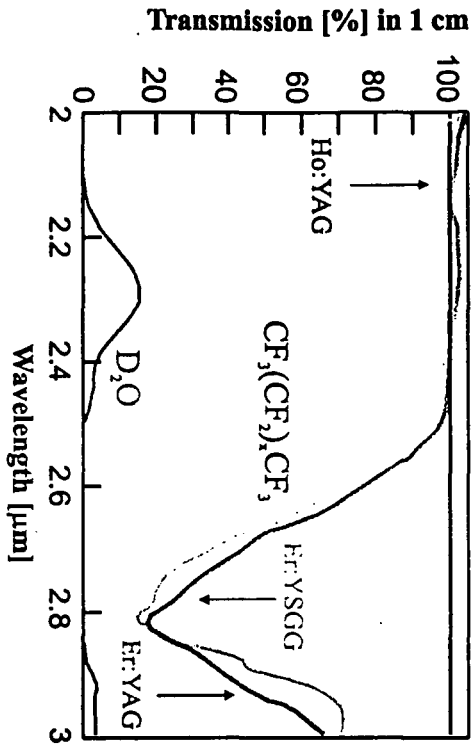
## How to avoid the adverse Effect of H<sub>2</sub>O ?

- high absorption - other liquid medium ?
- transmitting at 2  $\mu m$  and 3  $\mu m$
- biocompatible, also if it would be decomposed
- much lower vapor pressure is desirable

**Perfluoro - Octane**



# Optical Transmission in Perfluorooctane

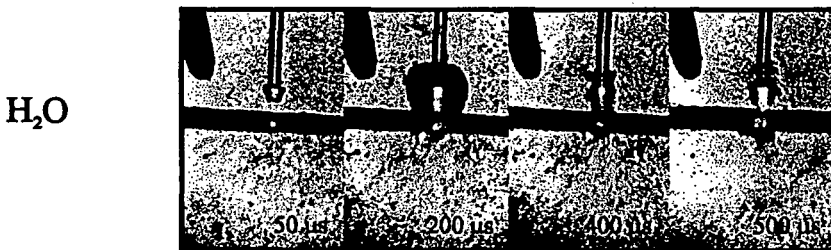


perfluorooctane,  $\lambda = 2.1 \mu\text{m}$

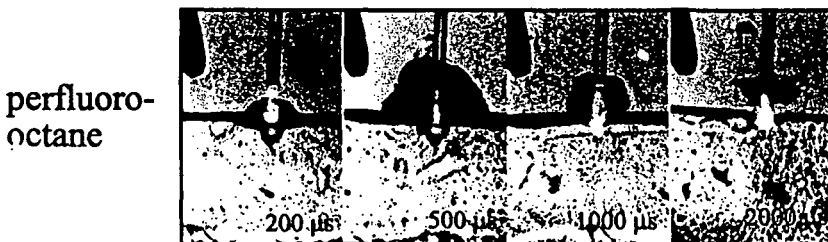
$$\alpha_{2.12 \mu\text{m}} = 0.01 \text{ cm}^{-1} \quad \alpha_{2.94 \mu\text{m}} = 0.5 \text{ cm}^{-1}$$



# Bubble Formation in Perfluoro - Octane

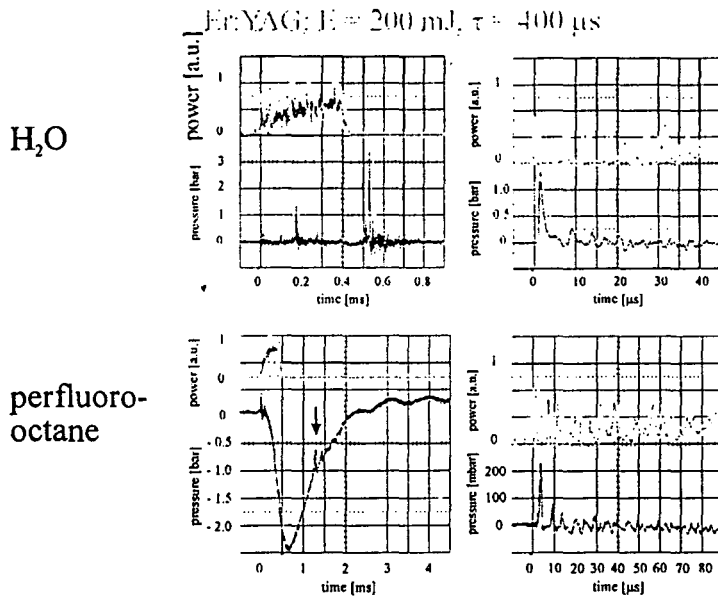


Ho laser:  $E = 500 \text{ mJ}$ ,  $\tau = 400 \mu\text{s}$

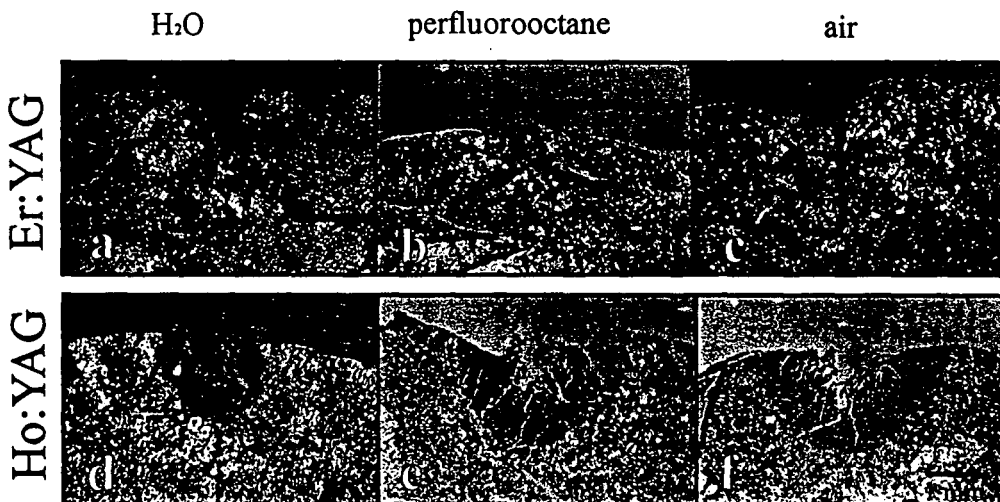




# Pressure Transient in Perfluoro - Octane



# Tissue Damage in different surrounding



Er:YAG: E = 100 mJ,  $\tau = 400 \mu\text{s}$ ; Ho:YAG: E = 500 mJ,  $\tau = 400 \mu\text{s}$



## Conclusions

- Underwater surgery with 3  $\mu\text{m}$  laser - radiation is possible, despite the shallow penetration (1  $\mu\text{m}$ ) in water. It becomes possible by opening a watervapor bubble with the leading edge of the laser pulse.
- The bubble helps to guide the radiation. Its form can be tailored by the laser parameters.
- Sidefiring is possible by use of the bubble.
- In part enormously high pressure transients in the form of shockwaves are generated.



- Dual wavelength set-ups can greatly reduce the size of the bubbles and the magnitude of the pressures.
- Other liquids like Perfluorooctane can almost completely avoid the occurrence of shockwaves
- For ear surgery there exists a “safe” fluence of 10  $\text{J}/\text{cm}^2$ , that allows an efficient surgical speed.
- As yet 25 patients were treated successfully.



## The optimum wavelength for TMLR? An in vitro and in vivo study with 3 different lasers.

M. Frenz  
B. Ott  
H.P. Weber

Institute of Applied Physics, University of Berne

U. Dittli  
T. Carrel  
B. Walpoth

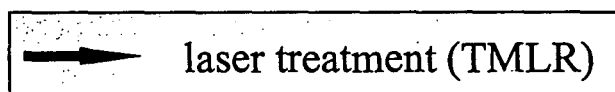
Clinic for Thoracic, Cardiac and Vascular Surgery, Insel Spital Bern

Th. Schaffner  
Pathological Institute, University of Berne

### Motivation 1



- Coronary artery disease is leading cause of death in modern western world
- Some patients are not amenable to conventional therapies



- Procedure: Channels are drilled to connect the left ventricle to the myocardium
- Hypothesis: new blood vessels grow inside myocardium and provide heart muscle with oxygen rich blood



## Motivation 2

University of Bern  
Laser Department

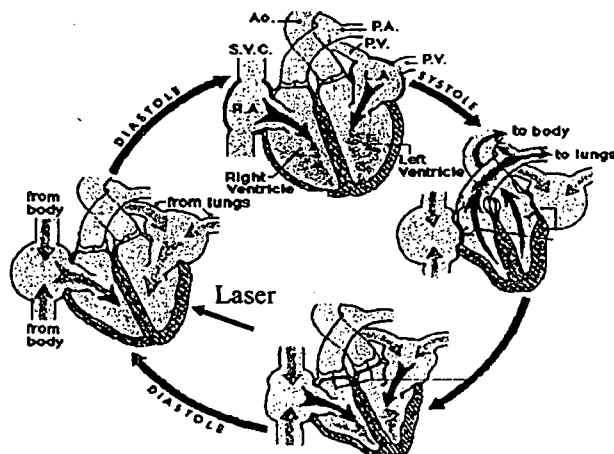


- Clinical results are promising but it is still unclear why.

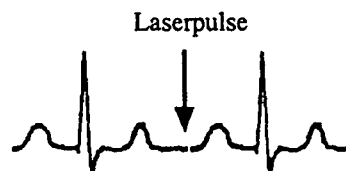
Since mechanism is unknown, we don't know whether we use optimum laser parameters

## Transmyocardial Laser Revascularisation TMLR

University of Bern  
Laser Department



Goal: Supply of blood to the left ventricle of the heart muscle by neorevascularisation



## Aim of this study

University of Bern  
Laser Department



- ⊙ Compare Er:YAG, Ho:YAG and CO<sub>2</sub> laser radiation
- ⊙ Visualize the ablation process using distilled water and polyacrylamide gel (tissue phantom)
- Determine
  - thermal and mechanical damage in porcine myocardium
  - laser induced pressure during treatment
  - ablation rate of myocardium as a function of fiber force and fiber delivery system
- Evaluate healing effects after 6 weeks

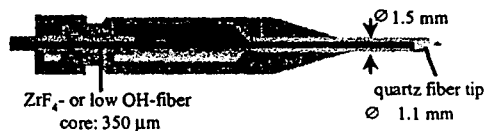
## Materials and Methods 1

University of Bern  
Laser Department



Laser	wavelength $\lambda$	penetration depth	pulse duration $\tau$	energy/pulse	delivery system
Er:YAG	2.94 $\mu\text{m}$	4 $\mu\text{m}$	800 $\mu\text{s}$	300 mJ	ZrF <sub>4</sub> -fiber with quartz tip ( $\varnothing$ 1.1 mm)
Ho:YAG	2.1 $\mu\text{m}$	330 $\mu\text{m}$	550 $\mu\text{s}$	2 J	low OH-quartz fiber with tip ( $\varnothing$ 1.1 mm)
					low OH-quartz fiber with lens ( $\varnothing$ 1.9 mm)
CO <sub>2</sub> (800 W)	10.6 $\mu\text{m}$	12 $\mu\text{m}$	40 ms	32 J	articulated mirror arm spot $\varnothing$ 1 mm

laser triggered by ECG (R-wave)



handpiece

## Materials and Methods 2

University of Bern  
Laser Department



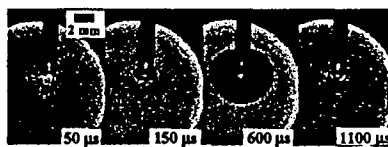
- in vitro:
- ⊙ Time-resolved flash photography
  - Pressure measurements (needle hydrophone)
  - Perforation of the myocardium  $\Rightarrow$  ablation rate
  - Histology
- in vivo:
- ⊙ 6 healthy pigs
  - ⊙ Open chest surgery (thoracotomy)
  - ⊙ Areas marked with small titanium-surgical clips
  - ⊙ Echocardiography to detect potential patent channels
  - ⊙ Final histological evaluation after 6 week survival

## Channel dynamics in water

University of Bern  
Laser Department



Ho:YAG  
lens-fiber  
E = 2 J  
 $\tau = 550 \mu\text{s}$



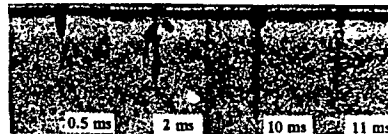
Ho:YAG  
bare-fiber  
E = 2 J  
 $\tau = 550 \mu\text{s}$



Er:YAG  
bare-fiber  
E = 300 mJ  
 $\tau = 800 \mu\text{s}$



CO<sub>2</sub>  
articulated arm  
E = 8 J  
 $\tau = 10 \text{ ms}$



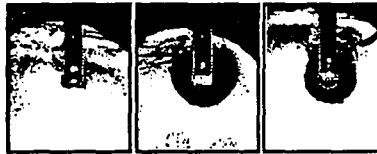
Annals of Thoracic Surgery, (1997), 63, pp 640-647

# Channel dynamics in gel

University of Bern  
Laser Department



Ho:YAG  
lens-fiber  
E = 2 J  
 $\tau = 550 \mu\text{s}$



150  $\mu\text{s}$       600  $\mu\text{s}$       900  $\mu\text{s}$

Ho:YAG  
bare-fiber  
E = 2 J  
 $\tau = 550 \mu\text{s}$



150  $\mu\text{s}$       450  $\mu\text{s}$       900  $\mu\text{s}$

Er:YAG  
bare-fiber  
E = 300 mJ  
 $\tau = 800 \mu\text{s}$



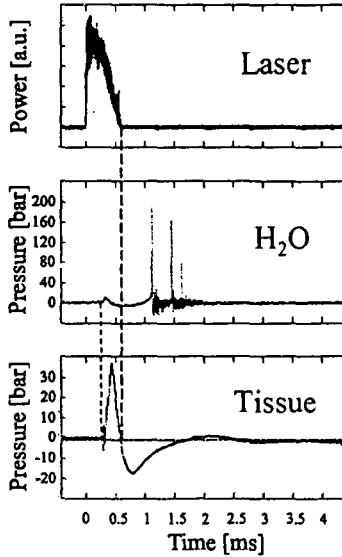
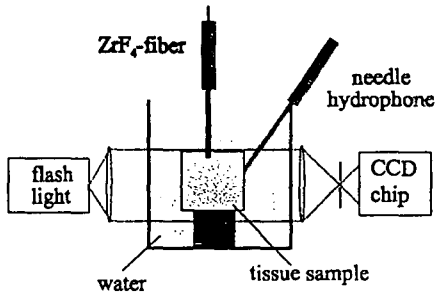
150  $\mu\text{s}$       600  $\mu\text{s}$       1100  $\mu\text{s}$

# Pressure measurement

University of Bern  
Laser Department



Ho:YAG laser  
bare-fiber  
E = 2 J



## Pressure

University of Bern  
Laser Department



Laser and fiber system	Medium	Maximum pressure	
		positive	negative
Er:YAG quartz-end fiber	deionized water	114.6 bar	-16.1 bar
	gel	15.4 bar	-4.0 bar
	myocardium	9.0 bar	-8.1 bar
Ho:YAG bare-fiber	deionized water	199.5 bar	-27.5 bar
	gel	92.2 bar	-15.1 bar
	myocardium	30.7 bar	-14.5 bar
Ho:YAG lens-fiber	deionized water	431.8 bar	-46.9 bar
	gel	92.3 bar	-9.9 bar
	myocardium	55.8 bar	-29.7 bar

## Ablation rate

University of Bern  
Laser Department



- ablation rate depends on the fiber force
- too high fiber force causes mechanically drilled holes
- ablation rate (fiber guided by hand):

Er:YAG (300 mJ):	1.24 +/- 0.4 mm/pulse
Ho:YAG (2 J) bare-fiber:	1.5 +/- 0.2 mm/pulse
Ho:YAG (2 J) lens-fiber:	0.8 +/- 0.1 mm/pulse
CO <sub>2</sub> (800 W):	~ 0.8 mm/ms

## Tissue damage in vitro

University of Bern  
Laser Department



Er:YAG  
bare fiber

Ho:YAG  
bare fiber

Ho:YAG  
lens fiber

CO<sub>2</sub>



157 +/- 79 $\mu\text{m}$	419 +/- 112 $\mu\text{m}$	714 +/- 60 $\mu\text{m}$	600 +/- 100 $\mu\text{m}$
⊥ 65 +/- 34 $\mu\text{m}$	237 +/- 90 $\mu\text{m}$	335 +/- 189 $\mu\text{m}$	250 +/- 100 $\mu\text{m}$

- highest mechanical damage with Ho:YAG caused by the high laser induced pressure waves

## in vivo evaluation after 6 weeks

University of Bern  
Laser Department



- Number of channels identified
- Extent of scar tissue around the channel
- Type and extent of neo-angiogenesis

## Conclusion 1



Laser	Thermal damage acute	pressure [bar]	number of channels identified	extent scar formation	angiogenesis
Er:YAG	157±79 μm	+9/-8 bar	1-2 of 3	0.8±0.6 mm	-
	⊥ 65±34 μm			0.6±0.4 mm	
Ho:YAG bare-fiber	419±112 μm	+30/-14 bar	2-3 of 3	2.5±0.7 mm	+
	⊥ 237±90 μm			1.5±0.5 mm	
Ho:YAG lens-fiber	714±60 μm	+55/-30 bar	2-3 of 3	1.7±0.8 mm	+
	⊥ 335±189 μm			1.0±0.4 mm	
CO <sub>2</sub>	600±100 μm	< 0.2 bar	2-3 of 3	2.3±0.4 mm	+
	⊥ 250±80 μm			1.8±0.5 mm	

## Conclusion 2



- The 4 lasers permitted to study outcome of pressure effects and thermal damage in vivo
- Minimal thermal damage by Er:YAG resulted in small scars.
- Angiogenesis depends largely on extent of thermal damage.
- High pressure damage by Ho:YAG led to tissue disruption with scars extending along separated fibre planes.



Because the underlying mechanism for beneficiary effects of laser treatment are largely unknown, optimum laser parameters are not yet defined. This study permits, however to apply distinct treatments to experimental and clinical studies.



---

## Dye-enhanced articular Cartilage Soldering

H.P. Weber, B.J. Züger, B. Ott, Th. Schaffner\*, P. Mainil-Varlet\*, M. Frenz  
Institute of Applied Physics, University of Berne,  
Sidlerstrasse 5, CH-3012 Berne  
Switzerland

phone: +41-31-6318943, fax: +41-31-6313765,  
E-mail: [frenz@iap.unibe.ch](mailto:frenz@iap.unibe.ch)

\* Institute of Pathology, University of Berne,  
Switzerland

---

Cartilage welding 1



### Indications:

- Meniscal surgery
- Abrasive chondroplasty
- Lateral release
- Synovectomy
- Osteoarthritis

---

Cartilage welding 2





### Advantages:

- Eliminate the use of multiple instruments
- Better access to tight joints (ankle, elbow, wrist)
- Improved properties of coagulation
- Diminished bleeding
- High precision
- Less pain

Cartilage welding 3



CO<sub>2</sub> ( $\lambda = 10.6 \mu\text{m}$ )

Excimer XeCl ( $\lambda = 308 \text{ nm}$ )

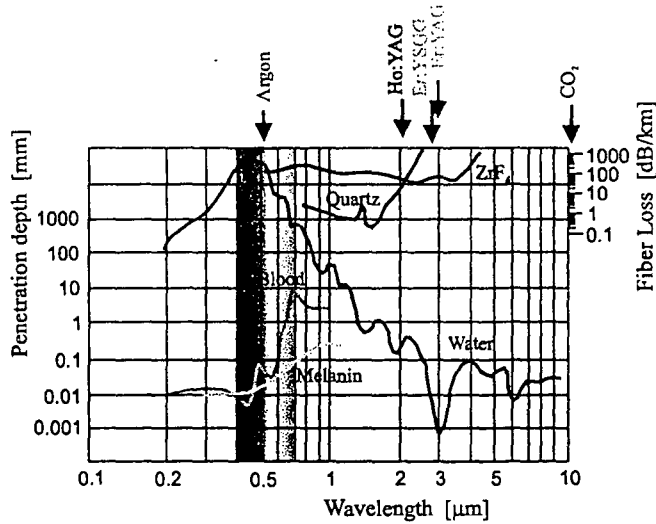
Nd:YAG ( $\lambda = 1.06 \mu\text{m}$ )

Ho:YAG ( $\lambda = 2.1 \mu\text{m}$ )

Er:YAG ( $\lambda = 2.94 \mu\text{m}$ )

Cartilage welding 4

# Absorption in Tissue

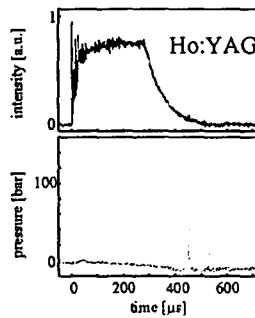
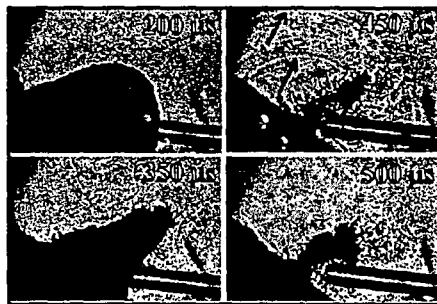


Cartilage welding 5

# Problems



- Influence of rapid bubble expansion and strong pressure transients on tissue unknown



- Extent of thermal damage controversially discussed

Cartilage welding 6

## Clinical case

University of Bern  
Laser Department



- Man, 1954
- Knee trauma
- Laser meniscectomy 1996  
(Ho:YAG laser)
- No history of trauma after meniscectomy
- 18 months post meniscectomy  
pain int. compartment



MRI



cartilage defect



tibia plateau defect

arthroscopy



condylus defect  
tibia plateau defect



Mosaic plasty

Cartilage welding 7

## Goal

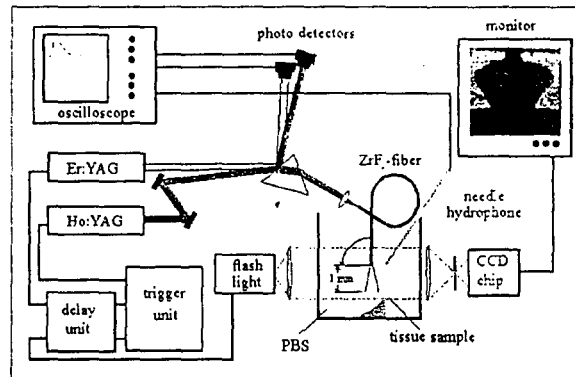
University of Bern  
Laser Department



- Evaluate laser-induced cartilage damage  
by determination of laser-effects on  
chondrocyte viability in an *ex vivo* model
- Calculate possible undesired side-effects

Cartilage welding 8

# Experimental setup



Er:YAG:  $E = 100 \text{ mJ}, 150 \text{ mJ}$   
 $\tau = 400 \mu\text{s}$

Ho:YAG:  $E = 500 \text{ mJ}, 800 \text{ mJ}$   
 $\tau = 400 \mu\text{s}$

$\nu = 8 \text{ Hz}$ , fiber diameter = 1 mm, 50% spot overlap

Cartilage welding 9

# Histology



Er:YAG

Safranin-O



$E = 150 \text{ mJ}, 2 \text{ shots}$

no visible  
thermal damage

Ho:YAG

Alcian-blue



$E = 800 \text{ mJ}, 1 \text{ shot}$

650  $\mu\text{m}$  thermal damage

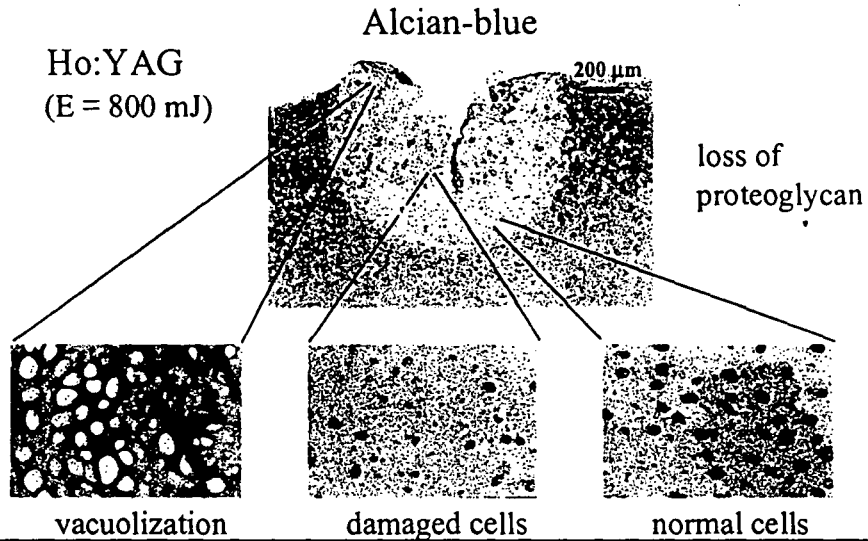
Safranin-O



Cartilage welding 10

## Direct tissue damage

University of Bern  
Laser Department



Cartilage welding 11

## Material and Methods

University of Bern  
Laser Department



- Bovine hyaline cartilage pieces (6 hours post mortem)
- Laser irradiation in PBS



### Histology

- 4% formaline + paraffin
- Masson-trichrome
- Safranin-O
- Alcian-blue
- light microscopy

### live/dead

- embedding in agar
- cutting 200  $\mu$ m with a tissue sectioner
- incubation (1h) in calcein AM and ethidium homodimer-1
- confocal microscopy

Cartilage welding 12

## Conclusion

University of Bern  
Laser Department



- Confocal microscopy is a powerful tool for assessing changes in tissue structure after laser treatment.
- Histology underestimates thermal damage zone
- Er:YAG: - Damage restricted to less than 100  $\mu\text{m}$   
- High ablation precision
- Ho:YAG: - Deep tissue damage (up to several mm)  
- Low ablation efficiency
- ⊙ Tissue damage by heat conduction

Cartilage welding 17

## Myoplasty

University of Bern  
Laser Department



### INDICATION:

- if too little cartilage is left for reshaping or a deep local defect exists

### PROCEDURE:

- mosaic plasty to replace areas with defect
- press fit is today standard

### PROBLEMS:

- long duration for regeneration of cartilage
- contact of entire surface of implant is needed
- gliding during movement of joint must be avoided

Cartilage welding 18

## Material and Methods: Cartilage

University of Bern  
Laser Department

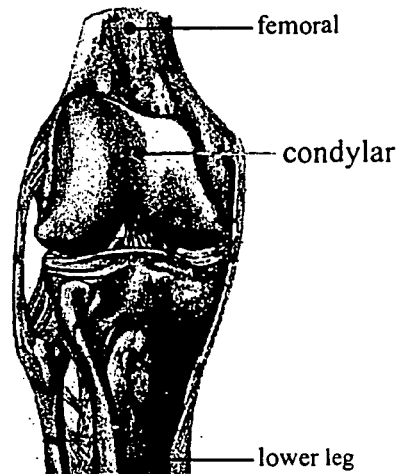


### TISSUE:

- condylar articular cartilage
- knee of 4 to 6 months old calves

### TREATMENT:

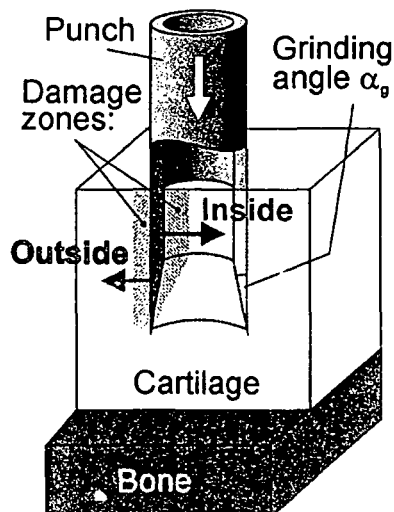
- dissection and welding two days post mortem
- kept moist in PBS solution



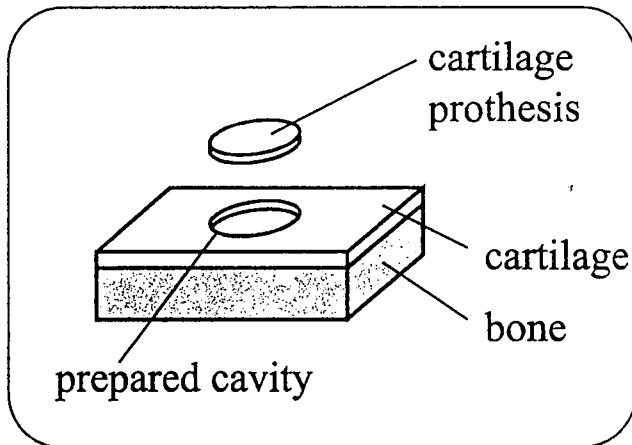
Cartilage welding 19

## Zechner Drill

University of Bern  
Laser Department



Cartilage welding 20



MOTIVATION:

- fixation of cartilage prosthesis using dye enhanced solder  
⇒ shorter recovery time of the lesion

INVESTIGATIONS:

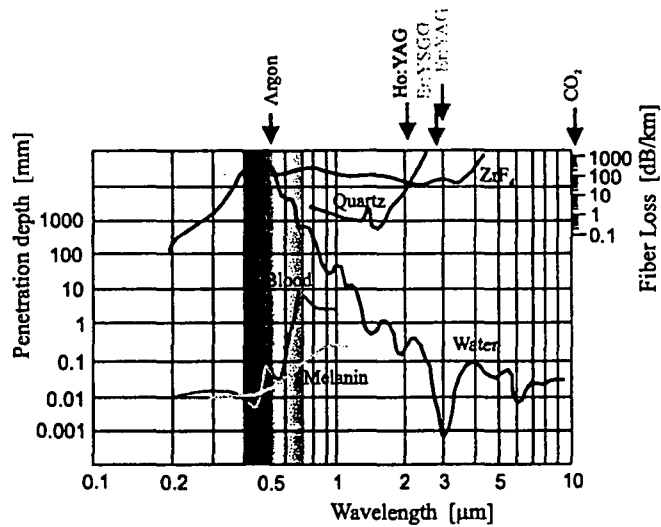
- tensile strength of welded cartilage repairs
- thermally induced damage of cartilage after laser irradiation compared to mechanically induced damage

GOAL:

- maximum tensile strength with as small as possible damage



# Absorption in Tissue



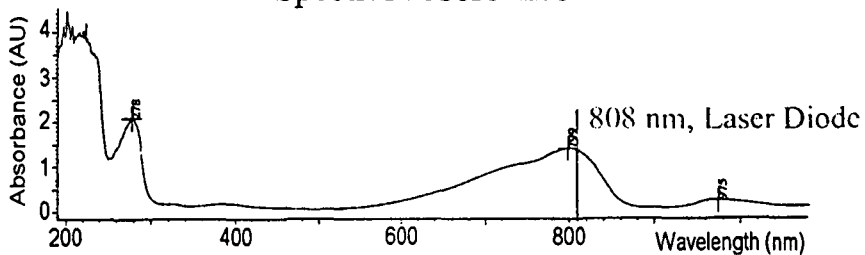
Cartilage welding 23

# Material and Methods: Solder



- Solder consists of:
- water
  - 25 % BSA (bovine serum albumin)
  - 0.5 % HA (hyaluronic acid)
  - 0.1 % ICG (indocyanine green)

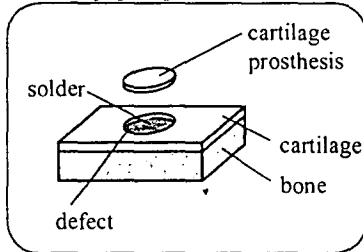
## Spectral absorbance



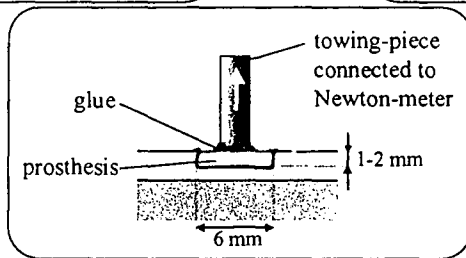
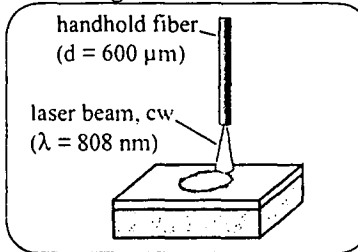
Cartilage welding 24



**Cavity preparation**



**Welding**



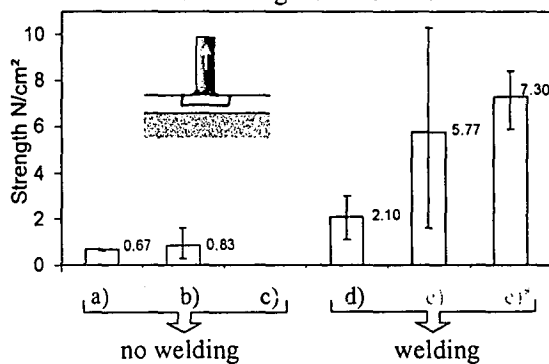
**Tensile strength measurement**

Cartilage welding 25

Results: **Tensile strength**



**Tensile strength measurement**



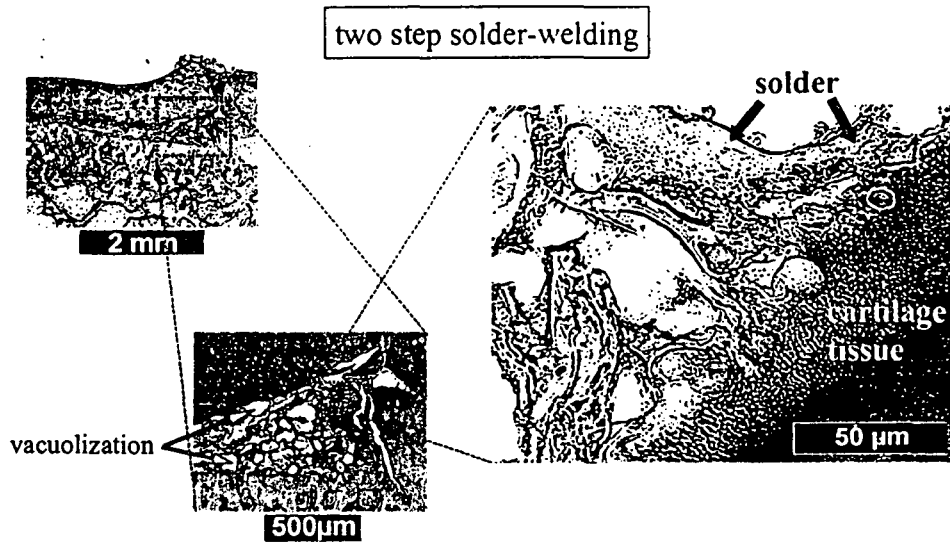
- a) defect untreated
- b) with solder not irradiated
- c) irradiated without solder
- d) one step solder welding
- e) two step solder welding
- e)\* with 48 h hydration

**Two step solder welding:**

1. drying defect → 1<sup>st</sup> layer solder → irradiation
2. 2<sup>nd</sup> layer solder → prosthesis → irradiation through cartilage

Cartilage welding 26

## Histology: Solder-Tissue compound



Cartilage welding 27

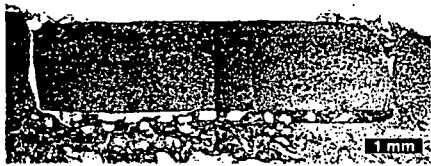
## Histology: Defect with Prosthesis

University of Bern  
Laser Department



Two step solder welding:

1. drying defect → 1<sup>st</sup> layer solder → irradiation
2. 2<sup>nd</sup> layer solder → prosthesis → irradiation through cartilage



'Shortly' welded defect:

- no visible cartilage damage
- usually smaller tensile strength

'Long' welded defect:

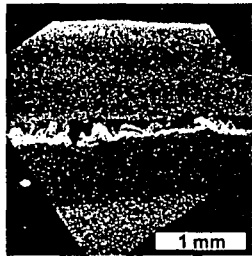
- desiccation and bending of cartilage
- good bonding but more thermal damage

Cartilage welding 28

# Histology: Cell viability



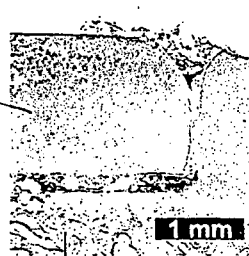
Live & dead staining with  
laser scanning microscope (LSM)



- red: dead chondrocytes
- ⊗ green: living chondrocytes
- yellow: solder

➔ Excellent indicator for thermal damage

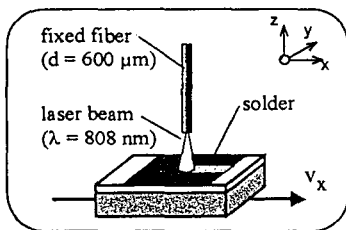
EVG staining with  
normal light microscope



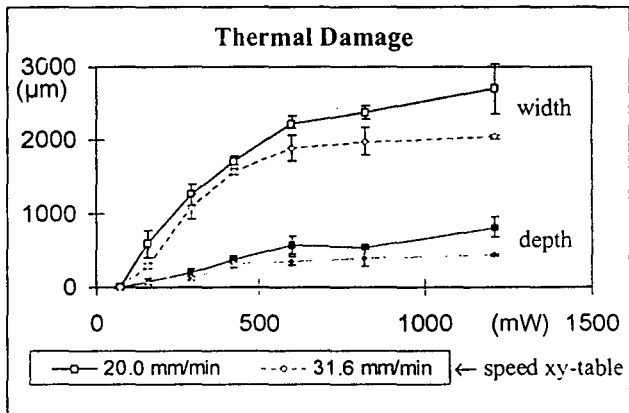
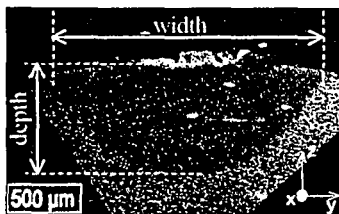
- reddish: cartilage
- ⊗ yellow/brown: solder

➔ No thermal damage is visible

# Results: Thermal damage



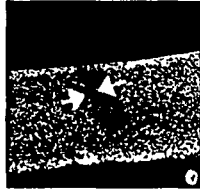
Cartilage moves on a xy-table



## Results: Mechanically induced damage

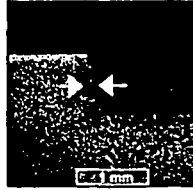


Punching



110 - 150  $\mu\text{m}$

Punching & drill



200 - 250  $\mu\text{m}$

Scalpel cut



30 - 55  $\mu\text{m}$

➔ Operating tools should be sharp and applied smoothly

Thermal damage in comparison with mechanically induced damage:

thermal damage depth  $\leq 200 \mu\text{m}$



radiant exposure must be smaller than  $40 \text{ J/cm}^2$

Cartilage welding 31

## Conclusion

University of Bern  
Laser Department



### Solder-welding:

- It is possible to **bond cartilage to cartilage** by solder-welding
- Solder-welding induces **considerable thermal damage**

### Life & dead staining:

- Live & dead staining is a powerful tool to **indicate cell viability *ex vivo***
- **Mechanical induced damage** depends on tool sharpness and handling



for a radiant exposure  $< 40 \text{ J/cm}^2$   
thermal damage  $<$  mechanical damage

Cartilage welding 32

# FIBRE BRAGG GRATINGS for Telecommunication and Sensing

by

Dr. Prabakaran Poopalan

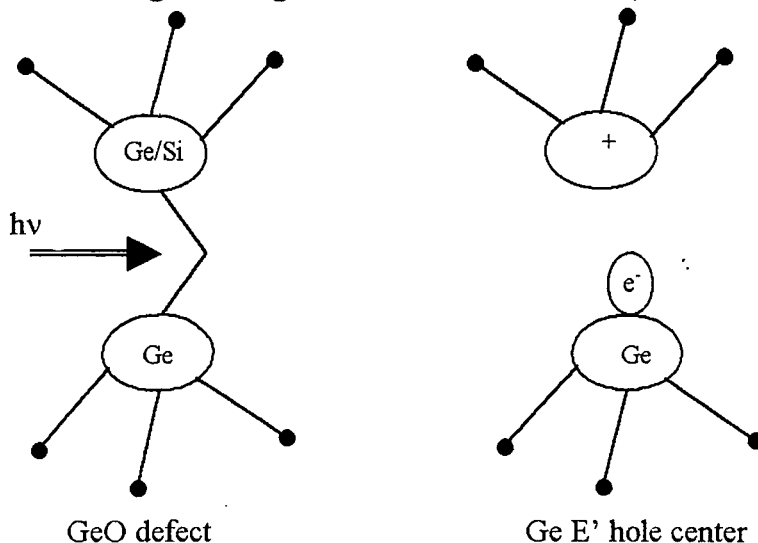
- important development aspect of Optical-Communication and Modern Optical Sensing (fibre based)
- enabling technology for DWDM as well as optical sensing, especially in structural sensing, temperature sensing, chemical sensing etc.
- the beauty
  - all fibre technology
  - easy integration into existing systems
  - low joining (splicing) loss
  - cheap → fibre, compared to other form

by virtue of diffraction of x-rays by crystals/crystalline form of matter as discovered by Sir William Bragg and Lawrence Bragg.

- Analysis ⇒ it looks like reflection but is actually diffraction combining interferometrically.
- Ge-SiO<sub>2</sub> fibre have a very high absorption of UV wavelengths (<300nm)
- early in 1978 it was shown that fibres exposed to SLM radiation from an Argon-ion laser at 488 nm produced index variations in the fibres. Kenneth Hill and co. from CRC.
- in 1992 discovery of lateral UV illumination spurred a tremendous flurry of activity and we are here today!

photosensitivity → permanent change in refractive index/capacity induced by exposed to light radiation.

formation of index change due to germanium – electron defect, GeE'



But effect not specific to Ge fibre other materials/ions in fibre form have shown such behaviors.

⇒ Proven that UV illumination increases index.

How do we harness this effect?

→ Falling back to optics,

Fresnel equations show that any variation in index of refraction a medium/media interface show up as a fraction.

→ for glass (fibre)/air interface

this reflection is between

3.6 % - 4 %

→ combining this with the early result of Kenneth Hill and Sir Bragg → Fibre Bragg Gratings (FBG)

### CONFLICT

Fresnel's equations do not show wavelength dependence – so all wavelength incidents on the FBG should be reflected equally.

BUT IT ISN'T SO

Bragg's law dictates wavelength dependence of the diffraction to periodic variations (in this case index) in the material.

SO PHYSICALLY

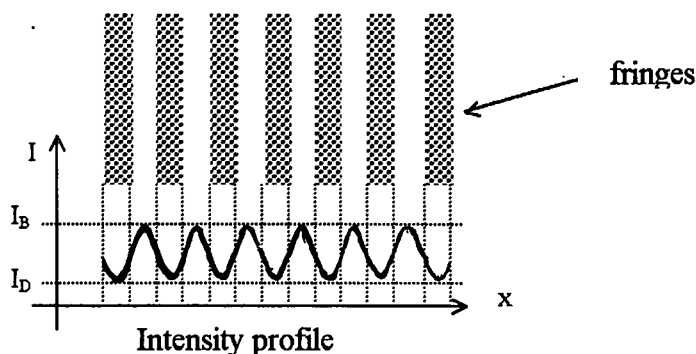
- a FBG essentially a periodic variation in the fibre core index of refraction
- a FBG only reflects (short period) a particular resonant wavelength (phase matching of incoming and outgoing and index period)

HOW DO WE CREATE THIS PERIODICITY?

- Searching all the optics texts we find .....

### INTERFEROMETRY

- Interferometry provides a means to incorporate periodic variations in the fibre index → interference fringes



- So, we now have all the spices,
- fibre
  - UV source
  - Interferometry

to cook it .....

1. Take UV source and shape it
2. Break UV beam to 2 beams
3. Create interferometry pattern by combining 2 beams (taking care not to exceed coherence length)
4. Focus point of beams crossing
5. Put fibre at focus point
6. Monitor growth, stop at desired point

ONE FBG IS READY

Before all that

- the photosensitivity depends on a photon of wavelength around 242 nm (which has  $> 100$  dB/mm absorption) to create a GeE' center (for Ge-SiO<sub>2</sub>, standard telecommunication fibre)
- ⇒ For this fibre, a source must be found to satisfy requirement.

KrF → 248 nm ( $\lambda$ )  
300  $\mu$ m - 1 mm ( $l_c$ )  
1 Hz - 50 Hz (f)

KrF-Dye → 240 nm  
1 Hz - 50 Hz

SHG-Ar<sup>+</sup> → 244 nm ( $\lambda$ )  
 $> 100$  mW (P)  
 $\geq 5$  cm ( $l_c$ )

CW

→ KrF radiation produces damage sites in the fibre

- too much power
- induced index → core/cladding difference
- denoted as Type II & IIA
- but good for production

→ CW Ar<sup>+</sup> radiation is low power but long coherence length allows greater room for intervening optics

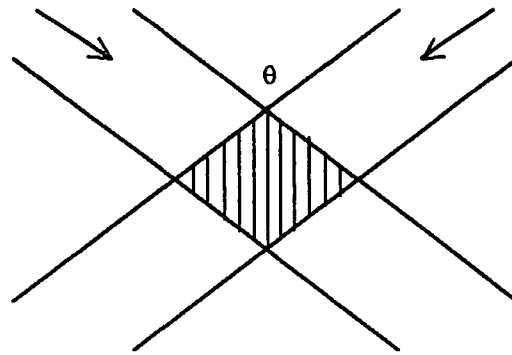
- produces Type I gratings
- good for fancy gratings & production

More or less the source problem is settled.



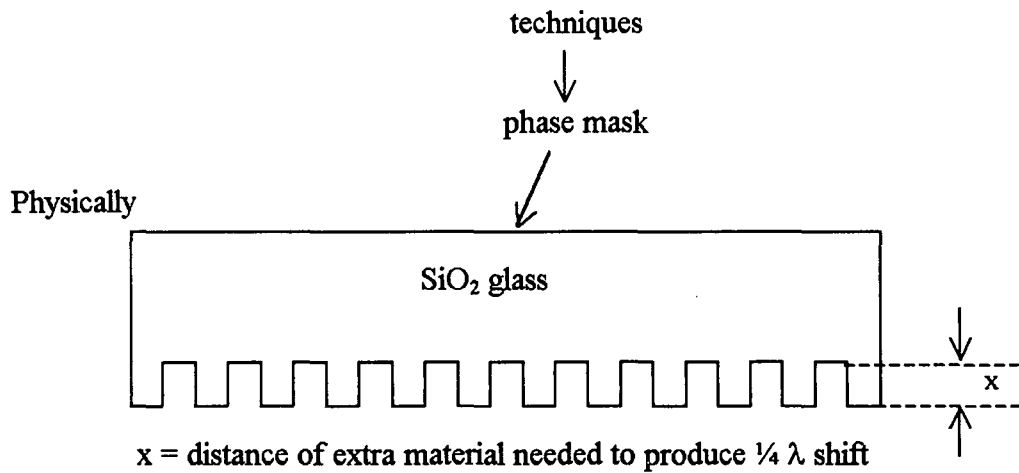
PRODUCING THE INTERFERENCE FRINGES

- Classic method is via 2 beams interferometry.



But with KrF lasers,  $\lambda_c \downarrow$

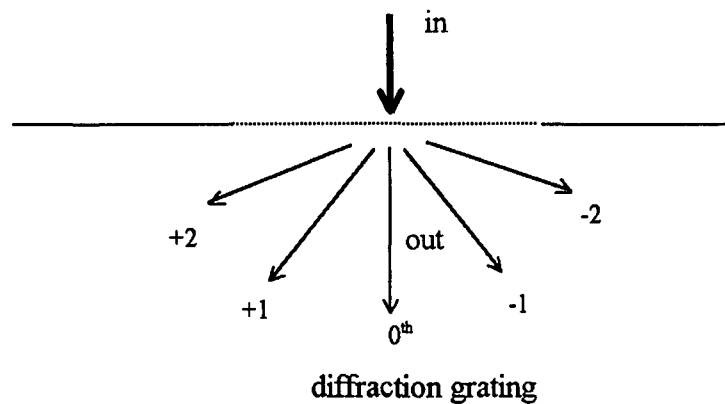
Alternatively → borrow semiconductor



A phase mask is essentially a transmission diffraction grating.

- 0th order
- ± 1st order
- ± 2nd order, etc.

but our requirement is 2-beams interferometry

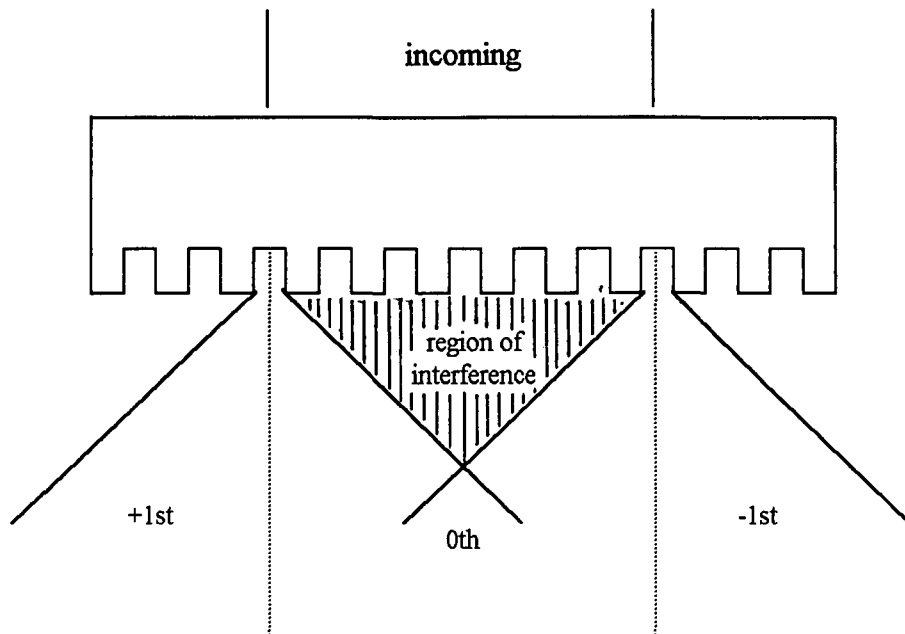


0th order beam is very strong → need to eliminate it → x amount of material to incorporate  $\lambda/4$  shift.

The result ....

- destructive interference reduces 0th order beam < 1 %
- increase  $\pm$  1st order to > 35 %

physically.....



..... and we have 2-beams interferometry

phase mask technique → "contact printing" due to low  $l_c$  of excimer lasers,

∴ fibre must be planed adjacent to the mask → must not touch → possible damage.

use of the CW SHG Ar<sup>+</sup> allows extension to full fledged 2-beam interferometry,.

- phase mask technique is limited to one resonant wavelength per mask
- interferometry "the old way" allows changing of wavelength by angular beam direction change.
- simpler but needs extreme care and stability.

## BACKGROUND

- the phase mask
  - fabricated by e-beam etching or UV-interferometry
  - has a  $\frac{\lambda}{4}$  x distance for the laser intended
  - has a period of  $\Lambda$
- the fibre grating has a period of  $\Lambda/2$
- strongest mode-coupling
  - at resonant Bragg wavelength

$$\lambda_B = 2 n_{\text{eff}} \Lambda'$$

where  $\Lambda' = \Lambda/2$  and  $n_{\text{eff}}$  = effective refractive index of fibre  
index perturbation :

$$\delta n(z) = \delta n_0(z) \left\{ 1 + m \cos \left[ \frac{2\pi z}{\Lambda'} + \phi(z) \right] \right\}$$

$m \rightarrow$  contrast  $\rightarrow$  determined by visibility of UV fringe pattern

$\delta n_0(z) \rightarrow$  "dc" index change spatially averaged over a grating period.

$\phi(z) \rightarrow$  grating chirp

for a step-index & uniform induced index change  $\delta n_{\text{co}}(z)$

then  $\delta n_{\text{eff}} \cong \tau \delta n_{\text{co}}$

$\tau$  = core power confinement factor for mode of interest.

To determine  $\tau$ ,

a solution for  $b$  is needed

$$V \sqrt{1-b} \frac{J_{1-1}(V \sqrt{1-b})}{J_1(V \sqrt{1-b})} = -V \sqrt{b} \frac{K_{1-1}(V \sqrt{b})}{K_1(V \sqrt{b})}$$

where

$V$  = normalized normalized frequency for mode  $LP_{1\mu}$

$J_1$  = 0th order Bessel function of 1st kind

$J_{1-1}$  = 1st order Bessel function of 1st kind

$K_1$  = 0th order Bessel function of 2nd kind

$K_{1-1}$  = 1st order Bessel function of 2nd kind

$$b = \frac{n_{\text{eff}}^2 - n_{\text{cl}}^2}{n_{\text{co}}^2 - n_{\text{cl}}^2}$$

and  $V = \frac{2\pi}{\lambda} a \sqrt{n_{\text{co}}^2 - n_{\text{cl}}^2}$

next,  $\tau = \frac{b^2}{V^2} \left[ 1 - \frac{J_1^2(V \sqrt{1-b})}{J_{1+1}(V \sqrt{1-b}) J_{1-1}(V \sqrt{1-b})} \right]$

which gives the effective refractive index perturbation, from which,

$$R = \tanh^2 \left[ \frac{\pi}{\lambda} \delta n_{\text{eff}} L \bar{g} \eta \right]$$

where  $R \rightarrow$  measurement reflectivity

$L \rightarrow$  length of grating

$\bar{g} \rightarrow$  envelope weighting function

$\eta \rightarrow \tau$

the factor  $\left[ \frac{\pi}{\lambda} \delta n_{\text{eff}} L \bar{g} \eta \right] = R$ , the coupling coefficient

R is a measure of the grating strength

### FABRICATION

As given in the Fig. 1

Basic needs are :

- (i) UV laser source
- (ii) some lenses
- (iii) phase masks (1 per wavelength)
- (iv) alignment stages
- (v) monitoring set-up
- (vi) patience

Fig. 3 & 4 provide some insight to an actual set-up may be used in laboratories.

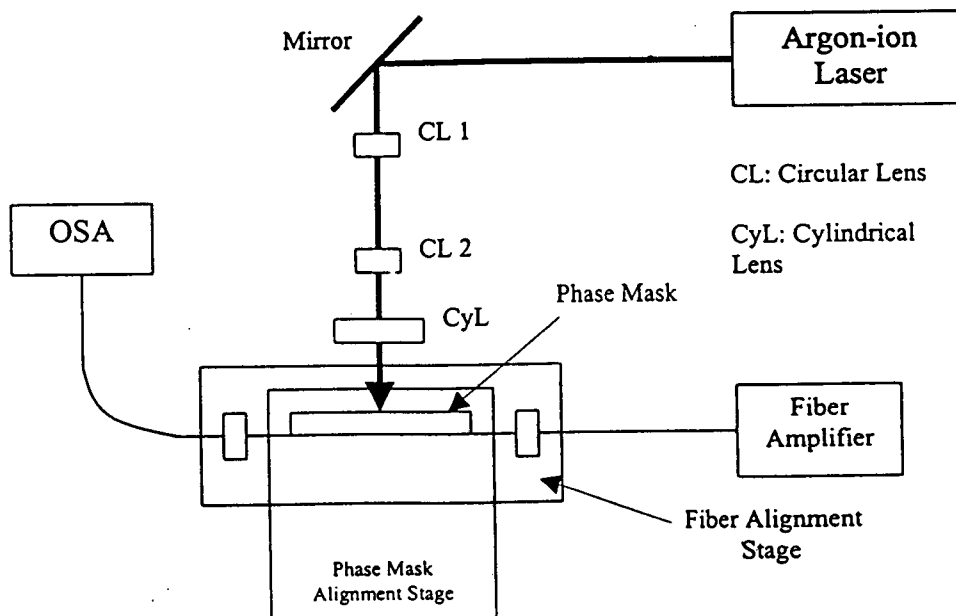


Fig. 1. Fabrication set-up

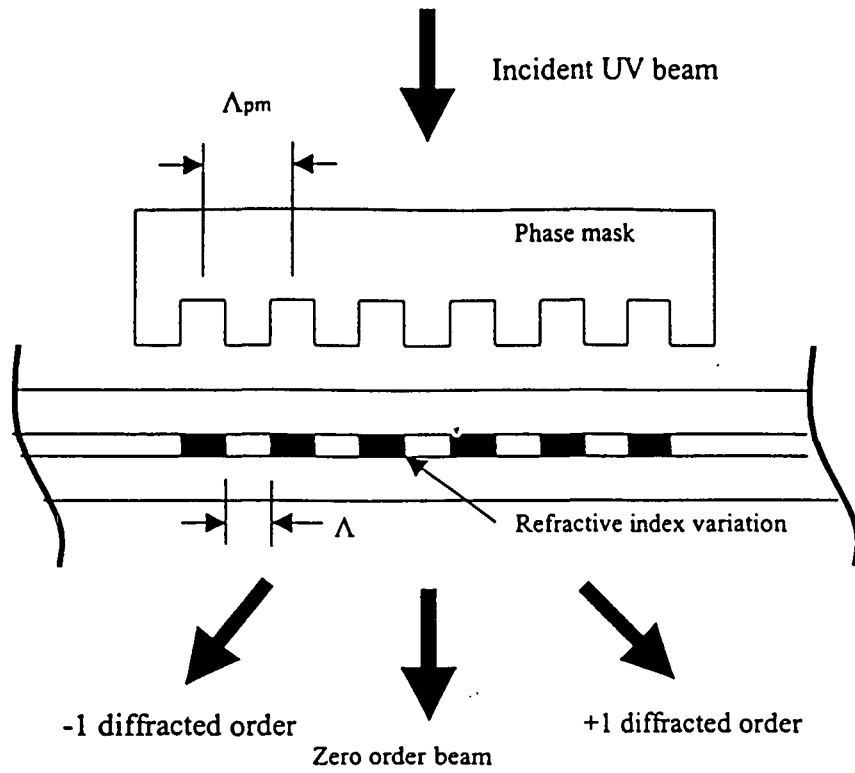


Fig. 2. Phase mask

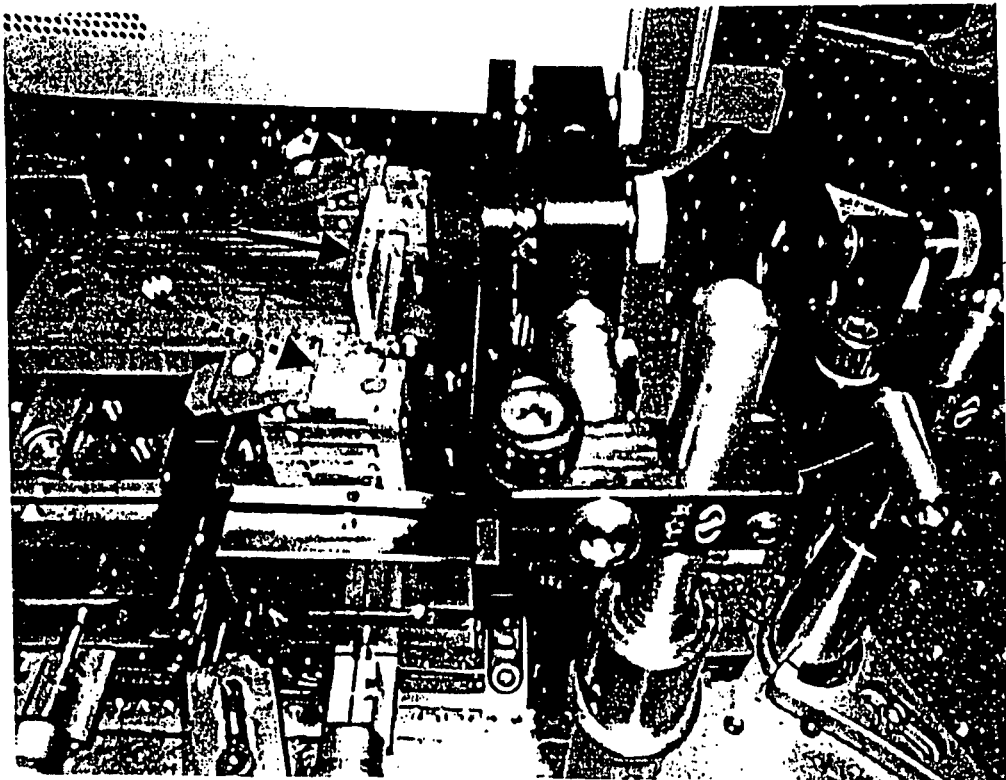


Fig.3. Position of mechanical set-up

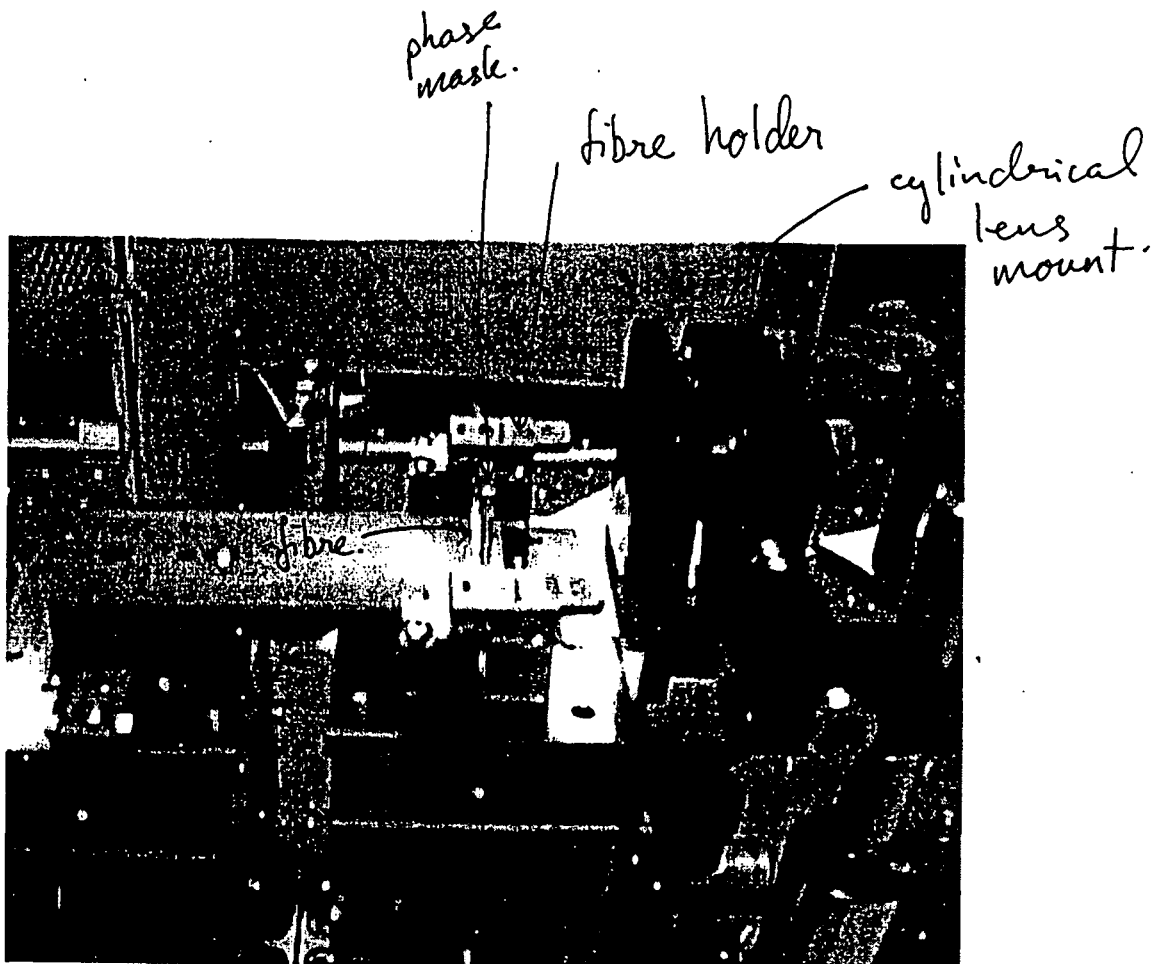


Fig.4. Set-up with fibre & UV in-plane

The FBG growth is monitored real time, as indicated by BB source and OSA in the experimental set-up.

Recording of growth time is also essential.

Fig. 5 & 6 detail some growth times. The difference is mainly due to human error ....

- a. CW Ar<sup>+</sup> beam is intrinsically smaller (~ 4mm x 1 mm) compared to excimer (1 cm x 3 cm)
- b. Ar<sup>+</sup> beam UV is of lower power → tighter focusing
  - easily miss the core
  - beam  $\omega_0 \sim 50 - 5 \mu\text{m}$
  - fibre  $2a \sim 8 - 6 \mu\text{m}$

### TYPICAL RESULTS

Once the growth is done → characterization ensues (naturally!).

The standard measurement are transmission & reflection

(i) transmission

→ a source emits light into the FBG and receiver (OSA) measures amount of "loss" at the resonant wavelength. Fig. 7 shows the set-up. Ideally, other losses are eliminated beforehand.

(ii) reflection

→ a source emits light into the FBG and receiver (OSA) measures the amount of reflected light via circulator. Characterising the circulator is critical. Fig. 8 shows this set-up.

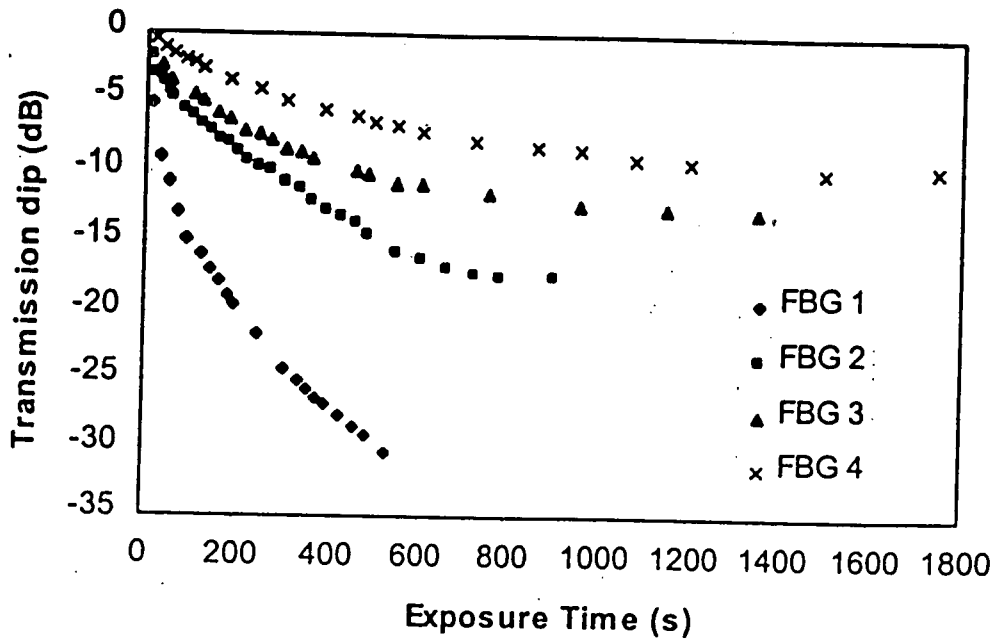


Fig. 5.

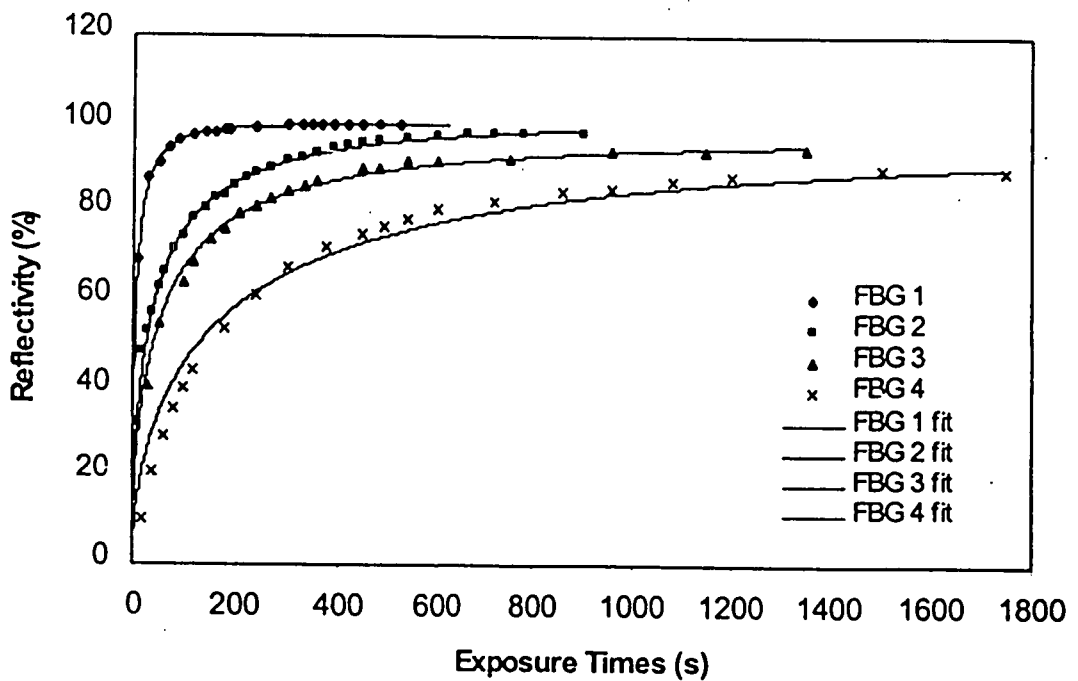


Fig. 6.

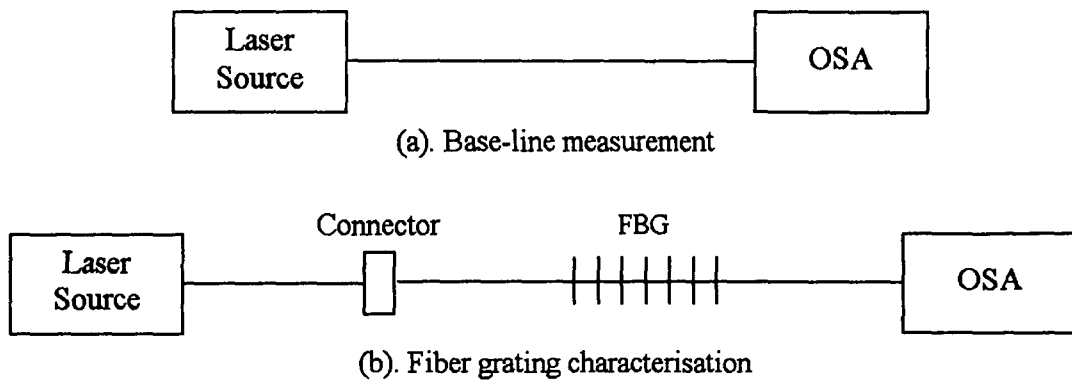


Fig.7. Transmission

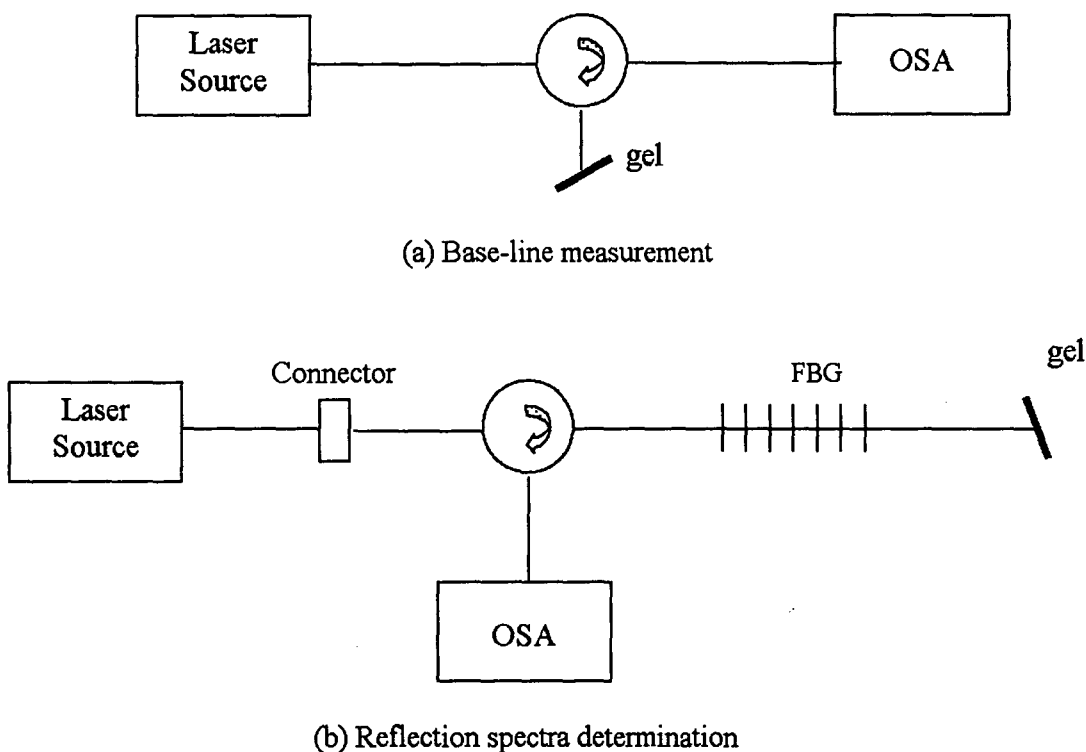


Fig.8. Reflection

The resultant spectrograms yield information such as peak reflectivity/transmissivity, bandwidth of reflection etc.

However, as seen from Fig. 9 & 10, there are some fine structures on the short wavelength side.

Further characterization reveals “fringe-like” structure (as in Fig. 11 & 10)

→ clue to index variation in-fibre, giving rise to PF characteristics.

The difference in the two sets of spectrograms is due to the type of source that is used.

In the first set a broad-band light-source is used with the OSA sweeping across the wavelength

→ spill-over.



In the second set, a narrow-band tunable external cavity semiconductor laser is used in synchronized sweep with the OSA. Combination of narrow light of large SMSR and synchronized sweeping eliminates noise.

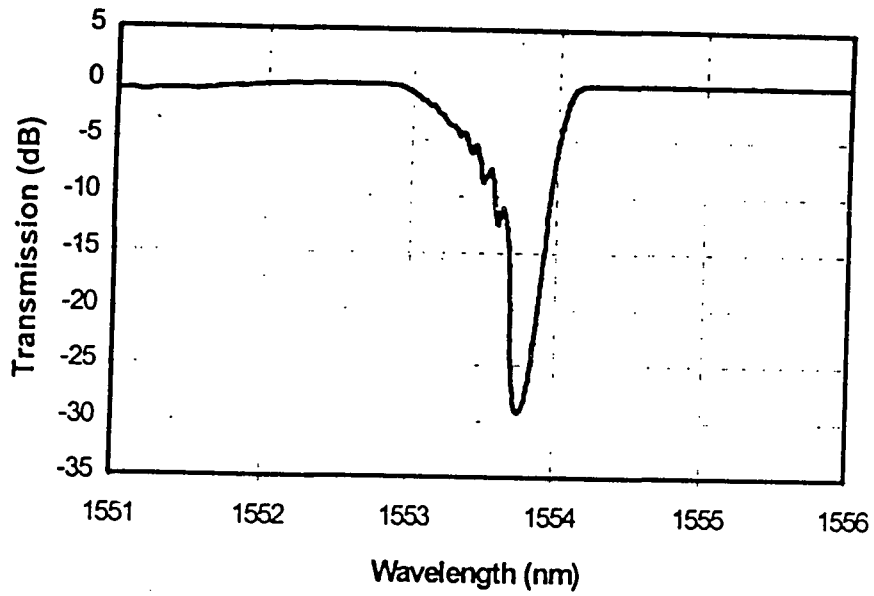


Fig. 9.

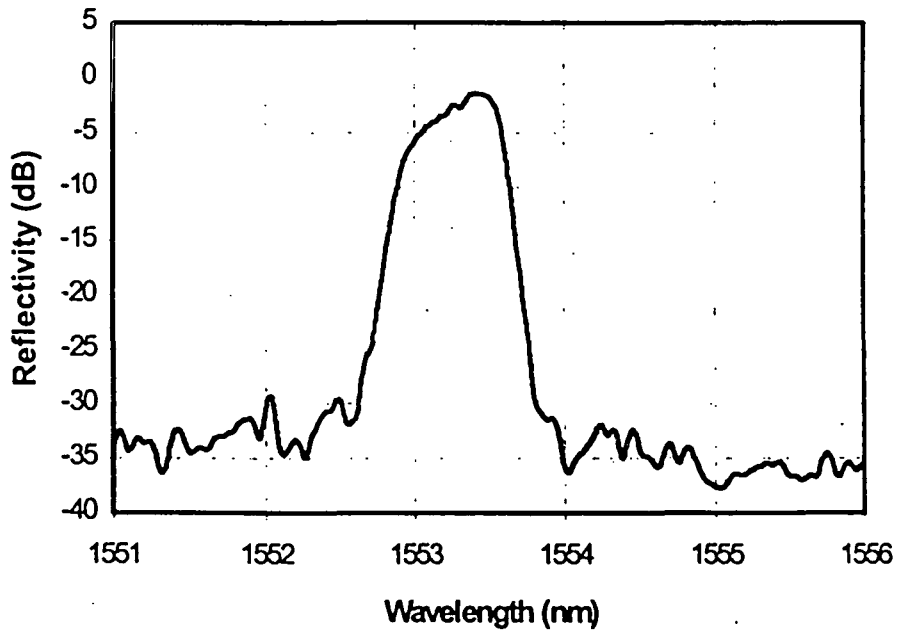


Fig. 10.

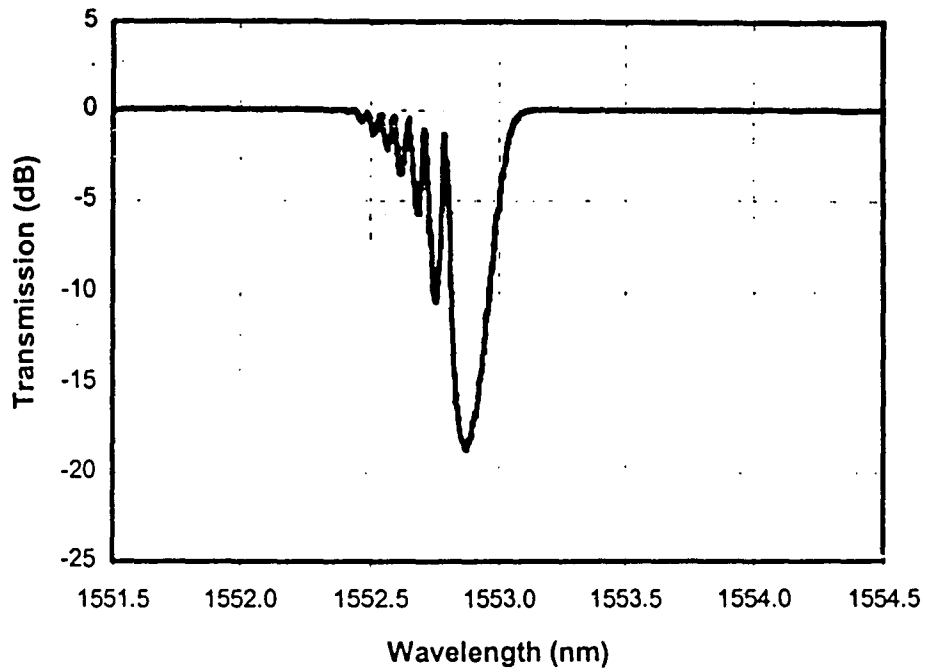


Fig.11.

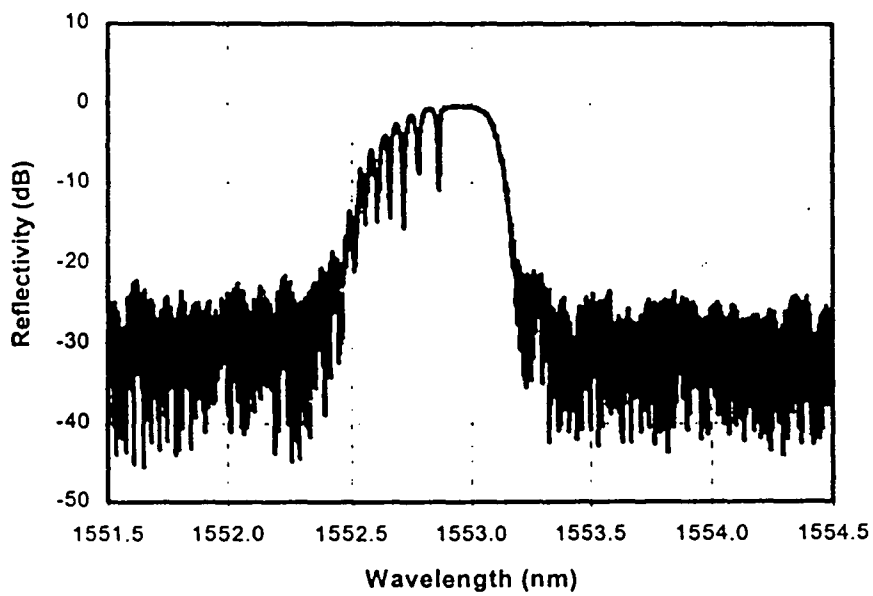


Fig.12.

## USES

→ telecommunication

⇒ enabling technology for DWDM

a) transmitters

→ wavelength locker

b) amplifiers

→ gain flattening filter

- c) dispersion
  - high-bit rate system dispersion compensators
- d) ADM
  - add-drop multiplexers
- e) receivers
  - demultiplexers for DWDM signals

→ sensing

advantages of fibre sensors over other types :

- electrically passive/isolated
- EMI immune
- high sensitivity
- multiplexing capability

FBG Sensors

- intrinsic sensing elements
- embedding into materials ( real-time tracking )
  - load
  - strain
  - temperature

⇒ Simplest case: stain & temperature

$$\Delta\lambda_B = 2n\Lambda \left\{ \left( 1 - \left[ \frac{n^2}{2} \right] [P_{12} - \nu(P_{11} + P_{12})] \right) \varepsilon + \left[ \alpha + \frac{dn}{dT} \right] \Delta T \right\}$$

where  $\varepsilon$  → applied strain

$P_{ij}$  → Pockel's coefficients of stress-optic tensor

$\nu$  → Poisson's ratio

$\alpha$  → coefficient of thermal expansion of fibre (silica)

$\Delta T$  → temperature change

factor  $\left( \frac{n^2}{2} \right) [P_{12} - \nu(P_{11} + P_{12})] = 0.22$

consequently, measured strain response at constant temperature is

$$\frac{1}{\lambda_B} \frac{\delta\lambda_B}{\delta\varepsilon} = 0.78 \times 10^{-6} \mu\varepsilon^{-1}$$

which gives a measure of grating shift with strain of 1 nm per 1000  $\mu\varepsilon$  at 1.3  $\mu\text{m}$ .

For temperature, the thermal response is dominated by the resolution of 0.001 nm is need to

resolved a temperature change of  $0.1^{\circ}\text{C}$  at  $1.3\ \mu\text{m}$ .

The strain response arises due to

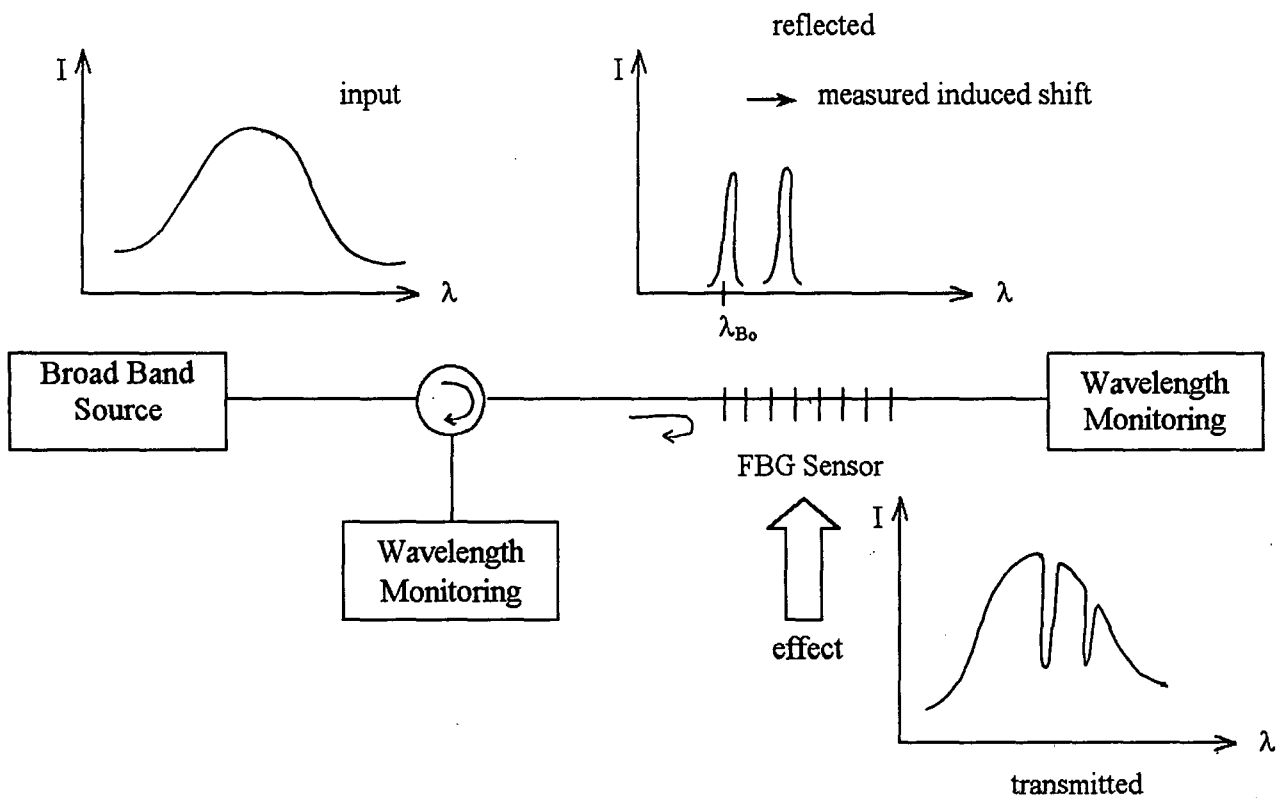
- (i) physically elongation  $\rightarrow$  grating pitch change and
- (ii) fibre index change by photoelastic effects

The thermal response is due to

- (i) inherent thermal expansion by fibre and
- (ii) temperature dependence of refractive index

As such its clear that the FBG sensor is “intrinsic”.

A simple set-up of a FBG sensor is given below



On the other hand, an array of FBG's of different resonant wavelengths can be detected by inserting a tunable filter that scans in synchronism with the OSA or just with a TLS and an OSA in synchronism.

### Temperature measurement

$\rightarrow$  a set-up as shown in Fig. 13 is utilized.

$\rightarrow$  peak wavelength change is plotted against temperature  $\rightarrow$  Fig. 14

a  $0.01\ \text{nm}/^{\circ}\text{C}$  thermal response is obtained for temperature range used.

Fig. 15 is a spectrogram of the recorded wavelength shift at  $44^{\circ}\text{C}$  and at  $121^{\circ}\text{C}$

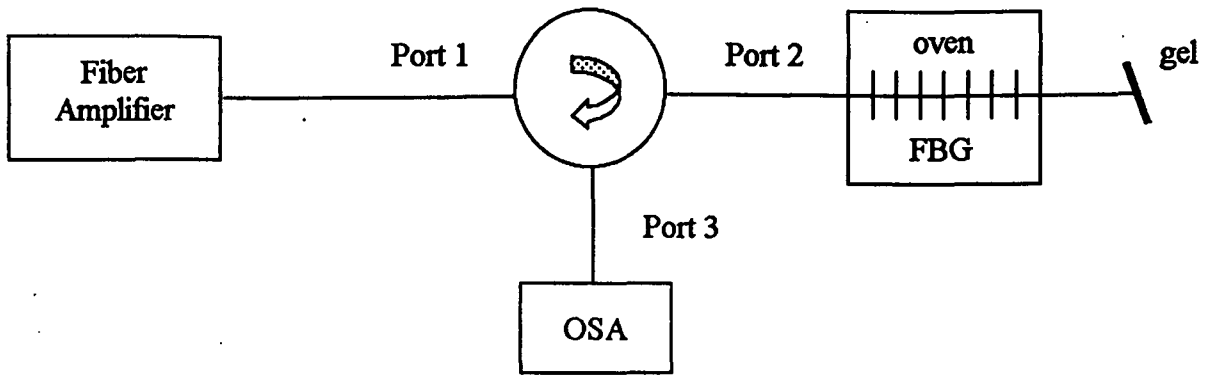


Fig.13

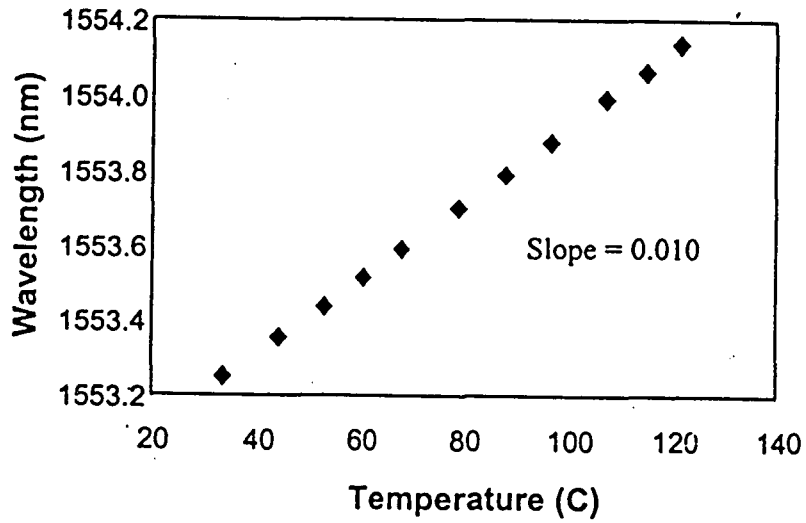


Fig.14.

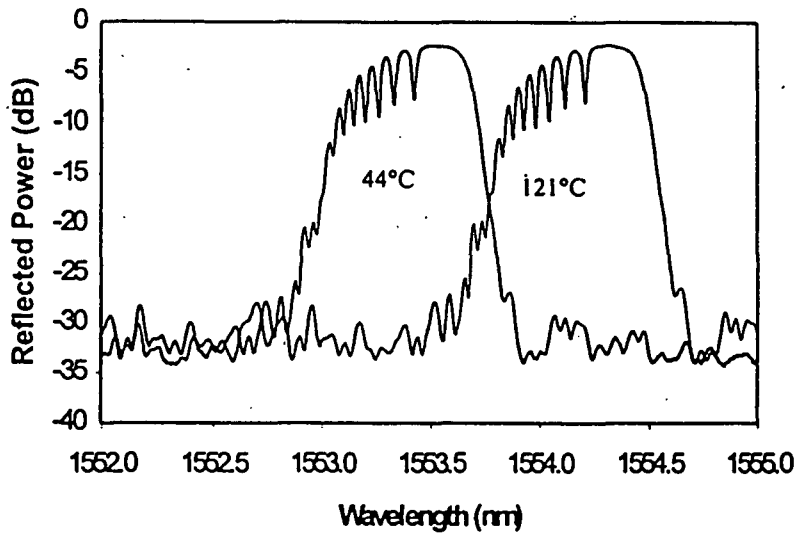


Fig.15.

To measure strain, a simple mechanical system of 2 alignment stages to which a FBG was glued and total elongation was recorded as was wavelength → a 2 mm elongation produced about 9 nm shift before the fibre broke.

THE END

# TELECOMMUNICATIONS OPTICALLY

by

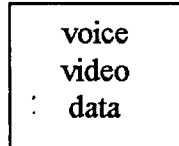
DR.Prabakaran Poopalan

- telecommunications

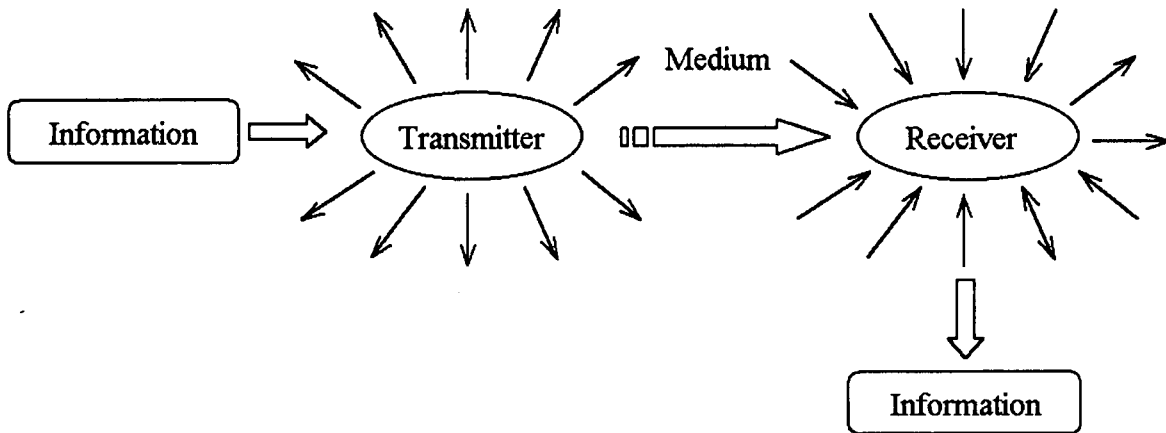
Greek → tele = over distance

→ communication = exchange of information

- presently - 3 types of information



- a basic "link"



Based on this the American - Indians are classic examples of optical communications

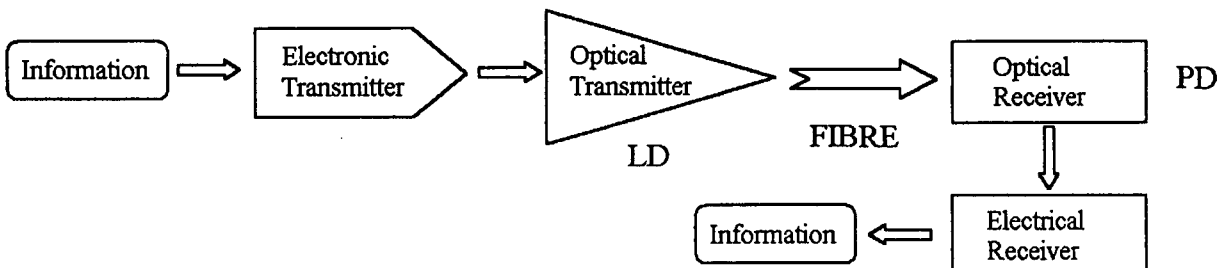
- complexity of links vary with need → LAN, MAN, LONGHAUL, etc.

but typically are variants of

- Mesh topology,
- Star topology,
- Ring topology, and
- Bus topology

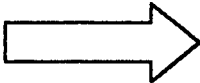
- optical communications, in-depth, is slightly different ⇒ need for conversion of Information from electrical to optical journal.

Hence,



- essentially comprises
  - LD
  - FIBRE
  - PD

## TRANSMITTERS

- depending on intended use and therefore the chosen topology - transmitters are either LED's or LD's.
  - both types operate by injection of carriers (holes/e<sup>-1</sup>s) to produce photons at optical wavelengths.
  - advantages
    - directly modulated by current (injection) variation/modulation.
    - small package & mass produced.
  - LED's were used first - historic development of semiconductor light emitters.
  - nowadays LED's are for short distances use (usually LAN).
  - LD's
    - coherent output
    - confined emission
    - narrow spectral-width
- 
- fundamental LASER properties
- wavelength
    - for LAN (& G-LAN) - 850 nm, 1310 nm.
    - for LONGHAUL - 1550 nm.
  - output pattern
    - for coupling into fibres ⇒ TEM<sub>00</sub>
    - in G-LAN development, VCSEL's have been vital.
      - circular beam output
      - intrinsic modulation BW ~ 200 GHz
      - many VCSEL's on 1 substrate - good for multichannel.
      - small resonant cavity ⇒ large FSR ⇒ single mode.
  - in Figs.1, 2 and 3: output spectra of LD's.

## RECEIVERS

- absorb photons - creating carriers (holes & e<sup>-1</sup>s)
  - ∴ current results →  $i \propto I \propto P^2$
- for optical communications → InGaAs
  - absorbs from ~ 800 nm → 1700 nm.
  - quantum efficiency,

$$\eta = \frac{\text{no. of electrons produced, } N_e}{\text{no. of falling photons, } N_p}$$

⇒ > 95% @ 1550 nm.

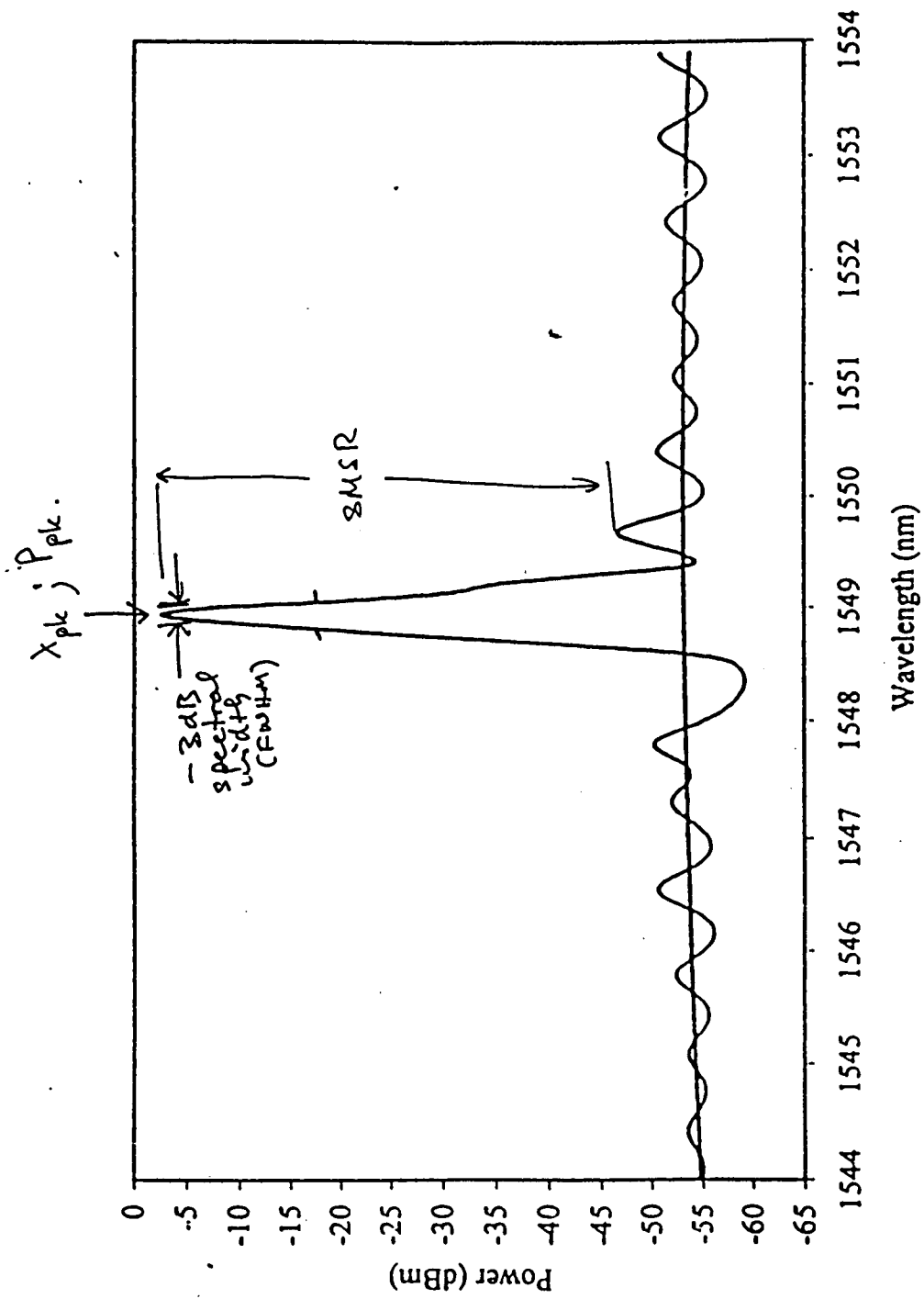
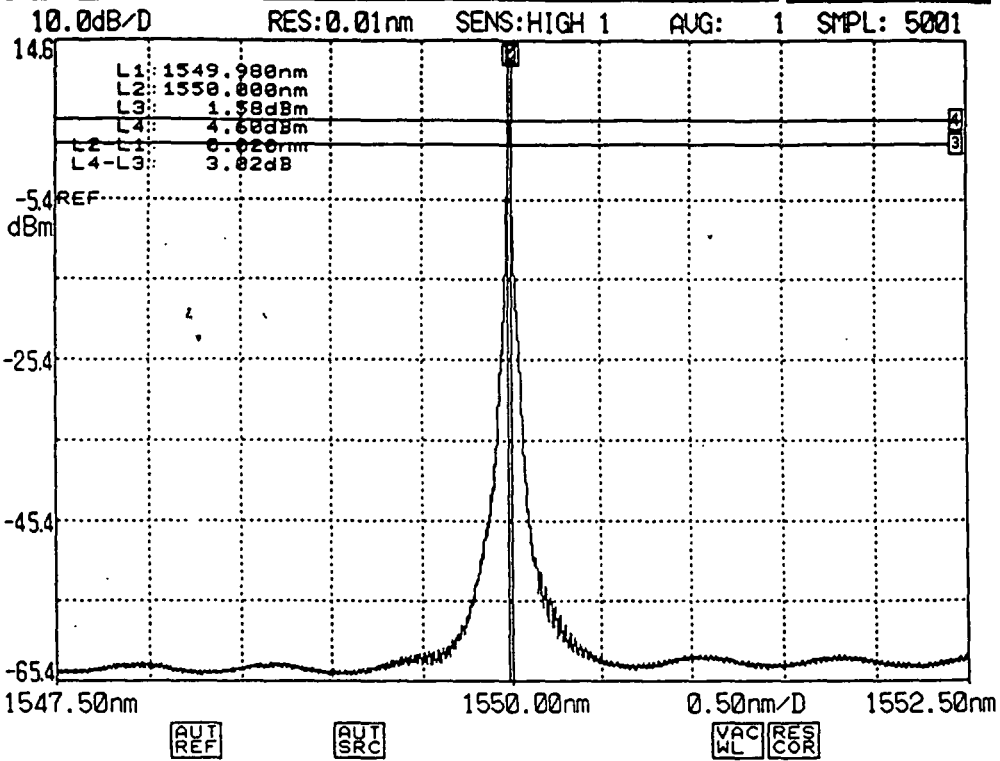


Fig.1. DFB - LD; from a 622 MB/s SDH Transmitter.

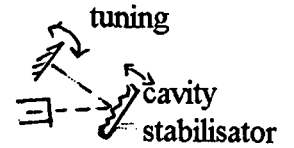


2001 Jun 20 16:45

SPACING: A:FIX /BLK  
B:WRITE /DSP  
FIT: FIT



External cavity LD



Littman cavity

2001 Jun 20 16:48

VPK : 1555.000nm-210.000dBm SPACING: A:FIX /BLK  
B:WRITE /DSP  
FIT: FIT

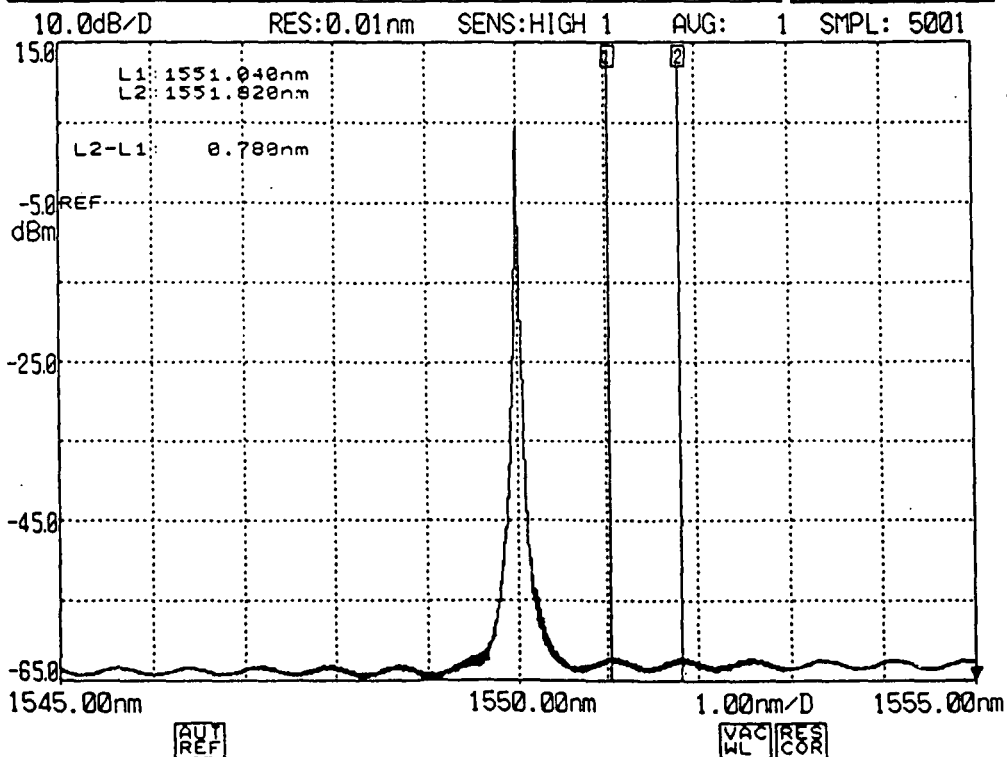


Fig. 2.

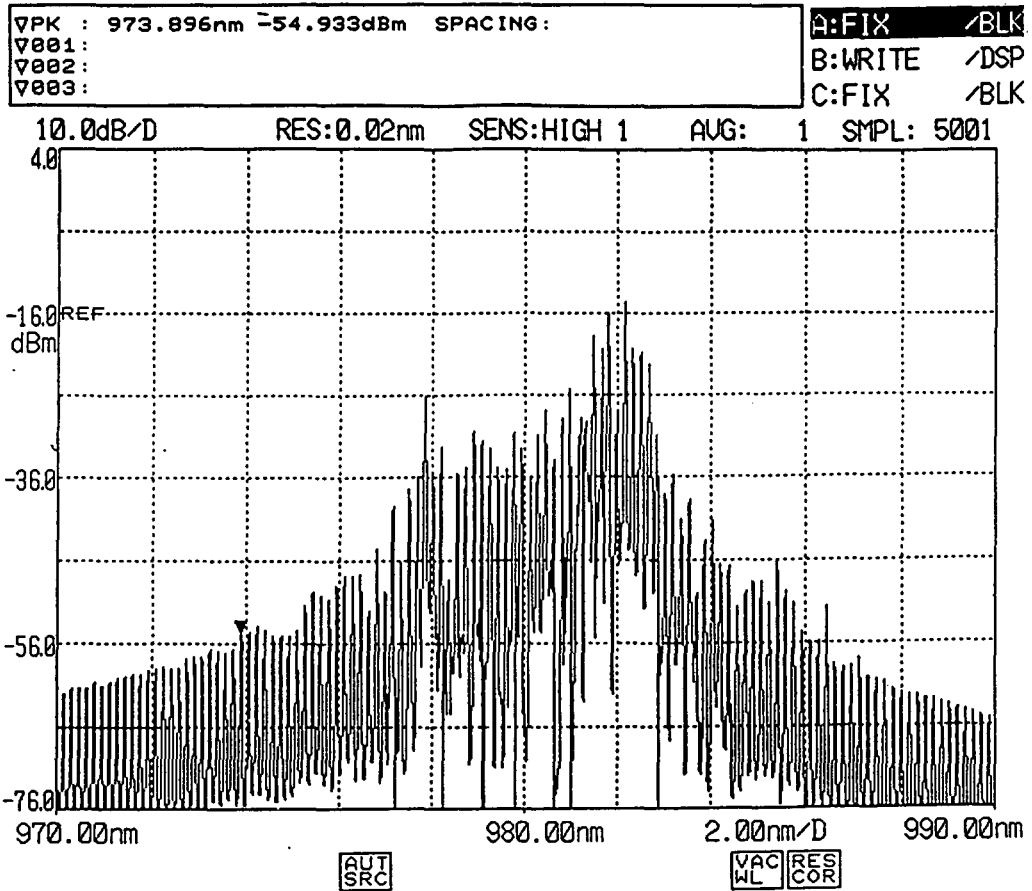


Fig.3. F - P LD

- receivers must have
  1. high quantum efficiency
  2. low dark current (temperature related)
  3. large Band-width → max. frequency.
- p-i-n PD's are most common
  - easy of fabrication
  - high reliability
  - low noise
  - low voltage
  - high BW
- APD's are useful for speciality functions as in OTDR's, etc.

TRANSMISSION MEDIUM ⇒ fibre

- depends on system employed & cost.
  - usually LAN, small - MAN ⇒ Multimode.
  - Longhaul exclusively → Singlemode.

- Singlemode telecommunication fibre [STF]

- step-index profile

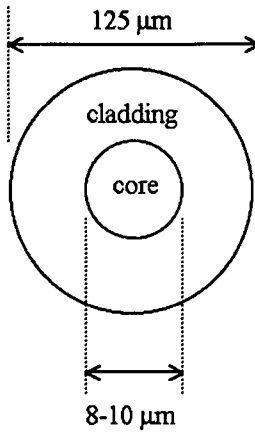
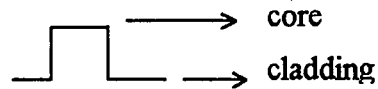
- weakly guiding  $\Rightarrow n_{\text{core}} - n_{\text{cladding}} \cong 0.003$

- core composition:  $\text{SiO}_2\text{-GeO}_2$

cladding composition:  $\text{SiO}_2$  or  $\text{SiO}_2\text{-Ph}_2\text{O}_5$

→ Germanium increases index

Phosphorus reduces index



- due to "nostalgic" behaviours, 80 nm & 1310 nm have remained until now → as LAN / MAN.

- Longhaul traffic uses 3<sup>rd</sup> telecommunications window → based on Fig.4.

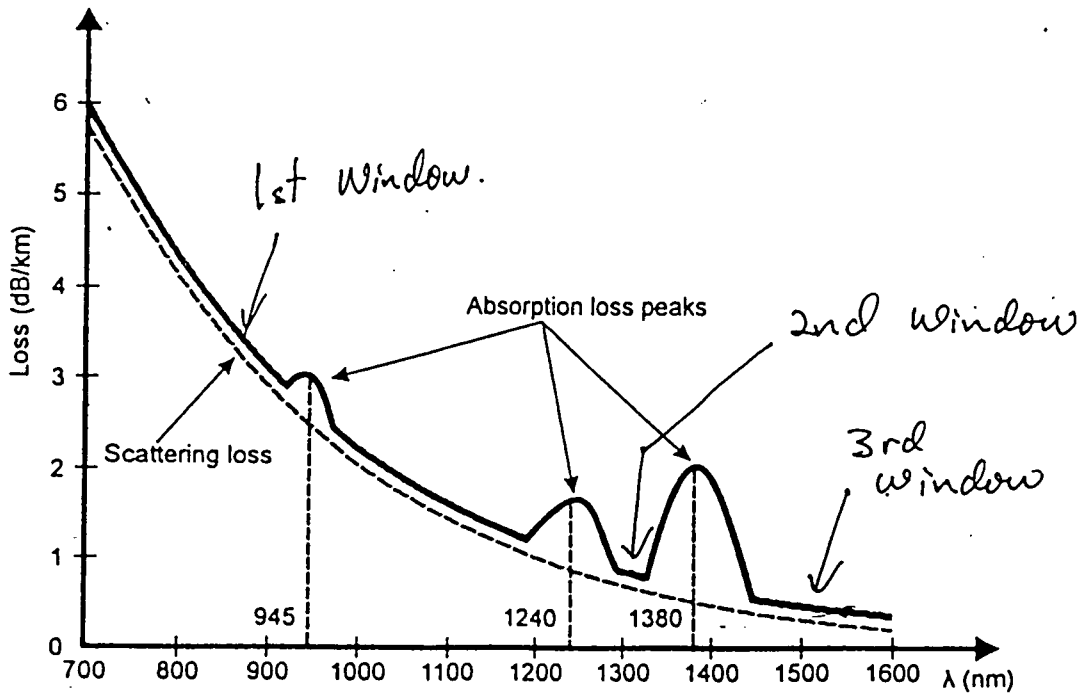


Fig.4. Loss spectra of silica fibres.

- Why fibre must replace copper? Bit rate.

- How fibre transmits information?

Optically & Digitally.

- What is singlemode fibre? No such fibre!
  - fibre are designed to keep the maximum possible light in the core
    - ⇒ confinement to core is determined by
      - (i) index of core & cladding
      - (ii) core size
      - (iii) propagating wavelength
  - solving Maxwell's equation for cylindrical boundary media → determines the wavelength limit above which, propagation is confined to the core in a single-mode.
  - below this limit ⇒ "cut off wavelength" propagation is in more than 1 mode, hence confinement is lost ⇒ eventual power loss, dispersion etc.
- What is a "mode" in fibres?
  - Electric & Magnetic [orthogonal] field patterns as determined by solving Maxwell's equations for a cylindrical boundary media.
    - Hybrid modes - power transfer longitudinally, also existed in fibres.
    - Natural modes are  $TE_{lm}$  ;  $TM_{lm}$ 
      - l → mode order = 0 for transverse modes
      - m → mode rank
  - On the other hand, these transverse modes do have longitudinal components
    - $TE_{0m}$  → longitudinal magnetic component
    - $TM_{0m}$  → longitudinal electric component
  - ⇒ hybrid modes arise
  - $l \neq 0$  →  $HE_{lm}$  &  $EH_{lm}$  do not exist
    - $HE_{lm}$  → magnetic field with longitudinal component
    - $EH_{lm}$  → electric field with longitudinal component
- from weakly guiding approximation  $n_1 - n_2 \ll 1$ , ( $\Delta \cong 0.003$  for practical fibres) these modes degenerate into linear-polarized modes [LP].

Table 1: LP mode composition

<u>LP mode</u>	<u>True mode</u>	<u>No. of degenerate modes</u>
LP <sub>01</sub>	HE <sub>11</sub> x 2	2
LP <sub>11</sub>	TE <sub>01</sub> , TM <sub>01</sub> , HE <sub>21</sub> x 2	4
LP <sub>21</sub>	EH <sub>11</sub> x 2, HE <sub>31</sub> x 2	4
LP <sub>02</sub>	HE <sub>12</sub> x 2	2

Do we need these fundamentals? YES!

→ better network design.

→ future improvements.

MFD → Mode Field Diameters →  $\frac{1}{e^2}$  pts. of electric field.

→ determined by core radius,  $a$

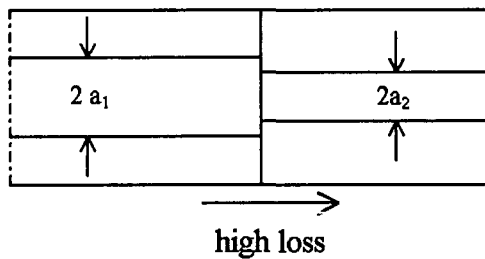
and

index of core,  $n_{co}$  & cladding,  $n_{cl}$

Knowing MFD enables

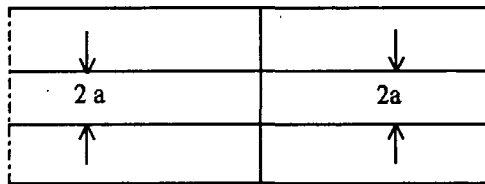
I.  $a$  and/or  $n_{co}$ ;  $n_{cl}$  to be determined → jointing / splicing loss.

(i) 2 fibres of different  $a$



(ii) 2 fibres of different NA [Numerical Aperture] where

$$NA = \sqrt{n_{co}^2 - n_{cl}^2}$$

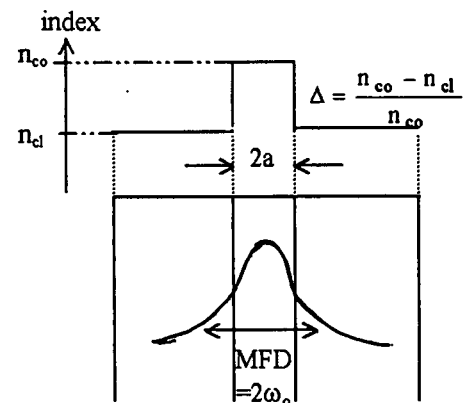
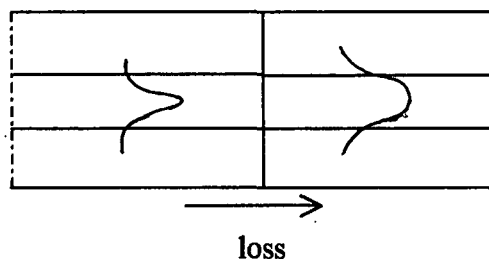


looks OK here but  $\Rightarrow \frac{MFD}{2} = \left[ 0.65 + \frac{1.619}{V^{3/2}} + \frac{2.879}{V^6} \right] a$

where  $V = \frac{2\pi a}{\lambda} NA \rightarrow$  normalized frequency.

$\lambda \rightarrow$  wavelength

therefore



knowing  $V$  helps, if  $< 2.405$  OK monomode.

if not  $\Rightarrow$  problem

II. estimation of light intensity in the core  $\rightarrow$  too high  $\rightarrow$  non-linear effects. [SBS, SRS]

III. MFD leads to  $V$ , which also determines the cut-off wavelength, above which higher order modes propagate.

$$V = \frac{2\pi a}{\lambda} \text{NA} = \frac{2\pi a}{\lambda} \sqrt{n_{\text{co}}^2 - n_{\text{cl}}^2}$$

setting  $V=2.405$  with known  $a$ ,  $n_{\text{co}}$  &  $n_{\text{cl}}$  determines  $\lambda \rightarrow \lambda_c$

Going to deeper waters .....

$\rightarrow$  light velocity in a medium

$$v = \frac{c}{n}$$

$c \rightarrow$  free space light speed

$n \rightarrow$  refractive index

ACTUALLY:  $n = n(\lambda)$

EVERYONE KNOWS THAT. SO WHAT?!

$\rightarrow$  referring to Fig.1 [typ. telecom DFB-LD]

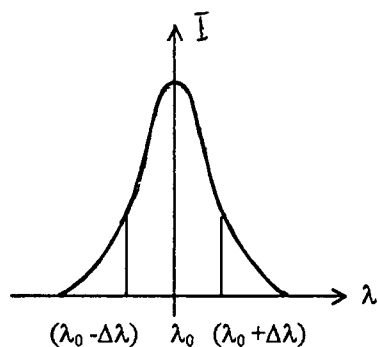
$\rightarrow$  output is not a single-line.

$\Rightarrow$  spectral width

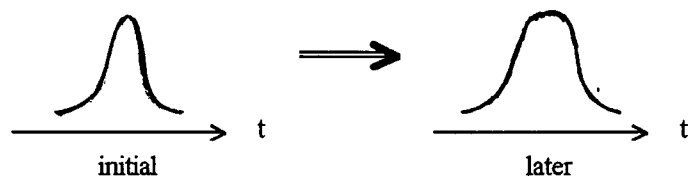
$\therefore$  impulse of LD is a collection of wavelengths.

### MATERIAL DISPERSION

long wavelengths travel faster than short wavelengths in a given medium



$\rightarrow$  after some distance  $(\lambda_0 + \Delta\lambda)$  has travelled further than  $(\lambda_0 - \Delta\lambda)$  therefore, temporally



- eventually, 2 digital optical pulses overlap.

- receiver is unable to extract information  $\Rightarrow$  BER  $\uparrow$

- hence high speed communications needs narrow spectral width output from transmitter lasers  
 ⇒ (we still need the lasers guys)

[best if SLM but very complex ⇒ bulk & cost]  
 the MFD determines proportion of light distribution in core & cladding.

since  $n_{co} \neq n_{cl}$  and  $V = \frac{c}{n(\lambda)}$

the guided [confined] light experiences pulse spreading (as detected by a PD)

⇒ WAVEGUIDE DISPERSION ⇐

The parameters discussed so far, give an indication on how to design future fibre's in addressing specific or combination effects.

Conventional step-index monomode fibre, with  $\lambda_c \cong 1250\text{nm}$  [⇒  $1300\text{ nm} < \lambda < 1700\text{ nm}$ ] has a zero dispersion @ 1300 nm.

Without delving too much, dispersion can be overcome by various methods. As far as fibres are concerned there's DSF, NZ-DSF.

DSF → zero dispersion @ 1.5  $\mu\text{m}$

NZ-DSF → -ve dispersion @ 1.5  $\mu\text{m}$  (conventional + ve)

Fundamental Mode, LP<sub>01</sub>

→ constitutes 2 HE<sub>11</sub> modes.

→ 2 orthogonally polarized electric fields.

→ in ideal fibres → both have the same propagation constants.

in reality ⇒ asymmetrical lateral stresses

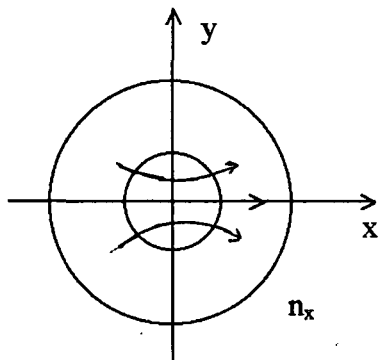
non-circular cores

refractive index variations



degeneracy of the 2 modes is broken.

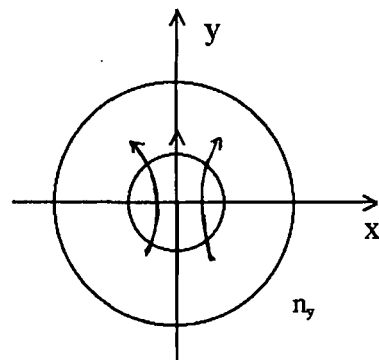
defining



horizontal mode

→ propagation constant,  $k_x$

and



vertical mode

→ propagation constant,  $k_y$

then the imperfections cause different phase velocities causing different effective refractive indices  
⇒ birefringence.

$$B = n_y - n_x$$

equivalently,  $\beta = k_o (n_y - n_x)$  where  $k_o = \frac{2\pi}{\lambda}$  (free space)

If light injections into core excites both modes → phase difference → if integral multiple of  $2\pi$  ⇒  
beating results in input polarization state reproduced; however at PD if no beating ⇒ PMD.

length over which beating occurs

→ beat length

$$L_p = \frac{2\pi}{\beta}$$

at conventional bit-rates

⇒ 2- 5 Gps ⇒ not too much of a bother

⇒ 10 Gps ⇒ getting uncomfortable

⇒ 40 Gbps ⇒ constant headache

higher bit-rate ⇒ small pulse width ⇒ more distinct differences!

Up to now - all were basics

From a systems stand-point, a few nugging problems persized.

- (i) world population ballooning (> 6.2 b)
- (ii) data communication increasing exponentially
- (iii) fibre loss needed repeaters

Addressing these had to await new developments: All optical repeaters & WDM.

The fibre attenuation demanded electrical repeaters every 50 km or so.

- 3R repeaters → costly
- fixed clock speeds
  - each fibre (> 20 per cable) needed one
  - conversion needed OEO

In the late 80's → rare-earth fibres → Univ. Southampton 1986

Thus was born the

### Erbium Doped Fibre Amplifier

(a good reference is: Emmanuel Desurvires, "Erbium Doped Fiber Amplifiers" Principles and Applications, John Willey & Sons Inc, 1994, ISBN: 0-471-58977-2)

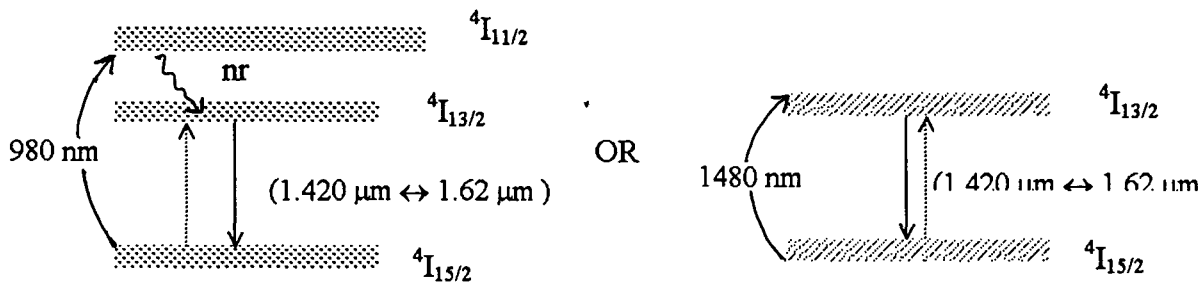


- Erbium  $\rightarrow$   $\text{Er}^{3+}$  (rare-earth element)

$\uparrow$   
incorporated into  $\text{SiO}_2$  core of fibre  $\Rightarrow$  EDF

an EDF is essentially a 3-level laser medium, if excited at 980 nm or pseudo 2-level, if excited at 1480 nm.

Other  $\lambda$ 's exist but not as attractive/economical/ well developed as these 2 wavelengths. Problems exist too.

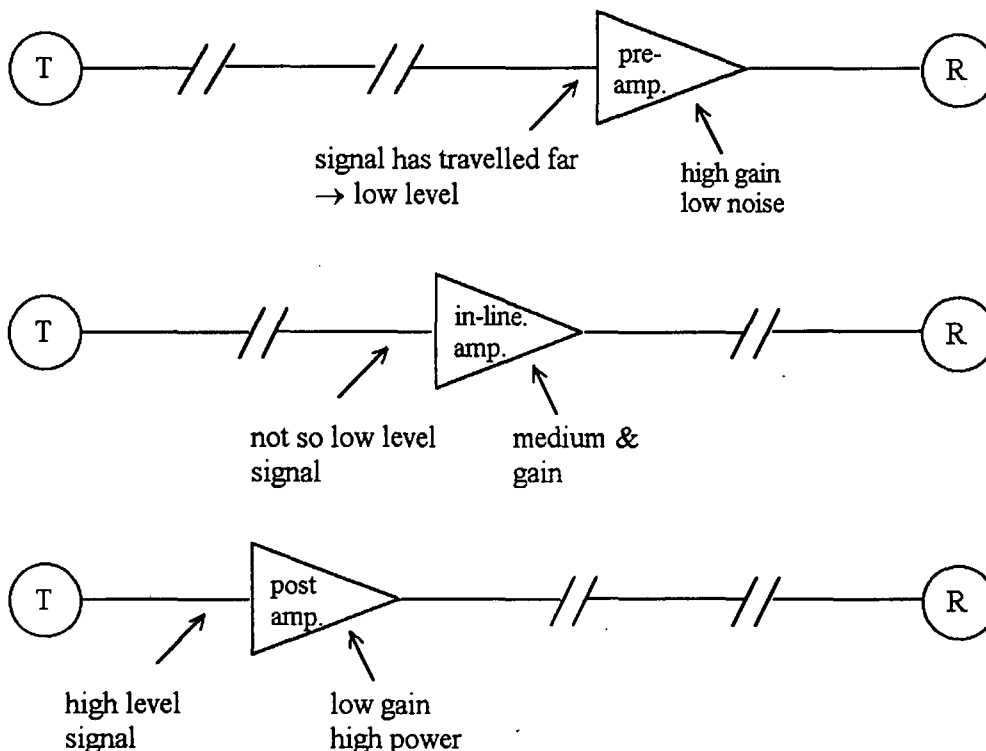


The beauty of this is that

- (i) the emission falls neatly in the 3<sup>rd</sup> windows
- (ii) there is no conversion to electric-forms
- (iii) as will be seen, its broad-band

A typical long haul span contains numerous amplifiers – 3 types

- pre-amp
- in-line amp
- post amp



Based on the 3 designs, the appropriate pump wavelength is chosen

$$\text{PCE}^{\max} (\text{Power Conversion Efficiency}) \cong \frac{\lambda_{\text{pump}}}{\lambda_{\text{signal}}} \rightarrow 1480 \text{ good}$$

$$\text{as } \frac{1480}{1550} \rightarrow 1$$

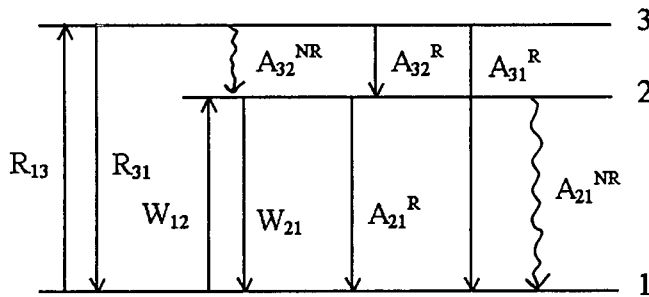
than

$$\frac{980}{1550}$$

1480 pump gives a high inversion of ions in EDF. So does noise

$\therefore$  980 is used for low-noise amplifiers

Going back to energy levels of  $\text{Er}^{3+}$  in  $\text{SiO}_2$  host (for a 3-level scheme)



where  $R_{13}$  = pump rate

$R_{31}$  = stimulated emission rate

$A_{31}^R$  = radiative decay

$A_{32}^R$  = radiative decay

$A_{32}^{NR}$  = non-radiative decay

$A_{21}^R$  = radiative spontaneous decay =  $\frac{1}{\tau}$  (fluorescence lifetime)

$A_{21}^{NR}$  = non-radiative spontaneous decay

$W_{12}$  = stimulated absorption rate

$W_{21}$  = stimulated emission rate

for  $\text{Er}^{3+}$  in  $\text{SiO}_2$  :

$$A_{32}^{NR} \gg A_{31,2}^R$$

$$A_{21}^R \gg A_{21}^{NR}$$

defining  $\rho$  = total  $\text{Er}^{3+}$  ion density

$N_1, N_2, N_3$  = fractional densities at energy levels 1, 2 & 3 respectively

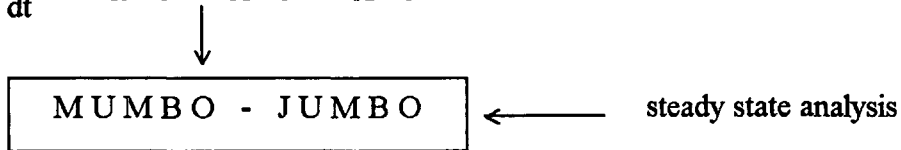
we have  $\rho = N_1 + N_2 + N_3$

hence the rate equations are:

$$\frac{dN_1}{dt} = -R_{13}N_1 + R_{31}N_3 - W_{12}N_1 + W_{21}N_2 + A_{21}N_2$$

$$\frac{dN_2}{dt} = -W_{12}N_1 - W_{21}N_2 - A_{21}N_2 + A_{32}N_3$$

and  $\frac{dN_3}{dt} = R_{13}N_1 - R_{31}N_3 - A_{32}N_3 \quad \rightarrow R_{31} = 0 \text{ for } 980 \text{ nm}$



↓

$$N_1 = \rho \frac{1 + W_{21}\tau}{1 + R_{13}\tau + W_{12}\tau + W_{21}\tau}$$

$$N_2 = \rho \frac{R_{13}\tau + W_{12}\tau}{1 + R_{13}\tau + W_{12}\tau + W_{21}\tau}$$

after FURTHER MUMBO - JUMBO

The evolution for pump & signal rate equations of the form

$$\frac{dy}{dz} \quad \text{is obtained}$$

These coupled equations are easily solved numerically.

Of importance is the existence of amplified spontaneous emission → the spontaneous emission from level 2 → 1 is amplified (for LP<sub>01</sub> light)

→ complicates solution analytically. Best left to computers !

Fig. 5 shows ASE, from a 8 m fibre excited at about 20 mW @ 980 nm.

Modern manufacturing processes have enabled a flat region between 1540 nm and 1560 nm

→ really flat amplification regions are obtained by interplay of EDF length and composition.

Of interest is the broad-band, flat-gain region. Gave birth to WDM.

Fig.6 shows a laboratory set-up for characterizing EDFA's

The parameters of interest are detailed in Fig. 7 and 8

A modern optical spectrum analyzer → essentially a grating monochromator with provisions for wavelength sweeping via motorized stages and fancy electronics, enable complete characterization of an EDFA. Typical analysis readouts give G, NF, ASE level and P<sub>sig</sub><sup>pk</sup>.

The usual method of analysis is interpolation, as shown in Fig.9

NF is defined as  $\rightarrow \frac{SNR_{in}}{SNR_{out}}$  (electrical)

By this definition,  $SNR_{out} < SNR_{in}$  is true as any amplifier will introduce noise.

By "interpolation", - certain regions are masked.

- other regions are curve-fit.

- resultant value of curve-fit at signal wavelength determines noise level.

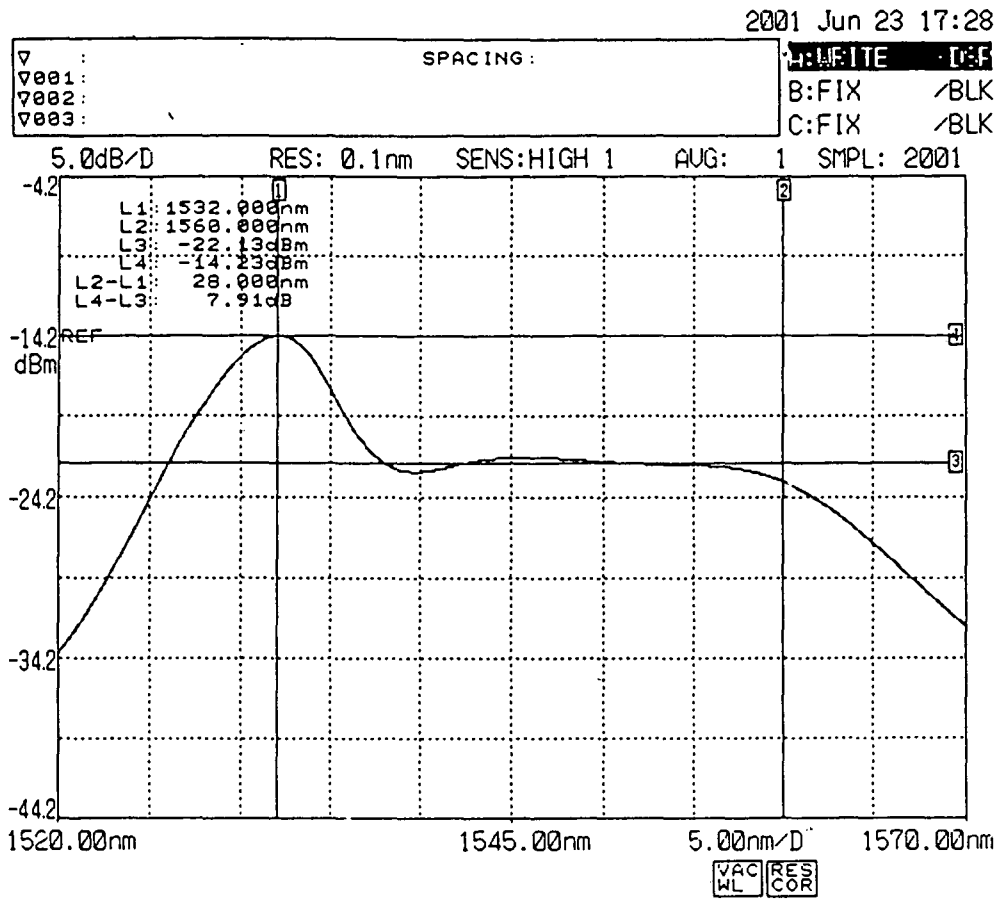


Fig.5. Amplified Spontaneous Emission (ASE).

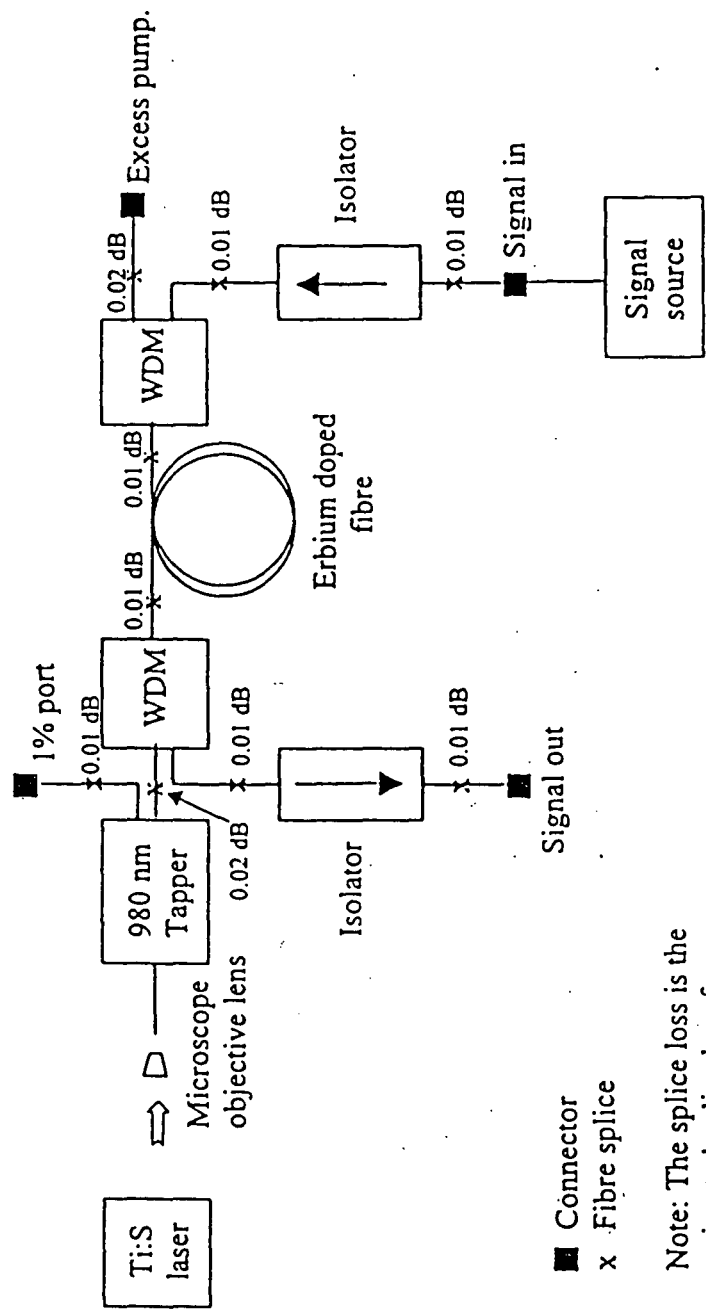


Fig.6. An experimental set-up, investigating the various parameters of an EDFA.

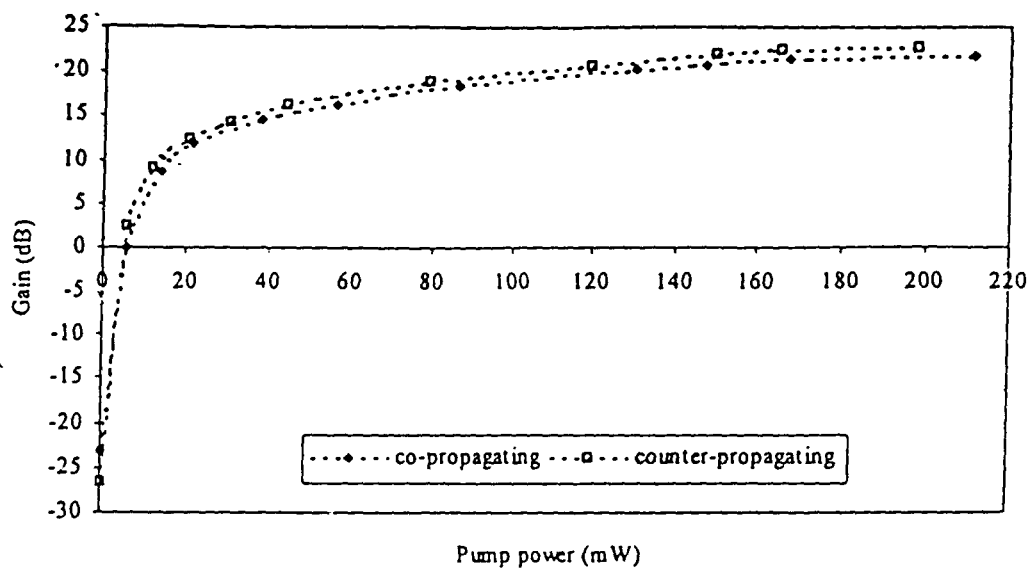


Fig.7. 12 m EDF.

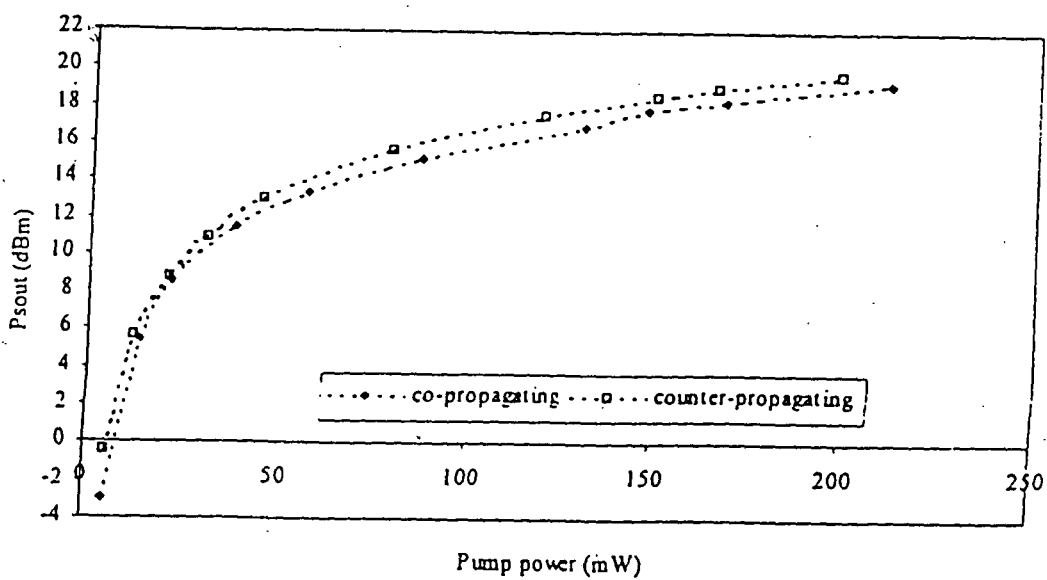


Fig.8. 12 m EDF.

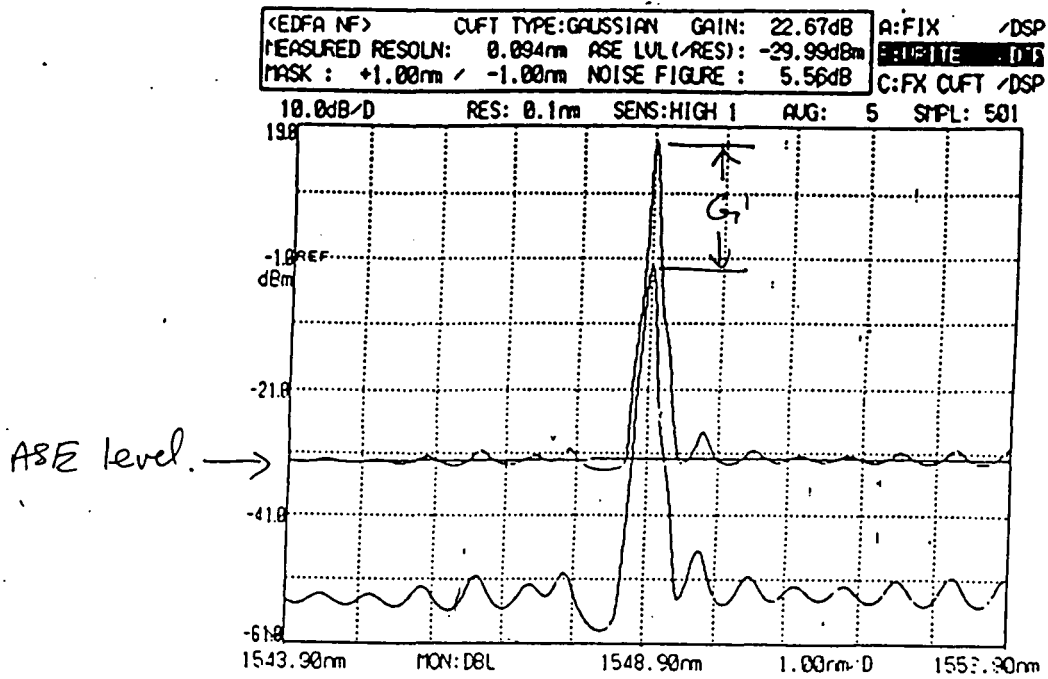


Fig.9. OSA spectrogram of input and amplified output.

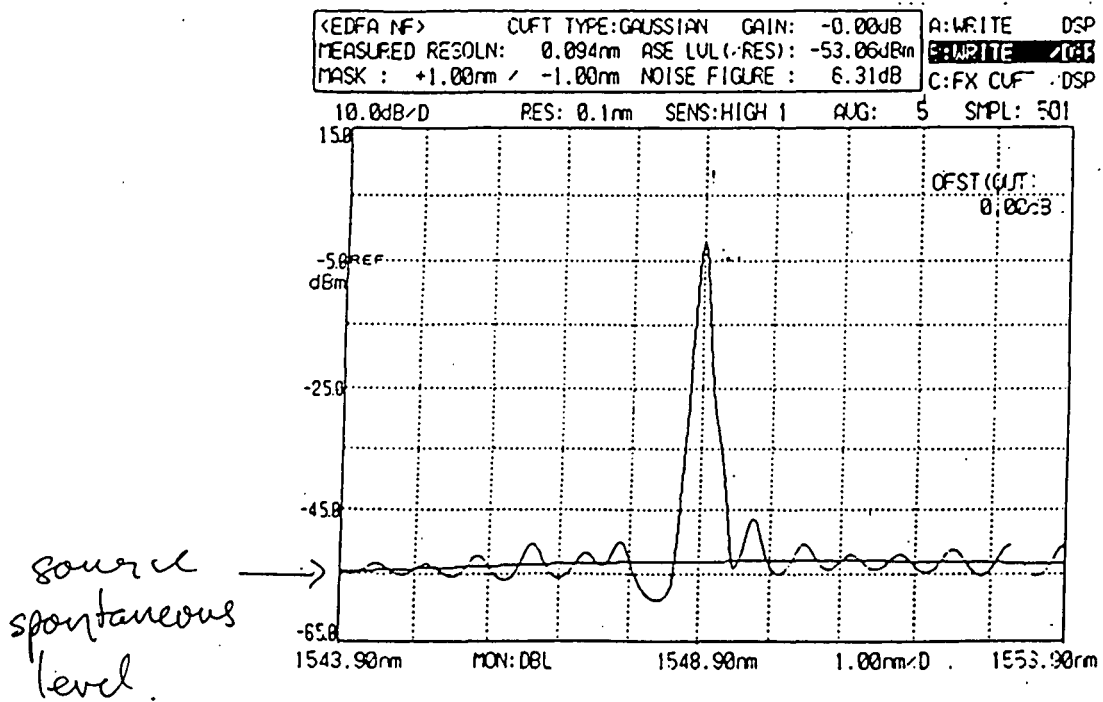


Fig.10.

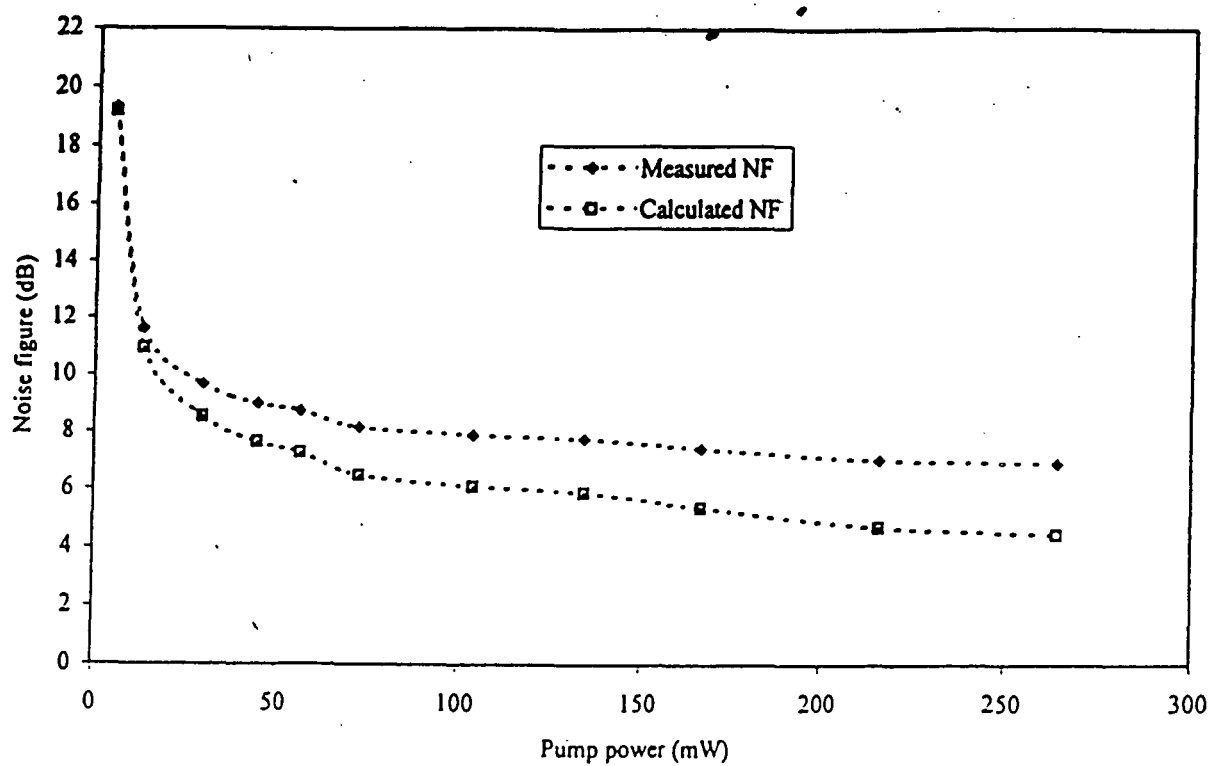


Fig. 11. NF improvement with power.

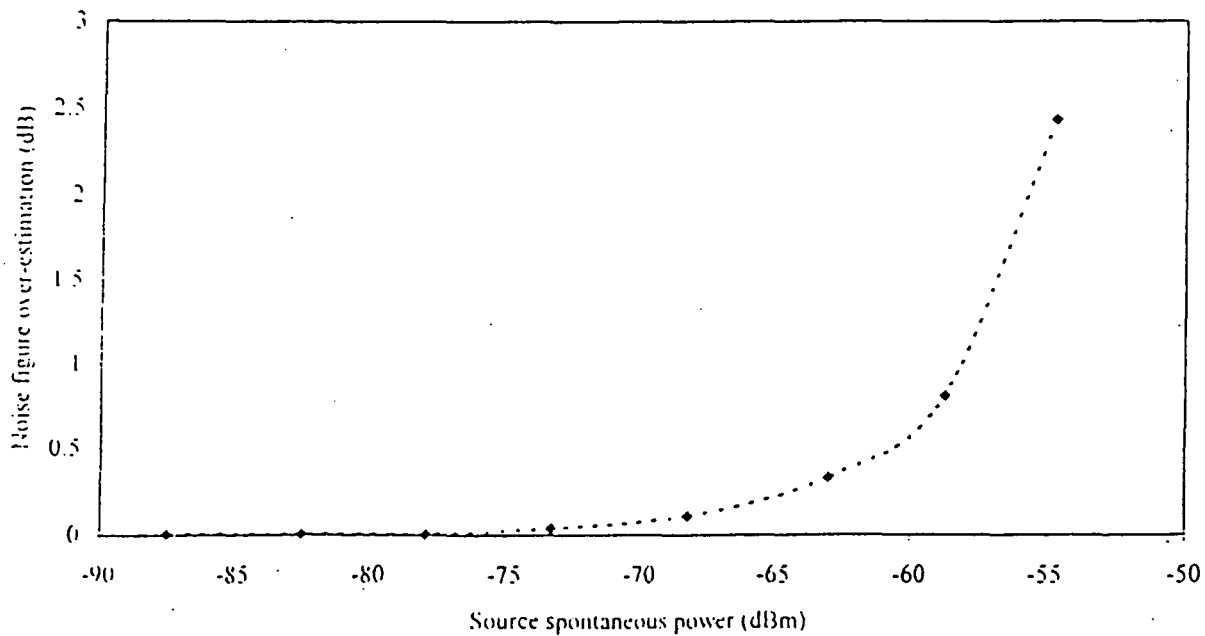


Fig.12. NF degradation with increasing SSE.



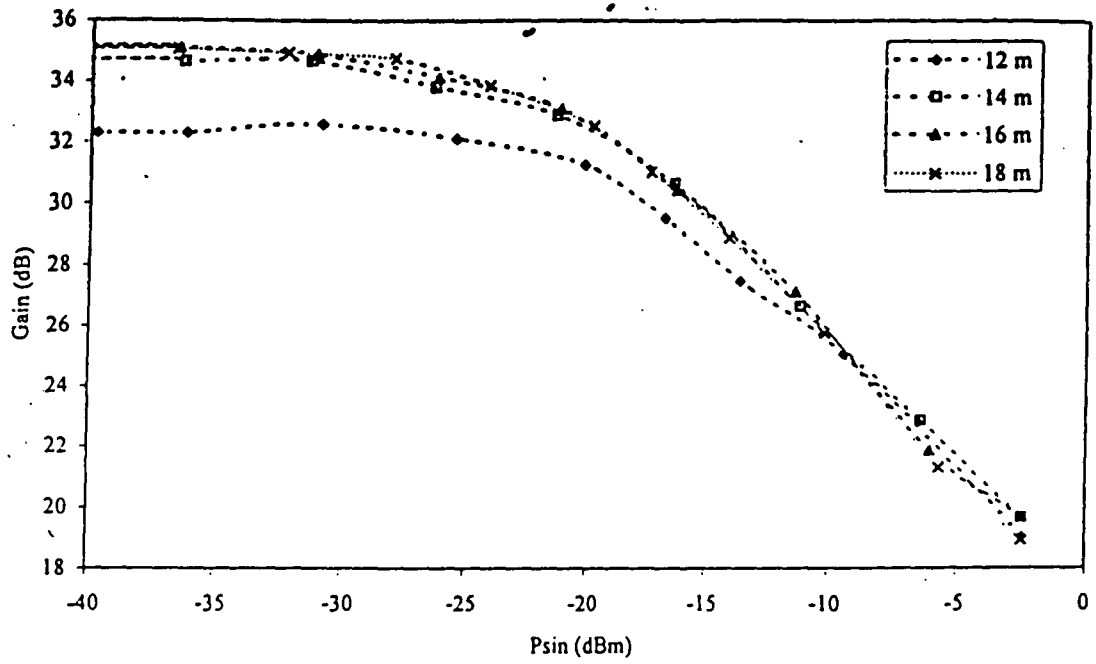


Fig. 13.

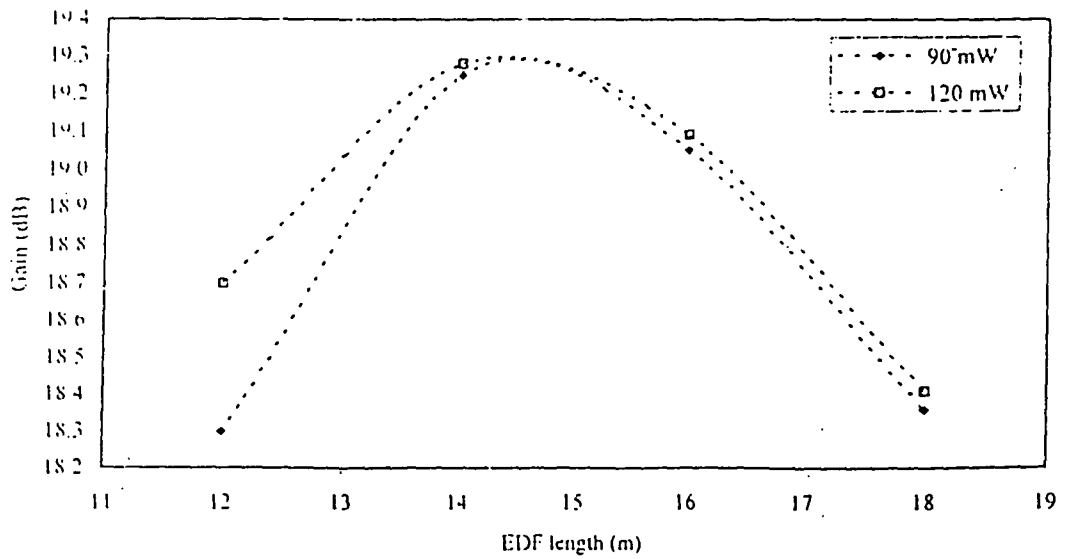


Fig. 14.

Going back to Fig.5,

→ flat region ~ 20 nm

→ can amplify multiple signals

→ birth of Wavelength Division Multiplexing

→ instead of laying more fibres/cables to increase capacity - alternatives are :

(i) TDM

(ii) WDM

(iii) both

TDM is traditional. Depends on advances in electronics. The optics part is/has/will always be there.

WDM enables multiple signals - at combinations of 8, 16, 32, 64, 96 etc channels. By standardization WDM is defined by signal spacing

200 GHz (1.6 nm)

100 GHz (0.8 nm)

50 GHz (0.4 nm)

12.5 GHz (0.1 nm)

WDM can be transmitted at standard 2.5 GBps or high-end 10 GBps or emerging 40 GBps. BUT at higher bit-rates – lots of other problems,

- wave mixing

- PMD

- fibre inhomogeneity (manufacturing)

WDM problems:

Usually systems span thousands of km far longhaul and a few hundred km for metro-networks (depends on topology also) ⇒ all signals must be amplified equally by all the intervening amplifiers. Typical spacing is between 70 km – 120 km for WDM amplifiers. For distance involved, there would be many EDFA's.

Can be solved with a GC-EDFA, shown in Fig. 15. Results of gain profile in Fig. 16 and 18.

Fig. 17 combines G & NF plot.

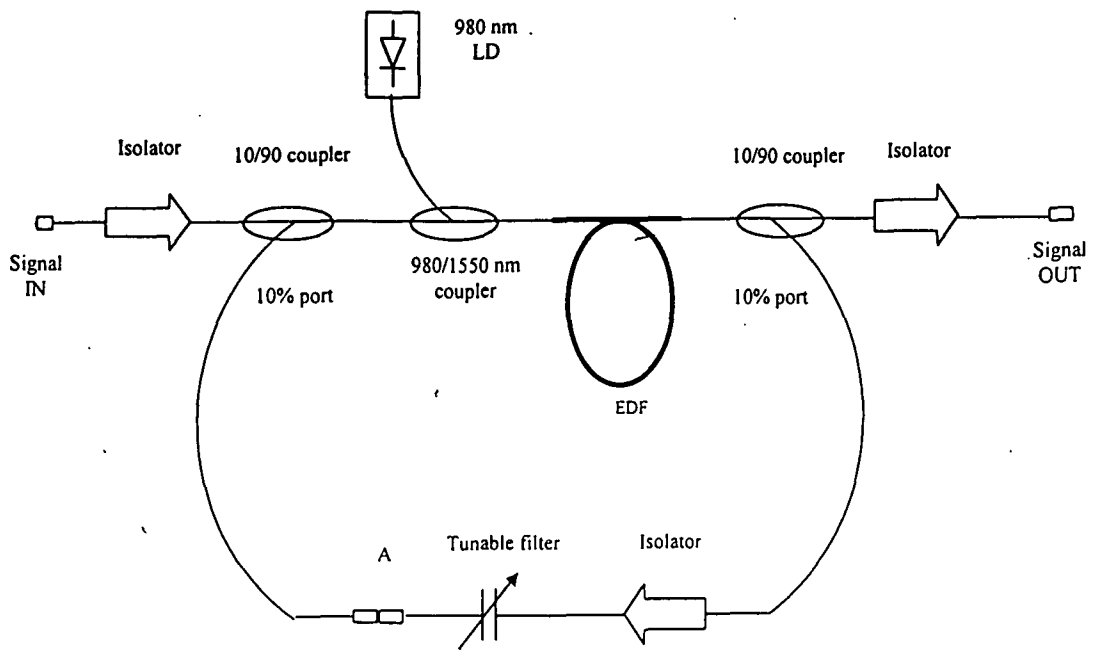


Fig.15. Set-up for co-propogating laser GC-EDFA.

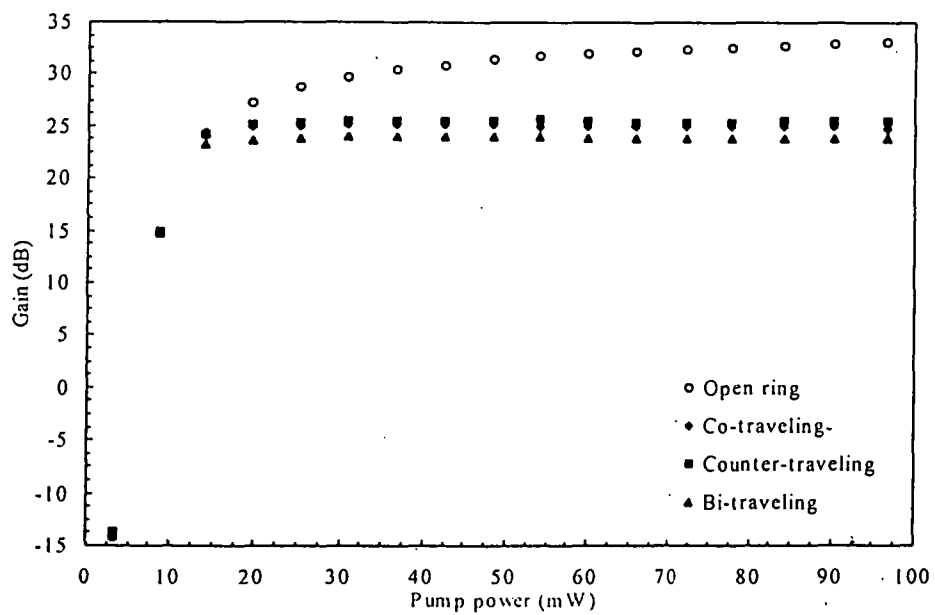


Fig.16. Resultant constant gain.

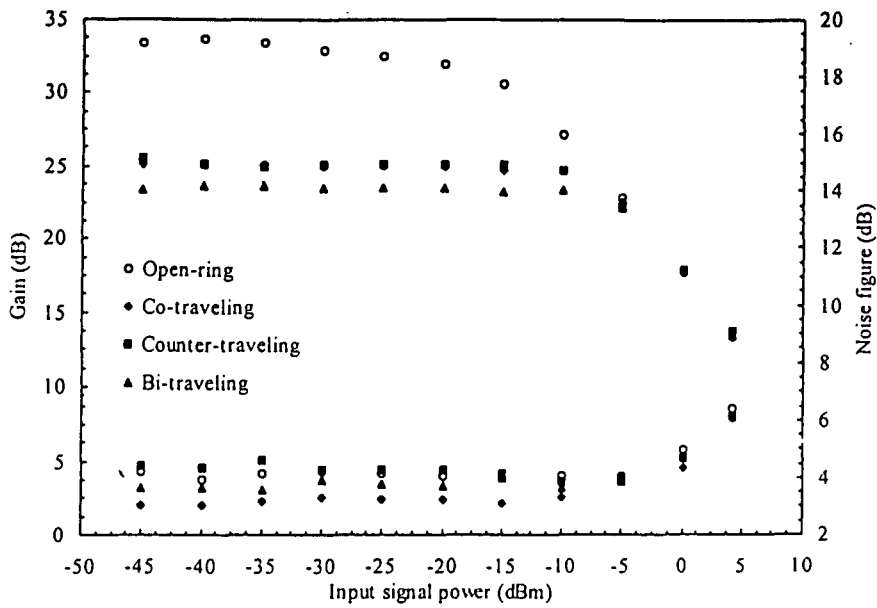


Fig. 17. Saturation point of GC-EDFA & NF.

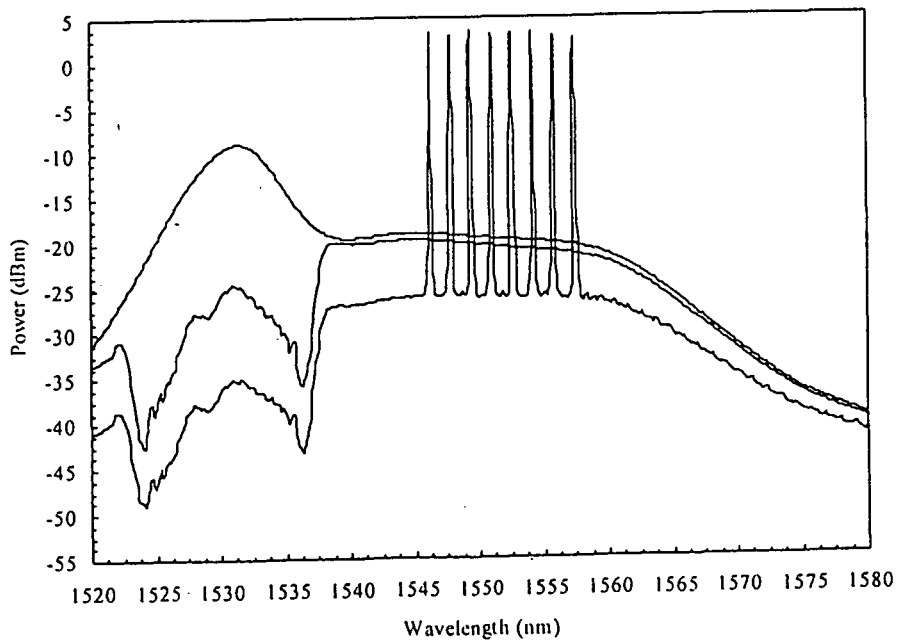


Fig.18. Multiple signals transmission & amplification.

Effort is under-way to increase WDM bandwidth – by having more signals in transmission system.

→ increase no. of signals ⇒ spacing ↓ (12.5 GHz)

→ increase amplifiers BW ⇒ L-EDFA.

$\text{Er}^{3+}$  in  $\text{SiO}_2$  fibre has emission spectra right up to ~ 1620 nm, but absorption/emission cross section is very low (compared to C-band)

Fig. 19 details the ASE output to 1628 nm.

How to bring this level up, to C-band level ?

→ EDF is 3-level laser system

→ reabsorption of signal occurs easily (Fig. 21 shows cross-sections)

→ increasing EDF length, beyond normal C-band operation needs achieves this. Fig 20 details this.

Fig. 22 shows effect of different EDF lengths Gain-flatness also a criterion.

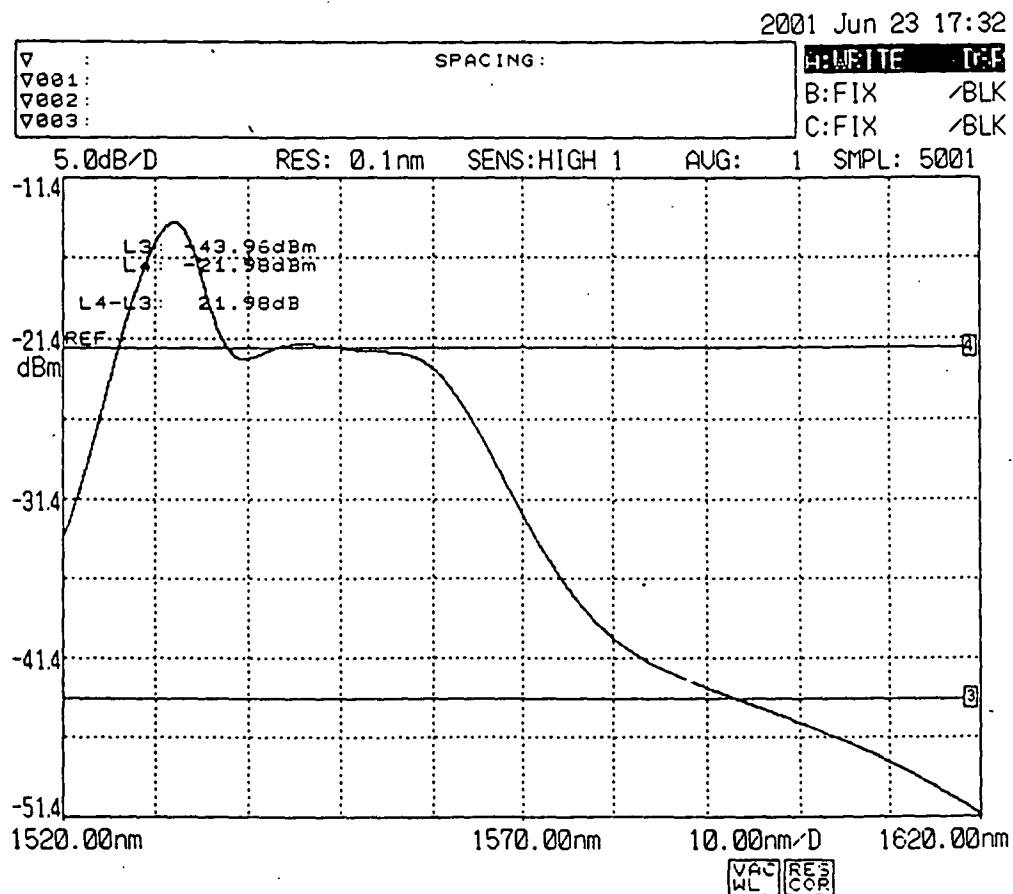


Fig.19. ASE spectra showing relatively low output at 1570 nm.

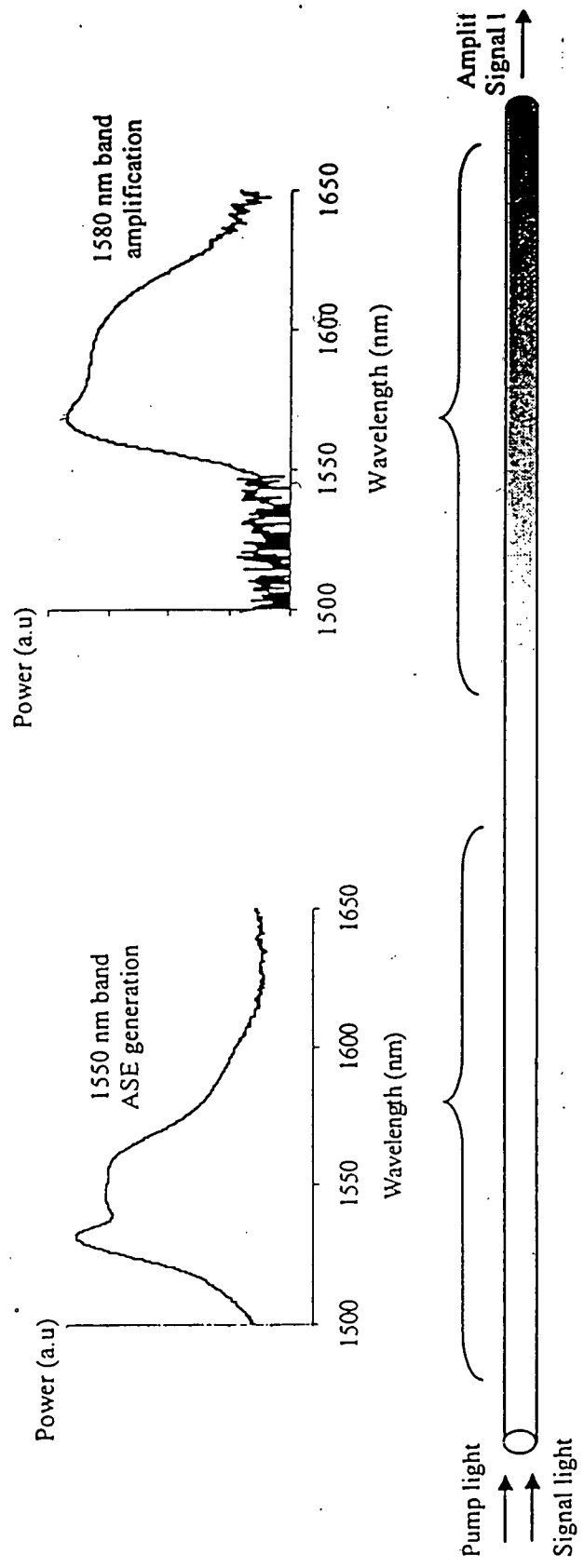


Fig.20.

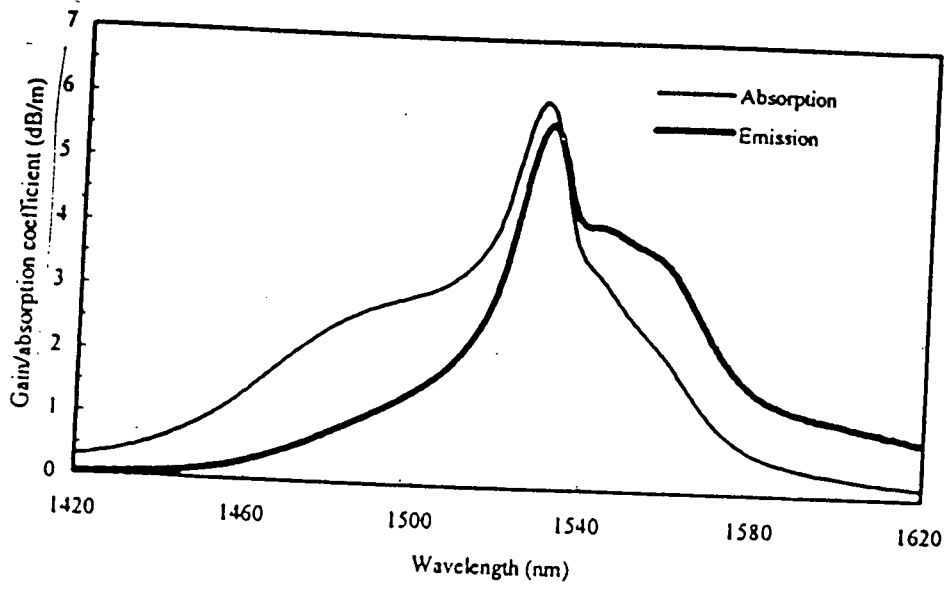


Fig.21.

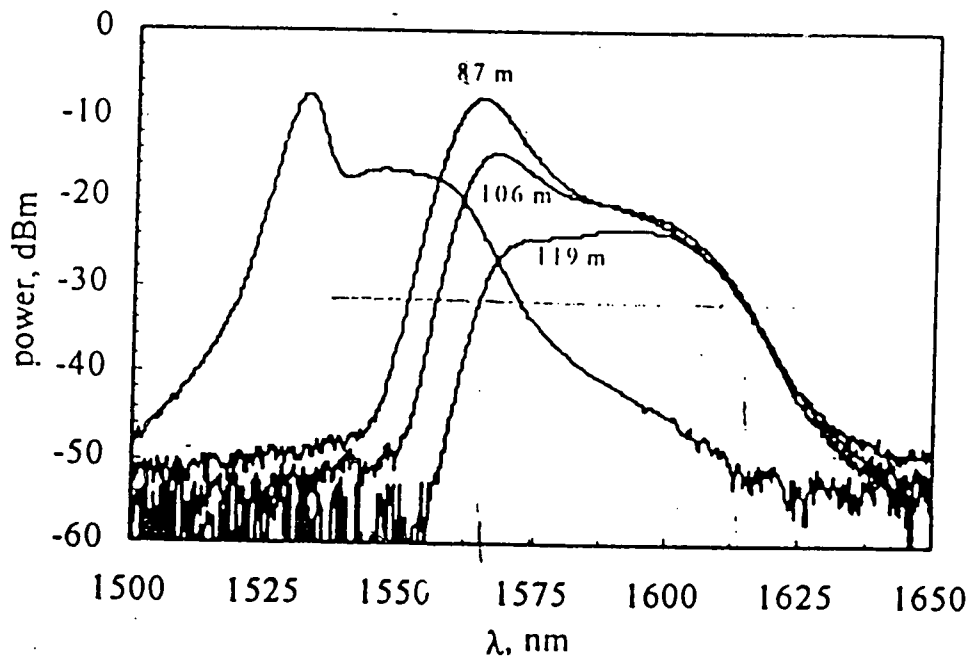


Fig.22. Spectra of ASE for  $L_1 = 10$  m and  $L_2 = 87, 106$  and  $119$  m.

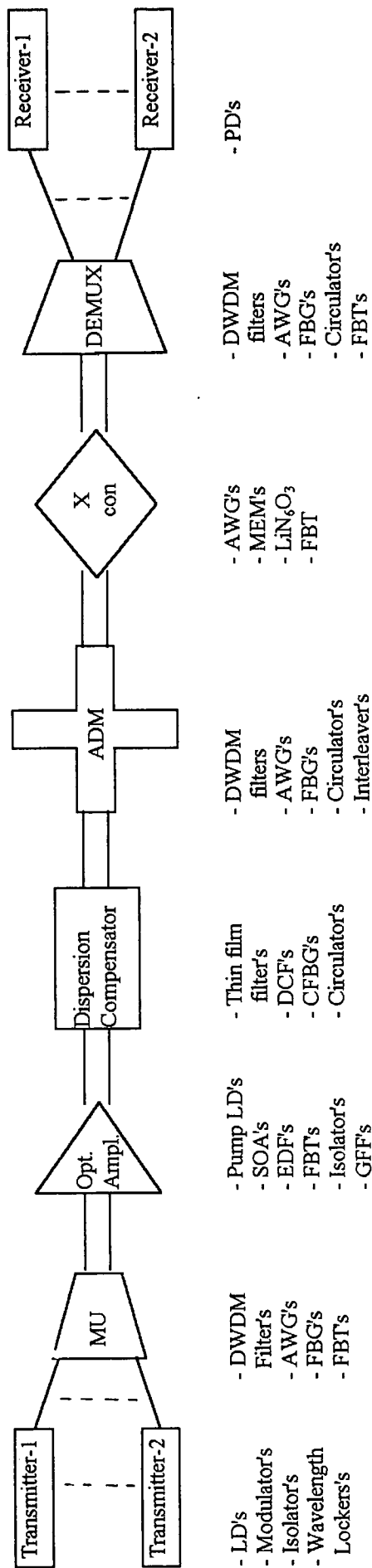


Fig. 23. A typical optical communications link. Incorporation for long-haul or metro-network topology does not change basic link much.



All said – a typical optical communications system employing both TDM and WDM is shown in Fig 23.

This system addresses need for re-shaping dispersed signals (for high bit-rate systems) adding or dropping channels at intermediate towns/cities/countries.

Cross-connects address re-routing of channels to different place. Shining now are MEMS system and bubble-jet systems.

END OF  
OPTICAL COMMUNICATIONS  
THANK YOU



**Laser Application in the Life Extension  
of Engineering Components**

**Dr. Nazmul Alam**

**CSIRO Manufacturing Science & Technology**

**Adelaide, Australia**

Prepared for:

*Regional Workshop on Lasers and Optoelectronics*, held in Jakarta in collaboration with ICS-UNIDO and Indonesian Institute of Science on June 25-July 6, 2001.

## **Abstract**

Engineering components in many industrial applications are subjected to wear that results in loss of efficiency. Applications included aircraft, mining, agriculture and power industries. Replacement cost for many components is extremely high. Therefore the extension of service life can result in significant savings and higher operating efficiency. Surface hardening and cladding of engineering components with conventional techniques are the standard practice for the extension of service life. Conventional techniques have many limitations with respect to providing adequate surface properties without damaging the bulk of the materials.

Although laser technology has been available for sometime, the use of lasers for hardening and cladding is a recent development. This is due to the introduction of high power laser systems suitable for fully or partially melting various metals and metal powders. In addition, laser processing can provide microstructures with improved surface properties without damaging the bulk body due to the rapid heating and cooling resulting from the high density of heat energy. The full potential of laser systems in material processing is beginning to emerge through continuous research and development, and many industries are already utilising laser processed components in the production plant.

## **1. Introduction**

Surface hardening and cladding by laser beam is an area of growing industrial application. The main reasons for this interest are the significant and distinct technological advantages of laser processing over competing methods, as well as an overall reduction in manufacturing costs. The potential benefit of using a laser beam

lies in the fact that it is able to generate a high power density ( $>10^6$  W/cm<sup>2</sup>) that enables increased processing speed.

Surface engineering involves the design of substrate surfaces providing a cost-effective performance enhancement. The surface composition and microstructures of engineering components greatly influence mechanical and chemical interactions with other components and the surrounding environment. There are enormous economic benefits if the service life of mechanical components can be improved and extended. This can be achieved by altering the surface composition and microstructure from the bulk property requirements to suit the appropriate application. Although the most important property attainable by surface engineering is improved wear (abrasive, erosive, impact abrasive and galling) resistance, good corrosion resistance and elevated temperature capability can also be achieved.

## **2. SURFACE HARDENING**

Lasers as heat sources are gaining much attention for surface hardening of steel [1-5]. This is due to the high energy densities that can be directed to any specific area on complex shapes. Laser surface hardening has been used in cylinder liners, ring grooves on diesel engine pistons, automobile camshafts and gear teeth to improve wear resistance and fatigue properties [6]. The wear resistance of cutting tools such as milling cutters, drills and reamers made from either low alloy tool steel [7] or high-speed steels [8] has been improved by factors from 1.5 to 4. The complete hardening cycle takes about 1 to 2 seconds and the maximum thickness of a laser-hardened layer is 1 to 2 mm. In most cases this depth is sufficient to ensure a good

improvement in wear resistance, strength and fatigue resistance.

Laser surface hardening can offer many advantages, some of which are listed below:

- very little or no distortion of the work piece
- rapid processing, allowing increased production with the potential for automation
- usually no external quenchant required to generate martensite
- potential to harden selected regions of complex shapes
- improved fatigue properties resulting from residual compressive stresses.

These advantages cannot be obtained from other conventional hardening processes. Flame or induction hardening often causes high distortion resulting in high rejection rates in the production line. Case hardening and nitriding require long treatment times and the precise control of the surrounding environment.

## **2.1 HARDENING PROCESS**

In operation the laser beam is defocused or oscillated to cover an area such that the average power density has a value of  $10^3$  to  $10^4$  W/cm<sup>2</sup> (see Fig. 1). By using suitable mirror arrangements the laser beam can be shaped to circular or square forms, Fig. 2. A relative motion between the work piece and the beam of 0.5 and 5 cm/s will result in surface hardening.

In application, the laser beam is absorbed at a steel surface and the central portion of the affected region is rapidly transformed to austenite. Since the surrounding mass

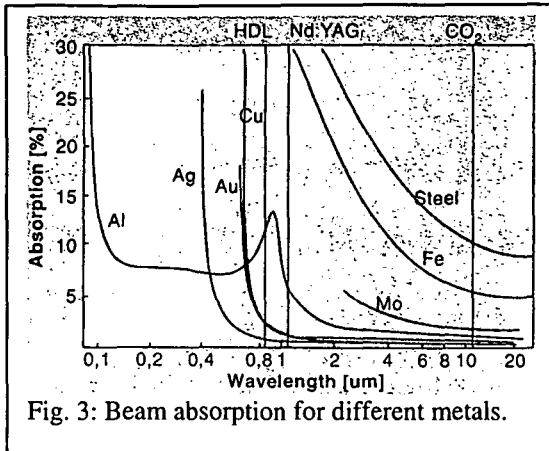


Fig. 3: Beam absorption for different metals.

temperature, and the wavelength of the laser light. Long wavelength laser light has a low absorption coefficient with metals, Fig. 3. This is why gold, silver, copper, or aluminium is less suitable for laser treatment. In order to increase the beam absorption an absorptive layer

(0.06-0.10 mm thick) is often used. Most suitable are colloidal graphite, cuprous or iron oxide or manganese phosphate.

### 2.2.2 Alloy Content

Steels are alloys of iron and small quantity of carbon (0.08-2 weight %), and the properties of steel are strongly dependent on the carbon content, Fig. 4. The carbon content determines the proportion of phases present in the steel microstructure. When a typical steel containing 0.4% carbon is heated to high temperatures it undergoes a phase

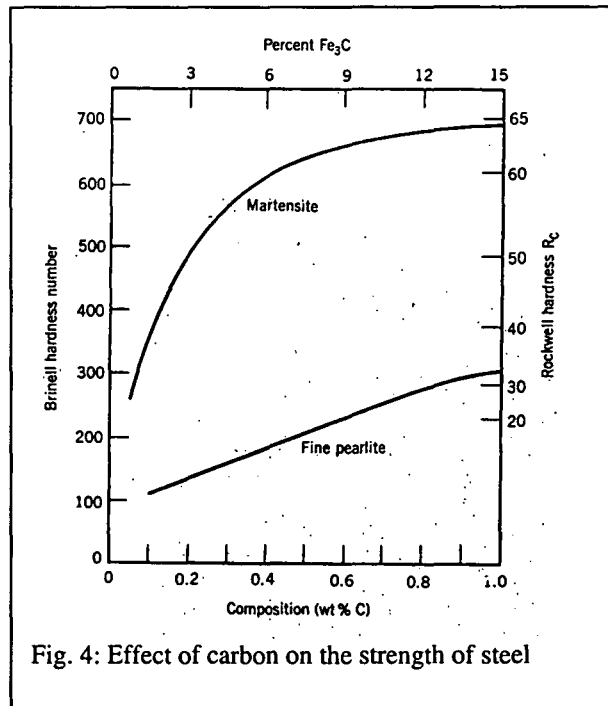


Fig. 4: Effect of carbon on the strength of steel

change, which occurs at about 723 C. The ferrite and pearlite, which are the original phases, transform to a single phase, austenite. If the steel is cooled slowly from austenite, the reverse transformations take place. Microstructural phases transformed under equilibrium heating and cooling conditions can be estimated from a phase

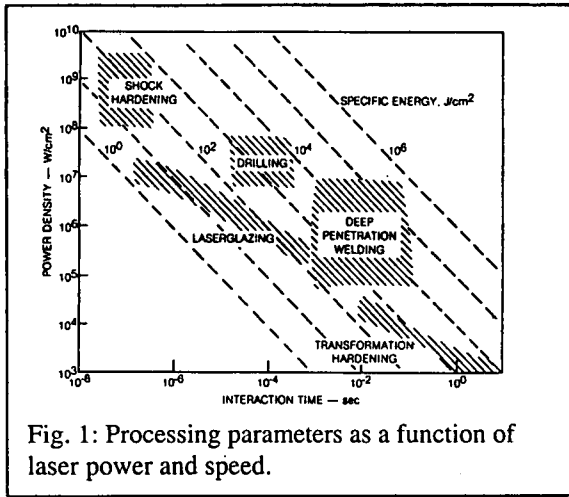


Fig. 1: Processing parameters as a function of laser power and speed.

of the steel is usually significantly larger than the beam interaction zone, it acts as a strong heat sink. When the laser beam is moved away, cooling is imposed by heat conduction into the work piece and leads to the formation of the hardened layer. The laser

power and scanning speed determine the interaction time of the beam with the work piece, and manipulation of these two parameters makes it possible to generate a hardened layer that is much shallower than that obtained by conventional heat treatment. In contrast, a hardened layer made with more conventional techniques exhibits different grades of microstructures associated with different peak temperatures and cooling rates, and a gradual decrease in hardness is often observed towards the boundary.

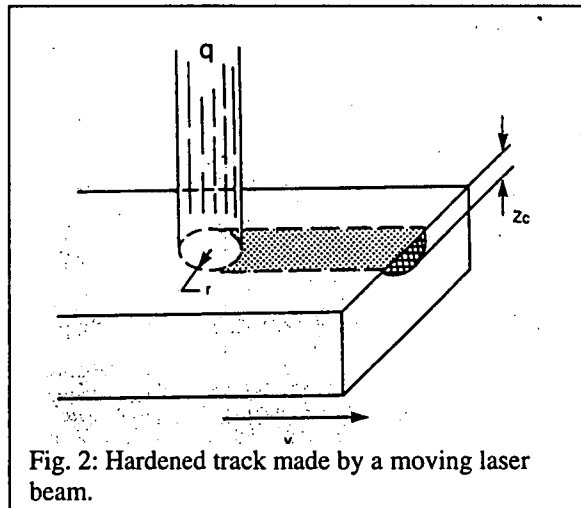


Fig. 2: Hardened track made by a moving laser beam.

## 2.2 FACTORS THAT AFFECT HARDENABILITY

### 2.2.1 Absorption of Laser Beam

Metals reflect most of the incident beam. The value of the absorption is a function of the optical properties of the materials, including the surface finish and the

diagram as shown in Fig. 5.

However, in practice equilibrium conditions are not maintained and transformation occurs under non-equilibrium conditions. Microstructural phases transformed in non-equilibrium conditions can be estimated from the isothermal transformation temperature (ITT) and continuous cooling transformation (CCT) diagrams (see Fig. 6). In rapid cooling the liquid steel

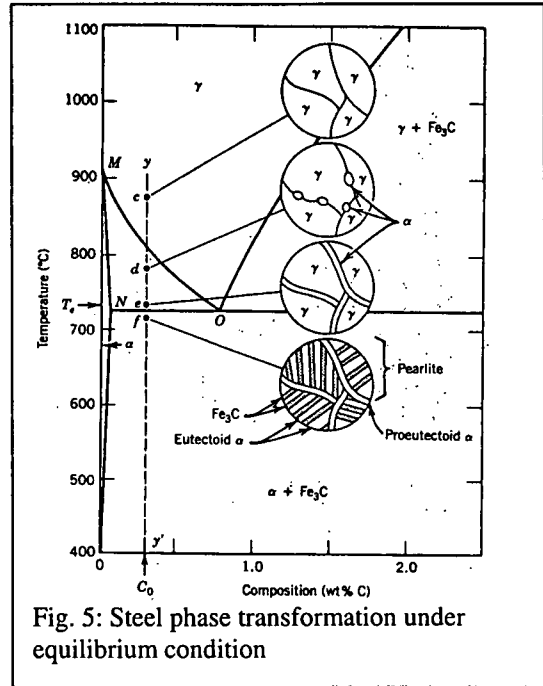


Fig. 5: Steel phase transformation under equilibrium condition

transforms to relatively hard microstructure known as martensite or bainite.

Steels may also contain additional alloying elements (Mn, Si, Cr, Ni, Mo) and impurities. These constituents can enhance or suppress the transformation. As the carbon content and other alloying elements are increased, the steel transforms to martensite at relatively slow cooling rates and hence the hardenability is increased.

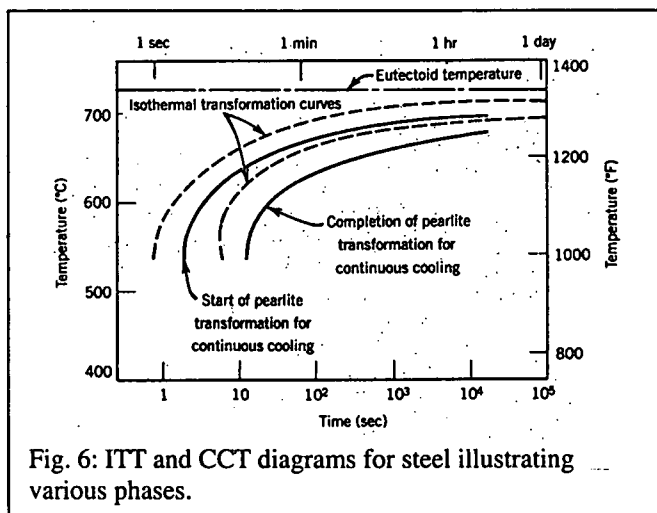


Fig. 6: ITT and CCT diagrams for steel illustrating various phases.

### 2.2.3 Heating Rate

However, the hardening process involves heating a metal above a critical



temperature and then rapidly quenching it rather than allowing equilibrium phases to form by slow cooling. During the laser hardening process it is essential that surface melting does not occur, and full austenitisation occurs in the heated region. Complete austenitisation is required during the heating cycle for effective hardening. At high temperatures the

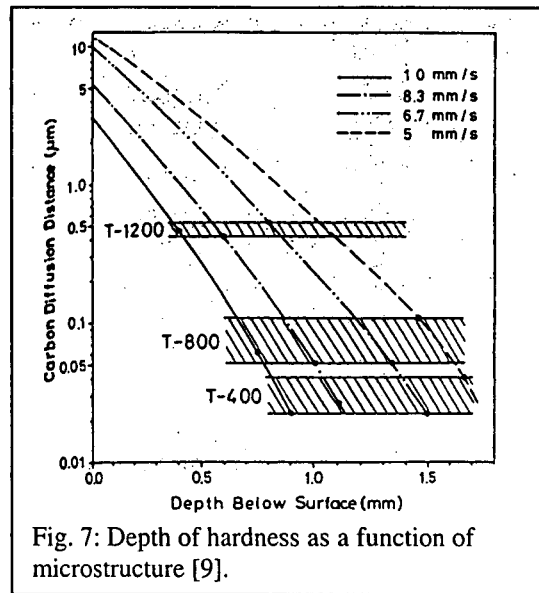


Fig. 7: Depth of hardness as a function of microstructure [9].

austenite phase accommodates more carbon than the ferrite, and a re-distribution of carbon occurs by a diffusion process, which is dependent on temperature, heating rate and type of microstructure. The heating rate in the laser hardening process is extremely rapid and thus little time is left for austenitisation. At a fixed heating rate and temperature the rate of carbon diffusion into austenite depends on the diffusion distance within the microstructure, which is longer for a coarse microstructure. It is possible to achieve full austenitisation for a fine microstructure. As a result a coarse microstructure produces a shallower hardened layer than a fine microstructure, Fig. 7.

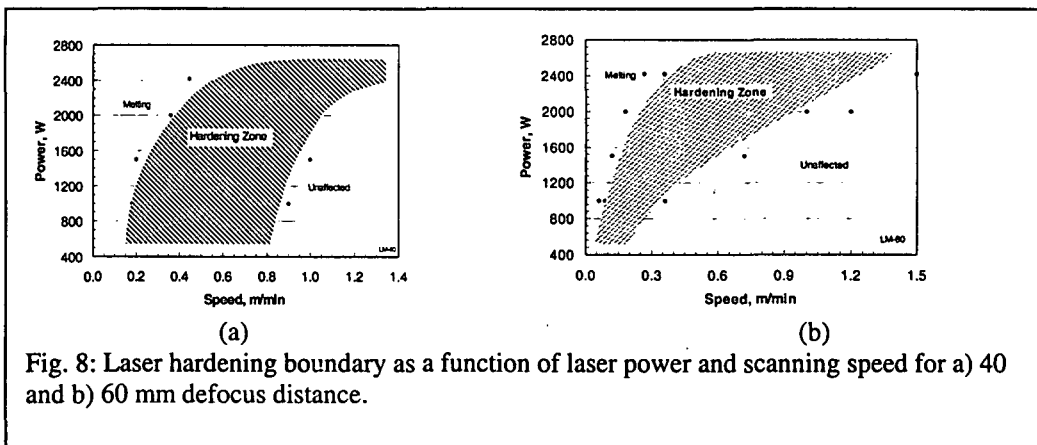
#### 2.2.4 Cooling Rate

For effective hardening it is also essential that rapid quenching occurs to prevent the carbon from diffusing out of the austenite, and results in the formation of martensite. The quenching in the laser hardening process is achieved by conduction of heat in to the body of the material. Therefore the process is 'self-quenching'. It has been reported that the cooling rate in laser hardening can exceed  $10^4$  C/s [10] and result in

fine martensitic structures not achievable by conventional heat treatment.

### 2.3 HARDENING OF AISI 4140 STEEL

The concentration of energy is a maximum at the focal point of the beam, and decreases with increasing distance from the focal point (defocus distance). At greater defocus distances the spot size of the beam is increased and consequently it has a lower power density at the work piece. In order to achieve austenitisation the diffuse beams must be scanned at a relatively slower speed, resulting in a longer interaction time for the laser beam with the work piece.

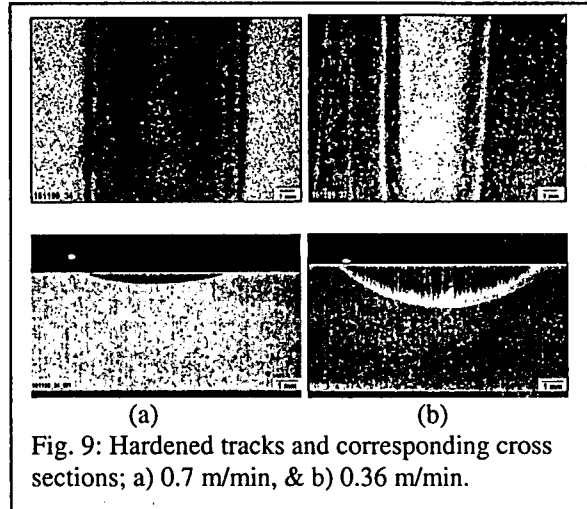


In one example, the surface of 5 mm thick AISI 4140 grade quenched and tempered steel was hardened by laser beam at defocus distances of 40 and 60 mm. The laser power and scanning speed were varied in order to determine an operating window bounded by the onset of austenitising and melting of the work piece surface, respectively. A graph of liquid-austenite boundary conditions for a 40 mm defocus distance is shown in Fig. 8a. It illustrates that for a certain value of laser power the operating range of scanning speeds for austenitising of the work piece is very wide. It is seen that lower laser powers require slower scanning speeds to achieve full austenitisation of the work piece. Liquid-austenite boundary conditions for a 60 mm

defocus distance are shown in Fig. 8b. In this figure the boundary conditions appeared to have shifted towards relatively slower scanning speeds.

### 2.3.1 Hardening Depth & Width

The appearance of the hardened track on the surface and respective cross sections are shown in Fig. 9, which illustrates that the appearance of hardened track can be quite variable. The difference in appearance is associated with the degree of austenitisation of the work piece.



The results at a 40 mm defocus distance as a function of scanning speed are shown in Fig. 10. It is evident from this figure that at a 40 mm defocus distance the maximum

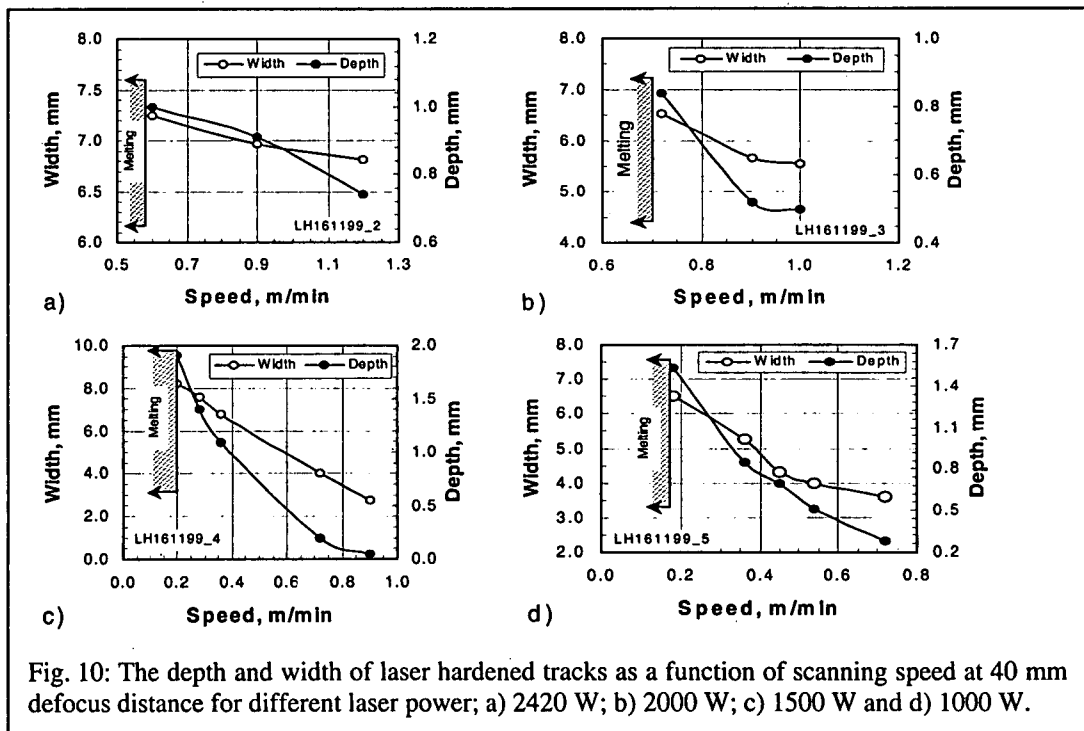


Fig. 10: The depth and width of laser hardened tracks as a function of scanning speed at 40 mm defocus distance for different laser power; a) 2420 W; b) 2000 W; c) 1500 W and d) 1000 W.

width and depth of the hardened layer were obtained at 0.2 m/min scanning speed and 1500 W of laser power (Fig. 10c). It is also obvious that the scanning speed at which the maximum depth and width of hardened track occurs increased significantly with the

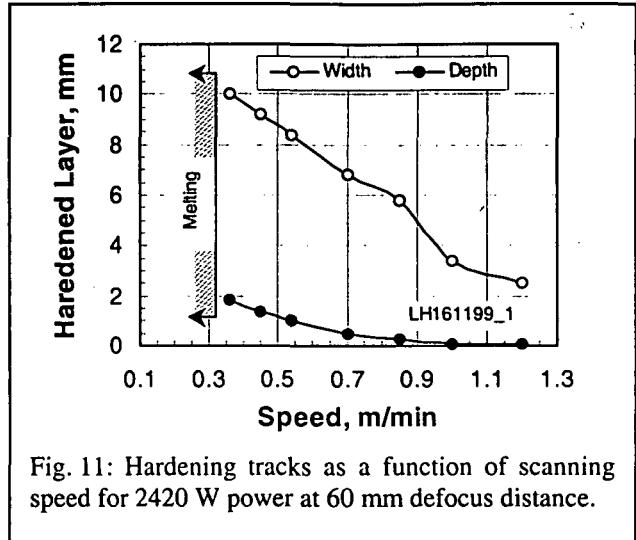


Fig. 11: Hardening tracks as a function of scanning speed for 2420 W power at 60 mm defocus distance.

laser power. The depth and width of the hardened layer at 60 mm defocus distance are shown in Fig. 11. This illustrates that the increased defocus distance provided a wider range of operating parameters for effective surface hardening without melting.

### 2.3.2 Microstructures

The microstructure of the hardened layer varied with the scanning speed for particular combinations of laser power and defocus distance. Like the width and the depth, the microstructure of the hardened layer, particularly near the surface, was

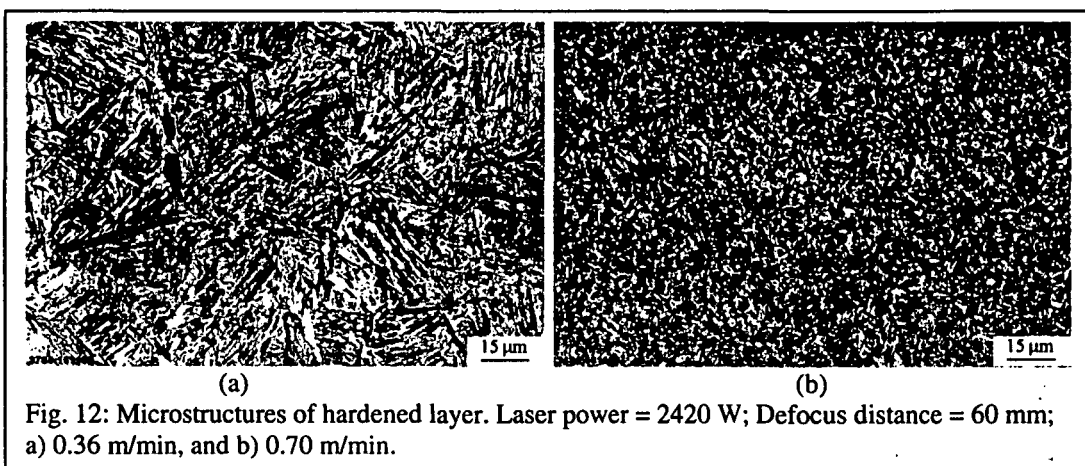


Fig. 12: Microstructures of hardened layer. Laser power = 2420 W; Defocus distance = 60 mm; a) 0.36 m/min, and b) 0.70 m/min.

found to be significantly affected by the scanning speed as shown in Fig. 12. At slower scanning speeds the microstructure near the top surface of the hardened layer was more martensitic (Fig. 12a) than at higher scanning speeds (Fig. 12b). At faster scanning speeds the beam-work piece interaction time was not long enough to transform the initial phase into full austenite, and only a partial austenitisation was most likely to occur. As a result, the microstructure exhibited fine martensite with non-aligned second phase.

### 2.3.3 Hardness

The hardness traverses made on the cross sections of hardened layers exhibited a variable extent of hardening during laser irradiation. Typical hardness traverses for the sample hardened with 2420 W of laser power scanned at 0.36 m/min with a 60 mm defocus distance are shown in Fig. 13.

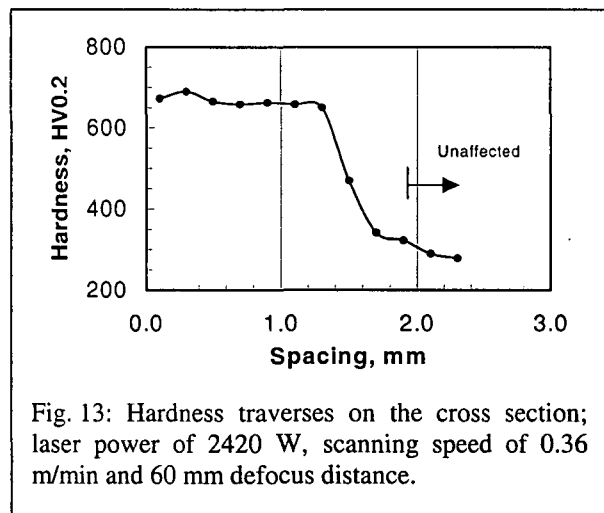


Fig. 13: Hardness traverses on the cross section; laser power of 2420 W, scanning speed of 0.36 m/min and 60 mm defocus distance.

## 2.4 CASE STUDIES

Drill stems are used in gas and oil exploration. Wear and galling of threads are a common problem for the stem in service. Threads are usually hardened by induction heat treatment for increased wear and galling resistance. However, this process hardens the critical region of the thread and may result in fracture during service. A

typical cross section of an induction-hardened thread is shown in Fig. 14. In addition, the distortion resulting from the hardening process can be so severe that the rejection rate during production processing will be substantial. Similar threads were hardened by a 3.5 kW Nd:YAG laser, which produced negligible distortion and a hardened layer that is away from the critical region of the thread, see Fig. 15.

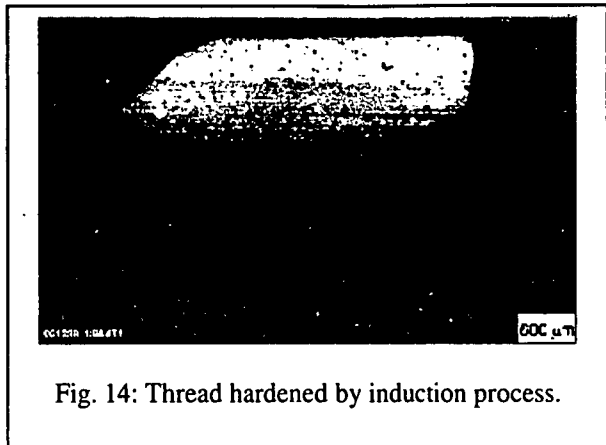


Fig. 14: Thread hardened by induction process.

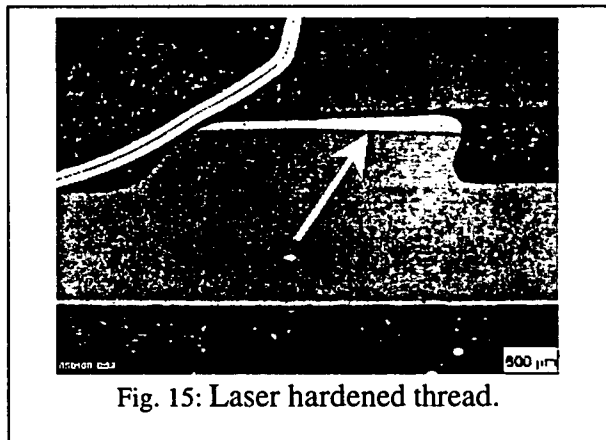


Fig. 15: Laser hardened thread.

### 3. LASER CLADDING

The laser assisted surface alloying and cladding is gaining recognition as being the most effective method for improving surface properties [11-13]. Due to potentially very high energy density, a laser beam can melt any combination of powdered metals and carbides to produce alloys on a substrate layer. In addition, the material conditions created by laser irradiation are far from equilibrium, and this enables the generation of alloys, structures, and residual stress fields that are unattainable by other means. A highly concentrated laser beam also permits the melting of a thin substrate layer resulting in strong metallurgical bonding to the substrate and only a low degree of dilution and minimum distortion in the component. As a result, laser

cladding, laser alloying and laser particle injection, in addition to heat treatment and surface remelting, have attracted scientific and industrial interest as a means of modifying and improving the surface properties of substrate.

Laser cladding generally provides the following advantages in comparison to conventional techniques such as plasma spray and tungsten inert gas (TIG) or metal inert gas (MIG) arc welding:

- (i) Improved metallurgy because of the guaranteed fusion bonding and refined microstructures resulting from rapid solidification (cooling rate  $>10^4$  °C/sec);
- (ii) Controllable dilution;
- (iii) An extended range of coating thickness from 0.1 to 5 mm;
- (iv) Reduced thermal distortion;
- (v) A consistent surface finish and coating thickness; and
- (vi) Easy automation.

A laser-clad layer can be produced by the following four methods:

- (i) Wire feed
- (ii) Pre-placed chip
- (iii) Pre-placed powder bed
- (iv) Powder injection

Each of these techniques has both advantages and disadvantages. However, powder injection and wire feed techniques are superior to the others with respect to process

control and deposit quality.

The most common problem for cladding using the conventional processes such as TIG welding or plasma transferred arc (PTA) is the high heat input that may be sufficient to alter the distribution of carbides in the matrix. This adversely influences the hardness and wear resistance of the clad. Another consideration is the high thermal and residual stresses that will develop if there are significant differences in the coefficient of thermal expansion and contraction between the substrate and deposit. Such stresses may cause the surface layer to generate cracking. Thermal spraying of metal powders are heavily used in industries, but the process suffers from poor bond strength with the substrate, in which case the interface becomes the source of cracking.

### **3.1 PROCESS VARIABLES**

The power density required for cladding and surface alloying is in the range of  $10^5$  -  $10^7$  W/cm<sup>2</sup>. Like surface hardening the characteristics of the clad or alloyed layer can be influenced by laser power used, its defocus distance and travel speed. For example, higher power and lower travel speed will increase the deposit thickness and the depth of the melt, resulting in the build-up of residual stresses and distortion.

In addition, the characteristics of the clad or alloyed layer are also influenced by the powder application technique. The two-step operation involves the pre-application of loose powder on the substrate as thin layer or coating, which is subsequently irradiated by laser beam, Fig. 16. When the powder is loosely placed on the



substrate, powder tends to be blown away by the plasma forces, resulting in low efficiency. In addition, the application of shielding gas becomes impractical. When the powder is applied as a paste it needs pre-mixing with binders, which can be an acrylic organic binder or ethyl

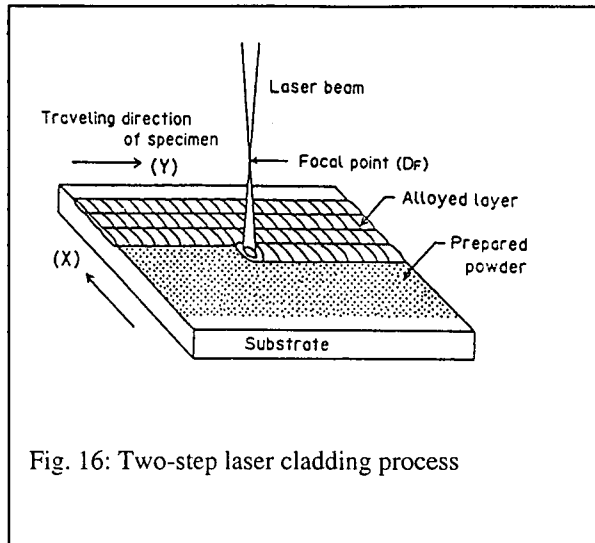


Fig. 16: Two-step laser cladding process

alcohol. In the single step operation (Fig. 17), the metal powder is injected into the beam substrate interaction zones. The position of powder injection relative to the laser beam and molten pool can affect the morphology of powder particles in the layer. If the powder particles interact

strongly with the laser beam before falling into the molten pool, there is a possibility that the powder particles will be fused and form a homogenous alloyed layer. However, if the powder particles are injected directly into the molten pool, the distribution of the

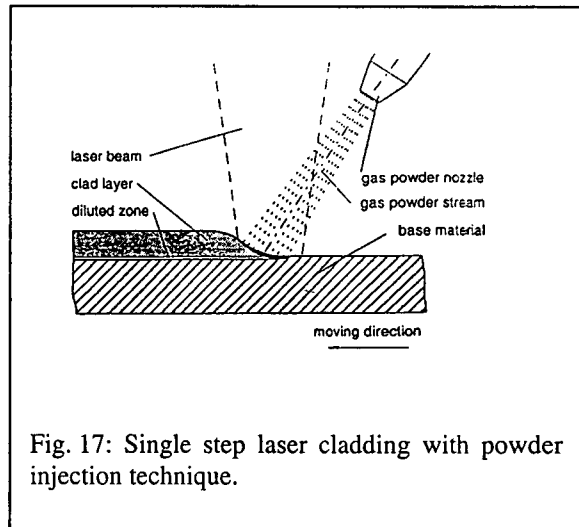


Fig. 17: Single step laser cladding with powder injection technique.

particles and the composition of the resultant alloy in the layer is likely to be different due to their reduced interaction with the laser beam.

Clad overlay can also be made using solid wire, which is melted by laser beam and deposited on the substrate. The cladding with solid wire is relatively more efficient than that with metal powder. The wire was fed through the wire feeder into the

beam-substrate interaction region, Fig. 18.

### 3.2 Choice Of Alloying Powders

The choice of alloying element depends on the properties required. In corrosive environments, the application of chromium on ferrous alloys greatly improves corrosion

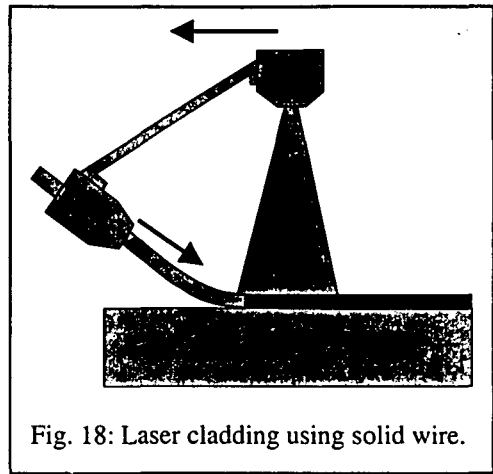


Fig. 18: Laser cladding using solid wire.

resistance. Additional additives are required to improve the mechanical properties and wear resistance. In other operations abrasive wear is the primary problem for the components and then carbide-based compounds can be used to give a high abrasion resistance.

One of the common hard particles used in the application of metal to earth abrasion is tungsten carbide (WC). These hard particles in the metal matrix provide wear resistance. Typically binders such as nickel (Ni) and chromium (Cr) are used with WC to increase corrosion resistance. Cobalt-based alloys are also used since they exhibit resistance to a variety of wear mechanisms by virtue of their deformation and fracture characteristics. Most of these composites possess resistance to sliding and crushing abrasion that is useful for applications that include shovel teeth, rock crusher parts and ploughshares. Cobalt-based alloys are also resistant to deformation and chemical attack in the high temperature range (500-900 °C) and are also used to protect dies and guide rolls in the steel and casting industries. Surface alloying of AISI 316L austenitic stainless steels by TiC, TiC+SiC, Si and C has been used. Ni-Cr-B-Si and Co-Cr-W self-fluxing alloy powders have been used to coat the seating surface of internal exhaust steel valves. These surfaces are usually subjected to wear

and corrosion at high temperature of 600°C to 800°C.

### 3.3 BACKGROUND STUDY

An experimental study was carried out to determine the appropriate laser parameters for the cladding of several metal powders. This constituted a scoping exercise for the newly installed Lumonics 3.5 kW continuous wave (cw) Nd:YAG laser.

#### 3.3.1 Melt Run

Prior to the application of metal powder a single track was made to determine the melt depth and width as a function of laser parameters (speed and defocus distance) for 6 mm thick mild steel plate, Fig. 19. This exercise was necessary to determine the optimum laser parameters, particularly the defocus distance and the resultant melt width for powder injection experiments. Single surface melt tracks of 100 mm

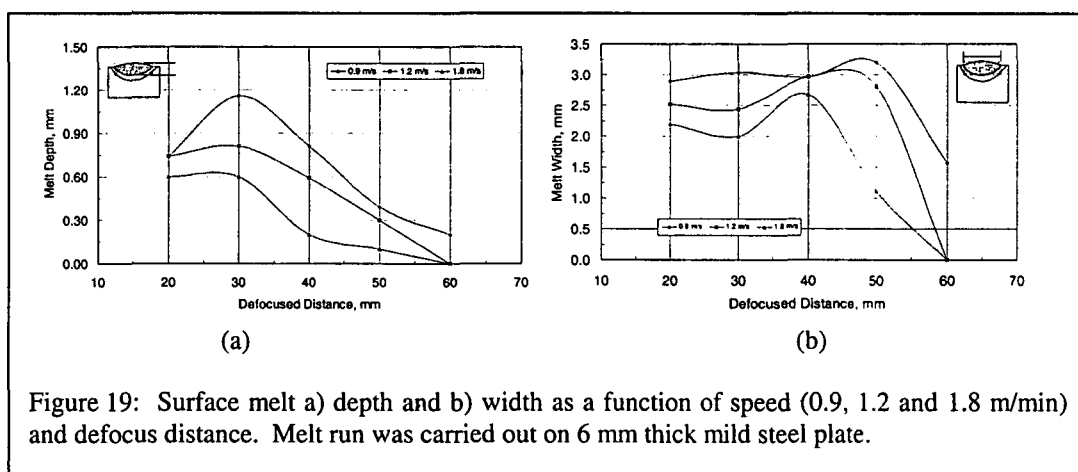


Figure 19: Surface melt a) depth and b) width as a function of speed (0.9, 1.2 and 1.8 m/min) and defocus distance. Melt run was carried out on 6 mm thick mild steel plate.

length were made on steel substrates using various defocus distances. The focus point of the laser beam was always above the substrate surface. The beam head was kept stationary and the steel substrate was positioned on a CNC controlled XY table under the laser head and the travel speed was varied by moving the XY table.

### 3.3.2 Cladding Process

The cladding process was carried out on the CNC controlled XY table and metal powders were deposited on 6 and 10 mm thick mild steel substrates. The metal powder was supplied to the beam area through a 4 mm diameter copper nozzle from a powder feeder. Powder was fed using argon gas (at a flow rate of 0.4 l/min) as a carrier gas. During operation, the laser beam head and the powder nozzle remained stationary while the XY table moved the substrate. The appropriate defocus distance was selected for the cladding investigation from the analysis of the melt run characteristics.

### 3.3.3 Deposited Alloy

Several alloys in the form of metal powders and wire were selected for the study. Some of these had the potential to increase resistance to adhesive wear while others were suited for abrasive wear resistance. The adhesive wear resistance powders include Co-Cr and Ni-Cr based metal powders and the abrasive wear resistance powders include WC based powders.

#### Co-Cr Based Powders – Stellite 6

A macroview of the clad surface and a cross sectional view of a Stellite 6 deposit is shown in Fig. 20. This shows negligible dilution and a relatively smooth

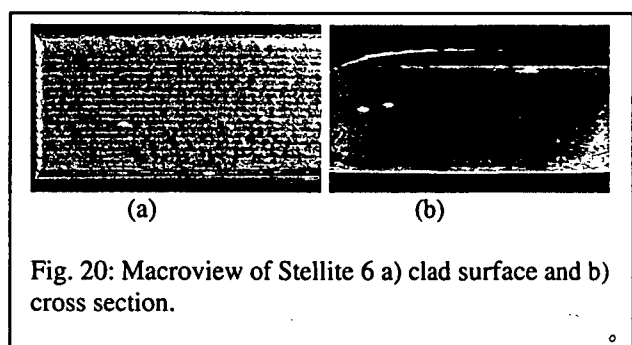


Fig. 20: Macroview of Stellite 6 a) clad surface and b) cross section.

layer of about 1.6 mm thick. No obvious cracking was observed on the surface. The interface region of the deposit exhibited no defects. However, surface contaminants

at the interface were found to initiate cracking and subsequent trials with appropriately cleaned surfaces eliminated this problem. This observation indicates that the substrate surface cleanliness is essential for high quality cladding. The deposit consisted of a dendritic microstructure, as shown in Fig. 21. Other parameters have been established for deposits thinner than 1.6 mm.

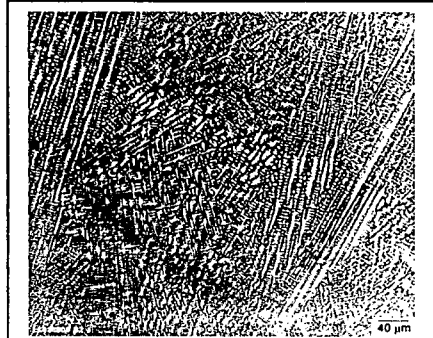


Fig. 21: Microstructure of Stellite 6 laser clad.

### Co-Cr Based Wire–Stellite 6

Clad overlay was also made using the solid wire in which case the laser head and wire feeder was moved by a robot over a stationary substrate. The wire was fed through the wire feeder into the beam-substrate interaction region.

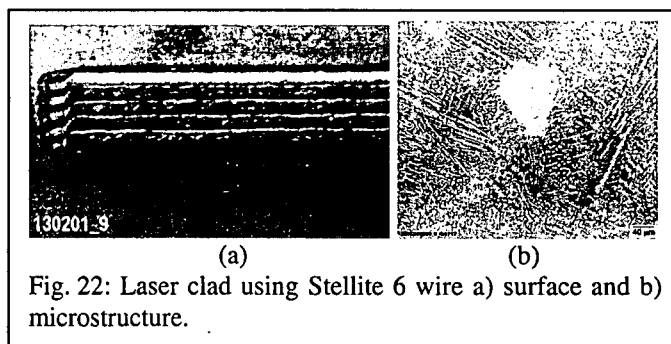
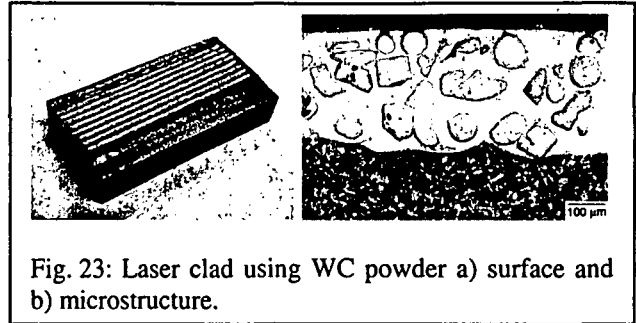


Fig. 22: Laser clad using Stellite 6 wire a) surface and b) microstructure.

Stellite 6 alloy in the form of 1.6 mm diameter cored wire was used to deposit laser clad on a 4 mm thick 3Cr12 stainless steel substrate. In this trial the substrate was kept stationary while the robot was used to move the laser head and the wire feed delivery system. The wire was fed from the wire feeder in front of the leading end of the melt. A macroview of the overlay is shown in Fig. 22a. The microstructure is mainly composed of columnar dendritic structures and contained occasional spherical carbide particles, see Fig. 22b.

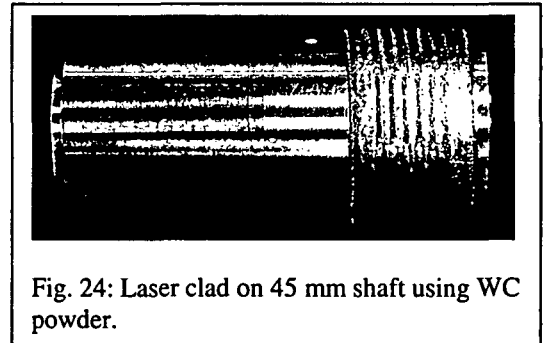
### WC Based Powder

Single-track cladding was carried out for the WC based EC11412 powder to determine the appropriate parameters for



cladding with multiple tracks. Based on the assessment of single-track deposit the parameters were identified and used to deposit multiple tracks. A macroview and typical microstructures of EC11412 deposits are shown in Fig. 23.

This powder was also used to deposit a layer on a 45 mm diameter cylindrical shaft of AISI 4140 steel. In this experiment the cylindrical shaft was rotated and the laser beam with powder



nozzle was held by the robot and moved along the length of the rotating shaft. The powder was injected into the pool. A typical appearance of the deposit is shown in Fig. 24.

### 3.4 CASE STUDIES

Break-in picks are used in crushing and breaking ores that contain highly abrasive silica. Typically the picks are made from quenched and tempered AISI 4155 steel. These picks were clad by laser cladding with tungsten carbide metal powder, as shown in Fig. 25. It is expected that the service life of these picks will be significantly increased. One of the challenges in WC cladding was to obtain uniform

distribution of WC. Due to high specific density the WC particles tend to sink to the bottom of the overlay, which caused significant cracking at the interface. In addition, the outer surface of the layer that contains less carbide particles can be subjected to high abrasive wear. This problem was rectified by injecting additional WC behind the molten region of the clad.

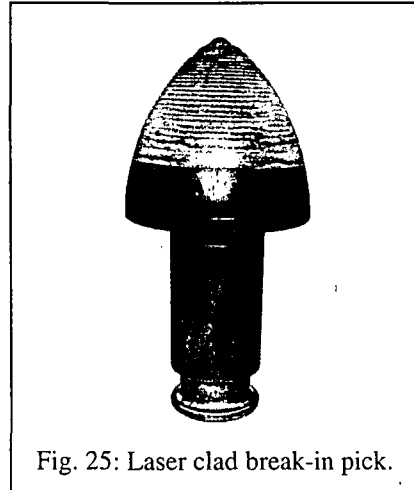


Fig. 25: Laser clad break-in pick.

The leading edges of the turbine blades of the low-pressure steam turbine are subjected to high erosion due to high velocity impact with water droplets, Fig. 26. In most cases the erosion-damaged region becomes the site for crack initiation. Fracture and failure of a portion of blade can cause excessive vibration and low efficiency in power generation. In the worst case this failure can cause complete shut down of the power station. Loss of revenue is substantial.

The leading edge of the blade is protected by a hardfacing erosion resistant shield. Despite this protection shield the erosion remains a problem. The usual practice is to attach

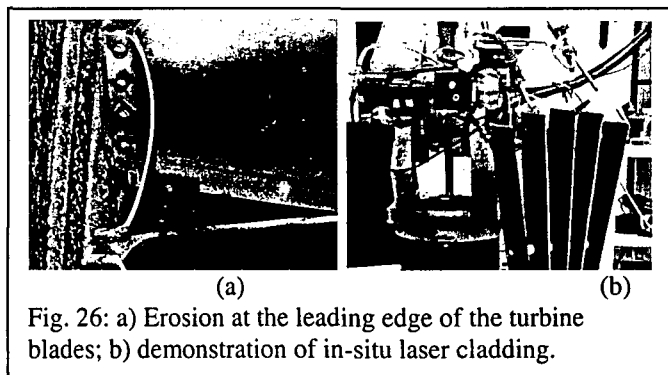


Fig. 26: a) Erosion at the leading edge of the turbine blades; b) demonstration of in-situ laser cladding.

the shield by brazing process. Two problems are associated with this process. First, the nickel based filler metal used for brazing can lead to the formation of brittle phases, which are detrimental to joint strength; and second, the brazing cycle itself

can cause temper embrittlement of the blade. Often the transition region becomes the site for high erosion and subsequent cracking.

The objective of the project is to deposit a high quality overlay with minimum damage to the blade by beam manipulation and changing the interaction time.

Both the clad overlay and the transition region of the blade will be subjected to simulated erosion testing for assessment. High-resolution microscopy will be used to elucidate the erosion process. The information will be used to design new alloys and laser processes.

In addition, the repair of damaged blades is very expensive. Each blade needs to be removed from the rotor for any repair. Removal of blade from the rotor is very difficult and time consuming. Damaged blades are usually repaired by a TIG welding process, which embrittles the HAZ due to high heat input and thermal effects.

The idea of in-situ repair of turbine blades with laser surfacing is highly significant, since industry can save millions of dollar. However, the issues associated with the in-situ nature of the repair are the most challenging and difficult. Some of the difficulties arise from the fact that the blades are highly twisted and flat surface of the leading edge is obscured by the adjacent blades, and from the restricted access between the rows of blades. Several alloy delivery techniques, including in the form of paste and wire in the out-of-position will be investigated. Depending on the alloy delivery the appropriate beam manipulation will be investigated.



## **5. CONCLUSIONS**

High power laser can be used in the surfacing of engineering components. Any components, which are subjected to wear are suitable for laser surfacing. The depth of hardening achieved with lasers can be varied from 40  $\mu\text{m}$  to 2 mm. High power beams can melt almost any combination of metal powders for clad overlay and it is possible to deposit up to 2.5 mm thick overlay in a single layer with minimum dilution.

## **ACKNOWLEDGEMENT**

The authors would like to thank L. Jarvis, A. Mundy and D. Harris for their assistance in carrying out many experiments. Thanks are also due to S. Jeremy, E. Murray and A. Soltan for cutting and polishing metallographic specimens.

## REFERENCES

1. Steen, W.M. and Powell, J. *Materials Engineering*, 1981, Vol. 2, No. 3, pp 157.
2. Seaman, F. D. and Gnanamuthu, D. S. *Metal Progress*, 1975, Vol. 108, No. 3, pp 67.
3. Benedek, J., Shachral, A. and Levin, L. *Opt. Laser Technology*, 1980, Vol. 12, No. 5, pp 247.
4. Harth, G. H. et al. *Journal of Metals*, 1976, Vol. 20, No. 4, pp 5.
5. Steen, W. M. and Courtney, C. *Metals Technology*, 1979, Vol. 6, No. 6, pp 456.
6. Donaldson, E. G. *Br. Foundryman*, 1986, Vol. 79, No. 6, pp 262.
7. Burakove, V. A. et al. *Izv. VUZ Mashinostr.*, 1985, No. 10, pp 113.
8. Cermak, J. et al. *Proc. 6<sup>th</sup> Intl. Symposium on High Purity Materials in Science & Technology*, Dresden, Germany, May 1985, pp 198.
9. Shiue, R.K. and Chen, C. *Metallurgical Transactions A*, Vol. 23A, January, 1992, pp 163-170.
10. Robert, C.C. and Crampon, J. and Foct, J. *Surface Alloying of Iron by Laser Melting: Microstructure and Mechanical Properties*, *Surface Engineering*, 1998, Vol. 14, No. 5, pp 381.
11. Fasasi, A.Y. et al. *Laser surface Melting of Mild Steel with Submicronic Titanium Carbide Powders*, *Journal of Materials Science*, 1994, Vol. 29, pp 5121.
12. Irving, B. *High Powered Lasers Gain Ground for Cladding and Hardfacing*, *Welding Journal*, August, 1991, pp 37.

**REGIONAL WORKSHOP ON LASERS AND OPTOELECTONICS  
SERPONG, TANGERANG, INDONESIA  
JUNE 25 – JULY 6, 2001**

**INTEGRATED OPTICS**  
**Principles and Applications**

**Dr. John E. Batubara**

**Universitas Pelita Harapan  
Lippo Karawaci, Tangerang, Indonesia  
June 2001**

**INTEGRATED OPTICS**  
**Principles and Applications**

**Dr. John E. Batubara**

## CONTENTS

<b>Chapter 1</b>	<b>INTRODUCTION .....</b>	<b>1</b>
<b>Chapter 2</b>	<b>THEORETICAL CONCEPTS .....</b>	<b>4</b>
<b>Chapter 3</b>	<b>INTEGRATED OPTICS COMPONENTS .....</b>	<b>7</b>
<b>Chapter 4</b>	<b>FABRICATION OF COMPONENTS .....</b>	<b>10</b>
<b>Chapter 5</b>	<b>SOME APPLICATIONS .....</b>	<b>14</b>
<b>Chapter 6</b>	<b>RECENT DEVELOPMENT .....</b>	<b>19</b>
<b>References</b>	<b>.....</b>	<b>23</b>

## CHAPTER 1 INTRODUCTION

### 1.1. BACKGROUND

Integrated optics has proven to be a very dynamic and active area, with new significant development being made at a very fast pace. The new area of integrated optics has been based primarily on the fact that light waves can propagate through and be contained by very thin layers or films of transparent materials. By combining such layers together and shaping them into appropriate configurations, integrated-optics technology has realized a large variety of components which can perform a wide range of operations on optical waves.

Area of integrated optics includes light guidance along thin dielectric films and stripes and light controlling by thin dielectric films. The wavelength of interest lie mostly in the range of 0.1 to 10  $\mu\text{m}$ ; for wavelength much larger than 10  $\mu\text{m}$ , metallic waveguiding techniques of the microwave variety provided a more efficient technology. For wavelengths around 0.1  $\mu\text{m}$  or smaller, the absence of suitable sources and the presence of large absorption and scattering losses impose limitations on the practical use of waveguiding effects.

### 1.2. DEVELOPMENT AND PERSPECTIVES

Integrated optics is based on the guiding of electromagnetic energy at optical frequencies by thin films was stimulated and influenced by microwave engineering and thin-film optics. A special role has also been played by semiconductors, which now appear to be most promising in promoting the goal of monolithic integrated optical circuits. Recent scientific efforts focus on planar thin film dielectric structures rather than metallic and circular configurations.

In 1963 Yariv and Leite, and Bond et al. reported the guiding action of planar layers in p-n junctions; the results were employed by Nelson and Reinardt showing that the planar guided modes in p-n junctions are instrumental in providing light modulation through electro-optic effect. In 1964 Osterberg and Smith carried out experiments with glass sheets and prisms that provided both

optical guidance by planar films and coupling of light beam into these films. The guiding along the glass surface was produced by the graded increase of the refractive index. In 1965 the microwave concepts were combined with photolithographic techniques to construct thin-film waveguides. In 1968 Shubert and Harris suggested to use the optical surface waves in data processing networks, and Anderson suggested the optical integrated circuits. In 1969 Miller suggested the term integrated optics as a developing reliable thin film technology for optical communications purposes.

From 1968, it was projected the ultimate goal of the activities to replace integrated-electronics circuits by equivalent, and possibly more effective, integrated-optics circuits. Integrated-optics components must be compact and miniature, reliable, with high mechanical and thermal stability, low power consumption and preferably integrable on a common substrate or chip. These requirements stimulated the development of improved thin-film fabrication techniques and promoted numerous studies of new materials, for both passive and active functions.

Since 1968 some efforts were intended to improve the properties of planar wave-guides and other passive components to meet the requirement of low absorption and scattering losses. In 1970 the problems on coupling light from laser sources into the thin-film waveguides have been solved in efficient manner by various researchers. The development of active components including light sources, modulators and detectors were also necessary to be developed. D. Hall et al. applied the electro-optic effect to achieve modulation in structures consisting of a high resistivity GaAs epitaxial film on a more heavily doped GaAs substrate.

The Bragg diffraction principle for deflecting an incoming surface wave was used by Kuhn et al. to achieve modulation by replacing the grating with an acoustic wave traveling through the thin-film. To achieve the goal of a truly integrated-optics circuit which much smaller dimensions, very promising candidates are  $\text{Al}_x\text{Ga}_{1-x}\text{As}$  heterostructure junction lasers, which have the required thin planar configuration.

In 1972 Kogelnik and Shank introduced distributed-feedback concept of lasers, and H.W. Yen et al. have been successfully applied the concept to the fabrication of AlGaAs lasers. After the infra-red diodes reported by Anderson (1966), more than eight years elapsed until a silicon p-n junction photo-diode was reported by Ostrowsky et al. (1973).

The studies on photo-detection in GaAs via epitaxial growth, electro-absorption and ion implantation have been carried out by H. Stoll et al (1973). The investigations show that photo-detectors for integrated circuits pose no fabrication difficulties.



## CHAPTER 2 THEORETICAL CONCEPTS

### 2.1 CONCEPTS OF RAY OPTICS

Ray optical techniques in connection with slab waveguides have been explored and used by Tien (1971), Maurer and Felsen (1967), Lotsch (1968) and others. For the purpose of simplicity, we choose the slab waveguide because it is relatively easy to understand and analyze, and it is of considerable practical interest in integrated optics. We use the ray-optical concept to introduce the basic principle and terminology of dielectric waveguide theory, including the nature of the modes of propagation, waveguide cutoff, the propagation constants and the effective guide width. In addition, we employ this concept to derive and provide a number of results of interest to the experimenter, such as plots of propagation constant and of the effective width of slab waveguides. The ray-optical concept is a very simple picture with great intuitive appeal, but it is not as complete a description as that provided by electromagnetic theory, which we discuss later. However, the results we present here are in perfect agreement with the latter.

The concept of light guidance in a slab waveguide is one of light rays tracing a zig-zag path in the film, with total internal reflection of the light occurring at the film-substrate and film-cover interfaces. As reflection and refraction at these dielectric interfaces play an important role in the guiding process, it is necessary to review the relevant laws and their consequences.

### 2.2 ELECTROMAGNETIC THEORY

In this section we propose to collect the fundamentals of the electromagnetic theory of dielectric waveguides. Some of the general properties of the waveguide modes will also be discussed. This includes a listing of relevant forms of Maxwell's equations and of the wave equations, a deduction of modal field properties following from symmetry considerations, a proof for the orthogonality of the modes, and a discussion of mode expansion and normalization, of the variation theorem, of power transport and stored energy, and of variational

principles applicable to dielectric waveguides. The discussion should be kept as general as possible to allow for the variety of planar and strip waveguides considered for integrated optics applications.

### 2.3 CONCEPTS OF PLANAR MODES

In this section we list formulas for the fields of the modes of a planar slab waveguide. We consider the structure and coordinate system where a film thickness  $h$  and uniform refractive index  $n_f$  is sandwiched between a substrate of uniform index  $n_s$  and a cover on uniform index  $n_c$ . This structure has also been called the "asymmetric" slab guide. The modal fields can be derived from the wave equations of the previous section, and the corresponding solutions have been discussed by McKenna (1967), Tien (1971), Marcuse (1974) and others. We have to distinguish between modes of TE and modes of TM polarization. Another distinction is between guided modes and radiation modes, the latter divided into the categories of substrate radiation modes, substrate-cover (also called "air") radiation modes, and evanescent modes.

In accordance with the wave equation we define various transverse decay ( $\gamma_i$ ) and propagation constants ( $\kappa_i$ ) by

$$\kappa_c^2 = n_c^2 k^2 - \beta^2 = -\gamma_c^2 \quad 2.1$$

$$\kappa_f^2 = n_f^2 k^2 - \beta^2 \quad 2.2$$

$$\kappa_s^2 = n_s^2 k^2 - \beta^2 = -\gamma_s^2 \quad 2.3$$

where the subscripts  $s$ ,  $f$  and  $c$  refer to substrate, film and cover respectively.

Table 2.1 shows the range of propagation constants  $\beta$  corresponding to the various mode types and categories, and also the associated ranges of the transverse propagation constant  $\kappa_s$  in the substrate. Because of its convenient range, the latter is chosen as the spatial frequency for the continuous mode spectrum. As we are dealing with a planar problem, all field solutions can be made independent of the  $y$ -coordinate.

Tabel 2.1 Mode with respective propagation constants

Modes	$\beta$	$\kappa_s$
Guided	$k n_f \rightarrow k n_s$	Imaginary
Substrate	$k n_s \rightarrow k n_c$	$0 \rightarrow k \sqrt{n_s^2 - n_c^2}$
Substrate-Cover	$k n_c \rightarrow 0$	$k \sqrt{n_s^2 - n_c^2} \rightarrow k n_s$
Evanescent	Imaginary	$k n_s \rightarrow \infty$

## CHAPTER 3 INTEGRATED OPTICS COMPONENTS

### 3.1 SEMICONDUCTOR LASERS DAN DETECTORS

The basic part of the optical communication system is the light source. For lightwave applications, the semiconductor laser act as an optical equivalent to the radio frequency or microwave oscillator. A simplest form of semiconductor lasers consists of a p-n junction diode in which the faces perpendicular to the junction plane are cleaved smooth and parallel. The top and the bottom faces, which are parallel to the junction, are contacted with metal electrodes. Upon forward biasing, electrons from the n region are injected across the junction where they combine with holes, giving off radiation at a wavelength determined by the semiconductor's band gap. If the resulting light is directed along an axis perpendicular to the diode mirror faces, it can bounce back and forth, stimulating more electrons to recombine and thereby amplifying the radiation. Because the mirrors have a small transmission coefficient, a portion of the radiation escapes the diode laser and propagates outward as a narrow beam of light.

To sense the emitted radiation, some types of detector are required. One of the simplest practical semiconductor detectors is simply a reversed-biased p-n diode. Incoming radiation incident near the diode junction region and having a sufficiently short wavelength creates hole-electron pairs via photoelectric effect. These pairs are separated and swept across the junction in opposite directions by the built-in junction potential and are subsequently collected as a current by the external circuitry.

### 3.2 DIELECTRIC WAVEGUIDES

The principle of optical confinement using a high dielectric material is based upon the phenomena of total internal reflection (TIR). A common example of TIR is that observed at the bottom of a swimming pool. For observation angles  $\theta$  greater than the critical angle  $\theta_c$  the top surface of the pool act as a mirror reflecting all light from below back toward the pool bottom. This phenomenon is a direct result of the fact that water has a higher refractive index than air. Suppose

next that two such interfaces exist, as is the case for simple glass microscope slide. Then light generated between the high refractive-index surfaces at an angle  $\theta > \theta_c$  will continue to bounce between the upper and lower glass-air interfaces through the process of TIR. More practical geometries for integrated optics can be fabricated, for example, by sputtering a thin, high refractive-index layer onto a lower refractive-index substrate. This yields a guiding film wedged between the lower refractive-index substrate and air regions. When such a guide is made from semiconducting materials, the additional potential exist for integrating electronic and electro-optic components in proximity with the optical ones.

### 3.3 MODULATORS AND INTERFEROMETERS

or information to be placed carrier frequency, the beam must be modulated in some fashion. One particular scheme involving the so-called Mach Zehnder interferometer make use of the coherent nature of laser light. A substrate material is chosen that is electro-optic, that is, one that allows the optical velocity or equivalently its wavelength to be modified by the application of a dc or low frequency electric field. One arm of the interferometer has an electric field placed across it whose amplitude may be varied. When no field is applied, the signals from each arm travel the same electrical distance and therefore recombine in phase. When a sufficiently large electric field is applied, the signals recombine 180° out of phase and therefore cancel. Thus, by varying the amplitude of low-frequency electrical signal, the amplitude of the laser radiation can be modulated. This scheme can therefore be used to place a modulated signal on the laser carrier. It should be noted that the interferometer principle described here is also useful for several other functions including high-speed analog-to-digital conversion, optical phase shifting, and the measurement of such physical parameters as temperature, pressure, and magnetic field.

### 3.4 DIRECTIONAL COUPLERS

When two identical waveguides are placed in proximity, the power carried by these structures is found to periodically exchange between them with distance.

Thus, for example, if the input to one guide is excited with an optical signal while the other is not, then after some distance it is found that all the power has been transferred to the opposite waveguide. The distance required for the exchange depends on the waveguide spacing and the velocity of light along the guides. This velocity-dependent coupling length is the principle behind the operation of the electro-optic switch. With no voltage applied, the coupling length is chosen to be exactly an even number of exchange periods, so that all optical incident on waveguide 1 exits from the same waveguide. By application of the appropriate dc bias, the velocity within the guides is modified by the electro-optic effect, changing the coupling length by exactly one period and causing the optical radiation to exit from waveguide 2. This technique allows, for example, a fiber optics switching network to be created in which light can be transferred from any incoming optical fiber to any outgoing fiber.

### 3.5 GRATINGS AND FILTERS

If an optical signal is passed through a waveguide having a grating consisting of a series of periodic grooves, the undulations in refractive index cause a small portion of the signal to be reflected at each groove. If the optical wavelength is  $\lambda$  and the groove periodicity is  $\Lambda$ , then the reflected signals will add in phase only when the distance from one groove to the next one and then back again is equal to a wavelength. That is

$$\lambda = 2 \Lambda \quad 3.1$$

For long gratings having small reflectivity per groove, the spread in wavelength over which strong occurs can be extremely small, on the order of a few angstroms ( $1 \text{ \AA} = 1 \times 10^{-10} \text{ m}$ ). Thus, such a grating can be used as either a notch filter in transmission or a narrow band-pass filter in reflection. In the latter case, a series of such filters with slightly different periodicities could be used, for example, to demultiplex a number of optical signals carried on the same fiber, each having a different carrier wavelength. Additionally, such gratings are useful as the end reflectors for semiconductor lasers.

## CHAPTER 4 FABRICATION OF COMPONENTS

### 4.1 FABRICATION OF PASSIVE COMPONENTS

The thin films for optical waveguides have quite particular requirements. First of all, the light is transmitted in the plane of the film, so that the optical path can easily be on the order of centimeters long. Secondly, in waveguide applications the optical thickness of the film is of no importance, but instead one needs to know separately its refractive index and its mechanical thickness, or at least its apparent refractive index  $n = \beta/k$ . Also, the light is not transmitted totally inside the film but rather it travels in a composite medium made up of the film, the substrate and the cladding. Therefore the materials used for all three layers have to be good optical quality and free scattering defects. In addition, the boundaries between the different layers should be smooth to avoid losses caused by scattering at the interfaces. Exactly how smooth the surfaces have to be depending on the particular design of the guiding layer and on the order of the mode. In general, the higher the difference in refractive index between the guide and the surrounding media and the higher the mode number, the higher will be the losses caused by scattering at the boundaries. Thus, a film of a high index material may appear to be more lossy when deposited on a low index substrate than when deposited on a higher index substrate.

The surfaces needed for the deposition of optical waveguides need not to be flat; i.e., no great deal of care is necessary to obtain the extreme flatness that optical polishers are so proud of. Rather one needs a surface that is free of defects such as scratches, pits and digs. Optical flatness is of only minor importance. As a result, new methods of film deposition and evaluation have been and are still being developed specifically for use in optical waveguides.

By employing thin films as planar waveguides, one can use useful information about new materials, new deposition techniques, and so on. To make an optical circuit, one has to be able to make patterns in these films. If these patterns are simple and relatively large, such as lenses, prisms, and others, they can be made

by the use of mechanical masks. However, if high-resolution patterns, such as gratings and strip guides, are required, the masks to be employed become more complicated. Some methods currently used to make the latter types of masks are described in a particular section.

The methods used to produce waveguiding layers can be divided into two classes: those in which the layer is made by the deposition of a material on a substrate, and those in which the higher-index layer is produced in the substrate itself by some chemical or physical reaction. In the first type, the index change between the guide and the substrate is discontinuous, whereas in the second type a gradual index change occurs.

Methods of the first class are sputtering, plasma polymerization and the production of a film from a liquid by spinning or by dipping. Vacuum evaporation – the method most commonly used for the production of thin films for classical optics applications – is seldom used in integrated optics since it produces films with relatively high losses. In the second class one finds proton bombardment, ion implantation and ion migration.

Before start with one of the aforementioned methods, the methods used for preparation of the substrates must first be considered.

## 4.2 FABRICATION OF SEMICONDUCTOR COMPONENTS

In monolithic integrated optics, all optical functions must be obtained in a single material. These optical functions can be broadly categorized as light generation, guiding, coupling, modulation and detection. Active functions such as light generation, modulation and detection generally require crystals rather than amorphous light guides. The only material to date in which all functions have been obtained is GaAs. The existence of continuous lasers in GaAs operating at room temperature is a prime incentive for considering this material. It is interesting to study the fabrication of optical circuit elements in crystals with special importance on GaAs and related III-V semiconductor compounds.

The first requirement for a crystal to be suitable for integrated optics is that it can be fabricated as a dielectric waveguide, in the form of a layer of good



optical quality with refractive index higher than the substrate. The refractive index can be controlled largely by changing the material composition. To a smaller extent, in semiconductor it can also be controlled by the electrical properties. Both of these effects have been utilized to make waveguides in crystals.

### 4.3 PATTERN FABRICATION

The patterns needed in integrated optics can be divided into two distinct classes: periodic pattern, such as grating couplers and filters, and pattern that have no periodicity at all.

#### 4.3.1 Periodic pattern

Because of their periodicity, the first type can be made conveniently by using optical interference patterns. If two beams intersect at an angle  $2\theta$ , the fringe spacings is

$$d = \lambda_0 / (2 n \sin \theta) \quad 4.1$$

where  $\lambda_0$  is the vacuum wavelength, and  $n$  is the refractive index of the material in which the two waves interfere. This interference pattern can be used to expose photoresist. The resulting resist pattern itself may then be used as an optical element, or it may be used as a mask in a subsequent etching process.

#### 4.3.2 Non-periodic pattern

A large amount of high resolution mask technology is used in the electronics industry for the manufacture of integrated circuits. Though much of this can be carried over to optical waveguide technology, there are some distinct differences. Two major differences are the need for very smooth edges and the aspect ratio of optical waveguides. Because of these points, the photolithography methods commonly used for integrated circuits cannot be used here. For example, an optical modulator with a guide 6 mm long and 2  $\mu\text{m}$  wide. If the mask for this guide were made by photographic reduction of a line 2 mm wide, this line would have to be 6 m long. The problem cannot be circumvented by a step and repeat method; even for 1% difference in index between guide and surround, the edges of the guide have to be smooth to better than 500  $\text{\AA}$  in order to keep the

attenuation below 1 dB/cm. This imposes tolerances on the step and repeat camera that are impossible to meet.

The unique requirement for very smooth long lines can be met by the use of a focused laser beam or a focused electron beam to write the patterns. For a proper appreciation of the problems involved in the making of masks, the final use of the generated pattern needs to be understood first. In general, four different ways of pattern generation and use can be distinguished:

1. The pattern is generated in a positive resist, deposited on top of a planar guide. After development, a metal coating is applied to the entire surface and subsequently the resist and the metal covering it are washed off. The remaining metal pattern is then used as a barrier in an etching procedure in which all but the wanted portions of the slab guide are removed.
2. The pattern is generated in either a positive or a negative resist and the resist itself is used as a barrier during a subsequent etching procedure.
3. The pattern is generated in a positive resist and the resist is used as a mask in ion implantation.
4. The pattern is generated in a material whose index increases as a result of exposure to the generating radiation, thus producing the guide directly. In a variation of this procedure, the pattern is written in a negative resist which, after development, forms the waveguide.

Other methods for producing guide patterns are electron beam writing and laser beam writing.

## CHAPTER 5 SOME APPLICATIONS

Considerable progress has been made in the sophistication, fabrication and in the theoretical analysis of planar and active components of the integrated optics. However, most of the components developed during the recent years rely on the same basic principles and general phenomenological aspects that are presented in the previous years.

Due to the strong continued interest shown by scientists from many disciplines, the demand for descriptive papers on integrated optics has motivated a number of tutorial reviews covering general or specialized aspects of this area.

### 5.1 PASSIVE COMPONENTS

Interest in producing optical waveguides with lower losses has motivated studies into guiding configurations that show desirable absorption and dispersion characteristics. While two-dimensional multi-layer waveguides have been investigated in order to better understand their guiding properties, special attention has been paid to anisotropic media, because of their potential for modulation and mode conversion, and to metal-clad waveguides which may serve as polarizers. However graded-index waveguides and three-dimensional waveguides having strip or other specialized cross-sections have been studied more extensively because of their greater suitability for use on small integrated-optics "chip". The fabrication of the various optical waveguides has also been reported in considerable details.

The problems associated with joining two separate waveguides have been explored. In particular, the step discontinuity that appears when two waveguides of different height or width are connected has been estimated. While the adverse effects of such a discontinuity can be reduced by tapers, studies on such tapers have revealed that considerable mode conversion may occur unless proper design is enforced. Different discontinuities, such as waveguide bends, branches, and other related transitional configurations have also been studied.

To avoid an abrupt transition from waveguide to another, the method of transferring energy by co-directional coupling has been further explored, and the advantages of using tapered rather than constant coupling have been demonstrated. Various fabrication methods for producing suitable transitions between waveguiding regions have also been developed.

Beam-to-waveguide couplers have continued to attract considerable attention because of their basic function in coupling a laser beam into a planar structure. As prism couplers had already been well developed, only a few studies have been concerned with them. In contrast, grating couplers have been considered much more extensively because of greater difficulties in the design and fabrication of this beam-coupler device. However, recent work has shown that, by choosing gratings with suitably blazed asymmetric profiles, it is possible to achieve a very efficient beam coupler whose operation compares well with that of a prism coupler. As recent fabrication techniques of such gratings have greatly improved, the construction of such blazed gratings now appears realistic.

A component that has recently attracted greater attention than in the past is the integrated-optics lens, which takes the form of an appropriate change in the thin-film waveguide and the substrate. While several lens shapes were explored, it was shown that geodesic lenses that are only slightly divergent from each other. As the spherical aberration introduced by such lenses can be made negligible, they are excellent candidates for data processing using multi-beam techniques.

## 5.2 ACTIVE COMPONENTS

Because semiconductor lasers can operate at room temperature and have small sizes, those devices are suitable for integration on small chips, and a large number of research papers have been issued since 1975.

Among the many varieties of heterostructure lasers, the distributed feedback (DFB) and the distributed Bragg reflection (DBR) structures have shown great promise for simple operation, spectrally pure laser output and possibly small sensitivity to wavelength variation with temperature. In the DFB laser, a periodic waveguide forms an integral part of the active lasing region and

serves to stabilize the laser operation because the wavelength and period dimensions must comply with a Bragg condition. The DBR laser also contains a periodic portion, but this is now outside the active region; thus the DBR laser consists of a lasing region with the end mirrors being replaced by periodic waveguides which provide total reflection at wavelengths satisfying a Bragg condition.

One difficulty with heterostructure laser outputs is that the outgoing beam has rather large vertical divergences due to the small height of the active film. This has been circumvented in twin-line lasers that consists of two coupled waveguides, of which one is a thin active waveguide whereas the other serves as a passive output waveguide which is relatively thick. Thus, the energy generated by the thin active guide is coupled to the passive thick guide, which can produce an output beam with considerably smaller divergence.

Detectors have usually been studied in conjunction with semiconductor laser investigations and results have been reported on in a few papers.

Intensive work has also continued in the development of faster broadband modulator, switches and beam deflectors. In this context, considerable progress has been made with devices using Bragg-type acousto-optic interactions, which also include schemes for achieving convolution of two separate acoustic signals. However, because of their lower power requirements and faster possible speed, more attention has been paid to devices using the electro-optic effect.

Most electro-optic switches consist of two or more sections of coupled waveguides, which are often subject to cross-talk because of the sensitivity to the coupling length and to other waveguide parameters. However, by dividing each of the waveguides into separate sections to which different switching voltages are applied, it was found possible to achieve very reliable configurations having a crossover ratio of better than 26 dB. This so-called  $\Delta\beta$ -reversal technique has stimulated the development of an impressive array of switching devices, which include an efficient switch and amplitude modulator having data rates in excess 100 Mbit/s with drive voltages as low as 3 V. Other electro-optic switches rely on

different mechanisms to implement the switching action, such as bifurcation, mirror action or total internal reflection, and others.

Although the stress on switches have been motivated by orientation towards digital processing, amplitude modulators have also been developed. While most of these are also based on electro-optic interactions, other mechanisms have been considered, including electrostriction, liquid crystal waveguides, electro-absorption, and optic-optic interactions. Devices for analog-to-digital conversion of signals have also been explored.

### 5.3 INTEGRATION AND OTHER ASPECTS

The aim of producing a fully integrated optical system on a small chip is still being pursued as a goal for the integrated-optics area. However, efforts at integrating many varieties of operational components on a single chip are still at the laboratory stage. Nevertheless, very promising results have already been obtained, particularly with sub-systems involving GaAs materials. The obstacles to large-scale integration occur because heterostructure lasers are based primarily on GaAs compounds whereas switches, modulators and passive components are more effectively fabricated in other materials that are less lossy and provide stronger electro-optic effects, such as  $\text{LiNbO}_3$ .

It is therefore very likely that the solution for large-scale integrated systems will be provided by hybrid integration, which involves two or more materials that may be bonded together. Alternatively, integrated optics may be restricted to monofunctional chips, which involve many elements of a single variety, rather than more complex multifunctional chips which include many or all varieties of components. Of course, the answer still lies with the materials technology that will be developed in the future.

Apart from the immediate needs dictated by optical communications, integrated-optics research has meanwhile directly generated a broad spectrum of other components characterized by guided light. In addition, integrated optics has played a creative role in related studies, such as wave interaction in passive and

active periodic media, which were probably stimulated by Bragg-type interactions in distributed-feedback lasers.

The great majority of the world-wide research and development activity for the past fifteen years is guided-wave optics for optical fiber communication. fifteen years On the other hand, even in the initial stages of research in fiber communications it was recognized that guided-wave technology also has potential uses in signal processing and sensing.

For processing applications, some of them can be mentioned, namely electro-optic processors (analog electro-optic processors, and analog-to-digital and digital-to-analog converters), guided-wave acousto-optic processors, fiber-optic delay lines, and hybrid processors. Similarly, for sensing purposes, some guided-wave sensors have been introduced, e.g. integrated optical sensors and integrated optical components for fiber sensors.

## CHAPTER 6 RECENT DEVELOPMENT

### 6.1 OPTOELECTRONIC INTEGRATED CIRCUITS

The monolithic integration of electronic and optical devices onto a single chip has become the focus of considerable research effort in the world. Various known component technology, the so-called monolithically integrated optoelectronics (MIO) or optoelectronic integrated circuits (OEICs), or simply integrated optoelectronic has the potential of giving a considerable boost to the sophistication and performance of existing as well as proposed advanced photonic systems. Although often confused with integrated optics, this technology is distinct from integrated optics which concerns itself primarily with the manipulation of purely optical signals. In contrast, integrated optoelectronics is an inherently hybrid technology, whereby both the photonic component (such as laser, modulator, or photodetector) coexist on the same chip as a functional electronic circuit (e.g., laser driver, or receiver preamplifier).

The starting point from which all OEIC devices must emerge is the requirements of the photonic system. There are only a few types of devices which are essential for virtually every system using optical signals, hence allowing one to concentrate on a limited number of building-block components.

To meet the requirement for the OEIC system, there are several challenges which must be met if high-quality integrated circuits are to be realized. The principal technical issues are the following:

1. The need for high-quality, low-defect-density substrates and high-uniformity epitaxial layers. In particular, InP substrates are of poorer quality and are smaller than GaAs substrates.
2. Minimization of device interaction, i.e., crosstalk – which is induced by the close proximity of photonic and electronic devices.
3. Independent optimization of material used for the photonic and electronic segments.
4. Heat removal from highly dissipative circuits.



5. Device interfacing. In addition to electrical interfacing to external circuitry, optoelectronic devices must be designed to facilitate optical interconnection to the transmission medium which might be either free space or a guiding medium such as an optical fiber.
6. Recognition of the appropriate hybrid interface. Integrated and hybrid interface points need to be identified at an early stage for each circuit attempted.

## 6.2 PROGRESS IN GaAs FOR OEIC SYSTEMS

The greatest amount of work directed toward monolithic optoelectronic integration is being pursued and is primarily focused on devices based on AlGaAs. Some examples can be mentioned, i.e.:

1. GaAs-based transimpedance amplifier with an integrated photodetector,
2. Integrated transmitter fabricated using GaAs consisting of a laser, drive circuit, and photodiode used in monitoring the total light output from the back facet of the laser ,
3. Vertical and horizontal integration scheme,
4. Hybrid 4 x 4 cross-bar switch module. The all-GaAs component has been modulated at bit rates of up to 560 Mbits/s, and represents the highest level of sophistication achieved with integrated components to date.

From those examples and some other work, it can be seen that integrated optoelectronics is achieving considerable success in the fabrication of both receivers and transmitters; at least in GaAs-based semiconductors. However, there are many applications for InP-based integrated circuits. Unfortunately, the success with this latter material system is somewhat limited in spite of its many potential applications.

## 6.3 PROGRESS IN InP-BASED FOR OEIC SYSTEMS

As discussed earlier that InP-based alloys have several advantages over GaAs-based components which make them particularly useful for monolithically integrated circuits. Some of the advantages are the following:

1. The ternary compound,  $\text{In}_{0.53}\text{Ga}_{0.47}\text{As}$  has a bandgap of 0.75 eV, and therefore can detect light at both the short wavelengths available to the GaAs-based devices (0.8 –0.9  $\mu\text{m}$ ) as well as at the long wavelengths used in long-haul optical communication systems (1.3 and 1.55  $\mu\text{m}$ ). Such a wavelength versatility is unavailable to the GaAs-based alloys.
2. InP has the largest bandgap (1.35  $\mu\text{m}$ ) of any of the alloys of InGaAsP which can be epitaxially grown onto these substances.
3. InP and  $\text{In}_{0.53}\text{Ga}_{0.47}\text{As}$  have the promise of being excellence high-frequency, high-gain transistor materials with superior room-temperature performance to that which can be achieved using GaAs.
4. Due to the very high electron peak velocity of  $\text{In}_{0.53}\text{Ga}_{0.47}\text{As}$ , this material has proven to be useful as a relatively sensitive photoconductor which can operate at moderate bit rates (<500 Mbits/s).
5. As in the case of AlGaAs/GaAs,  $\text{In}_{0.53}\text{Ga}_{0.47}\text{As}$  lattice-matched to semi-insulating  $\text{In}_{0.52}\text{Ga}_{0.48}\text{As}$  or InP can be useful in MODFET structures.

The InP-based alloy system traditionally has been utilized for long wavelength transmission systems due to the excellence transparency and low dispersion of silica fibers at 1.3 and 1.55  $\mu\text{m}$ . On the other hand, GaAs-based photonic devices have been specialized for use in local area networks (LANs) due to their low cost, and the lack of need of highly transparent transmission media for these short-haul systems. The use of two material systems for these two different applications is, in the long run, undesirable since it necessitates systems with wavelength interfaces, namely, if a LAN needs to be interconnected to a second network placed at a distance of greater than 3 km, a long-wavelength interconnect to this second network is desirable.

## 6.4 MATERIAL TECHNOLOGY

Until now we have considered the systems requirements for optoelectronic integrated circuits and how these requirement have led to the fabrication of many highly sophisticated devices. In most respects, the ability to grow the various

structures required for OEICs has been central to the progress made, as well as the limiting factor in realizing these devices.

There are essentially three basic means for growing II-V semiconductor epitaxial layers commonly used at present:

1. Molecular Beam Epitaxy (MBE): This growth technique is accomplished by vaporizing elemental sources of group III-V atoms in a high-vacuum chamber. The atomic species are then collimated into beams which are coincident on the crystalline substrate which serves as a site for epitaxial growth by adhesion of the incident atoms.
2. Vapor Phase Epitaxy (VPE): This technology has numerous forms. Of particular interest is chloride and hydride VPE, and metalorganic chemical vapor deposition (MOCVD). In VPE, the constituent group III and group V compounds are generally carried into the growth reactor in a complex molecular compounds. Once in the hot zone of the reactor, the compound dissociate, allowing the appropriate elements to condense onto the substrate. Unlike MBE, this technology can be used with equal ease to grow either GaAs- or InP-based compounds. However, with the exception of hydride VPE, it has proven difficult to grow good layers of the quaternary compound InGaAsP used in optical sources.
3. Liquid Phase Epitaxy (LPE): This is far the most common means to grow II-V compound semiconductors. This method is accomplished by bringing a substance (or seed) into contact with metallic liquids containing different concentrations of the various group III and group V elements to be used in the layer. The relative concentration of the various liquid constituents is adjusted to grow the desired composition of the solid, and thus depends on the temperature at which growth occurs. While LPE is the least expensive of the several techniques to implement, it can only give uniform growth over relatively small wafer areas (3 x 3 cm is considered large for LPE).

It has already been pointed out that OEICs place many demands on the materials growth technology. In practice, several device structures have required that layers be grown by two or more of the above methods. These hybrid

regrowths are employed such that one part of the circuit can be optimized independently of other parts of the device similar to the manner in which horizontal integration allows for the independent optimization of the electronic and photonic circuit components.

## References

1. T. Tamir (ed.): Integrated Optics, Topics in Applied Physics Vol. 7, Springer-Verlag, Berlin, 1979.
2. Joseph T. Boyd (ed.): Integrated Optics, Devices and Applications IEEE Press, New York, 1991.
3. Ronald L. Lee: Electromagnetic principles of Integrated Optics, John Wiley & Sons, New York, 1986.
4. Waryanto et al.: Near Field Characterization of LiNbO<sub>3</sub> Planar Waveguide Fabricated by Annealed Proton Exchange; MOC'99/International POF'99, 14-16 July 1999, Chiba, Japan, Post deadline paper.
5. John E. Batubara et al.: Effective Index Measurement of Propagated Modes in Planar Waveguide; Proceedings of SPIE; Design, Fabrication, and Characterization of Photonic Devices, Vol.3896, 30 Nov-3 Dec, 1999, Singapore.
6. A. Supit et al.: Reconstruction of Refractive Index Profile of Planar waveguide Using Inverse WKB Method; Proceedings of SPIE; Design, Fabrication, and Characterization of Photonic Devices, Vol.3896, 30 Nov-3 Dec, 1999, Singapore.
7. H. Susanto et al.: Application of FFT and Digital Filtering in Reconstruction of Refractive Index Profile of Surface Channel Waveguides From Near Field Intensity Pattern; Proceedings of SPIE; Design, Fabrication, and Characterization of Photonic Devices, Vol.3896, 30 Nov-3 Dec, 1999, Singapore.

# **LASER APPLICATION FOR POLLUTION MONITORING / LIDAR**

(1)

Mego Pinandito

R&D Center for  
Calibration Instrumentation Metrology,  
Indonesian Institute of Sciences

Lidar (laser radar) is an active remote sensing system using laser beam which be used to obtain such information of range, direction, size, concentration, etc.

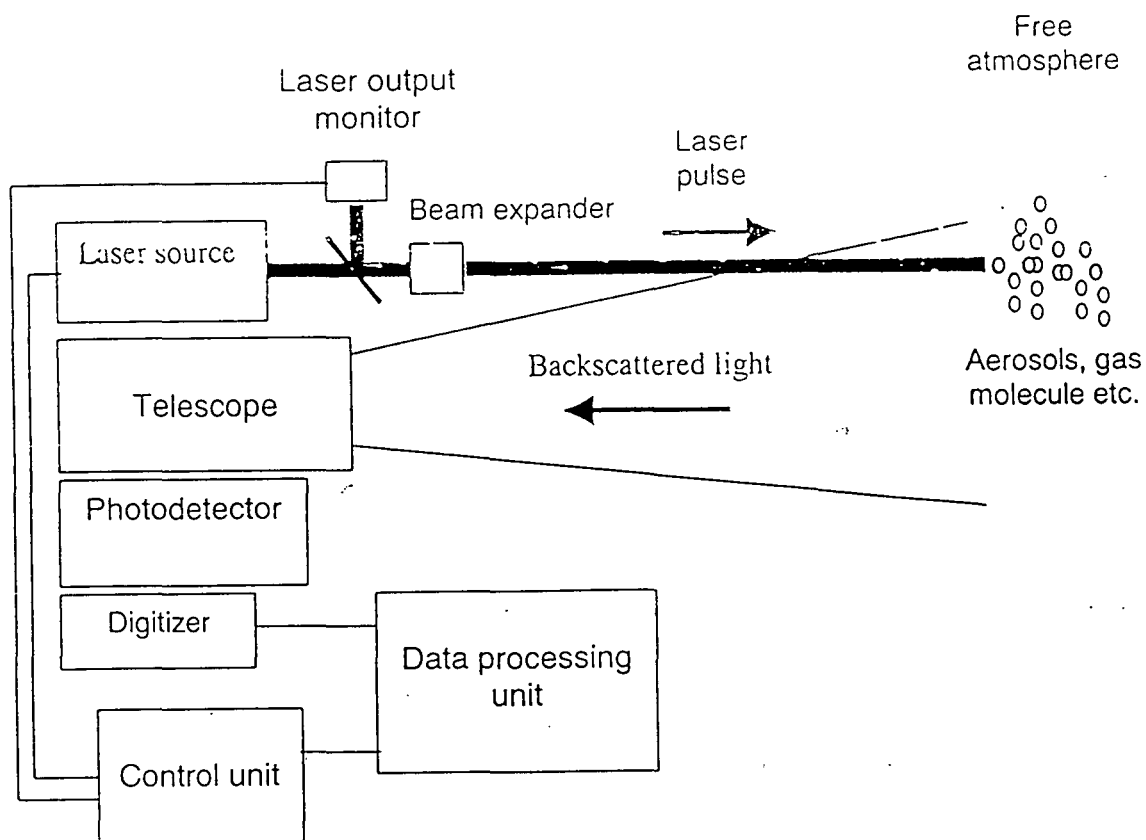
Lidar signal is determined by intensity of backscattered light from optical interaction of laser with the object.

Lidar application :

- (1) Range finder
- (2) Atmospheric environmental observation such as gas pollutants, aerosol, cloud, wind, etc.
- (3) Oceanography observation

Lidar System consists of :

- (1) Transmitter unit : laser source
- (2) Receiver unit : telescope, photodetector
- (3) Signal processor unit : digitizer, recorder



Schematic diagram of lidar system

## Optical Interaction Of Relevance To Laser Environmental Sensing

Technique	Description
Rayleigh scattering	Laser radiation <u>elastically scattered</u> from atoms or molecules is observed with no change of frequency
Mie scattering	Laser radiation <u>elastically scattered</u> from small particulates or aerosols (of <u>size comparable to wavelength</u> of laser radiation ) is observed with no change in frequency
Raman scattering	Laser radiation <u>inelastically scattering</u> from molecule is observed with a <u>frequency shift characteristic</u> of the molecule ( $h\nu - h\nu^* = E$ )
Resonance scattering	Laser radiation <u>matched in frequency to that of a specific atomic transition</u> is <u>scattered</u> by a large cross section and observed with no change in frequency
Flourescence	Laser radiation <u>matched to a specific transition of atom or molecule</u> suffers <u>absorption</u> and <u>subsequent emission</u> at lower frequency
Differential Absorption Scattering	Observe attenuation of laser beam when <u>wavelength matched to the absorption band</u> of given molecule



## Basic configuration of lidar :

- bistatic configuration : achieve spatial resolution
- monostatic : coaxial, biaxial

## Advantages of Lidar measurement :

- (1) Covered range
- (2) Minimum detecting concentration
- (3) Spatial resolution
- (4) Time resolution (accumulated signal )

## Problem considered in lidar system :

- laser source
- optical alignment
- noise

Noise :

Noise in signal	Statistical fluctuation of signal radiation
Background radiation noise	Fluctuation of background radiation
Dark current noise	Thermal generation of current carriers in the absence of an optical signal
Thermal noise	Thermal agitation of current carriers

Countermeasures of noise :

- high repetition laser
- optical shutter, optical filter
- cooling unit

## Lidar equation

When laser beam with pulse power  $P_0(\lambda)$  at wavelength  $\lambda$  is transmitted into free atmosphere, the total number of photoelectron  $P_r(\lambda)$  received from altitude  $r$  with a small range  $dr$  can be obtained by using lidar equation

$$P_r = P_0 A_0 K Y(R) \cdot (c\tau / 2R^2) \cdot \beta(R) \cdot \exp\left[-2 \int \alpha(R) dr\right]$$

where :

$P_r(\lambda)$  : received power

$P_0(\lambda)$  : transmitted power

$K$  : optical efficiency factor

$A$  : effective receiving area of telescope

$Y(R)$  : overlapping factor (overlapping between field of view of telescope and pulse laser)

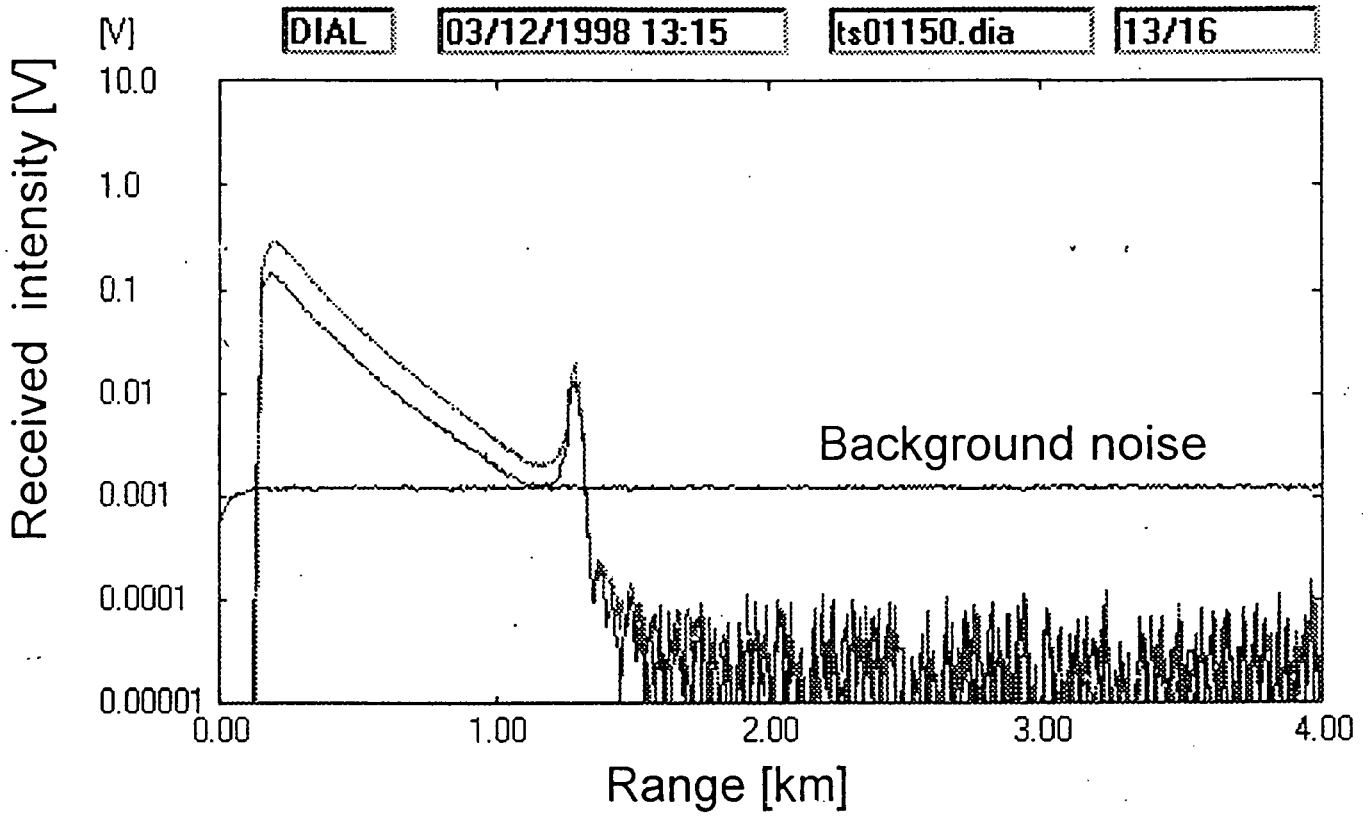
$c$  : light speed

$\tau$  : laser bandwidth

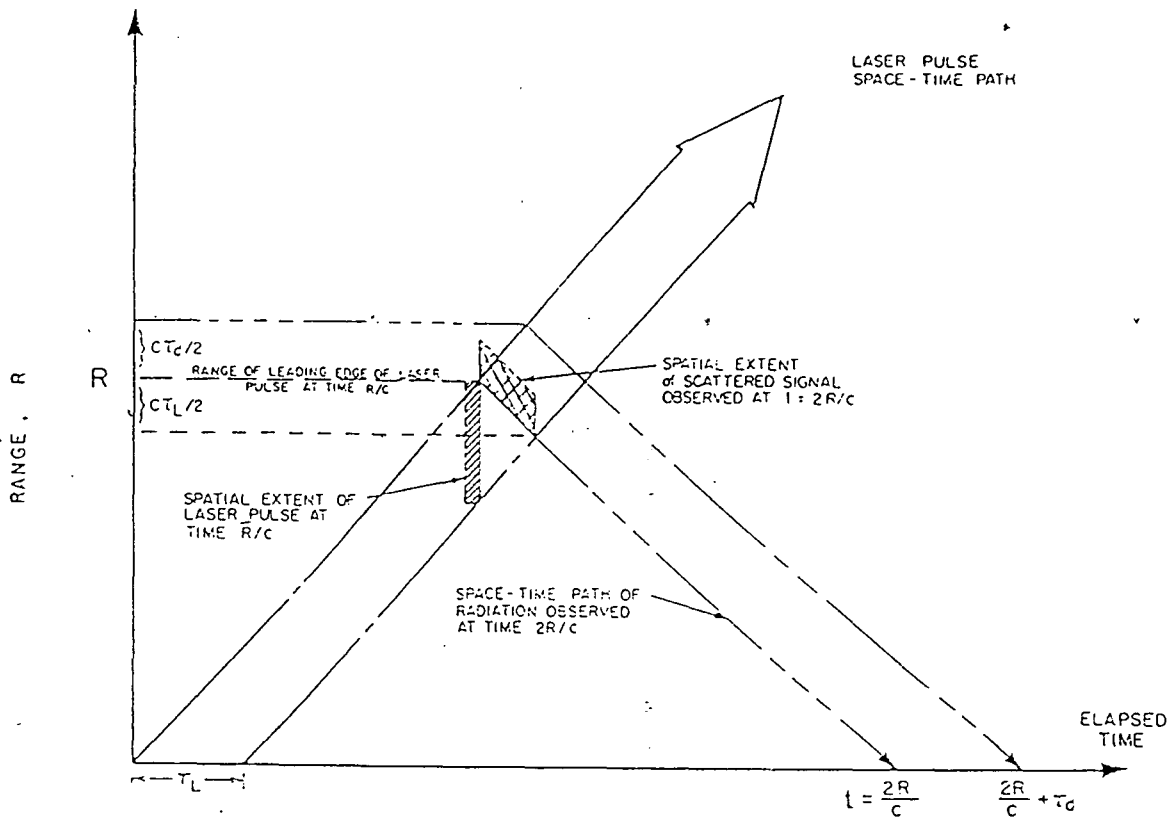
$\beta(R, \lambda)$  : coefficient volume backscattering (1/m sr)

$\alpha(R, \lambda)$  : coefficient attenuation (1/m)

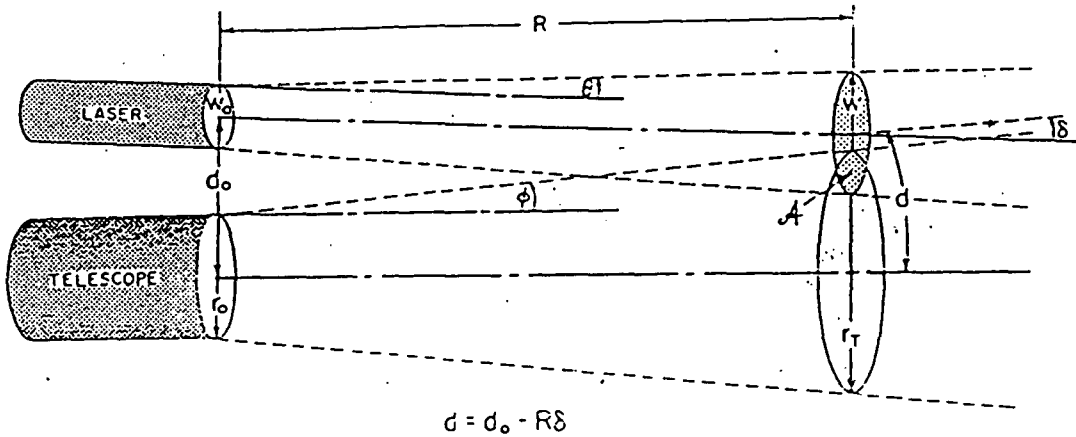
$R$  : range (m)



A-scope profile

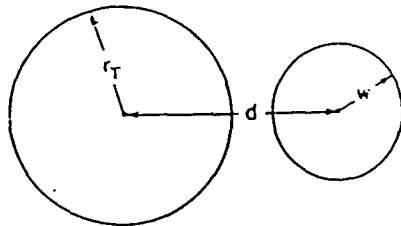


Spatial resolution for scattering phenomena as seen from the space-time diagram of a propagating rectangular-shaped laser pulse (Measures, 1977).

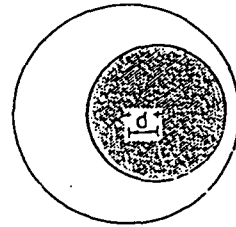


$$d = d_0 - R\delta$$

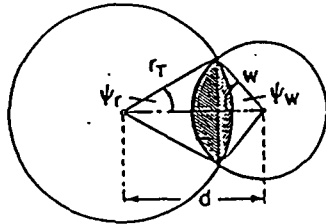
Geometry of a biaxial lidar, where the separation of the laser and telescope axes is  $d = d_0 - R\delta$  in the target plane.  $r_T$  is the radius of the circular field of view and  $W$  is the radius of the circular region of laser illumination.



(a)



(c)



(b)

Three overlap situations possible biaxial lidar.  $r_T$  is the radius of the circular field of view and  $W$  is the radius of the circular region of laser illumination.

## LASER APPLICATION FOR POLLUTION MONITORING /LIDAR (2)

Mego Pinandito

R&D Center for Calibration  
Instrumentation Metrology,  
Indonesian Institute of Sciences

1

1. Introduction
  - Background
  - Purpose
  - Approaches
2. Laser radar system
  - Lidar network system
3. Observation
4. Analysis
5. Conclusions

2

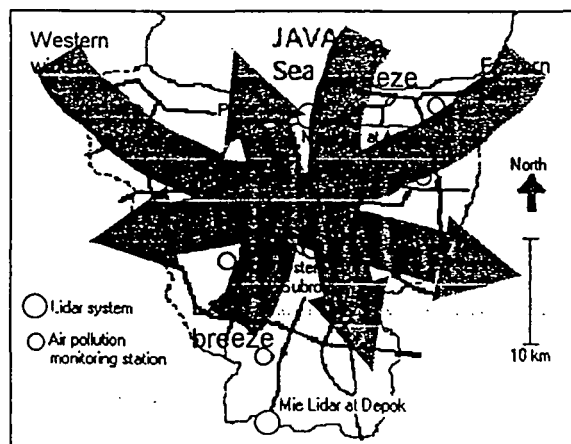
## Jakarta City (located in 6° S, 106° E)

- o High population
- o Decreasing air quality condition caused by number of cars, traffic jams, industrial sites
- o Geographical condition :
  - faces to sea in north
  - high mountain in southern
  - Equatorial region
- o Climatologically condition :
  - dry season from April to September
  - wet season from October to March in following year
  - sea/land breeze



3

## Map of Jakarta City



4



## Purposes

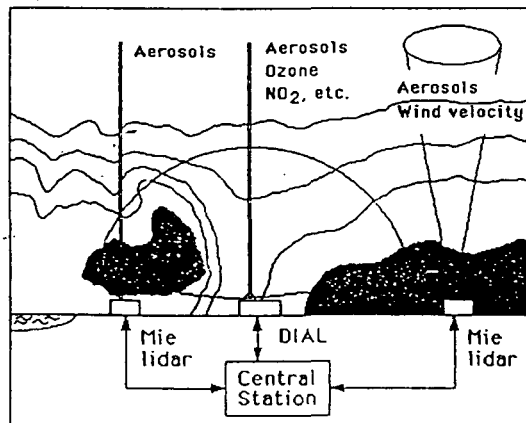
- To observe the characteristics of boundary layer structure related to air pollution, and understand the mechanism
- To measure the atmospheric structure in equatorial region in order to clarify and understand atmosphere dynamic

5

## Approaches

Concept of Lidar Network System :

- Three lidar systems in along a line perpendicular to coastal line
- Atmospheric boundary layer structures
- Atmospheric transportation mechanism



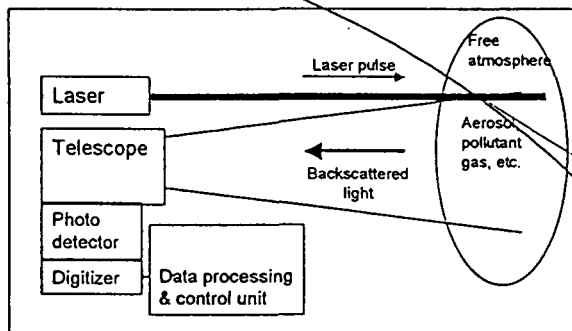
6

## Atmospheric Observation

- We have been using three lidar systems as Mie scattering lidar in different location to make aerosols measurement :
  - Boundary layer height and structures
  - Comparison between three location
  - Different characteristics between wet season and dry season
- DIAL is used for NO<sub>2</sub> and O<sub>3</sub> measurements

7

## Principles of laser radar system



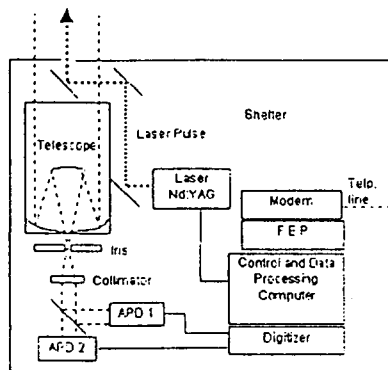
$$Pr(\lambda) = Po(\lambda) K A Y(R) (ct/2R) \beta(R, \lambda) \exp[-2 \int_0^R \alpha(R, \lambda) dr]$$

where :

- Pr( $\lambda$ ) : received power
- Po( $\lambda$ ) : transmitted power
- K : optical efficiency factor
- A : effective receiving area of telescope
- Y(R) : overlapping factor
- c : light speed
- $\beta(R, \lambda)$  : coefficient volume backscattering (1/m sr)
- $\alpha(R, \lambda)$  : coefficient attenuation (1/m)

8

## Block diagram of Mie scattering Lidar



Some challenges :

- Nd:YAG laser in wavelength 1064 nm
- Using two APDs as photo detector

9

## Specification of Mie Lidar systems

Laser	Compact flash lamp pumped Nd:YAG laser
Wavelength (nm)	1064
Output energy (mJ)	300
Pulse repetition (Hz)	10
Receiver telescope diameter (cm)	25
Field of view (mrad)	0.5 - 2
Filter bandwidth (nm)	9
Detector	Si Avalanche photodiode (APD)
Analog to digital converter (ADC)	
Sampling rate (Msamples/s)	20
ADC accuracy (bits)	12
Measurement mode	Vertical

10

## Photographs of Mie Scattering Lidar Systems



Mie Lidar 1

Mie Lidar 1 is installed in Depok

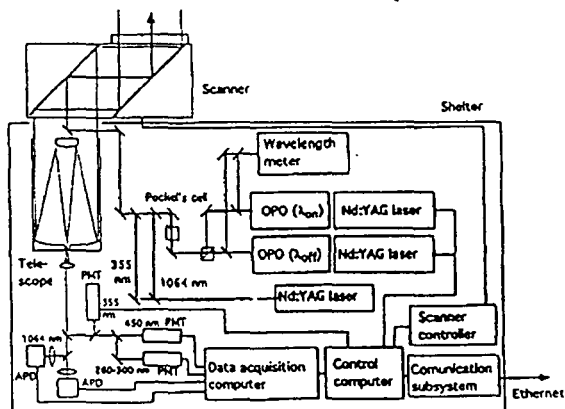


Mie Lidar 2

Mie Lidar 2 is installed in Ancol

11

## Block diagram of DIAL system



• OPO as tunable laser (change to solid state)

12

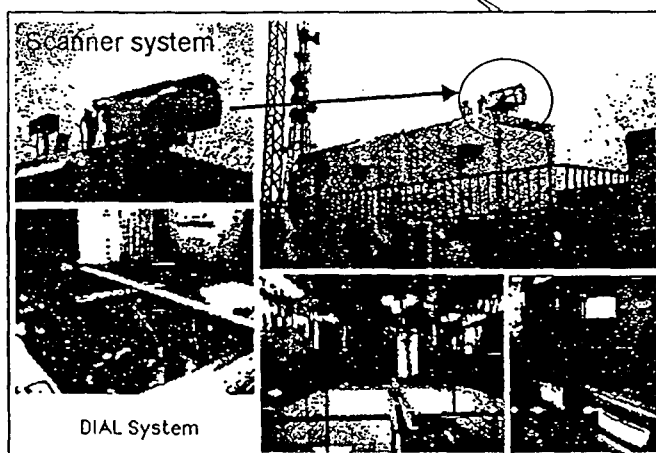
## Specification of Differential Absorption Lidar

Lasers	Nd:YAG laser pumped OPO (DIAL mode) Compact Nd:YAG (Mie lidar mode)			
Target	O <sub>3</sub>	SO <sub>2</sub>	NO <sub>2</sub>	Aerosol
Wavelength(nm)(on/off)	280.0/285.0	300.05/299.50	448.1/446.6	1064
Differential absorption cross section (m <sup>2</sup> )	2.0x10 <sup>-22</sup>	9.8x10 <sup>-22</sup>	2.2x10 <sup>-23</sup>	-
Output energy (mJ)	10	10	50	100
Pulse repetition (Hz)			20	10
Receiver telescope diameter (cm)			25	
Receiver field of view (mrad)			0.5 - 2	
Detector	Photomultipliers (DIAL)		APD (Mie at 1064 nm)	
Analog to digital converter(ADC) sampling rate (Msamples/s)			20	
ADC accuracy (bits)			12	
Scanner	Two mirror two axes scanner			
Measurement mode	scan / vertical			

13

## Photographs of DIAL system

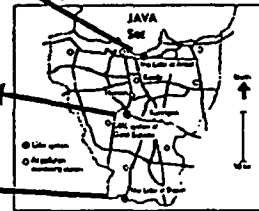
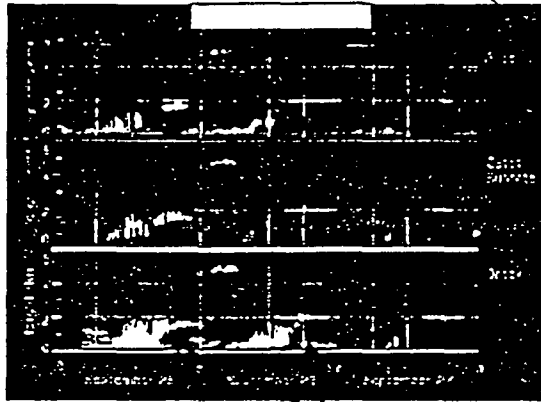
Dial System is installed in top of LIRI Headquarter Building  
(approx. 40 m height) in Gatot Subroto (central of Jakarta City)



14

## Aerosols measurement

Diurnal variation of boundary layer structure measured in Ancol, Gatot Subroto and Depok simultaneously

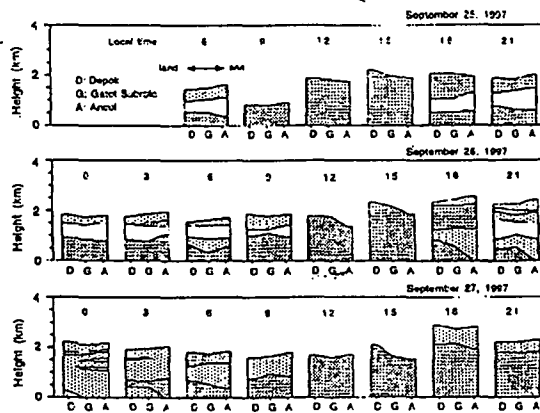


Sea breeze front

- Maximum boundary layer height is higher at inland locations
- Boundary layer structure at nighttime is lower at inland

15

## Comparison between three location



- Aerosol distributions near surface were complicated
- Sea breeze velocity of 5 m/s obtained from lidar data agreed qualitatively with the wind speed measured with radiosonde.

16

## DIAL measurement

Distribution of  $\text{NO}_2$  measured using DIAL system with scanning mode.



Distribution of  $\text{NO}_2$

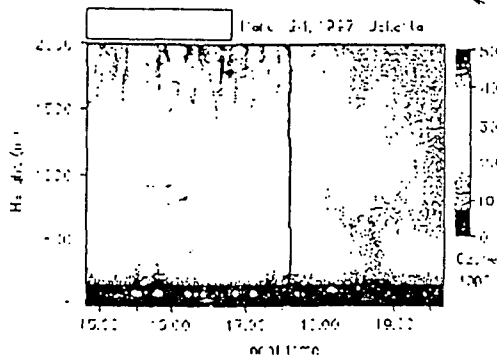
The direction angle of scanner was from 270-360 degree with elevation angle of 20 degree.

High concentration of  $\text{NO}_2$  is observed above the road.

17

## DIAL measurement

Temporal variation of  $\text{O}_3$  vertical profile measured using DIAL system in March 24, 1997



A relatively high concentration of  $\text{O}_3$  probably formed by photochemical reaction was observed in the atmospheric boundary layer. Clean air came at about 18:00 LT with a sea breeze

18

## Conclusions

- Lidar network consisting of three lidars at different locations, have been used successfully in monitoring the atmospheric environment in Jakarta.
- The continuous measurement have given number of data of aerosol vertical profile, pollutant gasses.
- The results show the structure of atmospheric boundary layer which is closely related to air pollution phenomena, structure of lower atmosphere layer, atmospheric transportation mechanism.
- The different characteristics between wet and dry season and the effect of global phenomena was observed.
- These information are very important and needed for further study on the global atmospheric environment observation.



## PROCESSING TECHNOLOGY OF SEMICONDUCTOR LASER\*

By

Sekartedjo\*\*

---

\* Regional Workshop on Lasers and Optoelectronics, June 25<sup>th</sup> to July 6<sup>th</sup>,  
Komplek Puspiptek Serpong, Tangerang, Indonesia.

\*\* Engineering Physics Department, Institute of Technology Sepuluh November  
Surabaya, Indonesia.

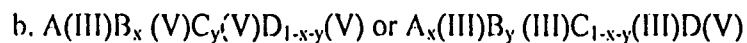
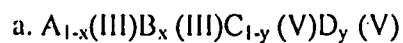
Address : Kampus ITS Keputih, Sukolilo, Surabaya 60111, Indonesia.

E-mail : [tekfis@rad.net.id](mailto:tekfis@rad.net.id) and [sekar@telkom.net](mailto:sekar@telkom.net)

## 1. Introduction.

Semiconductor lasers are widely used in various fields such as communication, instrumentation, optical data processing, multi media apparatus, medical, etc.

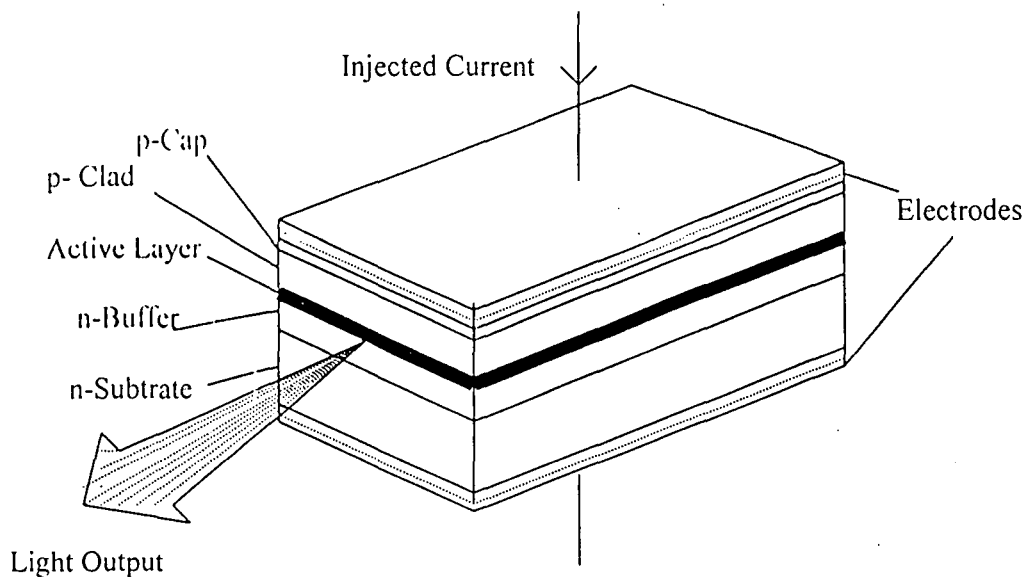
As other types of lasers, basic structure of semiconductor lasers consist of an active medium that generates light when pumping process is done and a resonant cavity for feedback mechanism. III-V and II-VI semiconductor alloys are considered to be suitable materials for ultra high speed microwave devices and also for high performance semiconductor lasers as light sources in large-capacity optical communication systems. A semiconductor laser with the desired wavelength can be obtained using ternary or quaternary alloys of III-V compound materials. Generally, quaternary alloys can be divided into two types :



The properties of the first type are basically the same as of the mixture of ternary compound and also, a ternary alloy can be thought of as a mixture of binary compounds. On the other hand, the properties of the second type are the same as those of a pseudo-ternary alloy. The double heterostructure contains a narrow band gap, active layer, sandwiched between large band-gap semiconductors. It shows important function as a waveguide by confining carriers in the active layer or resonator. In quaternary crystal, such as GaInAsP, both the lattice constant and the band-gap energy can easily be changed to suit the requirements. The wavelength of emitted light would be depending on the energy gap resulted from the double heterostructure according to the formula :

$$\lambda (\mu\text{m}) = 1.2398/E_g[\text{eV}]$$

A typical basic structure of a semiconductor laser is shown in the figure belows  
The improvement of diode laser's structure can be stressed on some aspects such as the double heterostructure's material composition, carrier and optical wave guiding mechanism, resonance cavity structure, facets structure, pumping schemes, etc.



Typical structure of Diode Laser

The optical resonator commonly consists of a waveguide and two mirror facets or corrugated structure. The above laser structure is changing in accord with the development of its varying fields of application, especially in optical communication and integrated optical circuit. The terms such as stripes lasers, index guided laser, short cavity laser, distributed feedback (DFB) laser, distributed Bragg reflector (DBR) laser, tunable laser, surface emitting laser, quantum well laser showing various types of lasers with different modified functional structures. It should be noted that the diode laser or integrated laser could be a part of more complicated structure such as optoelectronics integrated circuit (OEIC).

The fabrication process of semiconductor lasers are commonly consists of several techniques, i.e. : substrate and material preparation, crystal growth, photolithography, etching, metallization and their characterizations. These techniques will be described briefly. More detail descriptions would be discussed in the time of discussion.

## 2. Elements of Semiconductor Laser Processing Techniques.

### a. Substrate and material preparations.

A substrate is a semiconductor crystal on which the layers with double heterostructure are formed. GaAs and InP crystals are commonly used for optical devices. The (001) oriented substrate is displayed while (011) or (01 $\bar{1}$ ) cleaved facets are used as laser mirrors. The residual imperfections of the crystal could be checked from *etch pits* appeared on the etched surface. The etchant could be used for this purpose is  $\text{HF} : \text{CrO}_2 + \text{H}_2\text{O} = 2 : 1$ . The EPD (Etch Pits Density) represent the number of etch pits per square centimeters. The EPD spatial distribution on the substrate is varies according to the crystal growth technique. The popular dopants for n-type and p-type GaAs substrates are Si and Zn, respectively. For InP substrates, S or Sn are commonly used for n-type dopants and Zn is a p-type dopant. The substrates with 2 or 3 inches in diameter and about 350  $\mu\text{m}$  thick are commercially available.

### b. Epitaxial Techniques.

There are several techniques can be used for growth of epitaxial layers, i.e. Liquid Phase Epitaxy (LPE), Vapor Phase Epitaxy (VPE), Metal-Organic Chemical Vapor Deposition (MO-CVD), Molecular Beam Epitaxy (MBE) and Chemical Beam Epitaxy (CBE). In the LPE process, the solutes and the solvent materials are heated up to high temperature and after the soak and the cooling process with controlled rate the solution is melted to the substrate at a certain temperature and time. There are four schemes of epitaxial process according to the method cooling used to generate supersaturation in the solution, i.e. step cooling, equilibrium cooling, super-cooling and two phase solution. The VPE or CVD technique enables crystal growth from materials in the vapor state. The MO-CVD is one of the most advanced growth technique of vapor phase epitaxy and used to grow very thin layer or quantum well structure on the substrate. The metal-organic material used in this system such as TMG, TEG, TMA, TEA and TEP have a fairly high vapor pressure. MBE is an ultra low pressure process ( $\sim 10^{-10}$

Torr) in which beam like molecules of several kinds of materials leave the heated effusion cells and impinge on the heated substrate. Crystalization can be controlled by the shutters in front of the effusion cells, allowing an extremely abrupt transition layer as narrow as several Angstrom. The CBE equipment is similar to the MBE equipment except that gaseous materials are used entirely. Molecules of materials which are resolved at a high temperature reach a substrate and begin to grow. As a compensation method for the disadvantages of MBE, CBE is effective especially for GaInAsP system.

#### c. Lithography

Lithography is a process transferring geometric shapes on a mask to the surface of a wafer. A mask pattern is first transferred to the resist layer which is coated uniformly on a wafer surface with a thickness of a few tenths to one micrometer. For the transfer, UV light (photolithography), electron or ion beam (electron or ion beam lithography) or X-rays (X-ray lithography) could be used. Electron and ion beams also provide a feasible means of direct pattern delineation without using a mask by scanning a focused beam using computer control. Resists are typically radiation-sensitive organic materials such as AZ 1350 (photoresist) or PMMA (electron or X-ray resist) and produce negative or positive images. Positive resist becomes soluble to a developer solvent upon exposure to the radiation, negative resist is the opposite. A mask pattern is supported on a millimetre thick glass or quartz substrate for photolithography masks and on a few-micron-thick membrane for X-ray and ion beam lithography.

#### d. Etching Techniques.

The etching is a transferring process of mask pattern onto the material surface. There are two kinds of etching techniques, i.e. *wet etching* and *dry etching*. In wet etching, the transfer process is done by using *etchant*, a chemical solution which solute the substrate material. The etching process is preferably anisotropic since isotropic characteristic would make pattern

damages as a result of *undercuts*. In many cases, the etching of crystalline materials is in fact selective, depending on the material, its composition or its crystal orientation. Such selective etching is very useful for heterostructure system, for example for the fabrication of etched facet laser mirror, of buried structure active waveguides or of various passive waveguides, gratings and other photonic integrated elements. It is also useful for determining the crystal orientation, or the position of *p-n* junction or a heterojunction interface. There are various etchants have been developed for GaAs and InP. Since the wet etching techniques accuracy is depending upon material and crystal orientation, higher accuracy could be obtained by dry etching techniques which make use of sputtering and plasma or ion beam enhanced chemical reactions. Increase of etching selectivity or etching rate can be achieved by reactive ion etching (RIE) or reactive ion beam etching (RIBE), which uses a reactive gas and chemical reactions as well as sputtering. For IBE and RIBE, the etching is anisotropic and precise pattern fabrication can be done.

**e. Metallization.**

Metallization is a process of electrodes fabrication on the p-side and n-side of double heterostructure. The common material used for GaInAsP/InP is Au/Zn for p-side and Au/Sn for n-side. In order to improve the ohmic contact characteristic, Zn diffusion process is commonly used in the metallization process.

**f. Process Characterizations.**

The quality of each process in semiconductor laser fabrication should be accurately observed. The quality of crystal growth could be checked by SEM (Scanning Electron Microscope) for smoothness and size, X-ray diffractometer for lattice matching condition and photoluminescence measurement for light spectrum generated by double heterostructure materials. The quality of photolithography and etching processes is checked by optical microscope and SEM. The ohmic contact is checked by

measurement of V-I curve and light-current (I-L) device characteristic is observed by electrical pumping.

### **3. An Example, Fabrication of the Dynamic Single Mode Laser.**

A Dynamic Single Mode Laser is a type of laser that emitting light with single modes characteristic. i.e. single transverse mode and single longitudinal mode. These characteristics are obtained by the use of grating and narrow active stripes in the laser structure. This type of laser is required for high capacity, long distance optical fiber communication. The improved Distributed Feedback (DFB) and Distributed Bragg Reflector (DBR) lasers are the common examples. The procedure of fabrication of GaInAsP/InP DFB laser is described as follows :

1. Cut the n-InP substrate using surgery knife or saw according to the size of carbon boat substrate mount in the reaction tube of LPE system.
2. Clean the substrate using methanol, acetone, trichloroethylene, acetone and methanol (MATAM) successively. . Slight Br-methanol etching is sometimes used to improve surface smoothness.
3. Grow the epitaxial double heterostructure layers by LPE method. The layers are n-InP buffer layer, GaInAsP active layer, p-InP clad layer and p-GaInAsP cap layer, respectively. The soak temperature, cooling rate and growth temperature of active layer are typically 600°C; 0,7°C/min. and 590°C, respectively. Weight of source materials (In, InP, GaAs, InAs) and dopants (Te/In and Zn/In) are varied according to the required energy gap of band structure. . Growth quality is checked by SEM and lattice mismatch by X-ray diffractometer.
4. Do the SiO<sub>2</sub> stripes masking using SiO<sub>2</sub> CVD, photolithography and selective etching to obtain narrow active stripes in the <011> direction.
5. Use interferometry method using He-Cd laser and wet etching to obtain corrugated structure in <01 $\bar{1}$ > direction.

6. Grow the *blocking layers* consists of p-InP layer, n-InP layer and p-InP layer using LPE method.. LPE's schedule and the weight of source materials are determined according to the required layers structure.
7. Make the p-electrode (Au-Zn) on the stripes and n-electrode (Au-Sn) on the n-side of substrate using photolithography, selective etching and evaporation methods. Zn-diffusion is often used for improving the ohmic contact.
8. Cut the wafer into pieces by surgery knife or saw and check device characteristics by V-I, I-L and light spectrum measurements. The transverse modes can be checked by near field and far field pattern measurements.

#### 4. Closing Words

The elements of semiconductor lasers processing have been described briefly. Degree of fabrication process complexity would be depending on the number and size of functional structures and the choice of processing method based on the availability of apparatus..

#### Bibliography.

1. H.C. Casey and M.B. Panish, Heterostructure Lasers – part A & B, Academic Press, 1978.
2. K.Iga and S. Kinoshita, Procees Technology for Semiconductor Lasers, Springer-Verlag Berlin Heidelberg, 1996.
3. Y.Suematsu and A.R. Adams (Ed.), Handbook of Semiconductor Lasers and Photonic Integrated Circuit, Chapman & Hall, 1994.
4. J. Singh, Optoelectronics – An Introduction to Material and Devices, McGrawHill Inc., 1996.
5. Sekartedjo, Lasing Characteristics of Dynamic Single Mode Lasers, Thesis Disertation, 1981.



# **Interferometry by Holography and Speckle**

Ichirou Yamaguchi

Optical Engineering Laboratory,

RIKEN(The Institute of Physical and Chemical Research),

Wako, Saitama 351-0198, Japan

\*Correspondence: Email: [ichiyama@postman.riken.go.jp](mailto:ichiyama@postman.riken.go.jp); Telephone: +81 48 462 1111 ex.3241;  
Fax: +81 48 462 4653

## **ABSTRACT**

Basic principles and surveys are presented on automatic and quantitative deformation measurements using mainly CCD's and computers in holographic interferometry and speckle metrology for diffusely reflecting surfaces. For delivering relationships between object deformation and observed quantities we discuss formations of fringes and signals observed in these methods in terms of correlation functions of spatially randomly varying complex amplitude of light. Dependencies of the observed patterns on object deformation and optical systems are discussed. Physical meanings of the derived relationships are explained in terms of the dynamic behaviors of speckles resulting from surface deformation. Automatic measurements are described in chronological orders. They include analysis of fringe patterns resulting from photographic recording of specklegrams, video recording and analysis of speckle patterns used in ESPI as well as direct digital correlation techniques, and digital holography that uses both digital recording and reconstruction of holograms.

**Keywords:** Interferometry, holography, speckle, image processing, shape measurement, deformation measurement

## 1. INTRODUCTION

Holographic interferometry and speckle techniques made it possible to measure surface shape and/or deformation of diffusely reflecting surfaces with interferometric sensitivity. Advantages of these techniques are well-known and it is now desired to establish quantitative and automatic measurement using CCD cameras and computers. This effort started from electronic speckle pattern interferometry (ESPI) that produces fringe patterns by superposition of video speckle images. Automatic analysis of the resulting fringe patterns as well as those obtained from photographic recording of holograms and speckle patterns were also developed. Although digital fringe analysis has been successful for the fringe patterns observed from mirror surfaces (Schwider [1]), some problems arose in the case of those obtained from diffusely reflecting surfaces leading to speckle noise. However, speckles also constitute the fringe patterns which are observed in holographic and speckle interferometry and whose contrast is governed by dynamic behaviors of speckle caused by surface deformation (Yamaguchi [2]). These dynamic behaviors consisting of displacement and decorrelation can be described in terms of cross-correlation function of intensity distribution (Yamaguchi [3]). Speckle displacement was first used in speckle photography where Young fringes arising from optical Fourier transformation of doubly exposed negatives are observed. The fringes, always straight and periodic, are very suited for automatic analysis (Kaufmann [4]). Advances in microcomputers and linear image sensors enabled direct calculation of cross-correlation function that could be used for real-time measurement of translation, rotation, and strain (Yamaguchi [3]). More recently speckle patterns were recorded with a matrix CCD followed by a computer which calculates 2-D cross-correlation of subimages to deliver distribution of speckle displacement (Yamaguchi [3], Sjö Dahl [5]). Recent advances of computers and CCD's finally realized digital recording of holograms and computer reconstruction as called digital holography (Kreis [6]). It also strengthens the performance of conventional imaging

systems. In this paper we discuss fringe formation in the above methods to show how CCD cameras and computers have been introduced in holography and speckle metrology.

## 2. CORRELATION PROPERTIES OF SCATTERED LIGHT

All the quantities observed in holographic interferometry and speckle metrology that are applied to diffusely reflecting surfaces are expressed in terms of correlation functions of their complex amplitude or intensity (Yamaguchi [2],[3],[7]). Here we describe the functions for linear transmission system that includes both free-space geometry and imaging system. We assume first the linear system shown in Fig.1. The complex amplitude at the observation point  $R(X,Y)$  can be represented by a linear superposition of the complex amplitude arising from each point of the object. Hence the complex amplitudes before and after object deformation that is expressed by a distribution of displacement  $a(r)$  are represented by

$$U_1(\mathbf{R}) = \iint \sqrt{I_0(\mathbf{r})} \exp[i\phi(\mathbf{r})] \exp[ikL_S(\mathbf{r})] K(\mathbf{R};\mathbf{r}) d^2\mathbf{r} \quad (1)$$

and

$$U_2(\mathbf{R}) = \iint \sqrt{I_0(\mathbf{r} + \mathbf{a}_T)} \exp[i\phi(\mathbf{r} + \mathbf{a}_T)] \exp[ikL_S(\mathbf{r} + \mathbf{a})] K(\mathbf{R};\mathbf{r} + \mathbf{a}) d^2\mathbf{r}, \quad (2)$$

where  $I_0$  means the intensity distribution at the object,  $\exp(i\phi)$  the microscopic reflection function related to surface roughness,  $L_S$  the radius of curvature of the beam incident on the object,  $\mathbf{a}_T$  in-plane displacement, and  $K(\mathbf{R};\mathbf{r})$  the transmission function that means the complex amplitude to be generated at an observation point  $\mathbf{R}$  by a point source placed at the object point  $\mathbf{r}$ . The transmission function can be represented by a parabolic wave in the case of free-space geometry and the Fresnel diffraction at the lens aperture in the case of imaging configuration. The cross-correlation of the complex amplitude is defined as an ensemble average of the product of the complex amplitude at the point  $\mathbf{R}$  and  $\mathbf{R} + \bar{\mathbf{R}}$  that can be derived finally as

$$\langle U_1(\mathbf{R})U_2^*(\mathbf{R}+\bar{\mathbf{R}}) \rangle = \iint \sqrt{I_0(\mathbf{r})I_0(\mathbf{r}+\mathbf{a}_T)} \exp[ik\mathbf{l}_S(\mathbf{r}) \cdot \mathbf{a}(\mathbf{r})] K(\mathbf{R};\mathbf{r})K^*(\mathbf{R}+\bar{\mathbf{R}};\mathbf{r}+\mathbf{a})d^2r \quad (3)$$

where we assumed a sufficiently short correlation distance of the microscopic reflection function. The  $\mathbf{l}_S$  in this equation means the unit vector directed from the object point to the point source. The cross-correlation function of complex amplitude depicts the spatial fluctuation of complex amplitude reconstructed in holography. Intensity cross-correlation that describes dynamic behavior of speckles due to surface deformation is related to the cross-correlation of complex amplitude through the equation

$$\langle I_1(\mathbf{R})I_2(\mathbf{R}+\bar{\mathbf{R}}) \rangle = \langle I_1(\mathbf{R}) \rangle \langle I_2(\mathbf{R}+\bar{\mathbf{R}}) \rangle + \left| \langle U_1(\mathbf{R})U_2^*(\mathbf{R}+\bar{\mathbf{R}}) \rangle \right|^2, \quad (4)$$

if sufficiently many independent scattering centers contribute to the complex amplitude to guarantee the Gaussian random process. The second term on the right-hand side is equal to the cross-correlation of intensity fluctuation

$$\Delta I(\mathbf{R}) = I(\mathbf{R}) - \langle I(\mathbf{R}) \rangle \quad (5)$$

in such a way that

$$\langle \Delta I_1(\mathbf{R})\Delta I_2(\mathbf{R}+\bar{\mathbf{R}}) \rangle = \left| \langle U_1(\mathbf{R})U_2^*(\mathbf{R}+\bar{\mathbf{R}}) \rangle \right|^2. \quad (6)$$

In the whole-field measurement of displacement we observe interference fringes appearing on an image of the object. Hence for the transmission system we now consider the imaging system as shown in Fig.2. The object is imaged on to the observation plane by a lens system. The transmission function  $K(\mathbf{R},Z;\mathbf{r}+\mathbf{a})$  for this geometry is given by the Fresnel diffraction of the lens aperture with the pupil function  $P(\mathbf{s})$ .

After substitution of the transmission function and manipulation the cross-correlation of the complex amplitude proves to have the magnitude

$$\left| \langle U_1(\mathbf{R}, Z) U_2^*(\mathbf{R} + \bar{\mathbf{R}}, Z) \rangle \right| = \left| \iint P^*(s) P(s + A_p) \exp \left\{ ik \frac{s}{L_o + Z} \cdot [\bar{\mathbf{R}} - A(\mathbf{R}, Z)] \right\} d^2s \right|, \quad (7)$$

where

$$A_p = L_o \left\{ \nabla [l_s(\mathbf{r}) + l_o(\mathbf{r})] \cdot \mathbf{a} \right\}_{r_R} \quad (8)$$

means the speckle displacement at the pupil plane and is associated with the gradient of object displacement along the bisector between the source and the observation directions at the object point  $r_R$  conjugate to the observation point. The cross-correlation given by Eq.(7) takes the maximum for  $\bar{\mathbf{R}} = A$  that means the speckle displacement at the observation plane and has the components

$$A_X = ma_x - \frac{Z}{L_o} \left\{ ma_x - a_x \left( \frac{L_o \cos^2 \theta_s}{L_s} + 1 \right) + a_z \frac{L_o \cos \theta_s \sin \theta_s}{L_s} + L_o [\varepsilon_{xx} \sin \theta_s - \Omega_y (\cos \theta_s + 1)] \right\} \quad (9)$$

and

$$A_Y = ma_y - \frac{Z}{L_o} \left\{ ma_y - a_y \left( \frac{L_o}{L_s} + 1 \right) + L_o [\varepsilon_{xy} \sin \theta_s - \Omega_x (\cos \theta_s + 1) - \Omega_z \sin \theta_s] \right\}, \quad (10)$$

where  $q_s$  is the angle of incidence,  $m=L_o/L_o'$  the imaging magnification, and  $(a_x, a_y, a_z)$ ,  $(W_x, W_y, W_z)$ , and  $(e_{xx}, e_{xy}, e_{yy})$  mean translation, rotation, and strain of the region around the point  $r_R$ , respectively. Equation (7) implies that speckle decorrelation in the image field depends on the speckle displacement  $A_p$  ( $A_{px}, A_{py}$ ) at the pupil plane as compared with the pupil diameter. It is also accelerated by lens aberration that is represented by the phase of the pupil function  $P(s)$ .

### 3. HOLOGRAPHIC INTERFEROMETRY

In usual holographic interferometry the complex amplitudes before and after object deformation are superposed in the image field of the object as shown in Fig.3. The fringe intensity averaged over speckles is given by

$$\begin{aligned} \langle I(\mathbf{R}, Z) \rangle &= \langle |U_1(\mathbf{R}, Z) + U_2(\mathbf{R}, Z)|^2 \rangle = \langle I_1(\mathbf{R}, Z) \rangle + \langle I_2(\mathbf{R}, Z) \rangle \\ &\quad + 2 \Re \langle U_1(\mathbf{R}, Z) U_2^*(\mathbf{R}, Z) \rangle \end{aligned} \quad (11)$$

where  $U_1$  and  $U_2$  mean the complex amplitude before and after object deformation. The averaging is carried out mathematically over a statistical ensemble of the microscopic structure of the object and physically over an area much larger than speckle size and smaller than fringe spacing. This expression can be deformed into

$$\langle I \rangle = 2\langle I_0 \rangle \left\{ 1 + \gamma \cos[k(l_s + l_o) \cdot a + \alpha] \right\}, \quad (12)$$

where we have assumed  $\langle I_0 \rangle = \langle I_1 \rangle = \langle I_2 \rangle$ . The fringe pattern means the contour lines of the displacement component along the bisector between the direction of the illumination source and that of observation. The fringe pattern has the complex contrast given by

$$\gamma \exp(i\alpha) = \langle U_1(\mathbf{R}; Z) U_2^*(\mathbf{R}; Z) \rangle / \langle I_0(\mathbf{R}; Z) \rangle. \quad (13)$$

If we consider Eq.(7), the visibility becomes

$$\gamma = \left| \iint P^*(s) P(s + A_p) \exp\left\{ -ik \frac{s \cdot A(\mathbf{R}, Z)}{L_o + Z} \right\} d^2s \right| / \left| \iint |P(s)|^2 d^2s \right|. \quad (14)$$

We further assume that the speckle displacement at the aperture is much smaller than the pupil diameter as to make the speckle decorrelation negligible. This assumption also means that the fringe spacing is much larger than the resolution limit of the imaging system. Then we obtain the contrast represented by

$$\gamma = \left| \iint |P(s)|^2 \exp\left\{ -ik \frac{s \cdot A(\mathbf{R}, Z)}{L_o + Z} \right\} d^2s \right| / \left| \iint |P(s)|^2 d^2s \right| = \sqrt{C(A; Z) C(0; Z)}, \quad (15)$$

where the function  $C(\mathbf{R}; Z)$  means the autocorrelation of the intensity fluctuation given by

$$C(\bar{\mathbf{R}}; Z) = \langle \Delta I(\mathbf{R}; Z) \Delta I(\mathbf{R} + \bar{\mathbf{R}}; Z) \rangle = \left| \iint |P(s)|^2 \exp\left( -ik \frac{s \cdot \bar{\mathbf{R}}}{L_o + Z} \right) d^2s \right|^2, \quad (16)$$

whose width indicates the mean speckle size. Equation (15) means that the fringe visibility is nearly equal to unity when the speckle displacement is much smaller than the mean speckle size as illustrated in Fig.3. In that case the random phase differences between different speckles are canceled out to generate fringes representing the contours of displacement. The plane where  $A(R,Z)$  vanishes corresponds to the plane of fringe localization. When speckle displacement approaches the mean size, however, the visibility drops to zero. If the fringes become denser owing to increase of displacement gradient, the decorrelation caused by speckle displacement at the aperture also accelerates reduction of the visibility.

#### 4. SPECKLE INTERFEROMETRY

Speckle size in the image field can be adapted to resolution of recording media by adjusting the aperture diameter. In electronic speckle pattern interferometry (ESPI) speckle patterns formed by interferometric setups are recorded by a CCD camera, subtracted from the initial pattern, and squared by video circuits or a computer to display contour lines of object displacement. An arrangement used for measurement of out-of-plane displacement is shown in Fig.6. The displayed brightness is proportional to

$$V_S = \langle (I_{S1} - I_{S2})^2 \rangle = \langle I_{S1}^2 \rangle + \langle I_{S2}^2 \rangle - 2\langle I_{S1}I_{S2} \rangle, \quad (17)$$

where the intensities recorded by the CCD camera are given by

$$I_{S1} = |U_1 + U_R|^2, \quad I_{S2} = |U_2 + U_R|^2 \quad (18)$$

with the complex amplitude of the reference light arising from a fixed reference mirror. The averaging in Eq.(17) is physically carried out by the low-pass filter. Substitution of Eq.(18) into Eq.(17) yields

$$V_S = 2\left( \langle I_0 \rangle^2 + 2\langle I_R \rangle \langle I_0 \rangle - 2\langle I_R \rangle \Re \langle U_1 U_2^* \rangle - \langle |U_1 U_2^*|^2 \rangle \right), \quad (19)$$

where we considered the statistical independence between the reference amplitude  $U_R$  and the object amplitudes  $U_1$  and  $U_2$  at the image plane  $Z=0$ . The third term in the right-hand side of this equation represents the fringe pattern that is the same as that derived in Eq.(11) for holographic interferometry where we set  $Z=0$ .

Speckle interferometry is also used for contouring of in-plane displacement that cannot be directly performed by holographic interferometry. In the dual-beam method shown in Fig.5 and the double-aperture methods shown in Fig.6 the reference beam is not used and the object beam is divided into two paths and superposed on each other .

$$I_{S1} = |U_{a1} + U_{b1}|^2, \quad I_{S2} = |U_{a2} + U_{b2}|^2 \quad (20)$$

where  $a$  and  $b$  stand for dual illumination beams or each of the double aperture. Taking the statistical independence between the object waves arising from different illumination waves or transmitted through different apertures, we have the final representation of the fringe pattern

$$V_S = 2 \left[ 4 \langle I_a \rangle^2 - 2 \Re \left( \langle U_{a1} U_{a2} \rangle \langle U_{b1} \rangle \langle U_{b2} \rangle \right) - \langle U_{a1} U_{a2} \rangle^2 - \langle U_{b1} U_{b2} \rangle^2 \right] \quad (21)$$

whose second term in the right-hand side can be represented by

$$\Re \left( \langle U_{a1} U_{a2} \rangle \langle U_{b1} \rangle \langle U_{b2} \rangle \right) = \gamma_a \gamma_b \langle I_a \rangle \langle I_b \rangle \cos k(l_a - l_b) \cdot a, \quad (22)$$

where  $I_a$ ,  $I_b$  and  $g_a$ ,  $g_b$  are the intensity and the fringe visibility for single illumination or single aperture, respectively. The resultant fringe pattern represents the contour lines of in-plane displacement along the lines connecting the dual illumination or the double aperture.

The fringe patterns arising from shearography can also be derived in the same way as

$$V_S = 2 \langle I \rangle^2 \left[ 2 + \gamma^2 + \gamma^2 \cos \left\{ k(l_S + l_O) \cdot [a(-MR) - a(-MR + M\Delta R)] \right\} \right], \quad (23)$$



where  $M$  and  $DR$  are the imaging demagnification and the image shear. Equation (23) means the contours of derivatives of the displacement components along the bisector of the illumination and the observation directions.

## 5. SPECKLE PHOTOGRAPHY

Principles of speckle photography are illustrated in Fig.7. It consists of recording of a double exposure specklegram and analysis of Young fringes arising from optical Fourier transformation of the specklegram illuminated by a narrow laser beam. The transmission function of the specklegram is represented by

$$T_{12}(\mathbf{R}) = T_0 - \eta[I_1(\mathbf{R}) + I_2(\mathbf{R})], \quad (24)$$

where we assumed that the specklegram is recorded at the image plane of the object with  $Z=0$ . The intensity distribution of Young fringes that appear in the Fourier plane by probing a narrow laser beam of wavelength  $\lambda_0$  at a point  $\mathbf{R}_c$  is given by

$$J_Y(\mathbf{p}) = \left\langle \left| \iint U_B(\mathbf{R} - \mathbf{R}_c) T_{12}(\mathbf{R}) \exp(-i2\pi\mathbf{R} \cdot \mathbf{p} / \lambda_0 f) d^2\mathbf{R} \right|^2 \right\rangle, \quad (25)$$

where  $U_B$  is the complex amplitude of the probing beam. Equation (25) can be deformed into

$$J_Y(\mathbf{p}) = \hat{C}(\mathbf{p} / \lambda f) \left\{ 1 + \gamma_Y \cos[2\pi\mathbf{p} \cdot \mathbf{A}(\mathbf{R}_c) / \lambda_0 f] \right\}, \quad (26)$$

where  $\hat{C}(\mathbf{S})$  means the Fourier transform of the autocorrelation of the intensity fluctuation and becomes

$$\hat{C}(\mathbf{S}) = \iint C(\mathbf{R}) \exp(i2\pi\mathbf{S} \cdot \mathbf{R}) d^2\mathbf{R} = \iint |P(\mathbf{s})|^2 |P[\mathbf{s} + \lambda(L'_o + Z)\mathbf{S}]|^2 d^2\mathbf{s}. \quad (27)$$

The Young fringes show the contrast given by

$$\gamma_Y = \frac{\langle \Delta I_1(\mathbf{R}) \Delta I_2(\mathbf{R} + \mathbf{A}) \rangle}{\langle I_1(\mathbf{R}) \rangle \langle I_2(\mathbf{R}) \rangle} = \left| \iint P^*(\mathbf{s}) P(\mathbf{s} + \mathbf{A}_p) d^2\mathbf{s} \right|^2 / \left[ \iint |P(\mathbf{s})|^2 d^2\mathbf{s} \right]^2 \quad (28)$$

that depends on speckle decorrelation accompanying the displacement. Hence we can determine the direction and magnitude of speckle displacement from the orientation and spacing of the Young fringes whose contrast is governed by speckle decorrelation. However, the sign of the displacement remains ambiguous.

Young fringes are especially suited for automatic analysis (Yamaguchi [4]). An example of setup is shown in Fig.8 (Deng, Yamaguchi [8]). The specklegram is scanned by an  $x$ - $y$  positioner under illumination of a narrow laser beam and Young fringes are taken by a TV camera whose output is first stored in a frame memory and then analyzed by a personal computer. Fringe orientation is first determined by comparing the integration along a stripe going through the fringe center with various orientations and then the projection along the detected orientation is fitted to the projection of Eq.(26) to determine the spacing. By this method fringes spacing larger than the diffraction halo could also be determined. Serious problems on speckle photography is the time and trouble of photographic processing. Hence it is now being replaced by 2-D speckle correlation technique that is also called electronic or digital speckle photography. Applications to high-speed phenomena using a short-pulse laser would be useful.

## **6. ELECTRONIC SPECKLE CORRELATION**

Advances in CCD cameras and computers made it possible to analyze directly the cross-correlation of video speckles. It was first demonstrated by using a linear CCD whose output signals were analyzed by a micro computer (Yamaguchi [8]). The computation could be accelerated to real-time by binary correlation algorithm that makes use of high contrast of speckles. If we record speckle patterns at image plane by a matrix CCD we can derive a distribution of speckle displacement by calculating two-dimensional cross-correlation of subimages (Sjödahl [5], Takai, Asakura [10], Noh, Yamaguchi [11]). As common advantages of electronic speckle correlation techniques resolution can be improved by interpolation of cross-correlation peaks

and measurement range can be extended over the range limited by speckle decorrelation if references of cross-correlation are refreshed and incremental displacements are summed up. Evaluation of strain that is often required in practical applications is also straightforward from the distribution of displacements.

### 6.1. One-dimensional correlation

The setup for translation measurements by one-dimensional speckle correlation is illustrated in Fig.9. The object is illuminated by a narrow laser beam. A linear CCD is positioned in the diffraction field of the object. The speckle size is adapted to resolution of the CCD by adjusting an angular size of the beam spot as seen from it. The cross-correlation of the CCD signals is calculated either by a computer or a real-time correlator (Yamaguchi, Fujita [12]). The peak position of the cross-correlation indicates the speckle displacement along the CCD from which an amount of object translation can be evaluated. The number of pixels of the CCD was used up to 1024 with the pitch of 15 mm. If the pixel is longer in the direction normal to its axis, the attenuation of correlation peak due to speckle movement transverse to the array is slower to make the detected displacement more reliable.

The detected speckle displacement is analyzed by the coordinate system shown in Fig.10. The transmission function for this system is a parabolic wave emanating from the object point. The object is illuminated with a beam whose wavefront has a radius of curvature  $L_S$  at an incident angle  $q_S$ . The object is supposed to be subject to homogenous deformation. The cross-correlation of the intensity fluctuation at the observation plane located at a distance  $L_O$  and in the direction  $q_O$  from the center of the illuminated region is given by (Yamaguchi [3], [7]).

$$\langle \Delta I_1(X, Y) \Delta I_2(X + \bar{X}, Y + \bar{Y}) \rangle = \left| \iint \sqrt{I_O(x, y) I_O(x + a_x, y + a_y)} \exp \left[ -ik \frac{x(\bar{X} - A_X) \cos \theta_O + y(\bar{Y} - A_Y)}{L_O} \right] dx dy \right|^2 \quad (29)$$

with the intensity  $I_0(x,y)$  on the object and speckle displacement components represented by

$$A_X = a_x \left( \frac{L_O \cos^2 \theta_S}{L_S \cos \theta_O} + \cos \theta_O \right) - a_z \left( \frac{L_O \cos \theta_S \sin \theta_S}{L_S \cos \theta_O} + \sin \theta_O \right) - L_O \left[ \varepsilon_{xx} \left( \frac{\sin \theta_S}{\cos \theta_O} + \tan \theta_O \right) - \Omega_y \left( \frac{\sin \theta_S}{\cos \theta_O} + 1 \right) \right] \quad (30)$$

and

$$A_Y = a_y \left( \frac{L_O}{L_S} + 1 \right) - L_O \left[ \varepsilon_{xy} (\sin \theta_S + \sin \theta_O) - \Omega_x (\cos \theta_S + \cos \theta_O) - \Omega_z (\sin \theta_S + \sin \theta_O) \right] \quad (31)$$

which are linearly dependent on deformation parameters consisting of translation, rotation, and strain.

### 6.1.1. Speckle encoders

If deformation of an object is limited to one degree of freedom, we can measure its magnitude within 1 ms by using a binary correlator. Especially, in-plane translation can be easily detected by a simple setup without attachment of any marking or gratings on a surface. The speckle displacement in this case is expressed by

$$A_X = a_x \left( \frac{L_O \cos^2 \theta_S}{L_S \cos^2 \theta_O} + \cos \theta_O \right). \quad (32)$$

The sensitivity can be enhanced by divergent illumination (Yamaguchi, Fujita [12]).

### 6.1.2. Speckle strain gauge

Since in speckle displacement given by Eqs.(30) and (31) the proportional coefficients for translation, rotation, and strain differ from each other, we can

separate one of the deformation parameters by comparing speckle displacement at different points or illumination directions. For the strain measurement speckle displacements at two symmetrical positions about the surface normal are detected as shown in Fig.11(Yamaguchi [13], Yamaguchi, Takemori, Kobayashi [14]). Their difference depends only on the strain along the direction connecting the positions and on out-of-plane translation.

$$\Delta A_x = A_x(\theta_0) - A_x(-\theta_0) = -2\varepsilon_{xx}L_0 \tan \theta_0 - 2a_z \sin \theta_0.$$

(33)

The out-of-plane translation  $a_z$  that can be generally neglected in the case of in-plane extension although it may cause an error if it approaches  $\varepsilon_{xx}L_0/\cos\theta_0$ . In the dual beam configuration which takes the difference of speckle displacement at the same position but associated with two symmetrical illumination directions, the out-of-plane translation component can be completely canceled (Yamaguchi [13]). However, the data processing system becomes more complicated because the cross-correlation between the signals produced by the same illumination beams has to be computed.

The strain gauge is perfectly non contacting and has a small gauge length less than a few millimeters as given by the incident laser beam diameter. Because of the differential setup we could mount the strain gauge on a commercial loading machine. We developed a biaxial configuration to determine Poisson's ratios of various materials such as rubber, plastics, metals, and woods (Yamaguchi, Kobayashi [15]).

We also applied the gauge to measurement of thermal expansion coefficients by constructing a heating vessel which uses an infrared lamp and is evacuated for preventing from both air turbulence to cause extra speckle displacement and surface oxidation leading to drop-off of reflectivity and thus deteriorating speckle signals. Thermal expansion coefficients of such a small specimen as 10 mm in diameter and 1 mm thick could be determined even for a temperature change of 1 deg. C. We

could also observe drastic changes in thermal expansion of plastic materials which is caused by phase transition at room temperature. Photothermal strain of a plastic plate resulting from irradiation of laser beam has also been detected by the laser speckle strain gauge (Yamaguchi, Palazov, Natori, Kato [16]).

## **6.2. Whole field strain measurement using 2-D speckle correlation**

For the whole field measurement of strain also much demanded in experimental mechanics and nondestructive testing we can use speckles arising in the imaging geometry shown in Fig.5(a). At the conjugate plane of the object, speckle displacement is equal to that of the image, that is, the in-plane displacement times the imaging magnification as shown in Eqs.(9) and (10). A distribution of speckle displacements is evaluated from the video images taken by the arrangement and by using two-dimensional correlation analysis of the digital images (Sjödahl [5], Takai, Asakura [10], Noh, Yamaguchi [11], Yamaguchi, Noh[17]). Each frame of the images is divided into a number of subimages. In each of the subimages the two-dimensional cross-correlation function is computed by using the fast Fourier transform algorithm. The sensitivity of the method depends on the imaging magnification. By differentiating the distribution of the in-plane displacement vectors, we can derive values and contour lines of in-plane strain coefficients. Compared with electronic speckle pattern interferometry, which only delivers the distributions of in-plane displacement component decided by configuration of dual beam illumination, the present method delivers vectorial components simultaneously with a simpler optical setup and has wider range of measurement because the displacement is not limited by the speckle size. In correspondence to the laser speckle strain gauge mentioned above speckle displacement at the defocused plane can be used for direct detection of strain distributions by comparing those associated with four symmetrical illumination directions (Sjödahl [5]).

## 7. DIGITAL HOLOGRAPHY

Recent remarkable advances in CCD devices and computers have made it practical to record holograms by a CCD camera and to reconstruct three-dimensional images by computers. This technique, called digital holography, saves a trouble of photographic processing and delivers the distributions of both intensity and phase directly. In reconstruction focusing is adjusted numerically from a single recording. Since the distributions of not only intensity but also phase can be calculated, object displacement can be directly detected from the difference of the reconstructed phases before and after object deformation, which has only to be phase-unwrapped. No imaging lens is necessary even for the whole field measurement. These advantages ease quantitative measurements of shape and deformation three-dimensional objects. The main problem in digital holography is resolution of CCD devices that is much lower than photographic materials. In the off-axis setup that was first introduced pixel numbers are not fully used because the reconstruction also produces the zero-order and conjugate images (Goodman, Lawrence [18], Kronrod, Merzlyakov, Yaroslavskii [19], Schnars, Jüptner [20]). This limitation was overcome by phase shifting holography that uses both in-line setup to increase the fringe spacing and phase-shifting of the reference beam to evaluate directly the complex amplitude at the CCD plane (Yamaguchi, Zhang [21], Skarman, Becker, Wozniak [22], Zhang, Yamaguchi [23]). By this method we obtain only the desired image of high quality. The basic setup for phase-shifting digital holography is presented in Fig.12. The object beam and the reference beam reflected at the PZT mirror controlled by a computer are combined at the CCD in the in-line configuration. At least three interference patterns are acquired after stepwise phase shifts. For analysis of image formation we adopt the coordinate system depicted in Fig.13. The object wave at the CCD plane is represented as a Fresnel transform of the complex amplitude at the object plane  $U_0(x',y')$  by

$$U(x,y) = \iint U_O(x',y') \exp \left[ ikz_O + ik \frac{(x-x')^2 + (y-y')^2}{2z_O} \right] dx' dy', \quad (34)$$

where integration is carried out over infinity and  $z_O (>0)$  is the distance from the object plane to the CCD. This wave is combined with a reference wave having the complex amplitude  $U_R(x,y)$  to produce the intensity distribution

$$I(x,y;\delta) = |U_R(x,y)\exp(i\delta) + U(x,y)|^2 = |U_R|^2 + |U|^2 + 2\Re[U_R U^* \exp(i\delta)], \quad (35)$$

where  $d$  is the constant phase difference between the object and the reference waves. By using the phase-shifting procedure in which the reference phase is shifted by a step of  $\pi/2$  three times, we can derive the complex amplitude of the object wave such as

$$U(x,y) = \frac{1}{4U_R^*} \{I(x,y;0) - I(x,y;\pi) + i[I(x,y;\pi/2) - I(x,y;3\pi/2)]\} \quad (36)$$

in the case of four-step algorithm, and

$$U(x,y) = \frac{1-i}{4U_R^*} \{I(x,y;0) - I(x,y;\pi/2) + i[I(x,y;\pi/2) - I(x,y;\pi)]\} \quad (37)$$

in the three-step algorithm.

The reconstruction is performed by the Fresnel transformation of the derived complex amplitude in such a way as

$$U_f(X,Y,Z) = \iint U(x,y) \exp \left[ ikZ + ik \frac{(X-x)^2 + (Y-y)^2}{2Z} \right] dx dy, \quad (38)$$

where the integration should be carried out over the area of CCD. We assume first the sufficient extension and ideal resolution of the device. If we substitute Eq.(38) into Eq.(34), we find that the image plane is determined from the condition that the quadratic term of  $x$  and  $y$  in the exponent vanishes such as  $Z=-z_O$  where the complex amplitude becomes



$$U_I(X, Y, -z_0) = U_O(X, Y) \quad (39)$$

if we neglect limitation of the finite size of CCD array. Image reconstruction using Eq.(38) can be performed either by a single Fourier transformation or double Fourier transformation that carries out convolution integral.

The deformation measurement is carried out by calculating the argument of the conjugate product of the complex amplitudes before and after object deformation ( Pedrini, Schedin, Tiziani [24], Wagner, Osten, Seebacher [25]).

$$\arg[U_{O1}(x, y)U_{O2}^*(x, y)] = k(l_S + l_O) \cdot a(x, y) + \alpha \quad (40)$$

that only needs phase-unwrapping for deriving displacement  $a(x, y)$ . Surface contouring can also be performed by changing the wavelength or the angle of object illumination (Wagner, Osten, Seebacher [25], Yamaguchi, Ohta, Kato [26]). In the case of change of incident angle from  $\theta$  to  $\theta + \Delta\theta$  the phase difference is given by

$$\arg[U_{O1}(x, y)U_{O2}^*(x, y)] = 2k \sin \frac{\Delta\theta}{2} \left[ x \cos \left( \theta + \frac{\Delta\theta}{2} \right) - h(x, y) \sin \left( \theta + \frac{\Delta\theta}{2} \right) \right], \quad (41)$$

where  $h(x, y)$  means the height and the incident plane is assumed to be the x-z plane (Yamaguchi, Ohta, Kato [26]). The sensitivity coincides with that of the fringe projection, but we need no fringe analysis and depth of measurement can be extended by numerical focusing. In addition, the same setup can be used for both shape and deformation measurement.

## 8. CONCLUSIONS

In this paper we surveyed fringe formation in holographic interferometry and speckle metrology in terms of correlation properties of complex amplitude and intensity in observation fields. In holographic interferometry and speckle interferometry contour lines of phase change of the scattered light due to object deformation are observed as fringe patterns. In speckle photography orientation and spacing of Young fringes

are related to orientation and magnitude of speckle displacement. In electronic speckle correlation techniques the position of correlation peak directly indicates speckle displacement. For digital display of these patterns electronic speckle pattern interferometry was first introduced because the speckle size can be adapted to resolution of image sensors by adjusting an aperture of the imaging lens and electronic processing is so simple that only the difference of images is taken and squared. Then the automatic analysis of Young fringes appearing in speckle photography was introduced. In this case the patterns are always straight fringes whose orientation and spacing can be easily determined by digital image processing. This procedure can be regarded as a combination of high density storage on a photographic film and optical addressing to produce simple patterns that can be analyzed quickly by digital means.

Recently photographic recording has become less and less practical owing to its cumbersome processing and thus image recording by a CCD camera is becoming more and more common whose outputs are analyzed by computers. This transition has been pushed by quick advances of both CCD cameras and computers. Electronic speckle correlation technique that started first from one-dimensional analysis using a linear CCD for point measurement in earlier stages are now becoming more popular in two-dimensional analysis for the whole-field measurement. It will be realized in near future that we can monitor dynamic variation of strain distribution in real time. The used software is very similar to that employed for flow analysis. Finally holography has also been digitized in such a way that the recording is done by a CCD camera and reconstruction is performed by a computer. We can analyze three-dimensional structure or an object quantitatively by numerical focusing in the reconstruction. Phase distribution that had been only visualized by interference fringes can be directly derived. The simple recording setup without imaging lens can be used and imaging is carried out by computers. The serious issue in the digital holography, lower resolution of the CCD camera, can be substantially overcome by

phase-shifting digital holography that employs in-line setup and is free from the conjugate images. By digital holography shape and deformation measurements of three-dimensional objects are very simple and unified. Digital interferometry that started from automatic fringe analysis has progressed now to realize digital holography that is capable of handling three-dimensional objects and even improving functions of conventional optical systems.

### REFERENCES

1. J. Schwider. Advanced evaluation techniques in interferometry. In Wolf E., editor. *Progress in Optics*, Vol. 28, Amsterdam: Elsevier, 1990, 271-359.
2. I. Yamaguchi. Fringe formations in deformation and vibration measurements using laser light. In Wolf E., editor. *Progress in Optics*, Vol. 22, Amsterdam: Elsevier, 1985, 271-340.
3. I. Yamaguchi. Speckle displacement and decorrelation - theory and applications. In Rastogi P. and Inaudi D., editors. *Trends in Optical Non-destructive Testing and Inspection*, Amsterdam: Elsevier, 2000, 151-170.
4. G. H. Kaufmann. Automatic fringe analysis procedures in speckle metrology. In Sirohi R. S. , editor. *Speckle Metrology*, New York: Marcel Dekker, 1993, 427-472.
5. M. Sjö Dahl. Digital speckle photography. In Rastogi P. and Inaudi D., editors. *Trends in Optical Non-destructive Testing and Inspection*, Amsterdam: Elsevier, 2000, 179-196.
6. T. Kreis. Digital holography for metrologic applications. In Jacquot P. and Fournier J.-M., editors. *Interferometry in Speckle Light*, Berlin: Springer, 2000, 205-212.
7. I. Yamaguchi. Speckle displacement and decorrelation in the diffraction and image fields for small object deformation. *Opt. Acta*, 1981(10); 28: 1359-1376.

8. N. Deng and I. Yamaguchi. Automatic analysis of speckle photographs with extended range and improved accuracy. *Appl. Opt.*, 1990; 29(2): 296-303.
9. I. Yamaguchi. Real-time measurement of in-plane translation and tilt by electronic speckle correlation. *Jpn. J. Appl. Phys.*, 1980; 19(3): L133-L135.
10. N. Takai and T. Asakura. Vectorial measurement of speckle displacement by the 2-D electronic speckle correlation method. *Appl. Opt.*, 1985; 24(5): 660-665.
11. S. Noh and I. Yamaguchi. Two-dimensional measurement of strain distribution by speckle correlation. *Jpn. J. Appl. Phys.*, 1992; 31(9A): L1299-L1301.
12. I. Yamaguchi and T. Fujita. Linear and rotary encoders using electronic speckle correlation. *Opt. Eng.*, 1991; 30(12): 1862-1868.
13. I. Yamaguchi. A laser-speckle strain gauge. *J. Phys. E: Sci. Instrum.*, 1981; 14(11): 1270-1273.
14. I. Yamaguchi, T. Takemori, and K. Kobayashi. Stabilized and accelerated speckle strain gauge. *Opt. Eng.*, 1993; 32(3): 618-625.
15. I. Yamaguchi and K. Kobayashi. Material testing by the laser speckle strain gauge. *Proc. SPIE 1554A, Speckle Techniques, Birefringence Methods, and Applications to Solid Mechanics*, 1991; 240-249.
16. I. Yamaguchi, D. Palazov, E. Natori, and J. Kato. Detection of photothermal effect by laser speckle strain gauge. *Appl. Opt.*, 1997; 36(13): 2940-2943.
17. I. Yamaguchi and S. Noh. Deformation measurement by 2-D speckle correlation. *Proc. SPIE 1756 Interferometry: Applications*, 1992: 106-118.
18. J. W. Goodman and R. W. Lawrence. Digital image formation from electronically detected holograms. *Appl. Phys. Lett.*, 1967; 1(3): 77-79.
19. M. A. Kronrod, N. S. Merzlyakov, and L. P. Yaroslavskii. Reconstruction of a hologram with a computer. *Sov. Phys.-Tech. Phys.*, 1972; 17(2): 333-334.
20. U. Schnars and W. Jüptner. Direct recording of holograms by a CCD target and numerical reconstruction. *Appl. Opt.*, 1994; 33(2): 179-181.

21. I. Yamaguchi and T. Zhang. Phase-shifting digital holography. *Opt. Lett.*, 1997; 22(16): 1268-1270.
22. B. Skarman, J. Becker, and K. Wozniak. Simultaneous 3D-PIV and temperature measurements using a new CCD-based holographic interferometer. *Flow Meas. Instrum.*, 1996; 7(1): 1-6.
23. T. Zhang and I. Yamaguchi. Three-dimensional microscopy with phase-shifting digital holography. *Opt. Lett.*, 1998; 23(15): 1221-1223.
24. G. Pedrini, S. Schedin, and H. J. Tiziani. Lenseless digital-holographic interferometry for the measurement of large objects. *Opt. Commun.*, 1999; 171(1,2,3): 29-36.
25. C. Wagner, W. Osten, and S. Seebacher. Direct shape measurement by digital wavefront reconstruction and multiwavelength contouring. *Opt. Eng.*, 2000; 39(1): 79-85.
26. I. Yamaguchi, S. Ohta, and J. Kato. Surface shape measurement by phase-shifting digital holography. *Opt. Rev.*, 2001; 8(2): 85-88.

## Figure Captions

Fig.1 Linear transmission system

Fig.2 Transmission in an imaging system

Fig.3 Fringe formation in holographic interferometry.

Fig.4 Arrangement of TV speckle interferometry for out-of-plane displacement.

Fig.5 Dual illumination speckle interferometry

Fig.6 Double-aperture speckle interferometry

Fig.7 Principles of speckle photography. (a) recording of specklegram. (b) analysis of Young fringes.

Fig.8 Setup of an automatic speckle analyzer.

Fig.9 Basic setup of one-dimensional speckle correlation method.

Fig.10 Coordinate system of the diffraction field.

Fig.11 Setup of laser speckle strain gauge.

Fig.12 Basic setup of phase-shifting digital holography.

Fig.13 Coordinate system of phase-shifting digital holography.

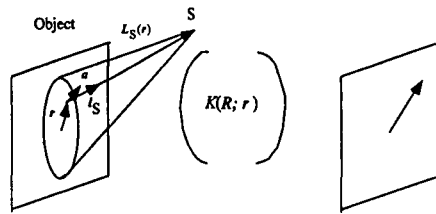


Fig.1 Linear transmission system

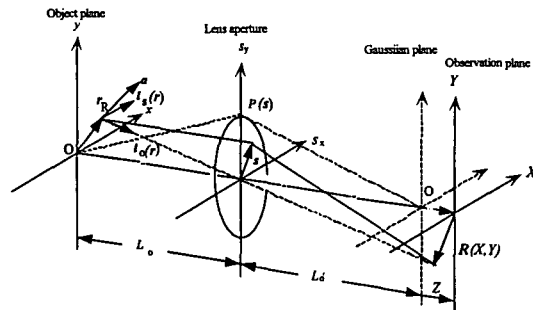


Fig.2 Transmission in an imaging system.

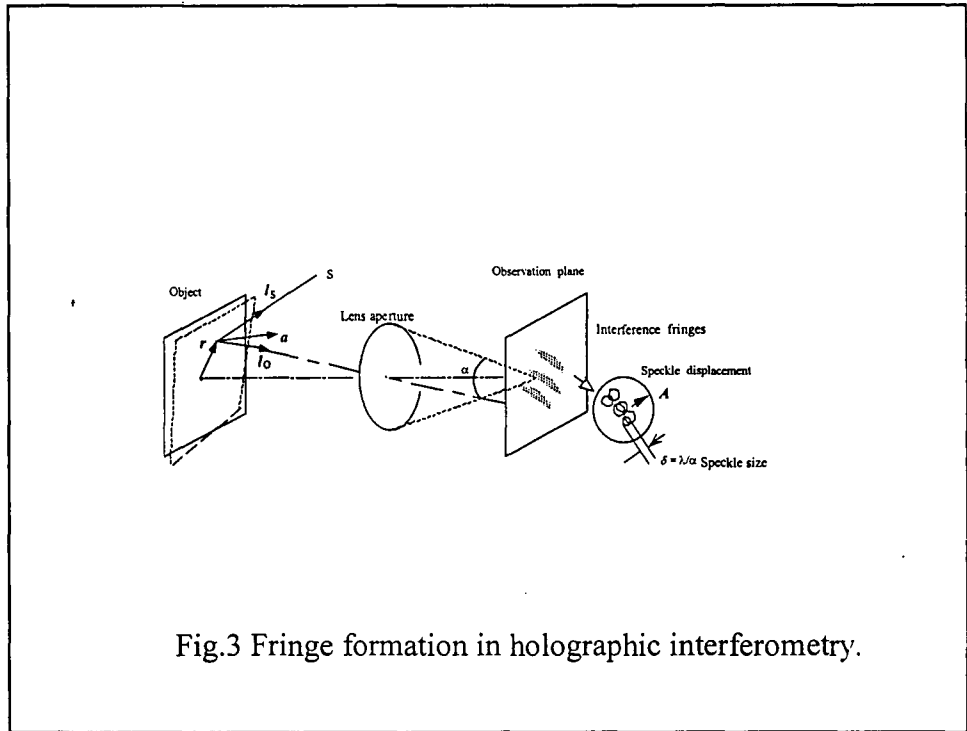


Fig.3 Fringe formation in holographic interferometry.

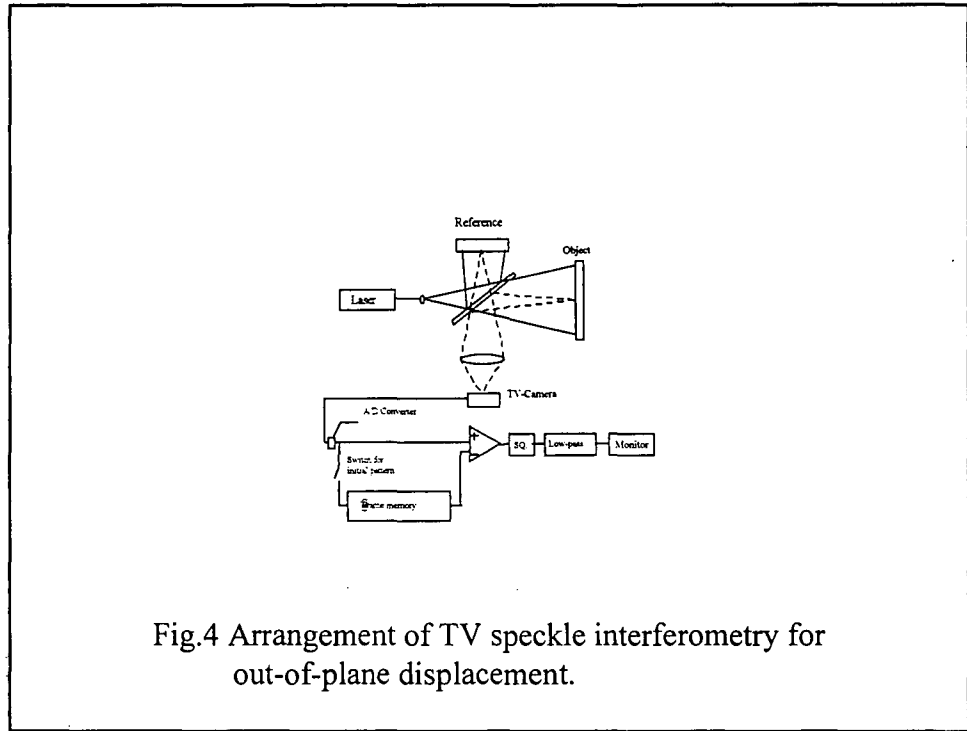


Fig.4 Arrangement of TV speckle interferometry for out-of-plane displacement.



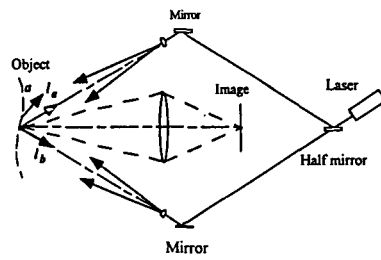


Fig.5 Dual illumination speckle interferometry.

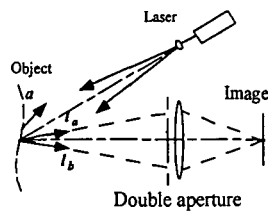


Fig.6 Double aperture speckle interferometry.

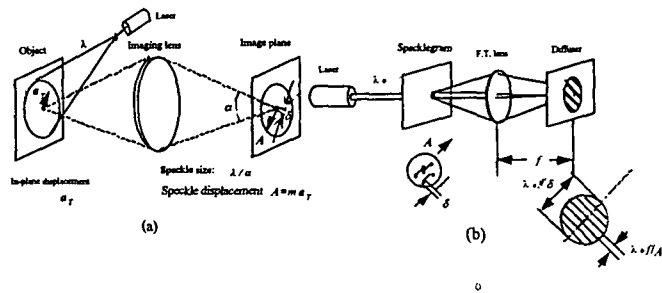


Fig.7 Principles of speckle photography. (a)Recording of specklegram. (b)Analysis of Young fringes.

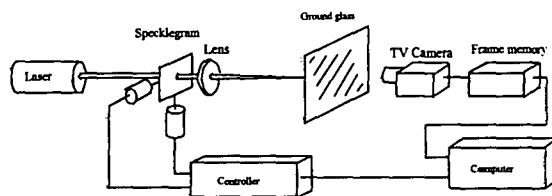
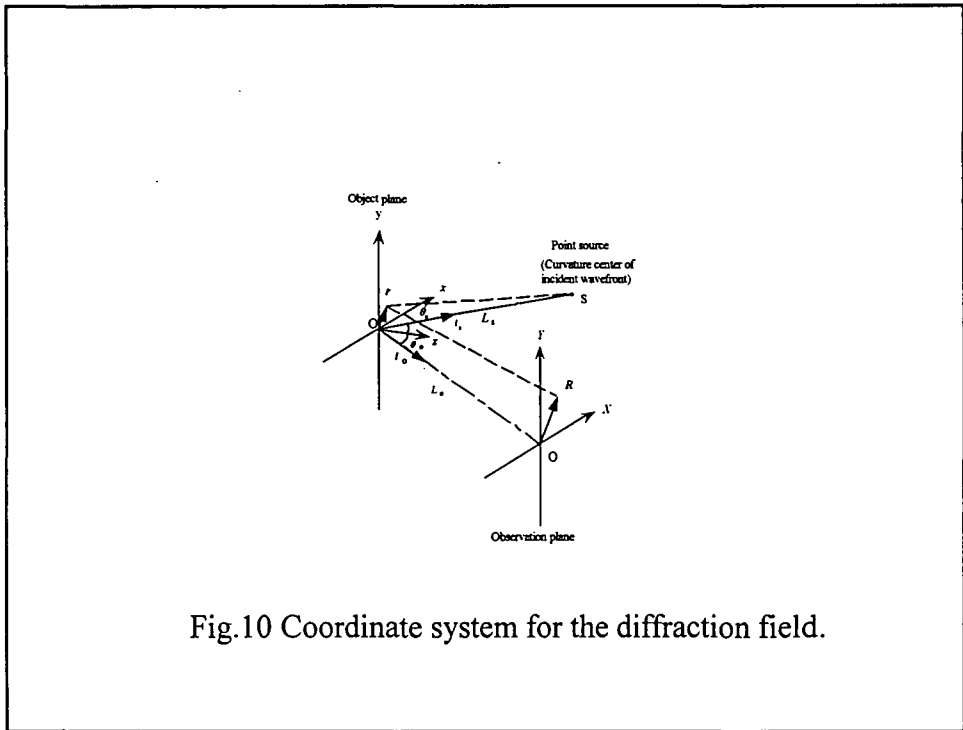
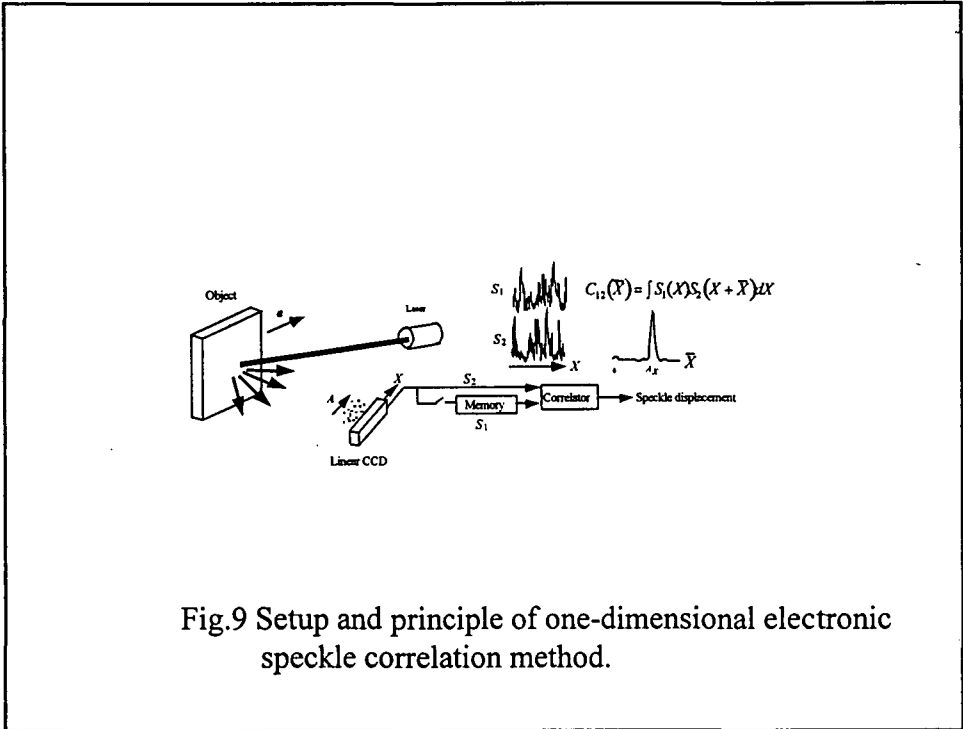
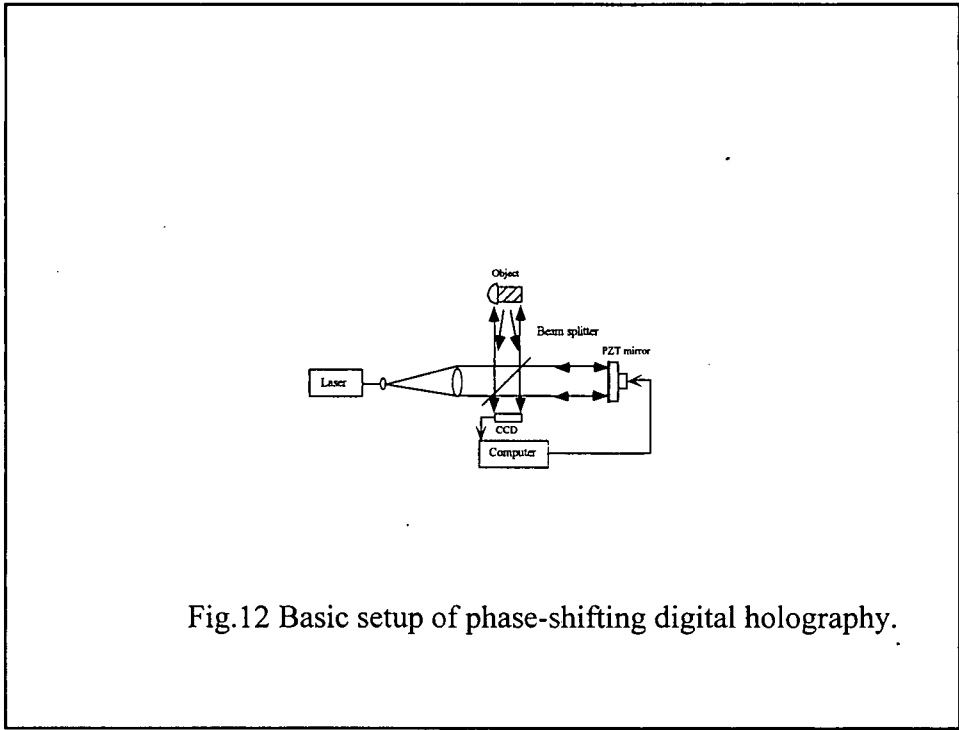
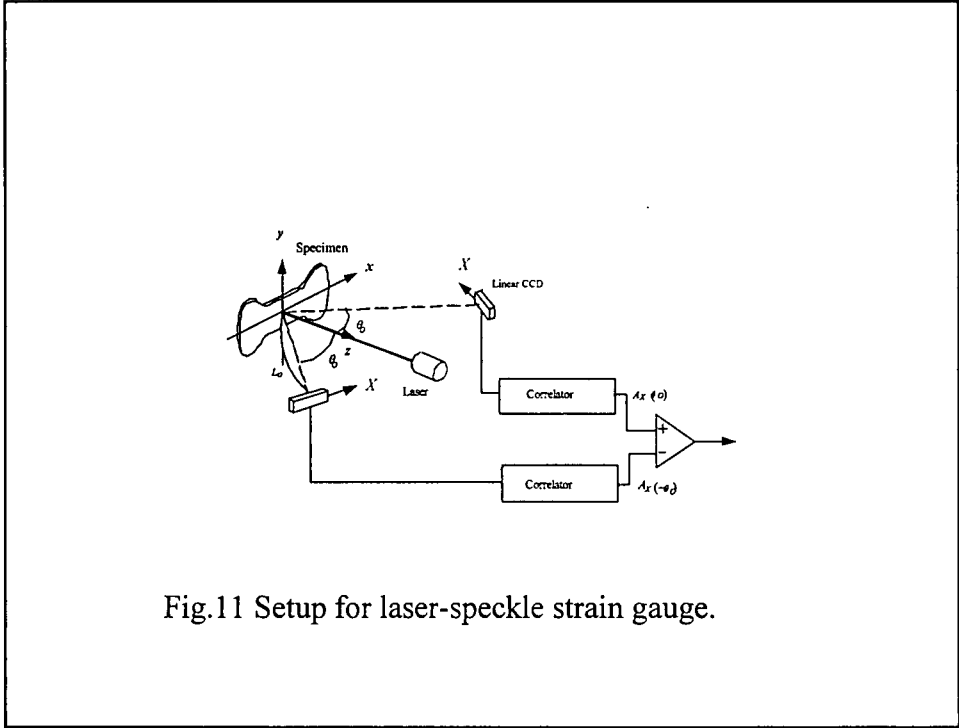


Fig.8 Setup of an automatic specklegram analyzer.





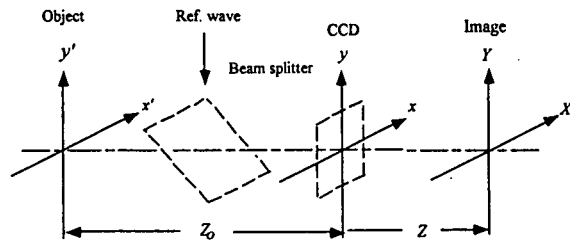
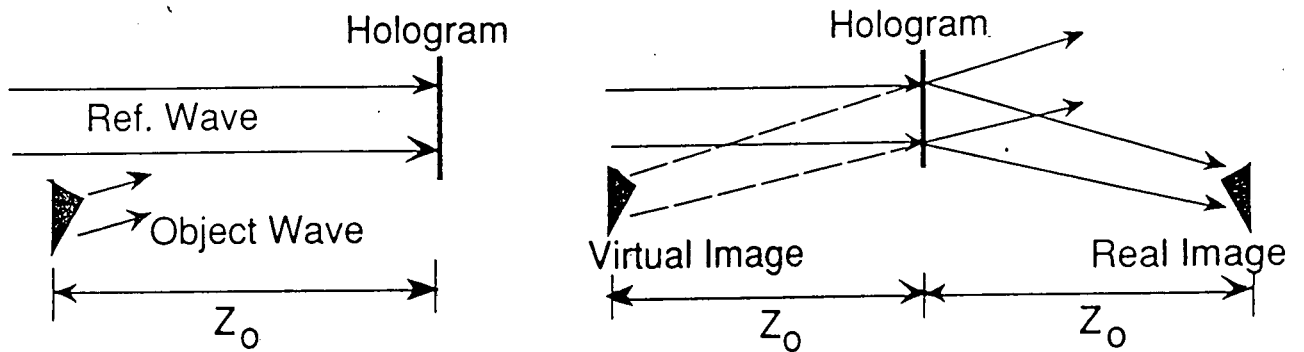


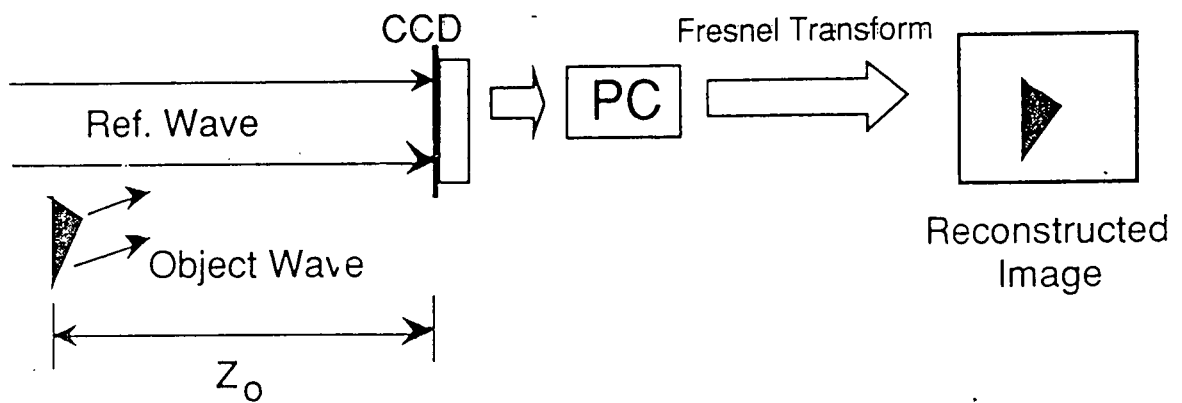
Fig.13 Coordinate system for phase-shifting digital holography.

# HOLOGRAPHY AND DIGITAL HOLOGRAPHY

## Conventional holography



## Digital holography



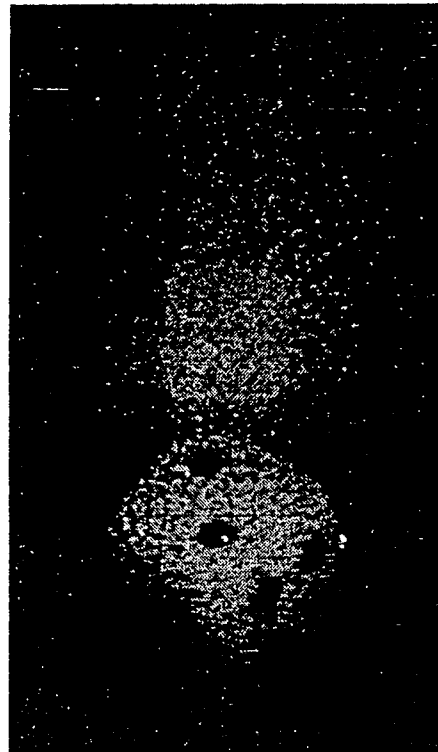
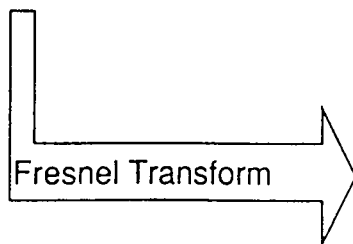
# CONVENTIONAL DIGITAL HOLOGRAPHY

## Feature

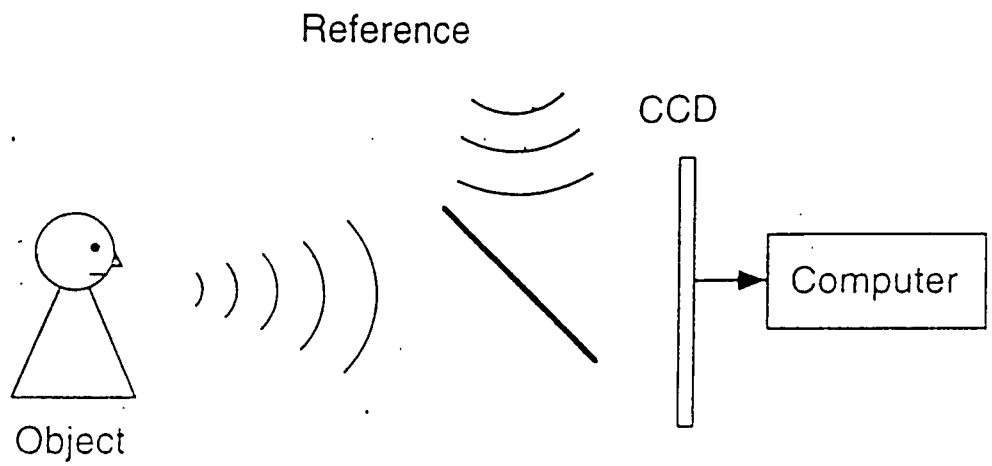
1. Off-axis setup.
2. Only intensity patterns are Fresnel transformed.

## Problem

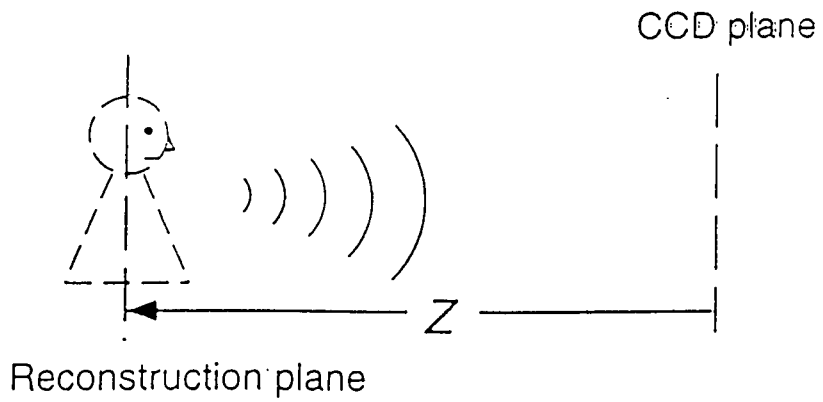
1. Presence of zero-order and conjugate image.
2. Limited object size.



U. Schnars, Appl. Opt. Vol.33, (179)1994.

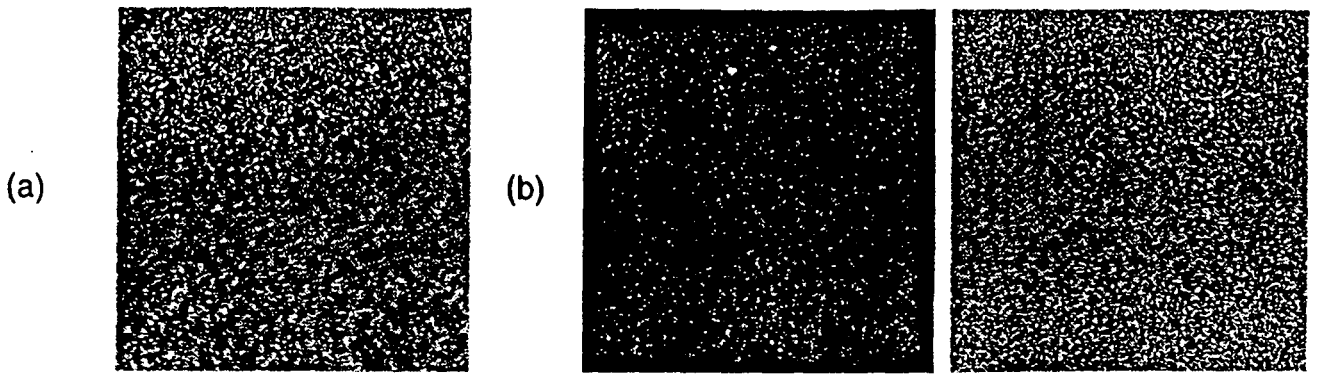


(a) **Hologram Recording**



(b) **Reconstruction**



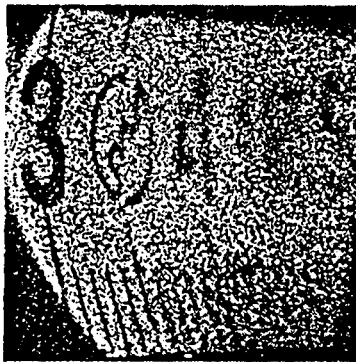


Interference pattern

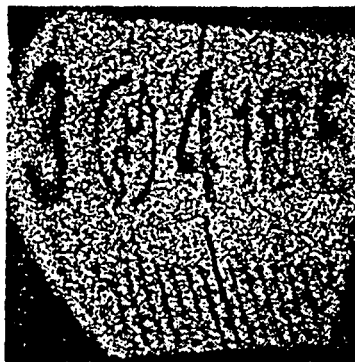
Amplitude

Phase

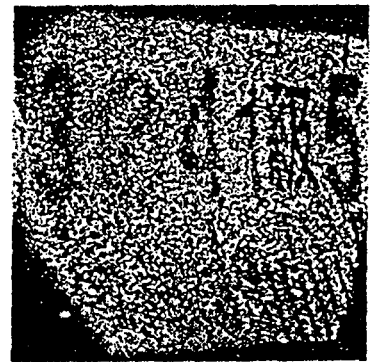
(c)  
Amplitude  
and  
Phase



Z=130.0 mm



Z=137.5 mm

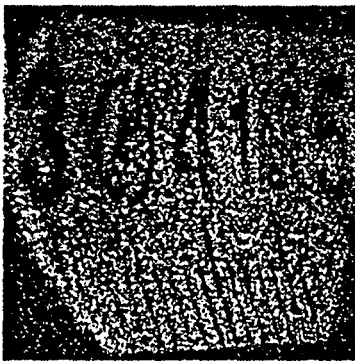


Z=145.0 mm

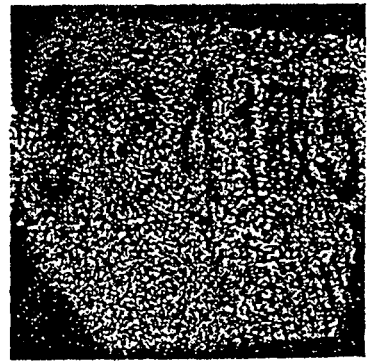
Phase  
only



Z=130.0 mm



Z=137.5 mm

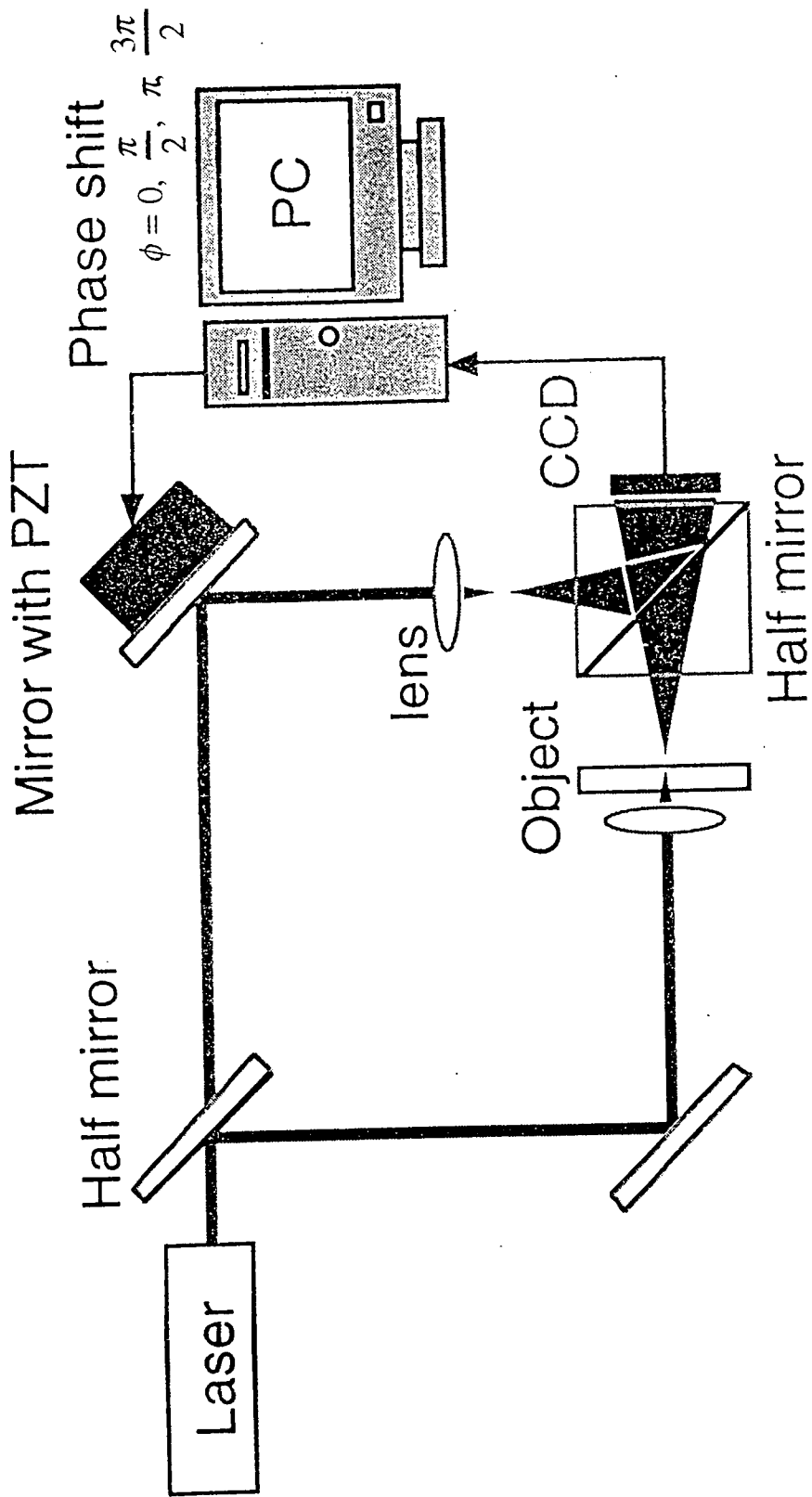


Z=145.0 mm

Interference pattern (a), amplitude and phase (b), and reconstructed images (c).

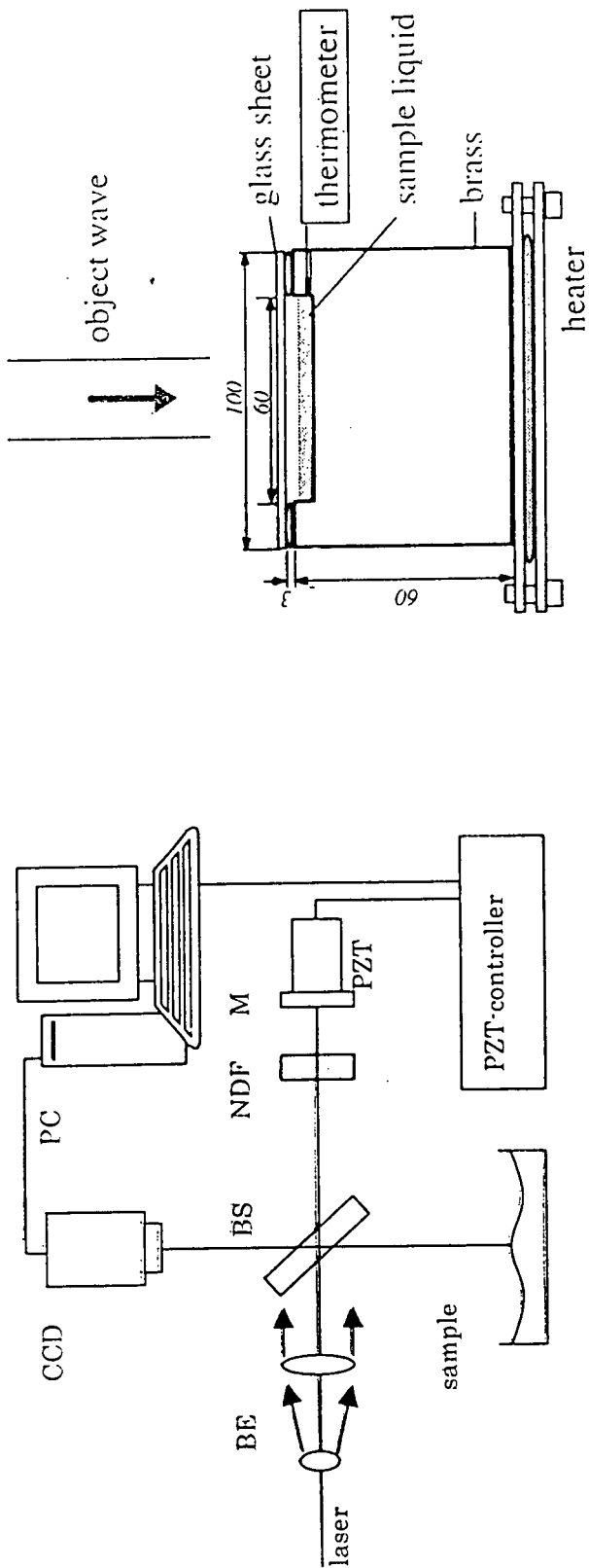
# Digital Holography

- Recording holograms by a CCD.
- Image reconstruction by a computer.
- Advantages
  - Quick and high sensitive recording.
  - Quantitative data on 3-d distribution of amplitude and phase.



Setup for microscopy using phase-shifting digital holography without imaging lens.

# Experimental Setup



Optical  
 light source He-Ne laser (633 nm, 20 mW)  
 phase shift piezo transducer (Physik Instrumente P-753.11C)  
 CCD 85fps, 512x480 pixels (KODAK Megaplus ES310)

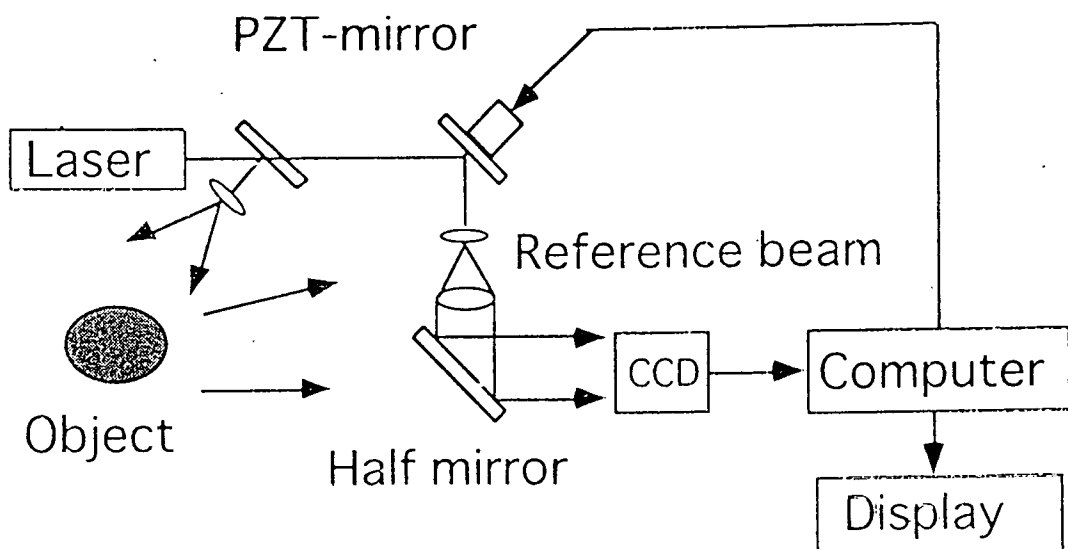
Fluid  
 sample silicon oil; viscosity  $2.2 \times 10^{-5} \text{ m}^2/\text{s}$   
 depth 1.0 mm; aspect ratio 1:60  
 temperature  $65 \text{ }^\circ\text{C}/\text{mm}$

# PHASE-SHIFTING DIGITAL HOLOGRAPHY

## *Direct Evaluation of Complex Amplitude by Phase-shifting Method*

### Advantages

1. Larger object.
2. Full use of image pixels for reconstruction.
3. Simple processing.
4. Scale adjustment in reconstruction.



Basic setup of phase-shifting digital holography

# Conclusions

- Imaging without lens
- Simple optical setup
  - Small objects, Biological specimen
- High-speed recording of 3-d objects
- Direct phase measurement by digital holography

# SURFACE SHAPE MEASUREMENT

## Mirror Surface

- ◆ Reconstruction of phase
- ◆ Simple procedure (phase unwrapping only)

## Diffusely Reflecting Surfaces

- ◆ Difference of reconstructed phases

Change in incident angle

Change in wavelength

- ◆ Sensitivity

- ◆ Procedures

Phase unwrapping

Change of reference plane

Suppression of speckle noise

Numerical focusing

# SURFACE CONTOURING

## Object phases

### Before mirror tilt:

$$\phi_1(x, h) = k[x \sin \theta + h(x) \cos \theta]$$

### After mirror tilt:

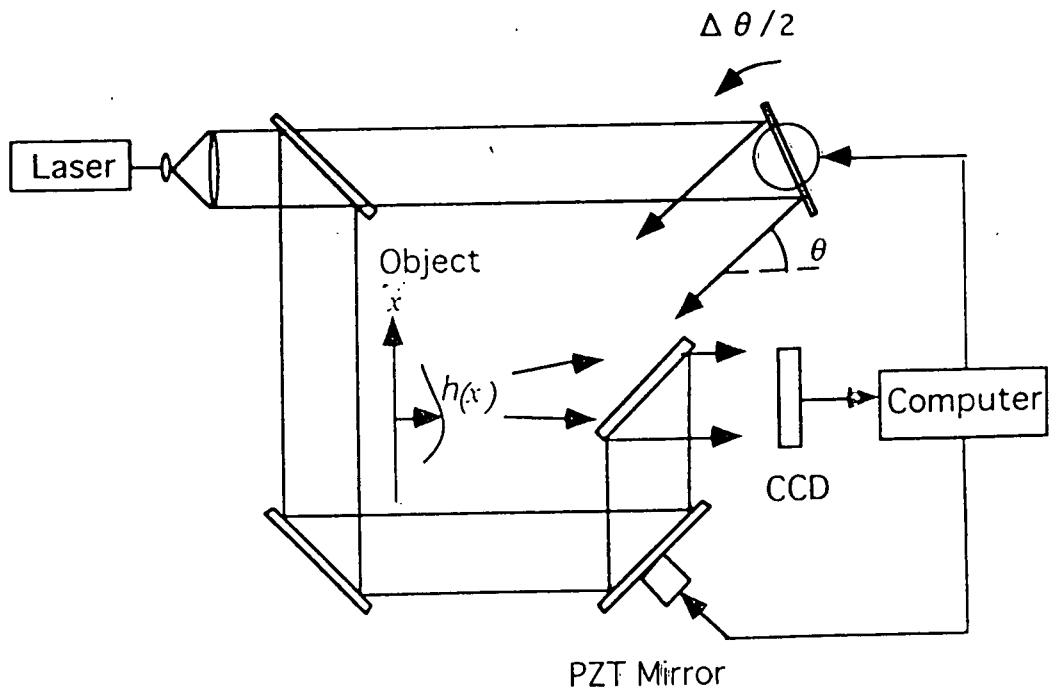
$$\phi_2(x, h) = k[x \sin(\theta + \Delta\theta) + h(x) \cos(\theta + \Delta\theta)]$$

## Phase difference

$$\Delta\phi(x, h) \equiv \phi_2(x, h) - \phi_1(x, h) = k \sin \frac{\Delta\theta}{2} \left[ x \cos \left( \theta + \frac{\Delta\theta}{2} \right) - h(x) \sin \left( \theta + \frac{\Delta\theta}{2} \right) \right]$$

## Height sensitivity

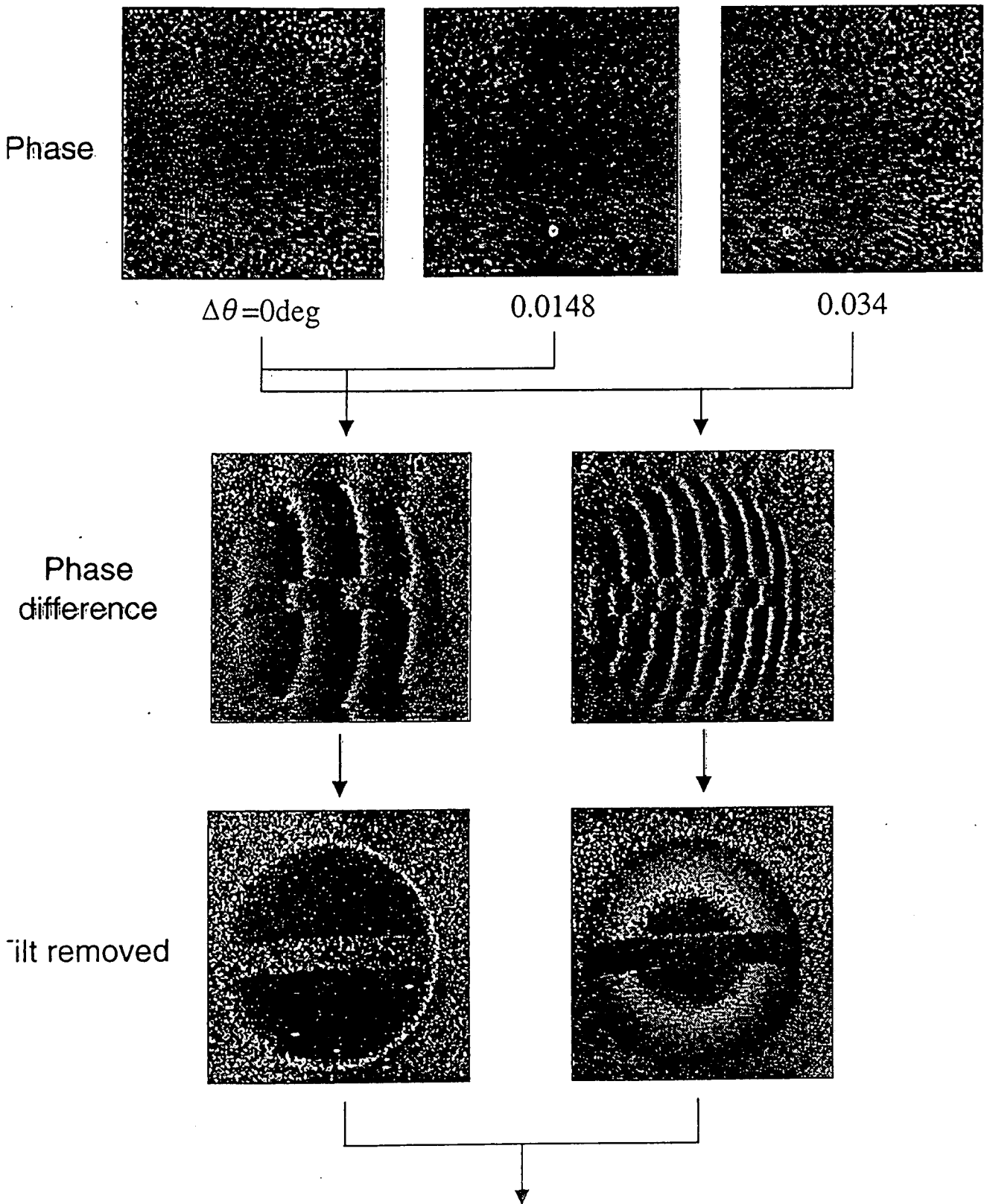
$$\Delta h = \lambda / 2 \sin \frac{\Delta\theta}{2} \sin \left( \theta + \frac{\Delta\theta}{2} \right) \approx \lambda / \Delta\theta \sin \theta$$



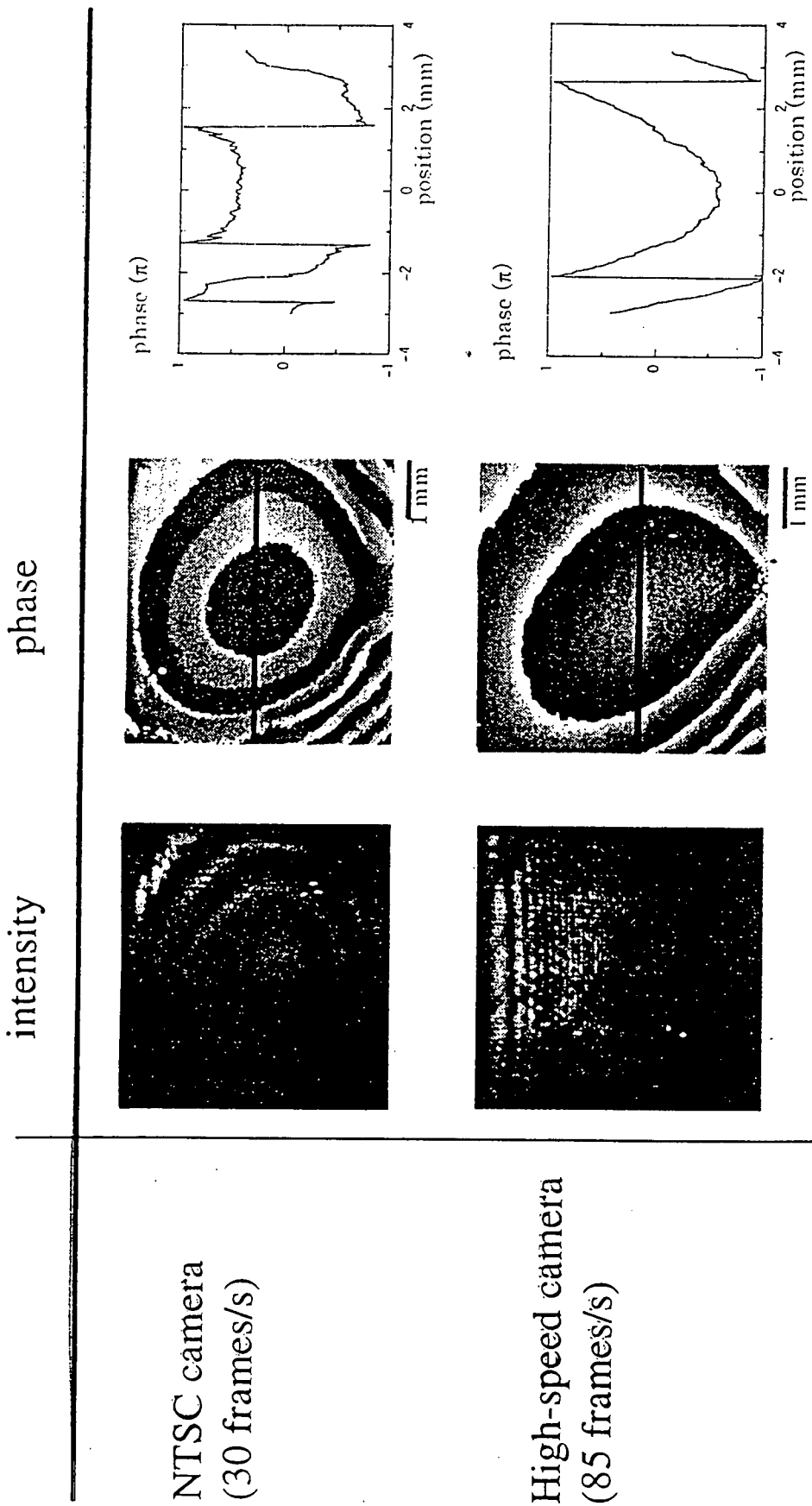
Arrangement for contouring diffusely reflecting surface by changing illumination direction.



# SURFACE CONTOURING



# Reconstruction of fluid surface due to phase-shifting method



Spatial resolution: 28  $\mu\text{m}$

# 3-D MICROSCOPY

- Magnification of 3-D Objects
  - ◆ Large focal depth
  - ◆ Phase imaging
  - ◆ Aberration compensation
- Setups
  - ◆ Direct recording
    - ✦ Simple setup
    - ✦ Resolution depending on CCD size
  - ◆ Use of a microscope objective
    - ✦ Resolution depending on NA of objective
  - ◆ Use of spherical reference wave
    - ✦ Lens function introduced by reference beam
    - ✦ Coarse fringe patterns

# CONCLUSIONS

- **Combination of Optics and Digital Image Processing**
- **Simple Optical Setup**
- **Quantitative Analysis of Amplitude and Phase**
- **Flexible Magnification and Display**
- **Robust against Surface Textures**
- **Wide Scalability**

## Laser-induced shock wave plasma spectroscopy

K. Kagawa<sup>1</sup> and H. Kurniawan<sup>2</sup>

<sup>1</sup>Department of Physics, Faculty of Education, Fukui University, Fukui 910, Japan. <sup>2</sup>Spectroscopy Laboratory, Graduate Faculty for Opto-electrotechniques and Laser Application, University of Indonesia, 4 Salemba Raya, Jakarta 10430, Indonesia

### Abstract

A review on the study of Laser-Induced Shock Wave Plasma Spectroscopy (LISPS), which was developed by the present authors, has been presented. It is demonstrated that characteristic laser plasma can be produced when a pulse laser (N<sub>2</sub> laser, XeCl excimer laser, TEA CO<sub>2</sub> laser and YAG laser) is focused on a solid target under reduced pressures (around 1–10 Torr), and this plasma has many characteristics favorable as the source of the emission spectrochemical analysis. On the basis of the results obtained by the experiments using unique time-resolved spatial distribution of the dynamical emission, it is proved that this plasma are excited by a shock wave induced by the laser ablation. Practical applications to the quantitative emission analysis are also presented.

### 1. Introduction

The study of Laser Atomic Emission Spectrochemical Analysis (LAESA) was first made by Brech et al. in 1962[1], and this LAESA became the most typical application of laser. At that time high power solid state lasers, Ruby and Nd glass laser, were employed, and photographic plate was used for spectrum recording. The advantages of this method over other spectrochemical techniques are that not only metal sample but also non-metal sample can be analyzed and that micro-area analysis can be made, and also rapid analysis can

be made without pretreatment. On the other hand, the disadvantages of this method is that the background of this emission spectrum is very strong due to high density and high temperature plasma, and self-absorption of the emission line takes place to a remarkable extent due to the generation of large temperature difference between the inside and outside of the plasma, which brings about the non-linear calibration curve.

In order to solve these problems excitation process was separated from laser ablation process. For this purpose auxiliary spark discharge was employed, and normal oscillation laser was used only for vaporizing the sample. Other methods to excite the evaporated atoms, such as microwave excitation, were also attempted[2,3]. However, the problem of non-linearity of the calibration curve and insufficient accuracy involved in these process were not be solved nevertheless many works were made on LAESA. As the result, the LAESA method was mainly used only for qualitative analysis or semi-quantitative analysis, and the research of LAESA had become inactive since in the early of 1980s[4].

Nowadays good quality laser system such as YAG is commercially available offering good shot to shot power stability and good beam quality which brings high focusibility of the laser light. Also the development of optical multi-channel analyzer (OMA) has contributed to the study of laser spectroscopy. Supported by these new instruments, recently the study of LAESA has become revival because the LAESA is still attractive to spectrochemist as the rapid quantitative analytical method for solid samples.

Roughly speaking, nowadays there are two directions in the development of LAESA. One is high pressure type, usually it is called Laser-Induced Breakdown Spectroscopy (LIBS)[5-9]. In

this method high peak power with short duration laser such as Nd:YAG laser was focused onto the sample at atmospheric pressure. In order to remove the disturbing background spectrum coming from high temperature and high density plasma, gated OMA was effectively incorporated in the detection system. Another method of LAESA is low pressure type[10-20]. Namely, laser plasma is produced under reduced pressure aiming the deduction of the background emission intensity in the spectrum.

We have shown in our previous experiments that laser-induced shock wave plasma is generated when a pulse laser such as N<sub>2</sub> laser, TEA CO<sub>2</sub> laser, or excimer laser and YAG laser, is focused onto a solid target at a reduced gas pressure of around 1 Torr[21-43]. The laser plasma consists of two distinct region. The first is a small area of high temperature plasma (the primary plasma), which gives off an intense, continuous emission spectrum for a short time just above the surface of the target. The second area (the secondary plasma) expands with time around the primary plasma, emitting sharp atomic spectral line spectrum with negligibly low background signals. On the basis of time-resolved experiments using a TEA CO<sub>2</sub> laser and an excimer laser, we demonstrated that atoms in the secondary plasma are excited by the shock wave, while the primary plasma acts as an initial explosion energy source[23,26,34,36]. We have referred this method as laser-induced shock wave plasma spectroscopy (LISPS).

We have also proved that the laser-induced shock wave plasma is excellent light source for emission spectrochemical analysis. In ordinary atomic emission spectrometry, such as arc discharge method, spark discharge method and ICP method, atoms are excited by means of an electric discharge. In general, in atomic emission spectrometry the detection limit of the elements is mainly determined by the intensity of the background emission, which arises from the process of electron-ion recombination or the electron-ion Bremstrahlung[44]. The lower the background emission intensity, the lower the minimum determinable concentration of the elements. In contrast to this, in plasma induced by the shock wave at low pressures, the background emission intensity is expected to be considerably reduced, because in the shock wave plasma the excitation of the atoms takes place by means of a purely thermal process, without employing any electric fields, and the excitation process is

substantially a non-equilibrium process.

In this review, section 3 deals with the generation of shock wave plasma and its characteristics. Section 4 is used to present some evidences to support shock wave model. Finally, analytical application of the laser-induced shock wave plasma is treated in section 5.

## 2. Experimental procedure

The basic experimental arrangement used in this research is shown in Fig.1. Three kinds of laser were used in this research, N<sub>2</sub> laser which was designed and constructed in our laboratory[45], XeCl excimer laser (Questek S-2000) and TEA CO<sub>2</sub> laser (Shibuya Co. SQ-2000). Usually these laser were operated at a repetition frequency of 5 Hz or 10 Hz. The pulse energy used for plasma generation was varied by using attenuators for N<sub>2</sub> laser and XeCl excimer laser, and by using aperture with different area for TEA CO<sub>2</sub> laser. The laser light was focused by a quartz lens (f=100 mm) or Zn Se lens (f=100 mm) through a quartz window, CaF<sub>2</sub> window or ZnSe window on to the sample surface.

The sample were placed in a vacuum-tight metal chamber (9 cm x 9 cm x 12 cm), which could be evacuated with a vacuum pump and filled with air or noble gas (He, Ar) at the desired gas pressure. Gas flow through the chamber was regulated by a needle valve in the gas line and a valve in the pumping line. The chamber pressure was measured precisely with the use of a Pirani gauge or digital pressure gage. Usually successive bombardment of the laser was made under rotating the target at 1 rpm in order to maintain the shape and the emission intensity of the secondary plasma, thus producing a channel of about 20 mm in diameter on the surface of the target. A Zn plate and Cu plate (Rare Metallic Co., 99.99 %) were mainly used in the experiment to examine the characteristics of the plasma. When quantitative analysis was performed, carbon steel standard samples (JSS low-alloy steel 150-155, BAS carbon steel 433-435) were mainly used.

The radiation of the laser-induced plasma was observed at a right angle to the laser beam with the aid a lens (f=100 mm) or two set of quartz lenses (f=150 mm) by making a 1:1 image of the plasma onto the entrance slit of a monochromator(Nikon P-250). The slit height of the monochromator was set at 2 mm in order to limit the observation zone of the plasma. When the emission spectrochemical analysis was performed with the secondary plasma,

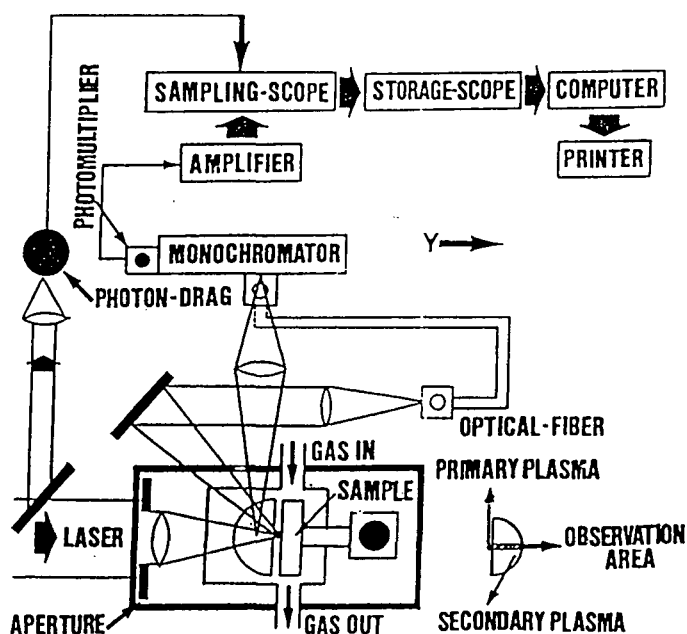


Fig. 1 Schematic representation of the experimental setup.

another monochromator (Jobin-Yvon HRS-2,  $f=640$  mm, 2400/mm) was used to improve the spectrum resolution, and the slit height was set at 15 mm.

The electric signal from the photomultiplier was fed through a wide-band preamplifier (NF Electronic Instrument, BX-31) to a sampling scope (Iwatsu, SAS 601-B), whose trigger signal was made from the part of the laser light with the use of a biplanar phototube for  $N_2$  and XeCl excimer laser or photon-drag detector for TEA  $CO_2$  laser. When time-integrated emission signals were obtained, a 500-k $\Omega$  resistor was attached to the photomultiplier, and the time axis of the sampling oscilloscope was fixed at 50  $\mu$ s. The signal from the sampling oscilloscope was memorized by a digital storage scope (Kikusui, DSS 6522) and sent to a personal computer through an interface.

In the measurement of time-resolved spatial distribution of the emission line, a 500- $\Omega$  external resistor was used for the photomultiplier, the time axis of the sampling oscilloscope was fixed at a desired time, and the stage on which the chamber and the focusing lens were fixed was moved at a speed of 32 mm/min in the direction of the laser

beam. The trigger signal of the digital storage scope was synchronized with the start of the stage movement with the aid of an optical switch. This new technique for observing the spatial distribution of the emission line of the plasma is very valuable because, without using expensive equipment, such as an high speed streak camera, we can carry out a spectroscopic study on the dynamic process of the laser plasma with fairly high precision.

In some limited experiments in this research OMA system (Optical Multichannel Analyzer system, Atago Macs-320) was also used. It consists of a 0.32 m focal length spectrograph with a grating of 1200 grooves/mm, a 1024-channel photodiode detector array, and a micro-channel plate image intensifier. In this case, the light emitted from the laser plasma was collected by an optical fiber.

### 3. Generation of Shock Wave Plasma and Its Characteristics

#### 3.1. Feature of the plasma

When the  $N_2$  laser pulse was focused on copper

target at 1 atm, the small plasma with a diameter about 2 mm is produced with intense continuous spectrum because of the generation of a high-density plasma. Below about 50 Torr we can see the secondary plasma which shows characteristic green color due to neutral copper atoms clearly discriminated from the primary plasma. The secondary plasma has a semi-spherical shape, and the radius of the plasma become larger with decreasing the pressure.

Figure 2 shows the series of the laser plasma observed when the N<sub>2</sub> laser radiation from the left-hand side is focused by a lens on the surface of a copper plate in air at various pressures; (a) is for 50 Torr (b) for 10 Torr, (c) for 4 Torr, (d) for 2 Torr, (e) for 1 Torr, (f) for 0.4 Torr and (g) for 0.2 Torr. The edge of the secondary plasma become vague when the pressure is reduced below 0.2 Torr as shown in (d). The color of the secondary plasma changes depending on the host elements of the sample; for zinc plate the color is magenta, for iron plate white, for aluminum very faint color because Al neutral atom does not have strong emission line in the visible region. When the sample contains Na in high amount such as NaCl pellet it gives bright orange

color[31], also when it contains Li in high concentration we can see beautiful red color[38].

We can qualitatively interpret the fact that the size of the secondary plasma changes with gas pressure according to our shock wave model. We assume the secondary plasma is excited by a shock wave, which will be discussed later. The relationship between the velocity,  $c$ , of the blast wave (shock wave induced by a point explosion) and the front position,  $r$ , of the blast wave can be derived as follows[23].

$$c = \frac{2}{5} \left( \frac{E_0}{\alpha \rho} \right)^{0.5} r^{-1.5} \quad (1)$$

where  $E_0$  is the initial explosion energy,  $\rho$  is the density of the surrounding gas, and  $\alpha$  is a constant involving  $\gamma$ , the ratio of the specific heat of the gas. The velocity of the shock wave decreases as the wave expands. Simultaneously, the heating effect due to the shock wave decreases, which results in a decrease in the temperature of the secondary plasma generated behind the shock wave. Taking  $c_1$  as the limiting velocity of the shock wave below which the emission of the secondary plasma disappears, we get a linear relationship between  $\log$

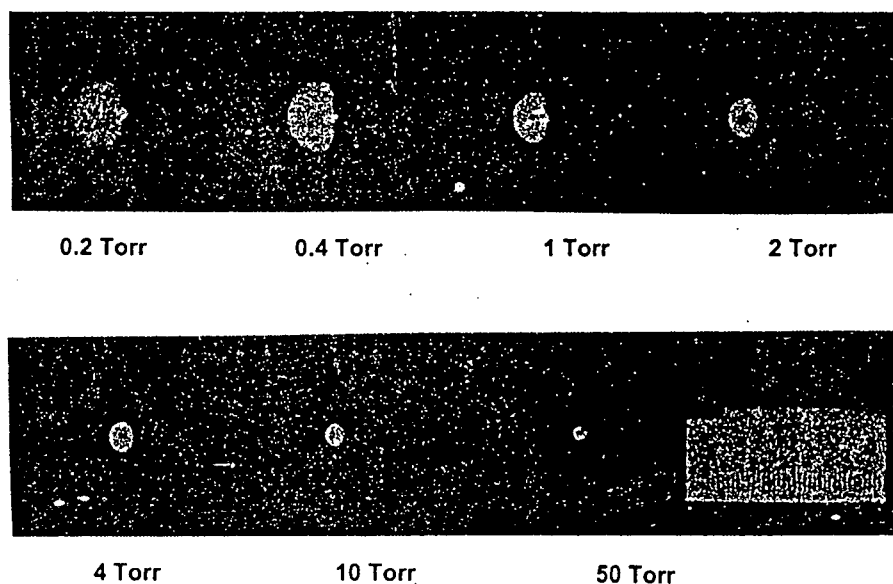


Fig. 2 The induced plasma when N<sub>2</sub> laser is focused on a copper target at 50 Torr (a), 10 Torr (b), 4 Torr (c) and 2 Torr (d), 1 Torr (e), 0.4 Torr (f) and 0.2 Torr (g).



$r_1$  and  $\log c_1$  with a slope of  $-1/3$ , where  $r_1$  is the size of the secondary plasma. We confirmed that this equation explains well the result on the secondary plasma produced by  $N_2$  laser irradiation. Also similar effect of the surrounding gas pressure on the size of the secondary plasma was obtained for XeCl excimer laser. However for TEA  $CO_2$  laser we could not increase the pressure above several Torr because of the occurrence of gas breakdown.

It should be noted that even when we reduced the pulse energy to around 1 mJ, still we can make the same kind secondary plasma, though the radius of the secondary plasma become very small. Important requirement to make secondary plasma is high power density which exceeds the value of about  $10^9$  W/cm<sup>2</sup>. It should be emphasized that when we use high power TEA  $CO_2$  laser with a pulse energy of about 3 J, a very big secondary plasma is produced; the size is almost the same as that of a baseball ball. The relationship between the pulse energy of the laser light and the plasma size is also interesting problem. In general, the plasma size increases with the pulse energy of the laser light. In order to explain this, we can also apply Eq. (1). From this equation we can derive  $r_1$  is proportional to the energy  $E^{1/3}$ . In approximation, explosion energy  $E$  is assumed to be proportional to the pulse energy of the laser light. Therefore, we can say the volume of the emission region of the secondary plasma is proportional of the laser pulse energy. In fact, it seems that this relation is fulfilled in the plasma induced by excimer laser irradiation with pulse energy between 10 and 100 mJ.

It is also interesting to see the change of the plasma feature when we intentionally make defocusing on the sample. It was demonstrated that when XeCl excimer laser light was defocused to make rather large spot size on the surface of zinc plate, the shape of the secondary plasma changes to cylindrical shape rather than semi-spherical shape. For some limited analytical purpose the secondary plasma with such cylindrical shape is also useful to increase the detection sensitivity or to reduce self-absorption effect.

### 3.2 Primary plasma

The primary plasma is the source of the secondary plasma. From the primary plasma atoms gush with high speed, and compress the surrounding gas to form shock wave. Therefore, to know the characteristics of the primary plasma is also important when we use the secondary plasma as the source of the spectrochemical analysis.

Fig.3 shows the time correlation between the instant of the bombardment of the  $N_2$  laser light and the generation of the primary plasma. The time history of the emission of the primary plasma, which emits a continuous spectrum, was monitored at 495.0 nm. It is seen that the primary plasma begins to emit within a few nanoseconds after the beginning of the bombardment of the laser light, and it ceases within about 30 ns; in general the time duration of the primary plasma is a few times longer than that of the half width of the laser pulse. It is seen from the time behavior of the Cu I 521.8 nm line that immediately after the cessation of the emission of the primary plasma, atoms gush from the target, producing the second plasma.

Fig.4 shows the time-resolved emission spectra in the visible region of the primary plasma obtained for  $N_2$  laser irradiation on the sample of low-alloy steel, brass, copper and platinum targets at different delay times ( $t=5, 10, 20$  and  $30$  ns) after the formation of the primary plasma[25]. It is recognized that the primary plasma emits a continuous emission spectrum for a period of about 10 ns, and the spectral distribution is almost independent of the type of target. We also detected the time-resolved emission spectra of the primary plasma using TEA  $CO_2$  laser[42]. By assuming that the light from the primary plasma is due to black-body radiation, the temperature of the primary plasma can be estimated to be around 8000 K using the Wien's displacement law.

Fig.5 shows the relationship between the power of the  $N_2$  laser and the intensity of the primary

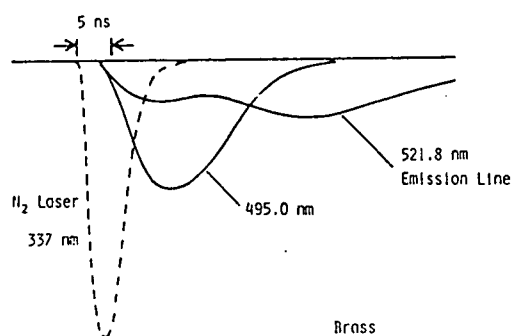


Fig.3 Time correlation between the instant of the bombardment of the laser light and the generation of the primary plasma when  $N_2$  pulse was focused on brass target.

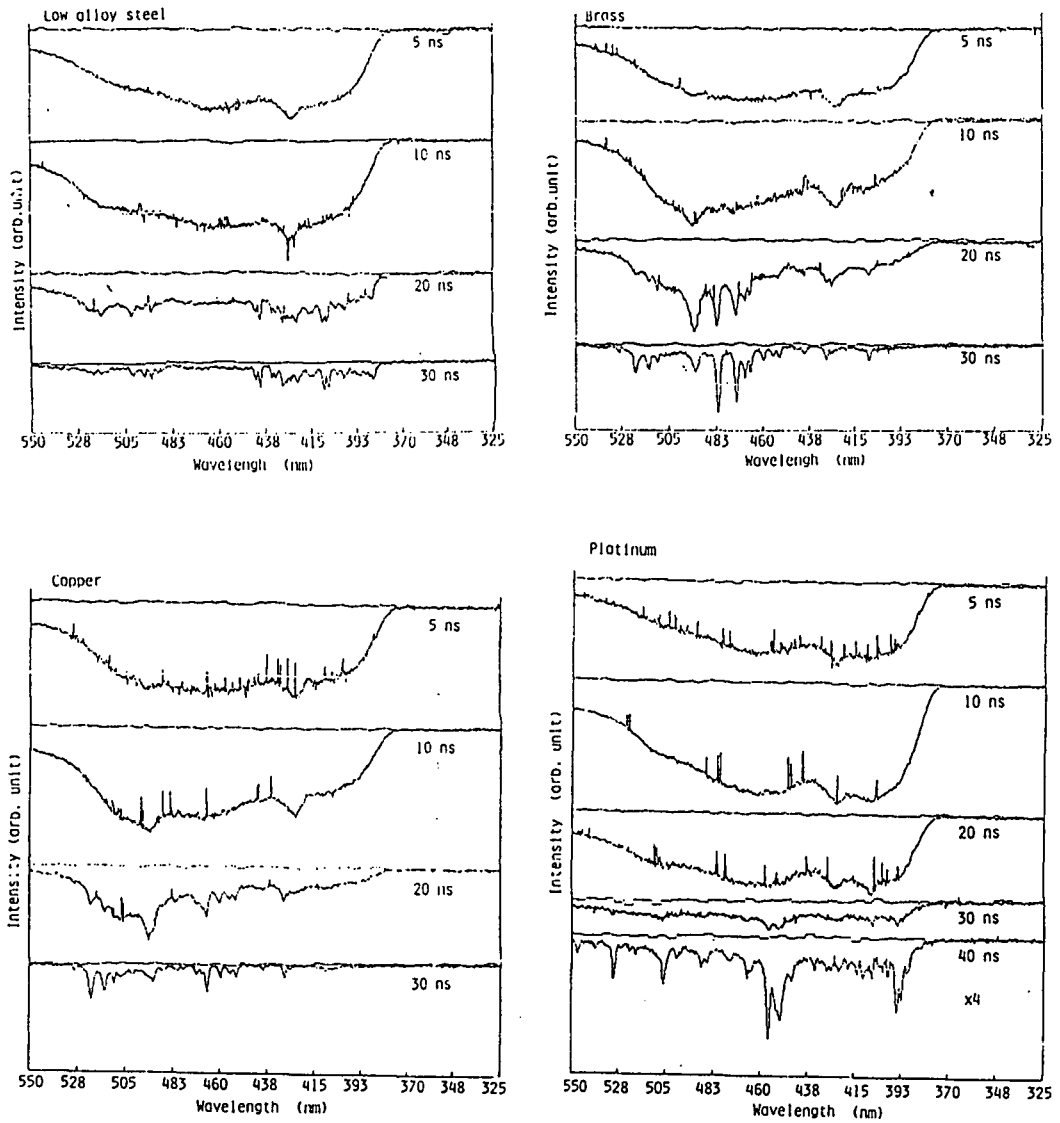


Fig. 4 Time-resolved emission spectra in the visible region of the primary plasma obtained for  $N_2$  laser irradiation on the sample of low-alloy steel (a), brass (b), copper (c) and platinum (d) at different delay times: UV region emission light was cut off by a filter.

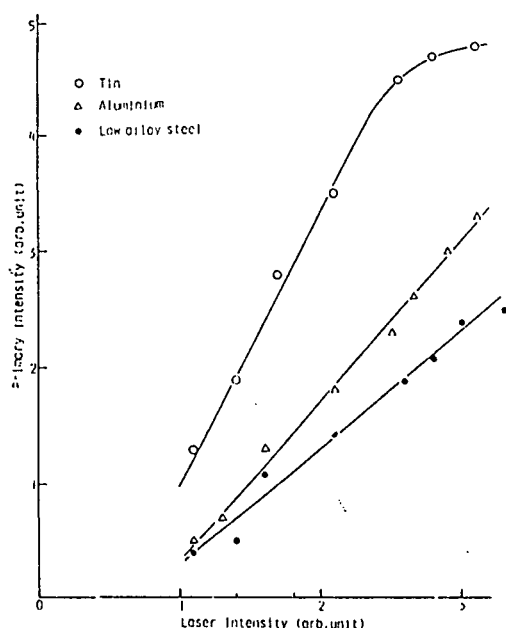


Fig.5 Relationship between the power of the N<sub>2</sub> laser and the intensity of the primary plasma on three different targets: A, tin; B, brass and C low-alloy steel.

plasma[25]. It is likely that the intensity of the primary plasma is highly dependent on the thermal properties of the target, such as the melting point, the latent heat and thermal conductivity. In all instances, however, the intensity of the primary plasma increases linearly with the power of the laser after the threshold at which the generation of the primary plasma takes place. It can also be observed by the naked eye that the size of the primary plasma and the power of the laser has close correlation; the higher the power of the laser light, the bigger the size of the primary plasma. These features are always noticed regardless the kind of the pulse laser used in this work.

The relationship between the intensity of the primary plasma and the vaporized amount of the target material was also examined. As the result it was shown that there is a linear relationship between them[25].

It was proved experimentally using N<sub>2</sub> and XeCl excimer laser that the emission intensity of the

primary plasma scarcely depend on the pressure of the ambient gas in the range around from 0.1 Torr and 50 Torr in air. In contrast to this, Piepmeier et al. demonstrated using Nd:YAG laser that the laser pulse energy is partly absorbed by the plasma produced in the surrounding gas near the focusing point[10]. This shielding effect is induced by the absorption process of the laser light in free-free transition of electrons.

The absorption coefficient,  $K$ , due to the free-free transition of electrons can be expressed as follows

$$K = N/\omega^2\tau \quad (2)$$

Where  $N$  is a density of electron in the initial plasma,  $\omega$  is a frequency of the laser light, and  $\tau$  is a function of the electron temperature, the plasma density and the degree of ionization[16]. As known from Eq. (2), with increasing the wavelength of the laser light the absorption coefficient increases. Therefore, when we use TEA CO<sub>2</sub> laser for plasma generation, the shielding effect become conspicuous because of its long wavelength. The shielding effect is more remarkable for metal samples; It is believed that in case of metal samples electron is easily ejected from the surface by multiple photoelectron effect, and the electron absorb the laser light by free-free transition. In fact, for metal samples evaporated amount from the target decreases with increasing the pressure of the surrounding gas, and above 10 Torr strong gas breakdown takes place, and almost no crater formation is observed.

### 3.3 Emission Spectrum of Secondary Plasma

Fig. 6 shows the spectral distribution of the secondary plasma taken by the time-integrated method at different positions (5, 10, 15, 20, 25 and 30 mm from the target of zinc plate) when a XeCl excimer laser light with a pulse energy of 70 mJ was focused on the target at an ambient gas pressure of 200 Pa in air[34]. The image of the secondary plasma was made on the entrance slit, and the slit height was 2 mm. It is observed that the intensity of the continuous emission spectrum is comparatively strong until 5 mm from the surface, but decreases with distance. The emission lines due to Zn ions are observed only at positions close to the target. It should be noted that, above 15 mm from the target, only neutral emission lines are observed. The excitation energy of the Zn (I) 480.1 nm is 6.6 eV, and Zn(I) 636.2 nm is 7.7 eV. Therefore, we can say neutral atoms are highly excited in the secondary plasma. In case of N<sub>2</sub> laser induced plasma, almost no ionic emission line is observed.

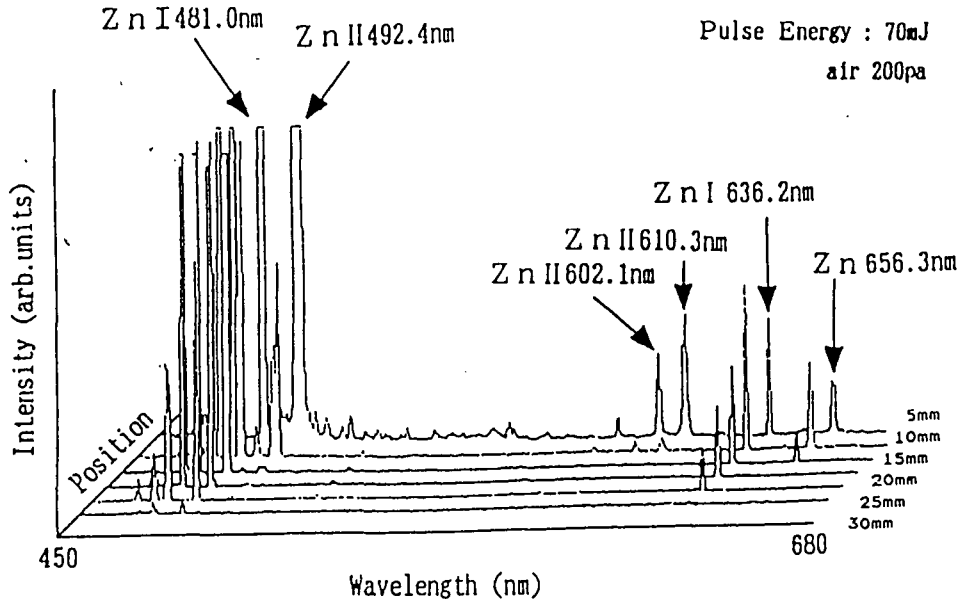


Fig. 6 Time-integrated emission spectrum of the secondary plasma taken at various positions from the target when XeCl 70 mJ pulse was focused on Zn target.

In contrast to this when we use high power TEA CO<sub>2</sub> laser with a pulse energy of 500 mJ, ionic emission lines can be seen appreciably even at 12 mm from the surface[42].

#### 3.4 Pressure Dependence of the total emission intensity of Secondary Plasma

The pressure dependence of the total emission intensity of the secondary plasma is important not only for practical application to spectrochemical analysis, but also for clarifying the mechanism of the production of the secondary plasma.

In order to obtain spatially integrated total emission intensity of the secondary plasma, we employed the following equation[22,34].

$$I_{total} = \int \pi y l(y) dy \quad (3)$$

This was derived considering the symmetrical shape of the secondary plasma, where  $l(y)$  is the observed emission intensity at position  $y$ . Using this equation we examined how the total emission intensity changes with the pressure of the ambient

gas for N<sub>2</sub> laser and for XeCl excimer laser. It was observed that there is an optimum pressure at around 1~10 Torr to give maximum in total emission intensity. Also it should be emphasized the fact that under the constant gas pressure the spatially integrated total emission intensity of the secondary plasma increases linearly with the laser pulse energy after the threshold.

Another method to obtain the total emission intensity of the secondary plasma is to collect the emission directly by the mirror of the monochromator through a slit without using the imaging lens[40]. Fig.7 shows the result obtained by this method for the ambient gas of air. The time and spatially integrated emission intensity increases with pressure up to about 10 Torr and, after that decreases with pressure. By the separate experiment using N<sub>2</sub> laser we demonstrated that below 1 Torr the emission intensity drastically decreases with lowering the pressure. Fig. 8 shows the comparison of the intensity for various gas kind.

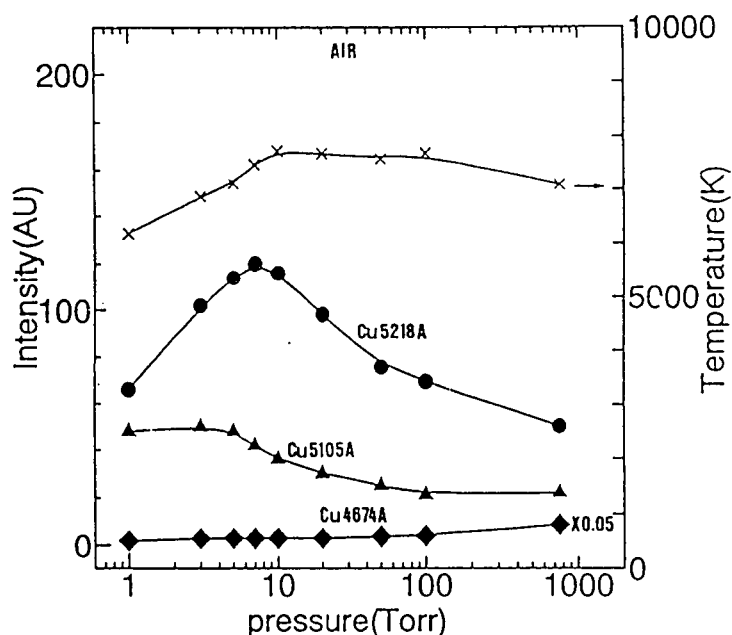


Fig. 7 Spatial and time integrated total emission intensity of Cu(I) 521.8 nm, Cu(I) 510.5 nm and Cu(II) 467.4 nm as a function of pressure when XeCl 10 mJ pulse was focused on Cu target.

It should be noted that the emission intensity for noble gas is higher than air. However, the difference is not so much, at most two times. Therefore, in usual analytical application we can choose air as the surrounding gas. The steep reduction of the emission intensity observed for He is probably attributed to the cooling effect due to its high thermal conductivity of He gas[14]. For TEA CO<sub>2</sub> laser we cannot obtain similar pressure dependence because of the shielding effect taking place under the TEA CO<sub>2</sub> laser irradiation as described in 3.2.

### 3.5 Time-Resolved Spatial Distribution of the Secondary Plasma

Basov et al.[47,48] proved for the first time the generation of a shock-wave by a laser pulse irradiation. They used high power Nd glass laser (6 J, 15 ns), and observed a thin shell structure using shadowgraph and schlieren photographic technique. Bobin et al.[49], Hall [50] and Emmony [51] employed high-speed streak cameras to detect

the emission front associated with the shock wave. Hughes [52] reviewed these laser-induced shock wave. However, no report has been made by other researchers on the application of laser-induced shock wave to spectrochemical analysis. In our study we use rather lower pulse energy to excite the shock wave compared to the experiments made by other researchers. Therefore, in our case shadowgraph and schlieren technique cannot be applied to detect the shock wave because density jump induced by the shock wave is very faint. We can use only the information from the emission of the secondary plasma and its time-development for proving the generation of the shock wave. On the basis of our characteristic technique of time-resolved emission spectroscopy using XeCl excimer laser and TEA CO<sub>2</sub> laser, we demonstrated that atoms in the secondary plasma are excited by the shock wave.

Fig. 9 shows the time-resolved spatial distribution of the intensity of Zn(I) 481.0 nm emission line for two cases of different surrounding gas pressures of

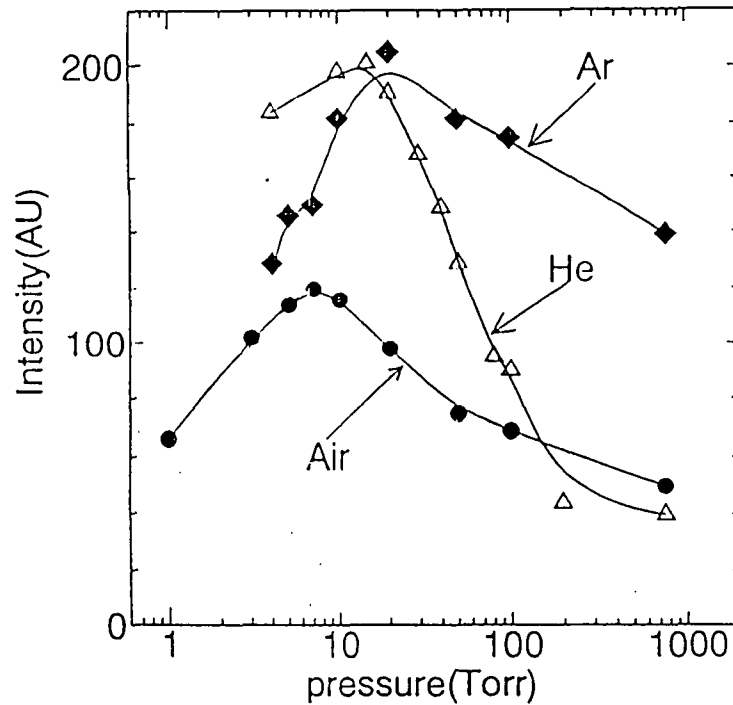


Fig. 8 Spatial and time integrated total emission intensity of Cu(I) 521.8 nm as a function of gas pressures for three different gas kinds, Air, He and Ar when XeCl 10 mJ pulse was focused on Cu target.

air at various times after the initiation of the bombardment of XeCl laser pulse of 50 mJ [34]. At the initial stage of the secondary plasma expansion, a steep jump in the distribution of the Zn(I) 481.0 nm emission begins to develop at 0.4  $\mu$ s for 200 Pa and at 0.2  $\mu$ s for 1000 Pa, as indicated by arrows in the figures. The steep jump means the existence of a contact surface with the shock wave. Fig. 10 shows the relationship between the propagation length of the front of the secondary plasma,  $r$ , and the propagation time,  $t$ . These data were obtained by reading the rising point in each curve in Fig. 9. Fig. 11 is a log-log plot representation based on the data in Fig. 10. A linear relationship between  $\log r$  and  $\log t$  is observed, with a slope of 0.4, which means  $r$  is proportional to the 0.4 power of time.

Sedov [53] derived, for a blast wave, a theoretical

relationship between the propagation time,  $t$ , and the distance of the front from the position of explosion,  $r$ , as follows:

$$r = \left( \frac{E_0}{\alpha \rho} \right)^{1/5} t^{2/5} \quad (4)$$

,where  $E_0$  is the initial explosion energy,  $\rho$  is the density of the surrounding gas, and  $\alpha$  is a constant involving  $\gamma$ , the ratio of the specific heat of the gas. The experimental result shown in Fig. 11 is in good agreement with this equation. However, it should be noted that, at a later stage in secondary plasma expansion, plots of the experimental results deviate from a straight line. This fact may imply that with time the front of the secondary plasma separates from the real front of the blast wave induced in the surrounding gas. In other words, the front of the

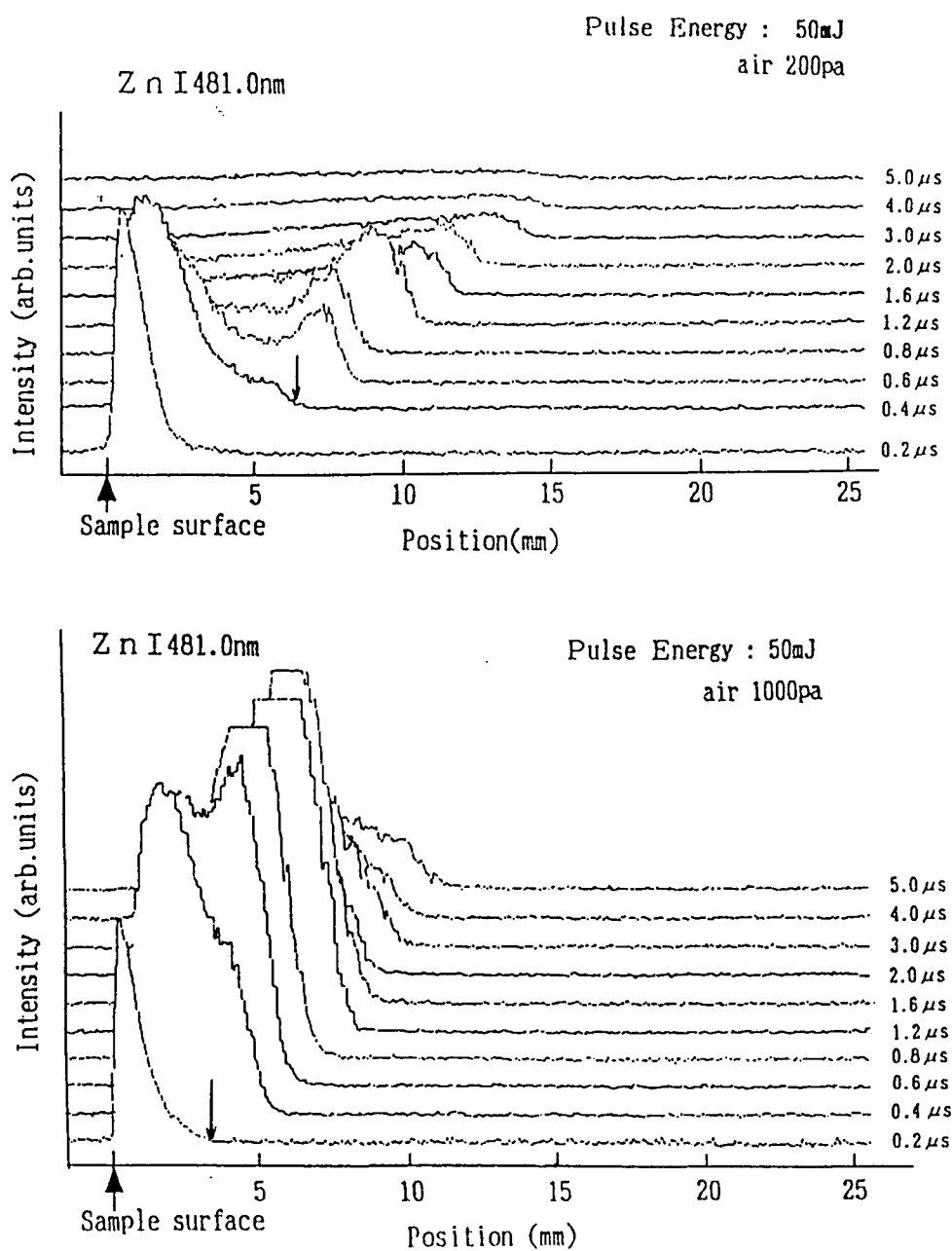


Fig. 9 Time-resolved spatial distribution of Zn(I) at 481.0 nm at various times (a) 200 Pa; (b) 1000 Pa when XeCl 50 mJ pulse was focused on Zn target.

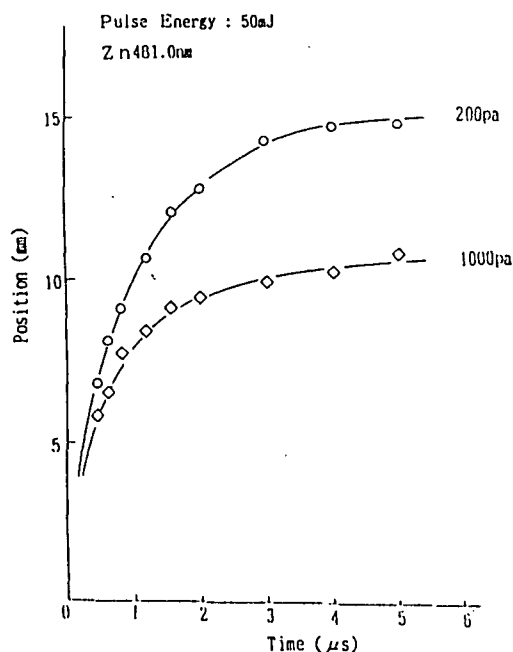


Fig.10 The relationship between the propagation time,  $t$ , and the propagation length of the front of the secondary plasma,  $r$ . This data were obtained from the curves in Fig.9

secondary plasma which consists of gushed atoms might slow down in the course of propagation more rapidly than the real blast wave induced in the surrounding gas. Similar phenomenon can be seen in the bomb explosion experiment using shadow photograph or schrielen photograph technique[54].

Figure 12 shows how the secondary plasma expansion depends on the pulse energy of the laser light. The position of the front of the secondary plasma were plotted as a function of the pulse energy in a log-log scale at two different times, 0.4  $\mu$ s and 1.2  $\mu$ s, after the laser bombardment. The pressure of the surrounding gas was kept at 200 Pa. From this result, it is seen that the propagation length of the secondary plasma is proportional to the 0.2 power of the pulse energy of the laser light under the condition that the time and the pressure of the surrounding gas are fixed. We can say this result also coincides with the Eq.(4);  $E_0$  is approximately proportional to the pulse energy of

the laser light.

Experiments to examine the relationship between the propagation length of the front of the secondary plasma and time were also made using  $N_2$  laser (6 mJ), XeCl excimer laser 10 mJ and Dye laser 5 mJ. Similar curves with 0.4 slope in log-log plot between  $t$  and  $r$  were obtained in the early stage of the secondary plasma expansion under these laser pulse irradiation. However, the rising of the front emission signal was not so steep as shown in Fig. 9, because of the generation of weak shock wave [22,23].

### 3.6 Shock Wave Generation under atmospheric pressure

As we mentioned above, it is supposed that the front of the secondary plasma and real shock front separate with time at the later stage of the plasma expansion. This phenomenon will become more apparent when the pressure of the surround gas is increased to near atmospheric pressure. In such case the gushed atoms soon be slowed down, but the shock wave would still propagate in the surrounding gas. Under this condition we may expect to detect the shock wave itself by shadow photograph method or schrielen photograph method because of its high gas density in the surrounding gas. We demonstrated the generation and expansion of the blast wave by means of shadow graph using He-Ne laser as a probe light.

Fig.13 shows the observed time history of the probe light setting at various distance from the surface of the target when XeCl laser pulse of 18 mJ was focused on the metal target under atmospheric pressure. The signal change observed in the figure is due to the arrival of shock wave, by which refractivity of the gas is changed instantaneously. It is seen that the shock wave move with time. From these data the thickness of the high density region is estimated to be about 0.2~0.3 mm, and the slope of log-log curve is about 0.45. We regards this as the evidence of the generation of the shock wave. We also confirmed that shock wave is produced even when we used small pulse energy as low as 3 mJ. On the basis of this experiment, we can say our assumption of the generation of the shock wave under the reduced pressure is possible, though the pressure is different in two cases.

### 3.7 Shell Structure in the Secondary Plasma

In order to know the excitation mechanism of the secondary plasma, the data on the emission



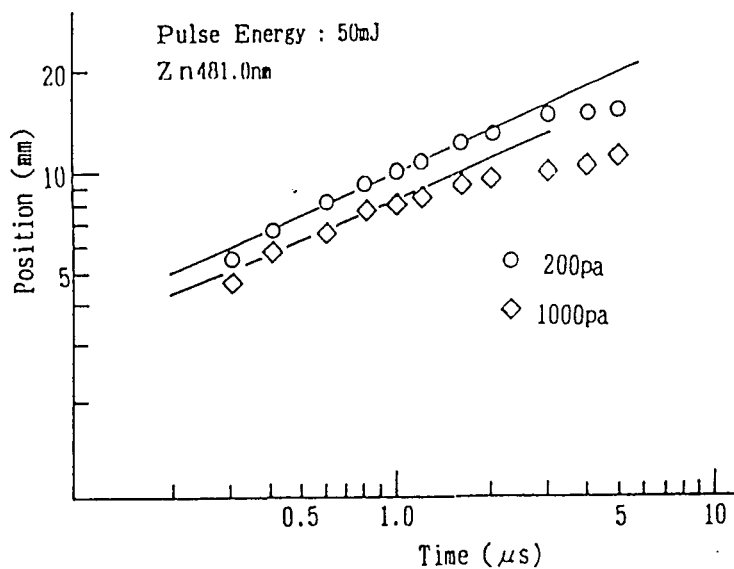


Fig. 11 The relationship between the propagation time,  $t$ , and the propagation length,  $r$ , in a log-log plot.

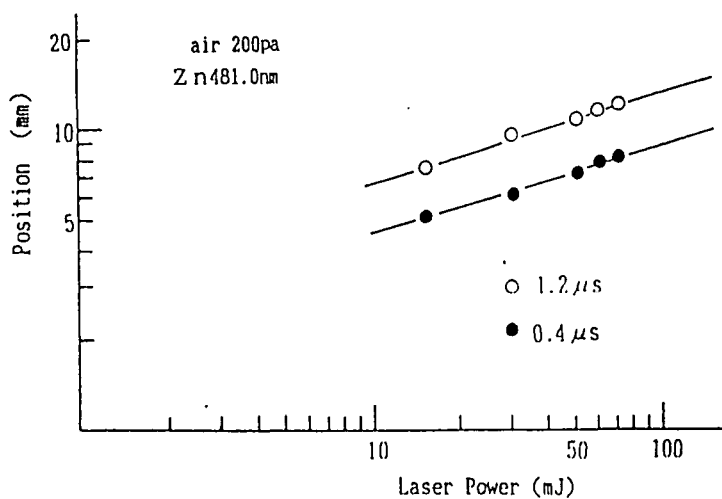


Fig. 12 The relationship between the propagation length of the front of the secondary plasma and the laser power in a log-log plot.

Laser Power 18mJ

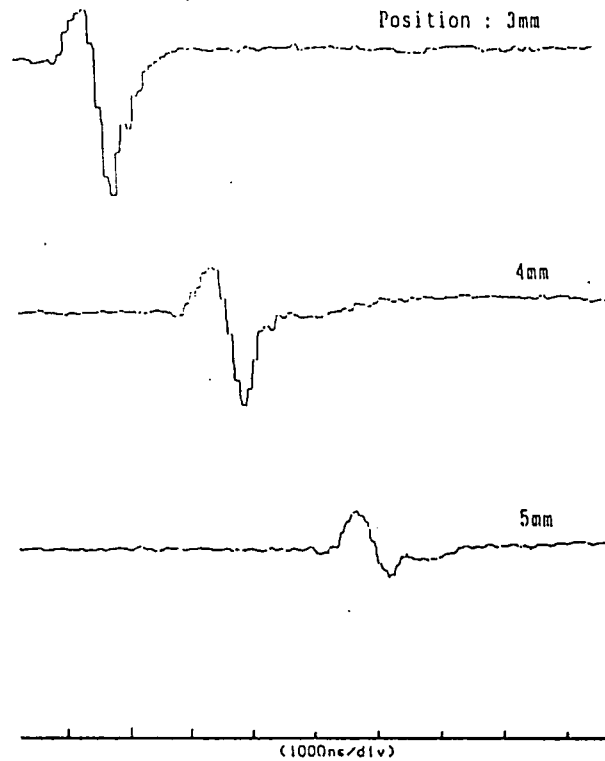


Fig. 13 Time history of the signal of a He-Ne probe light used for shock wave detection at various distance from the surface when XeCl laser pulse of 18 mJ was focused at 1 atm.

structure of the plasma is indispensable. However, such measurement is rather difficult because the structure of the emission profile cannot be determined directly because of the overlapping in the emitted light coming from inside and outside of the plasma, which is always encountered when spectroscopic measurement is made. Fortunately our plasma has good symmetry with a hemispherical shape. In such case we can employ Abel conversion method. Also our plasma is very stable in the shape and the emission intensity under the repeated irradiation on the rotating target.

Therefore high precision measurement can be made by means of sampling method. If single shot measurement were made, such high precision measurement would not be realized.

Fig. 14 is the illustration to explain the principle of the Abel conversion. We can measure the emission intensity,  $I$ , as a function of  $y$ .

$$I(y) = 2 \int_0^{(a^2 - y^2)^{1/2}} \epsilon(r) dx = 2 \int_0^{(a^2 - y^2)^{1/2}} \frac{\epsilon(r)r}{(r^2 - y^2)^{1/2}} dr \quad (5)$$

By the Abel conversion, we can obtain the emission

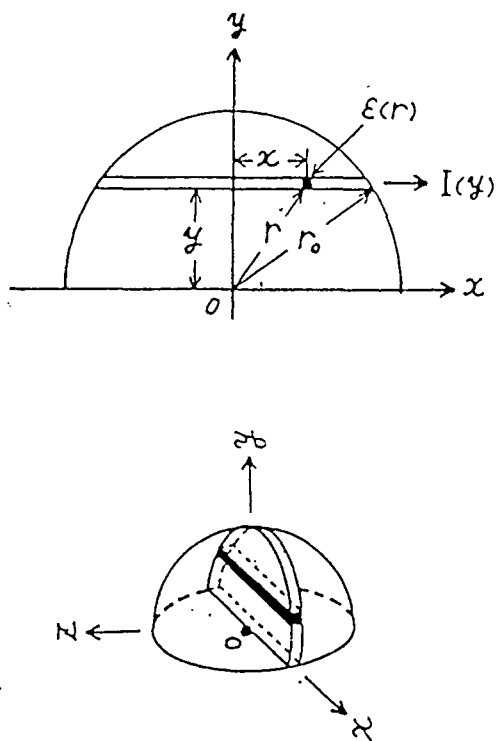


Fig.14 Illustration to explain the principle of the Abel conversion on the plasma with a hemispherical shape.

intensity as a function of r,

$$\epsilon(r) = -\frac{1}{\pi} \int_0^r \frac{I'(y)}{(y^2 - r^2)^{1/2}} dy \quad (6)$$

, where  $I'(y) = dI(y)/dy$ . In general this calculation is made using computer [55,56]. In this paper, we employed more convenient and simplified method proposed by Bockaten [57]. In the method, the radius of the plasma is divided into n equal division. Then  $y_k = k r_0/n$  ( $k=0,1,2, \dots, n-1$ ).  $r_0$  is the radius of the plasma.  $I_k$  is the intensity observed at division k. The coordinate to show the distance from the center of the plasma is  $r_j = j r_0/n$  ( $j=0,1,2, \dots, n-1$ ), and the emission intensity at the position  $r_j$  can be expressed as

$$\epsilon_j = \frac{1}{r_0} \sum_{k=0}^{n-1} a_{jk} I_k \quad (7)$$

, where  $a_{jk}$  is the coefficient. We calculated using

this equation for  $n=20$  of which coefficient was already calculated by Bockasten.

Fig. 15 shows the time-resolved spatial distribution of the intensity of the Zn neutral emission line (481.0 nm) when TEA CO<sub>2</sub> laser pulse was focused on Zn target. Fig.16 shows the result of Abel conversion for different time after the initiation of the laser bombardment. It is seen that the emission region is localized in a thin region, and move with time. The movement of the shell structure also coincide with the Eq.(4). This existence of shell structure and of its movement observed in this experiment are strong evidences to support our shock wave model. In the case of N<sub>2</sub> laser we cannot make the measurement on the time-resolved spatial distribution because the emission intensity is too weak to detect the signal.

### 3.8 Production of Ions

In ordinary atomic emission spectrometry, atoms are excited by means of an electric discharge. In general, in atomic emission spectrometry the detection limit of the elements is mainly determined by the intensity of the background emission, which arises from the process of electron-ion recombination or the electron-ion Bremsstrahlung [58]. In plasma induced by the shock wave, the background emission intensity is expected to be considerably reduced, because in shock wave excitation ion production can be suppressed significantly due to its purely thermal process, without employing any electric fields.

Fig.17 shows a comparison of the time-resolved spatial distribution between the Zn neutral emission line (481.0 nm) and the Zn ion emission line (492.4 nm) when XeCl 50 mJ laser pulse was focused at 200 Pa. It should be noted that the point at which the emission intensity of Zn ion line rises is behind that of Zn neutral emission line. This fact means that the ionization of Zn atoms takes place later, as compared to the excitation of Zn atoms; the delay of ion production become larger with decreasing the speed of the front of the secondary plasma, and finally almost no ion production takes place when the speed reduces below a certain value. In contrast to this observation, no disagreement could be detected in the rising point between the emission of Zn(I) at 481.0 nm (6.6 eV) and that of Zn(II) at 307.2 nm (8.1 eV). The delay of ion emission has already been observed in ordinary shock tube experiments; namely, emission of the N<sub>2</sub><sup>+</sup> ion takes place later, as compared to that of the N<sub>2</sub> neutral, when a shock wave moves with high Mach-number

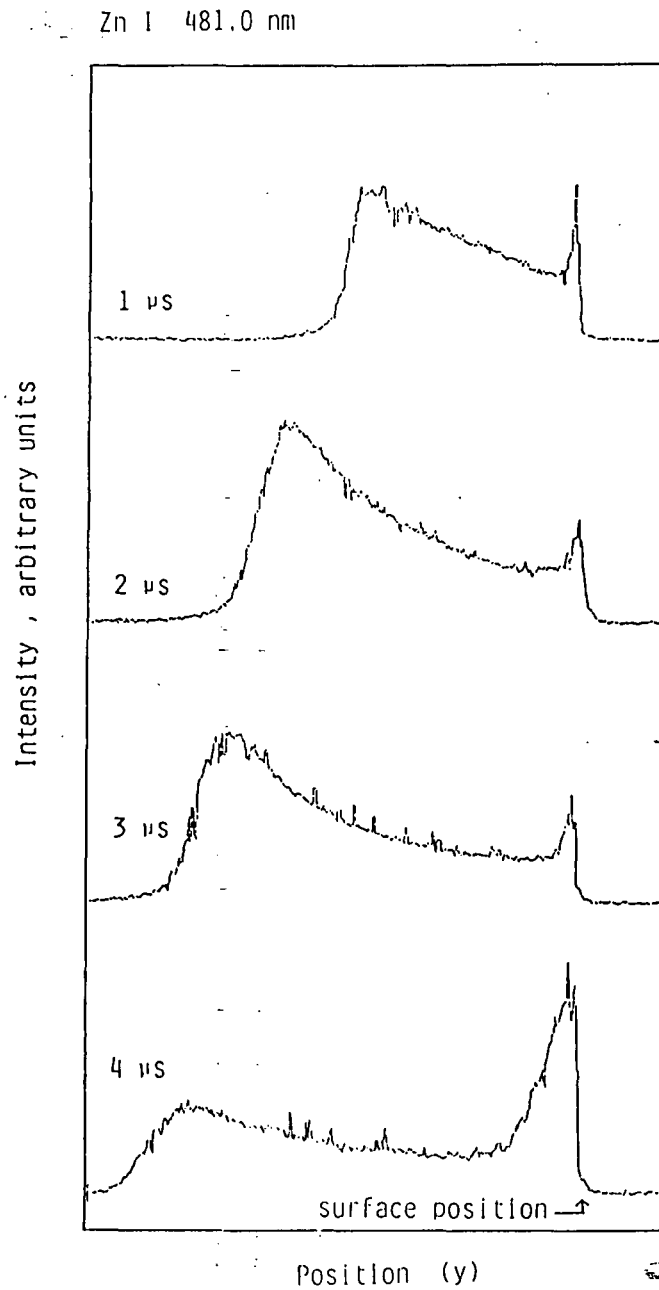


Fig.15 Time-resolved spatial distribution of Zn(I) 481.0 nm when TEA CO<sub>2</sub> laser (500 mJ) pulse was focused on Zn target at 1 Torr.

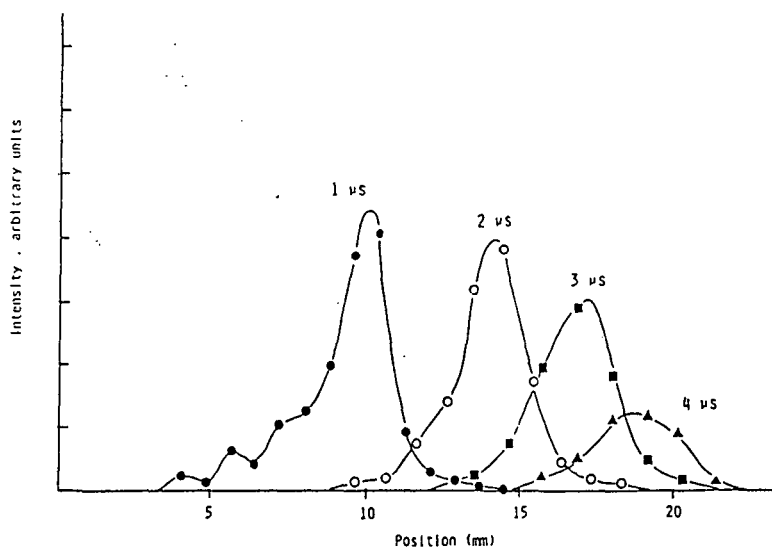


Fig. 16 Time-resolved spatial distribution of Zn(I) 481.0 nm as a function of  $r$ .

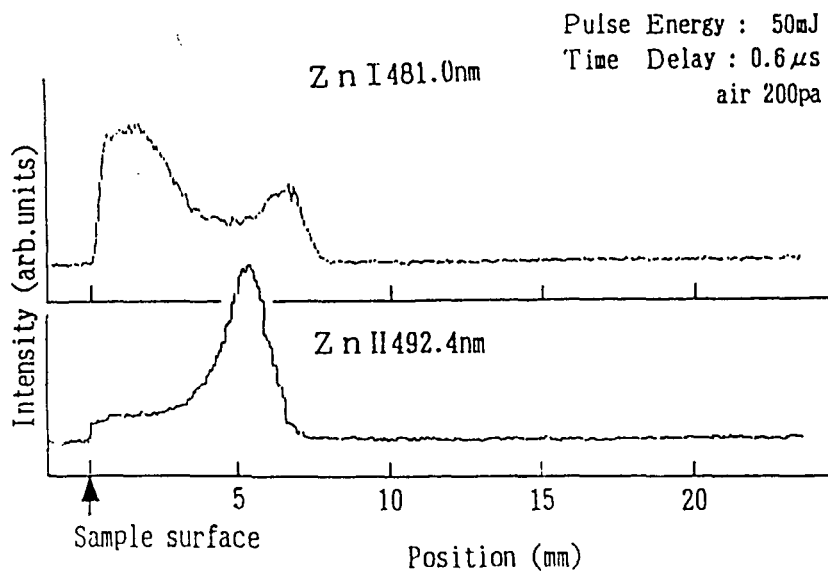


Fig. 17 Time-resolved spatial distribution of the emission of Zn(I) 481.0 nm and Zn(II) 492.4 nm. The measurement was made at 0.6  $\mu$ s under the surrounding gas of 200 Pa when XeCl 50 mJ pulse was focused on Zn target.

in a shock tube filled with low-pressure air [59]. This experimental result also supports the shock wave model to explain the mechanism in forming the secondary plasma.

Silfvast [60, 61] demonstrated that Cd plasma, induced by laser ablation under reduced pressure around 1 Torr, can be used as a laser medium because population inversion takes place by the recombination process between Cd<sup>+</sup> ions and electrons in the plasma. Also there are still many people who believe excitation process of the laser plasma produced under reduced pressure is due to recombination process. However the recombination process cannot be the major process to explain the excitation process of the secondary plasma. This is clearly shown in our experiment on the measurement of time profile of the spatially integrated emissions. Fig.18 shows changes in the spatially integrated emission intensity as a function of time. Curve c is for Zn(I) 481.0 nm and d is for Zn(II) 492.4 nm. The time history of the total emission intensity of the continuous emission spectrum (background emission) was also detected at a wavelength 495.0 nm, where no emission line due to Zn is recognized in the MIT table; this background emission is mainly due to the signal of the primary plasma. It can be seen that the emission line of the ion rapidly decays in a short time, within 150 ns, while the emission line of the neutral atom increases with time with a large time constant. As a result, we can state there is no reversal correlation between the emission intensity of Zn(I) 481.0 nm and that of Zn(II) 492.4 nm line.

Generally speaking, in the case of Laser Induced Shock Wave Plasma the emission of ion is considerably weak compared to the case for the excitation due to electrical discharge. Especially when the pulse energy of the laser light is as low as several mJ, the emission from ions scarcely can be detected. Table 1 shows the comparison of the intensities of the neutral emission lines with those of the ionic emission lines observed in the secondary plasma induced by N<sub>2</sub> laser. The values for arc discharge were derived from MIT table. As described later section, the temperature of the secondary plasma is fairly high showing above 8000K, nevertheless the emission from ion is very weak. This means the low probability in producing ions in the secondary plasma.

### 3.9 Emission of the surrounding gas

In LISPS gas is very important as a damping material for the atoms gushing from the target when

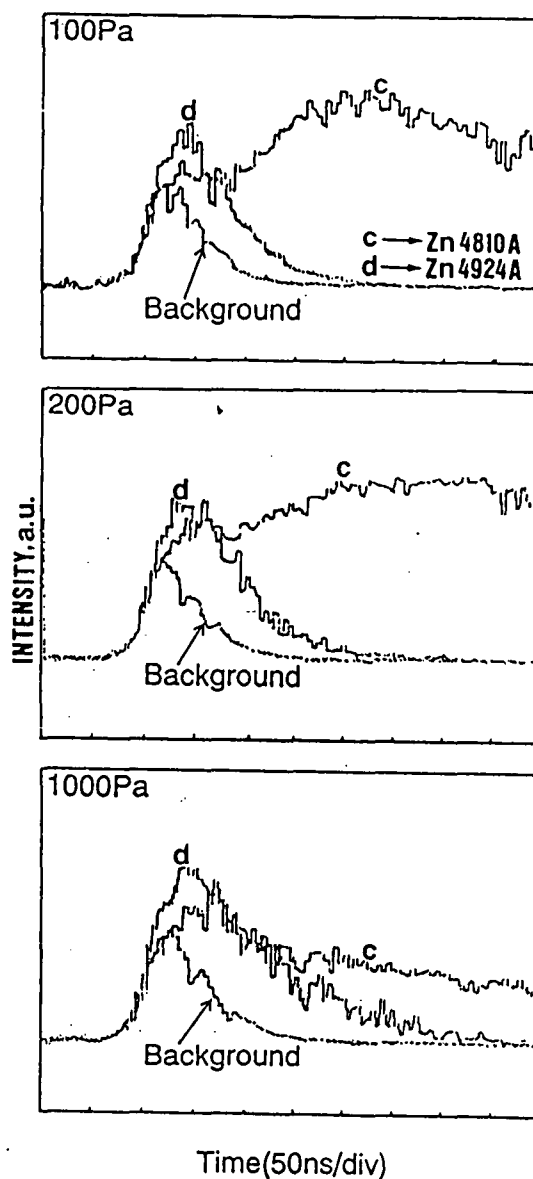


Fig.18 Time history of spatially integrated emission intensity of Zn(I) 481.0 nm and Zn(II) 492.4 nm when XeCl 10 mJ pulse was focused on Cu target. The emission at 495.0 nm was used for monitoring the background emission intensity.

Table 1 Comparison of the intensities of the neutral emission lines with those of the ionic emission lines observed in the secondary plasma induced by N<sub>2</sub> laser. The values for arc discharge were derived from MIT table.

	Wavelength (nm)	Arc discharge	N <sub>2</sub> laser plasma
Cu (I)	406.2	500	500
Cu (II)	467.4	200	0.8
Zn (I)	468.0	300	300
Zn (II)	405.7	80	No detect.
Ca (I)	422.6	500	500
Ca (II)	396.8	500	145

shock wave is produced. Owing to the mechanism of shock wave generation gas density is more meaningful factor than the pressure itself. Gas kind is rather insensitive to the formation of the secondary plasma, and emission from gas is usually very weakly detected in LISPS. In contrast to this, other spectrochemical source such as Grim discharge [62] and ICP [44], depending on the gas kind the plasma has quite different in the characteristics. Also in these spectrochemical source atoms or molecules of the gas are highly excited in the electric field, and strong emission lines are emitted from the gas, which may interfere spectrochemical analysis on other elements.

It is very favorable thing to use the secondary plasma for a spectrochemical analysis because gas gives almost no emission in the secondary plasma. We confirmed weak gas emission from the secondary plasma induced by N<sub>2</sub> laser irradiation. By using high sensitivity of the photomultiplier we barely observed the emission, N<sub>2</sub> 355.7 nm band, N<sub>2</sub> 380.5 nm band for N<sub>2</sub> gas, and He 388.9 nm and 447.2 nm for He [70]. With increasing the energy of the pulse laser used for plasma generation gas emission become notable, but still weak.

When high power TEA CO<sub>2</sub> laser is focused on alkali halide targets, emission from He gas become very strong. This fact seems to imply that electrons and ions are easily generated under the shock wave excitation when alkali halide crystal is bombarded with a high power laser pulse, and He is excited by the electrons.

### 3.10 Background Emission Intensity

In the emission spectrochemical analysis the

detection limit of the elements is strongly influenced by the background emission intensity of the spectrum. The lower the background level, the lower become the detection limit.

The continuous emission spectrum intensity emitted from plasma can be expressed as follows:

$$I_c = (4\pi)^{-1} N_e \sum_z N_z (\gamma_v^z + \sum_n \alpha_{nv}^z) \quad (8)$$

Where  $I_c$  represents the continuous emission intensity at  $\nu$  wavelength,  $N_e$  are electron density and  $\gamma_v^z$  are the Bremsstrahlung emission coefficient for a free electron on the  $Z$  ionization state,  $\alpha_{nv}^z$  is the recombination coefficient of  $n$ th ion energy level at a given wavelength [63]. From the above equation, it is clear that the continuous emission intensity is proportional to the electron number density times the ion density. As we described before, in LSPS ion production is suppressed considerably compared to other discharge excitation method. This is a reason why background emission intensity is low in LISPS.

In Laser-Induced Breakdown Spectroscopy gated OMA system is employed to avoid strong background emission, and S/B (signal vs. background ratio) is improved so as to make good analytical result [5-9]. However, in some cases even when we employ the gating method, S/B can not be improved. Fig.19(a) shows the time-dependent change of the ratio of the emission intensity of Li(I) 610.3 nm to the background emission intensity. This was obtained at 1 atm when 50 mJ XeCl laser pulse was focused on glass target containing Li 1n 20%. It is seen that maximum S/B is at most 12 during the plasma lifetime. Therefore, in such case, we can not get good result on the S/B ratio, even though we employ gating mode in OMA system. However, as shown in Fig.19(b) by decreasing the pressure of the surrounding gas S/B is considerably improved.

Generally speaking, the background emission intensity decreases with increasing the distance of the slit setting from the surface of the target, while the emission line intensity give maximum value at a certain distance from the target. Therefore by choosing the position of slit of the monochromator the optimum position can be searched at which S/B ratio has a maximum. By this method S/B is further improved compared to the case for spatially integrated detection method. Fig. 20 shows how the S/B ratio changes as a function of the position of the slit of a monochromator in various pressures of the surrounding gas. In this experiment XeCl laser pulse was focused on Zn target, and Zn(I) 481.0 nm

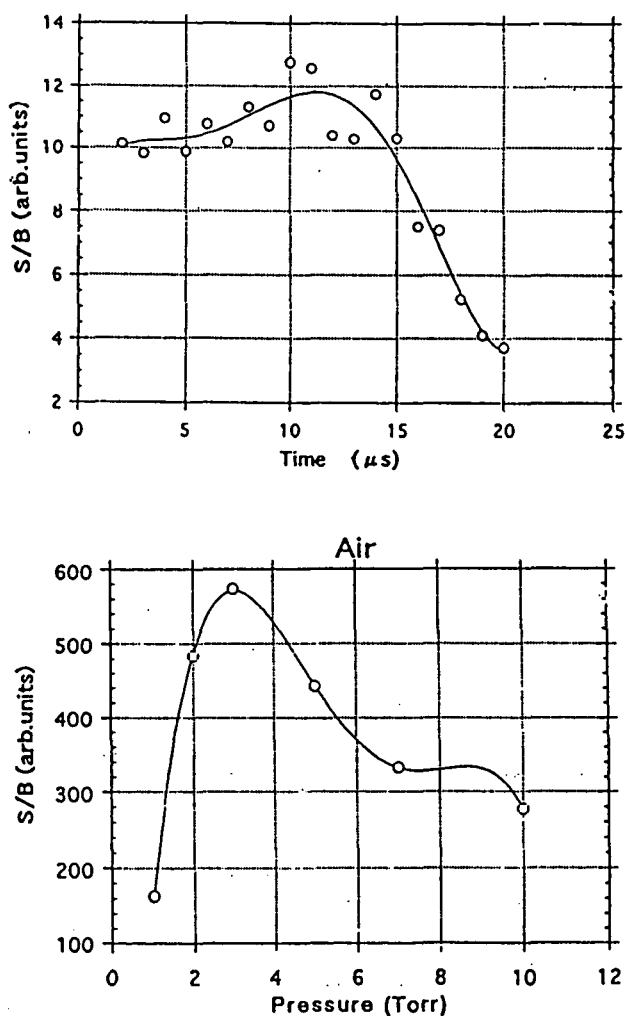


Fig. 19 (a) Time-dependent change of the ratio of the emission intensity of Li(I) 610.3 nm to the background emission intensity, (S/B), produced at 1 atm in air. (b) Pressure dependence of S/B which was obtained by time-integrated mode. These data were obtained when XeCl 50 mJ pulse was focused on a glass containing Li in 20%.

emission line was detected in time-integrated method with a photomultiplier. It should be emphasized that S/B for 200 Pa is higher than that for 1000 Pa, although the Zn(I) 481.0 nm itself is higher for 1000 Pa.

### 3.11 Plasma Temperature

One of the favorite characteristics of the secondary plasma is rather high excitation temperature, which can realize high sensitive analysis. In order to estimate the excitation



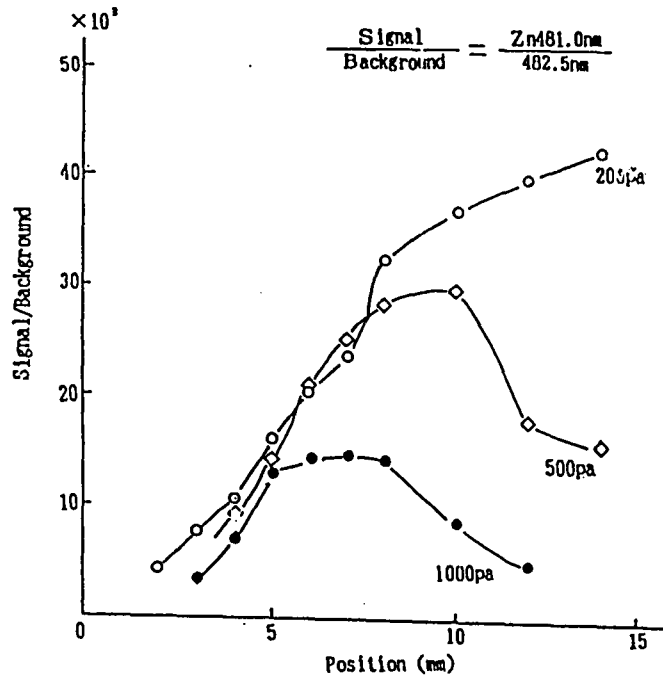


Fig. 20 S/B ratio as a function of the slit position in various pressures of the surrounding gas of air. XeCl laser pulse with 50 mJ was focused on Zn target.

temperature of the secondary plasma induced by  $N_2$  laser irradiation, the line pair of Zn 307.2 nm and 307.6 nm was measured with time-integrated method [23], and the temperature was calculated using the following equation on the assumption that the Boltzman's distribution is fulfilled in the plasma [55].

$$T = \frac{20510}{(2.580 + \log(I_{307.6} / I_{307.2}))} \quad (9)$$

Fig. 21 shows the distribution of the excitation temperature as a function of the distance from the center of the plasma. This was obtained after making Abel conversion. It should be noted that the temperature is as high as around 8000K.

In case of  $N_2$  laser plasma, time-resolved observation is difficult to do because of its totally weak emission intensity. Using excimer laser induced plasma we confirm the Boltzman's distribution. For this purpose iron sample was used,

and emission intensities were measured with time-resolved technique on some emission lines of which coefficient such as transition probability has already known[64]. In order to escape from the problem of overlapping detection of the light emitted between inside and outside, we detected the emission at just front position of the plasma. From the result shown in Fig.22, we can say the plasma at the front region of the secondary plasma has Boltzman distribution with a temperature of 10850 K.

In case of mechanical shock wave generation, it is known that the temperature behind the shock wave is determined by the following equation [65]

$$T = T_0 \left[ \frac{2\gamma M^2}{\gamma + 1} - \frac{\gamma - 1}{\gamma + 1} \right] \left[ \frac{\gamma - 1}{\gamma + 1} + \frac{2}{(\gamma + 1)M^2} \right] \quad (10)$$

where  $T_0$  is the room temperature,  $\gamma$  is the ratio of the specific heats and  $M$  is the Mach number. The comparison of the temperatures estimated by above two different ways was made; the Mach number

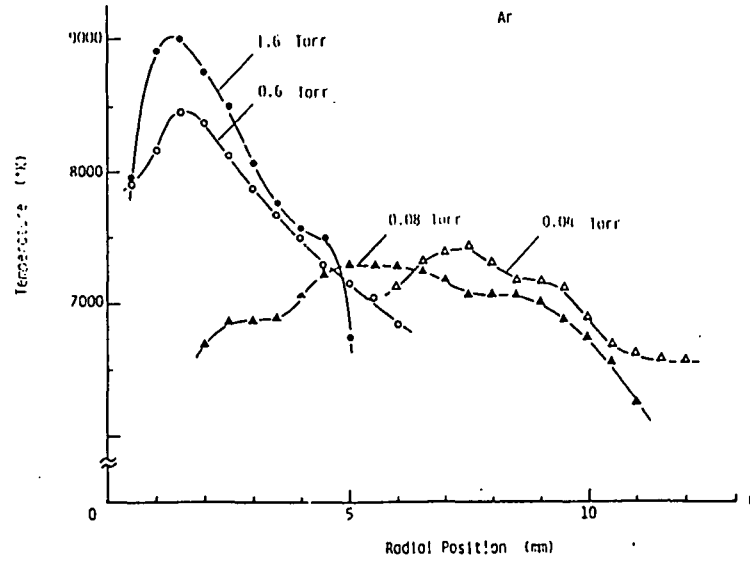


Fig. 21 The distribution of the excitation temperature in the  $r$  direction (after Abel conversion) at various pressure of Ar when  $N_2$  laser was focused on brass target.

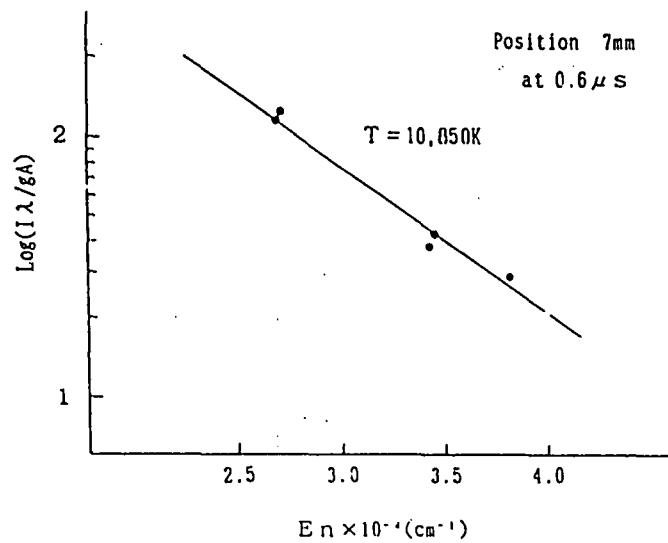


Fig. 22 Boltzmann plot for Fe(I) levels obtained from the secondary plasma induced by the irradiation of XeCl laser pulse (50 mJ) in air at 200 Pa. The measurement was made at 7 mm from the target at the time when the emission signal of the secondary plasma just started.

was replaced by the speed of the emission front of the secondary plasma when the temperature was calculated using Eq.(10). It was shown that there is so much discrepancy between the temperatures calculated by Eq.(9) and Eq. (10). Namely, at the early stage of the secondary plasma the temperature calculated by Eq.(10) is far higher than that obtained by Eq.(9), and at the later stage become opposite. In this stage we cannot explain this well. However, this may be due to the fact that at the early stage the temperature of the gushed atoms is lower than that of shock wave because of insufficient thermal equilibrium, and at the later stage the secondary plasma keep high temperature by retained heat when the temperature at just behind the shock wave already greatly decreases. However, in our preliminary experiment on the shock wave plasma induced by very high power TEA CO<sub>2</sub> laser (about 2J pulse energy), a relatively good coincidence was observed in the temperatures obtained by two different ways. Further studies are required to interpret the excitation temperature of the secondary plasma.

#### 4. Other evidences to support the shock wave model

In order to make clear the excitation process of the secondary plasma from different angle, we intentionally confined the secondary plasma in a small tube, and made colliding the secondary plasma with an obstacle placed in front of the target. Also some qualitative evidences to support the shock wave model are presented in this section.

##### 4.1 Confined plasma

The length of tube used for plasma confinement is 20 mm, the tube cross section is 7 mm x 7 mm. The tube consists of an aluminum block and a glass plate. The emission profile of the confined plasma was observed through the glass window of the tube. The TEA CO<sub>2</sub> laser of 500 mJ pulse was focused through the small tube on the Zn plate which was attached to the aluminum block [32].

The secondary plasma traveled in the tube with a very high speed, and from the exit of the tube free expansion takes place. The transient emission structure was examined using our time-resolved spatial distribution technique, and in Fig.23 the result is shown. It should be noted that the emission intensity distribution drastically changes on the front side of the secondary plasma like a tidal

wave, and the rising points of the emission align in a straight line perpendicular to the Y-axis. This implies that a shock wave with a plane wave structure is formed in the tube. Furthermore it should be noted that the emission takes place only in a limited region of about 3 mm in thickness. Similar phenomenon has already been confirmed in the shock wave produced by mechanical way in a shock tube when the shock speed is so fast as to give rise emission from the gas [59].

##### 4.2 Reflection and Diffraction

In order to prove the fact that hydrodynamic effect is essential in the excitation process of the secondary plasma, we tried to detect the reflection and diffraction of the secondary plasma [33]. For this purpose, an obstacle with a shape of wedge was placed in front of the target. As illustrated in the Fig. 24, the appearance of the secondary plasma changes from the ordinary free expansion plasma proving the reflection of the shock wave.

Fig.25 shows the comparison of the time-integrated spatial distribution of the intensity of neutral and ion emission lines of Zn for two cases: (a) is that observed without the block and (b) is that observed with the block. The measurements are made along the y axis in Fig.24. It is seen that Zn ion emission intensity is enhanced near the surface of the block. This is due to further heating effect taking place in this region when the secondary plasma collides with the wall of the wedge. This implies that the kinetic energy of the atoms gushing from the primary plasma at supersonic speed is converted into heat energy of the plasma due to adiabatic compression. Also, it should be noted that the secondary plasma curves to the back of the block, a position which corresponds to the shaded area when seen from the primary plasma side. Namely, the diffraction phenomenon takes place even in the secondary plasma, as in the case of ordinary shock wave experiments. The speed of the front of the secondary plasma was obtained by observing the arrival of the Zn 481.0 nm emission along the z axis in Fig. 24. As the result, it is proved that the secondary plasma moves downward with a speed faster than sound. Therefore, it is concluded that the diffraction phenomenon of the secondary plasma is not due to the diffusion process occurring in the surrounding gas.

##### 4.3 Selective vaporization

TEA CO<sub>2</sub> laser induced shock wave plasma has also excellent characteristics for high sensitive

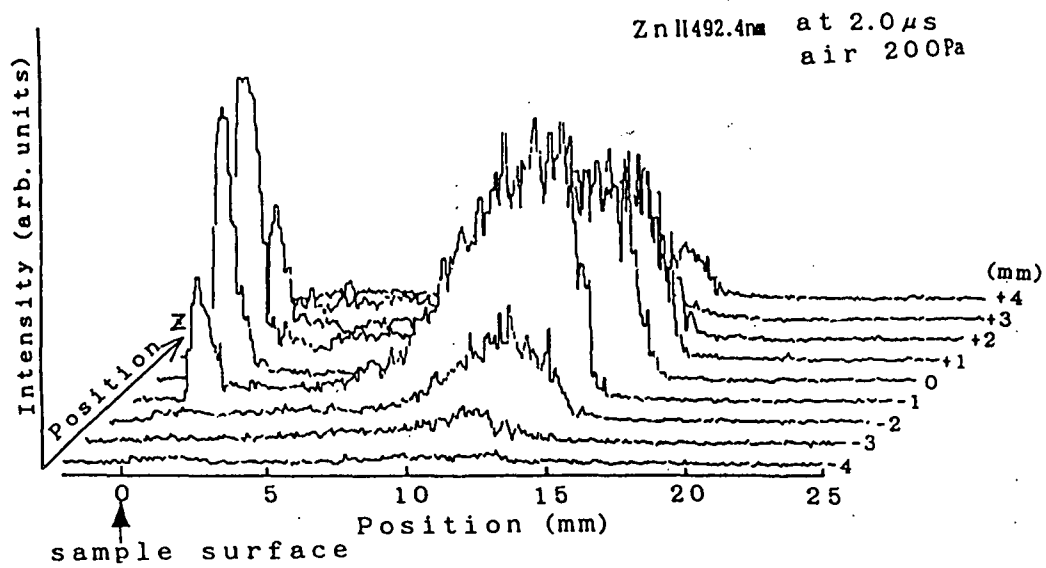
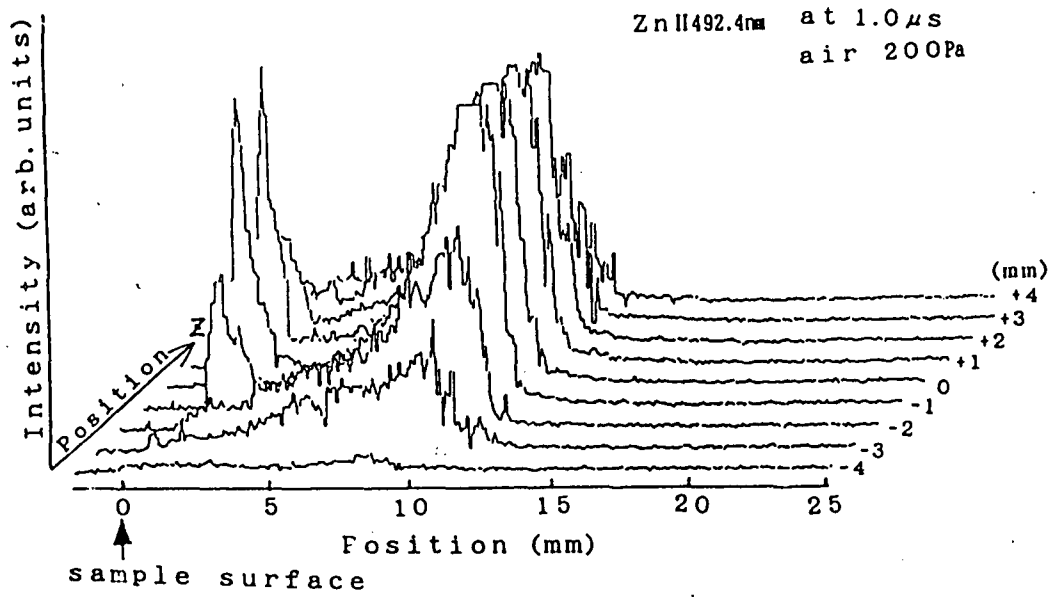


Fig. 23 Spatial distribution of the Zn(II) 492.4 nm emission line as a function of distance from the target at different position in the Z-axis in the tube when TEA CO<sub>2</sub> laser (500 mJ) was focused on Zn target through the small tube: (a) for 1  $\mu$ s; (b) for 2  $\mu$ s.

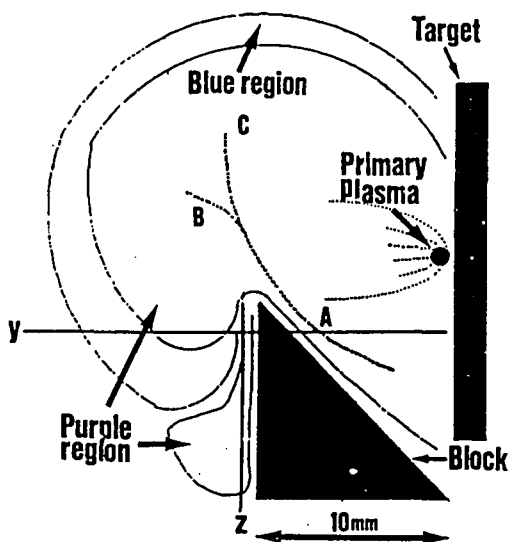


Fig. 24 Illustration of the laser plasma observed when the TEA CO<sub>2</sub> laser (500 mJ) is focused from the left-hand side onto the surface of Zn target in air at 1 Torr. A block is placed in front of the target.

spectrochemical analysis of glass samples, alkali halide pellet samples and low-alloy steel samples. However, some serious problem happen, depending on the type of samples. For example, when we focused a 500 mJ TEA CO<sub>2</sub> laser (pulse duration of 100 ns) onto a brass sample, the characteristic bright green color associated with copper atoms can be seen only for the initial several laser shots under repeated irradiation at a fixed position of the sample, and the green color soon completely disappears, even though the blue color associated with zinc is very bright over the entire hemispherical shape of the plasma. This is a very strange phenomenon which cannot be observed for the case of an ordinary plasma produced in atmospheric pressure.

For the case of LISPS, atoms must be gushed out with high speed in order to compress the surrounding gas. We assumed that, in the case of brass samples, the gushing of Cu atoms takes place late in the process and at a low speed, compared to Zn atoms because the power density of the laser light of TEA CO<sub>2</sub> laser is not so high due to

difficulties in precisely focusing the TEA CO<sub>2</sub> laser light. In order to prove this speculation time-profile of the emission of Zn 481.0 nm and Cu I 327.4 nm were compared near the surface of the target. The result is shown in Fig. 26. It can clearly be seen that the emission of Cu comes later and continues for a long time, as compared to the Zn-emission. It is seen that Zn are evaporated sooner and gush out from the target surface with high velocities to form a shock wave, while Cu atoms evaporated later with lower speed. Being unable to generate its own shock wave and being left behind the shock wave generated by the evaporated atoms of the first batch, Cu atoms would not be expected to experience excitation. The phenomenon of the selective vaporization also supports our laser-induced shock wave model.

#### 4.4 Sub-target effect

We also confirmed that high speed gushing from the target is really necessary condition to make secondary plasma. We compared the characteristics of the laser plasma induced by focusing a laser pulse on the surface of glass samples by using XeCl laser and TEA CO<sub>2</sub> laser under the reduced pressure of around 1 Torr. It was observed that shock wave plasma could not be generated by the TEA CO<sub>2</sub> laser on low-melting-point glass, while for excimer laser irradiation shock wave plasma can be produced even in the case of low-melting-point glass [37]. The pulse duration of the TEA CO<sub>2</sub> laser is considerably longer compared to that of XeCl laser. It is considered that by the long pulse irradiation the surface of the low-melting point glass become soft and recoil energy of the atom is absorbed on the surface. As the result, atoms gushing out from the primary plasma would not get enough speed to form the shock wave. If the process is true, we can overcome this problem by setting sub-target on the back side of the sample so as to make the repulsion force to push out the atoms with high speed. In fact we confirmed the sub-target effect on the samples such as low-melting-point glass tightly and silicon grease painted on copper plate. This experimental result also become strong evidence to support our model to explain the mechanism of laser-induced shock wave plasma.

The proposed model for the production of the secondary plasma is summarized here as follows: First, the primary plasma is produced by the bombardment of the laser light. From the primary

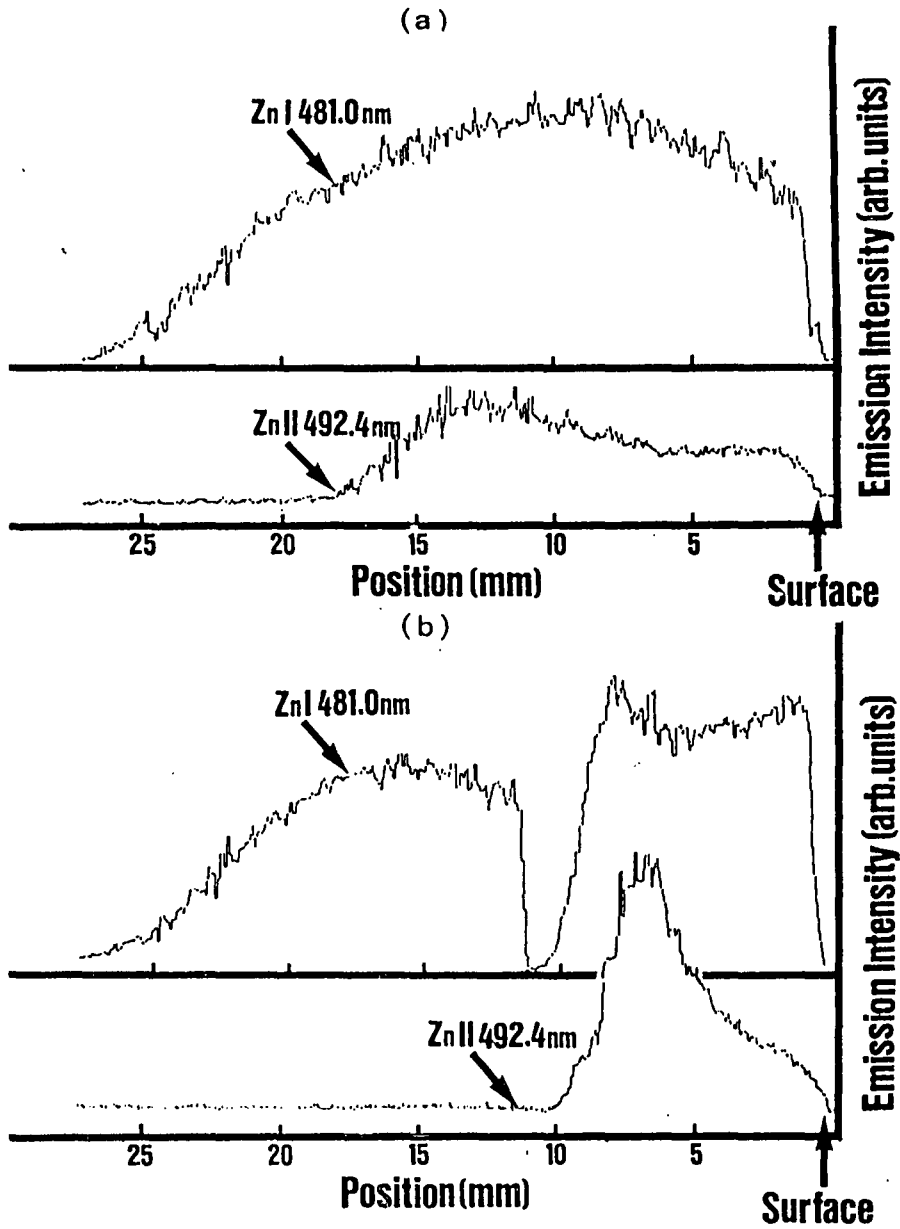


Fig. 25 Time-Integrated spatial distribution of Zn(I) 481.0 nm and Zn(II) 492.4 nm as a function of the distance from the target, along the y axis in Fig. 24.: (a) is for without the block, (b) is for with the block as shown in Fig. 24.

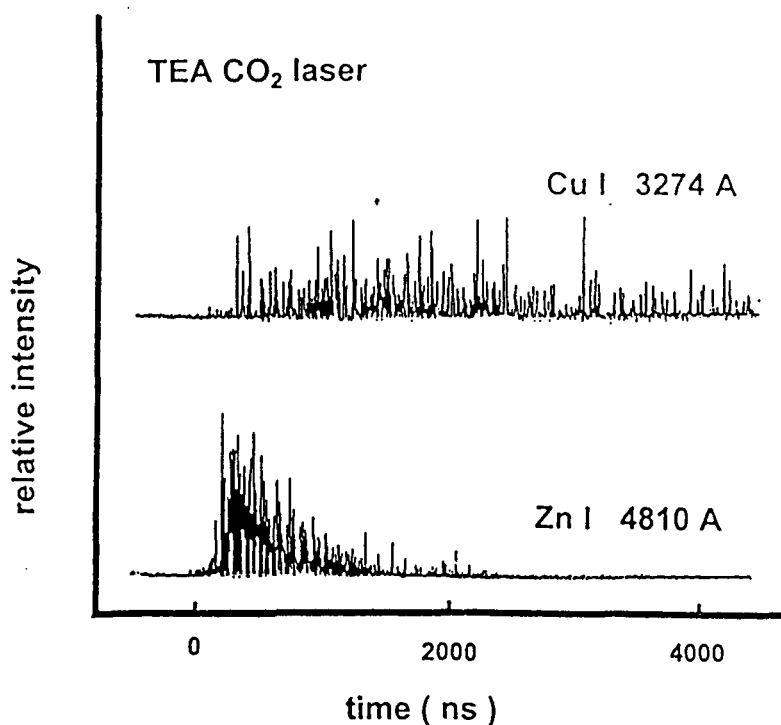


Fig. 26 Time-profile of the emission intensity of Cu(I) 327.4 nm and Zn(I) 481.0 nm using TEA CO<sub>2</sub> laser. Data was collected at 5 mm above the sample surface at a reduced pressure of 1 Torr.

plasma atoms come out with high speed, several tens of km/s. The movement of the gushed atom is intercepted by colliding with the surrounding gas molecules, and stagnation takes place at a certain place distance from the primary plasma. By the adiabatic compression, high temperature plasma is produced. The most important point of the shock wave model is that the energy to produce the secondary plasma is supplied in the form of kinetic energy of the atom, and is converted to heat energy, by which atoms are excited. Therefore, the excitation takes place within a limited region just behind the shock wave. With time the separation between the shock wave and the secondary plasma become large, and the secondary plasma is cooled slowly.

Recent studies on film production using laser ablation techniques [66-68], which were made by other researchers, also prove that shock wave

generation is closely related to the transportation and the excitation of gushed molecules from the target. The experimental results, obtained in a different research field, also support the shock wave model.

##### 5. Application to emission spectrochemical analysis

As we already described in Introduction, in the ordinary LAESA high power Ruby and Nd solid state laser pulses are bombarded on the sample surface under atmospheric pressure. In this case, there exist some problems regarding the precision and sensitivity of this method. Therefore, the LAESA method has been mainly used for semi-quantitative analysis. We have shown that the secondary

plasma has characteristics quite suitable for emission spectrometric analysis. Especially, the low background emission intensity and the linear relationship between the emission line intensity and the content of the elements are most advantageous. Here we offer some example of the quantitative analysis by LISPS method.

### 5.1 Steel analysis

Quantitative analysis on steel samples were made using  $N_2$  laser, excimer laser and TEA  $CO_2$  laser [21,34,35,69, 70]. The radiation of the laser-induced secondary plasma was observed by making 1 : 1 image of the plasma onto the entrance slit of a monochromator (Jobin-yvon G40). The slit position was selected so that the S/B ratio become maximum because the background emission intensity decreases with increasing distance from the target. By scanning the wavelength of a monochromator under the successive production of the plasma (5-10 Hz), the emission spectrum was directly recorded on a chart as shown in Fig. 27, which was obtained using  $N_2$  laser. This result shows the high reproducibility of the emission spectrum which leads to high precision analysis. The internal standard method was used, in which the line intensity of the element to be examined was measured with respect to that of the host material. Fig. 28 shows the examples of analytical curves for iron steel samples. In contrast to conventional laser

spectrochemical analysis a definite linear relationship is obtained. It is believed that this linear relationship is due to the fact that the secondary plasma has a thin shell structure. When this is the case, the effect of self-absorption becomes negligible as the case for ICP.

Similar good linear analytical curves were obtained both for XeCl excimer laser irradiation and TEA  $CO_2$  laser irradiation on low alloy steel samples. However, in the case of high speed steel samples which has high melting point and boiling point, it was confirmed that W atoms could not be detected when TEA  $CO_2$  laser was used, in spite of the fact that the sample contained 10 % of tungsten, while the emission lines for Fe are very strong; only limited region near the primary plasma emission of W could be observed [35]. This is probably due to the effect of selective vaporization of W atoms (see section 4.3).

In order to estimate the possible minimum determinable concentration of the element, the value of the BEC (Background Equivalent Concentration) is usually employed [44]. Fig. 29 shows the Cr 425.4 nm emission spectrum taken under the condition that the pulse energy of the excimer laser was set at 30 mJ and the position of the slit of the monochromator was set at 7 mm from the surface of the target. From this spectral distribution, the BEC of the Cr 425.4 nm analytical line is estimated to be about 12 ppm [34]. Therefore

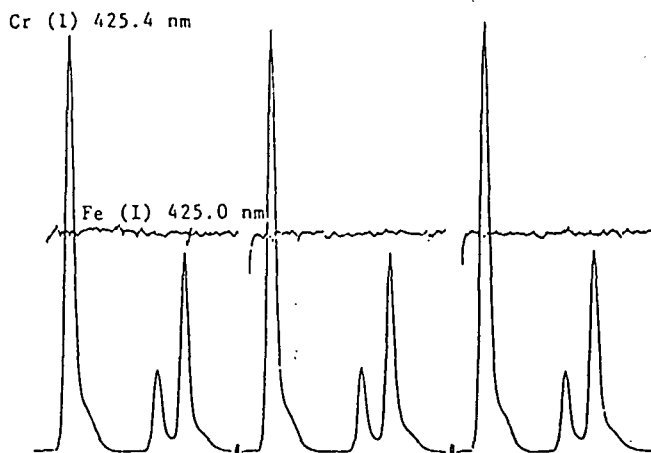


Fig. 27 Examples of emission spectrum of the secondary plasma taken from low-alloy steel when  $N_2$  laser was used for plasma generation. The measurement was repeated 3 times.



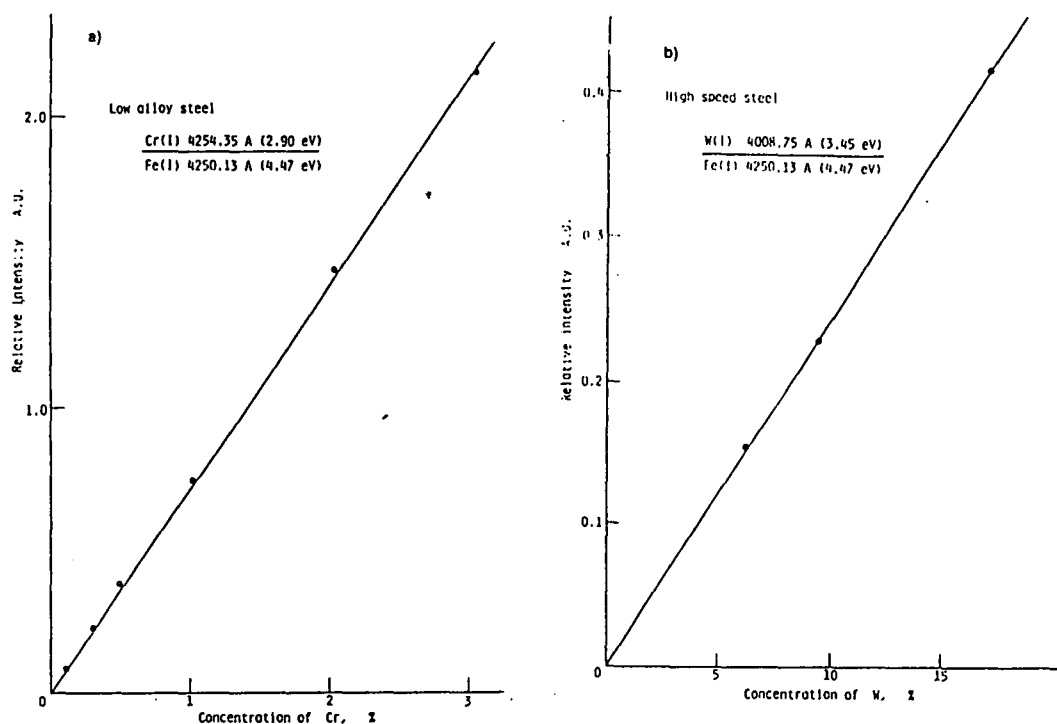


Fig. 28 Plot of the relative intensity of emission line in relation to the Cr content in low alloy carbon steel (a) and W in high speed iron steel (b).  $N_2$  laser was used for plasma generation.

it is expected that the minimum determinable concentration of Cr in steel samples will be attained to less than 1 ppm; while the detection limit of Cr obtained on steel samples by the ordinary LAESA was about 200 ppm. Also it is expected that by choosing the pulse energy and the pressure of the surrounding gas the determinable minimum concentration for LISPS may be decreased more.

### 5.2 Glass analysis

It should be emphasized that LISPS method using a TEA  $CO_2$  laser is especially suitable for glass samples. One advantage is the low threshold energy of the plasma production. As the result, a very stable secondary plasma was produced under the successive bombardment of the laser light even when the sample was rotated. Another advantage of applying the TEA  $CO_2$  laser is that a glass

sample never emits fluorescence during irradiation; in contrast, for UV lasers, a glass sample fluoresces, thus raising the background level in the spectrum measurement using time-integrated method[37].

Superiority of LISPS over the Laser Induced Breakdown Spectroscopy was clearly shown in the quantitative analysis of glass samples containing high concentration of Li and K (10%, 15% and 20%)[38]. In this case XeCl excimer laser was used. It is shown that the plasma produced at 1 atm cannot be applied to the elemental analysis due to the strong background emission and self-absorption effect in the plasma, and broadening of the emission line spectrum due to strong interaction in the plasma. It was confirmed that these problem cannot overcome even when we use time gating method using OMA system. In contrast to this, the shock

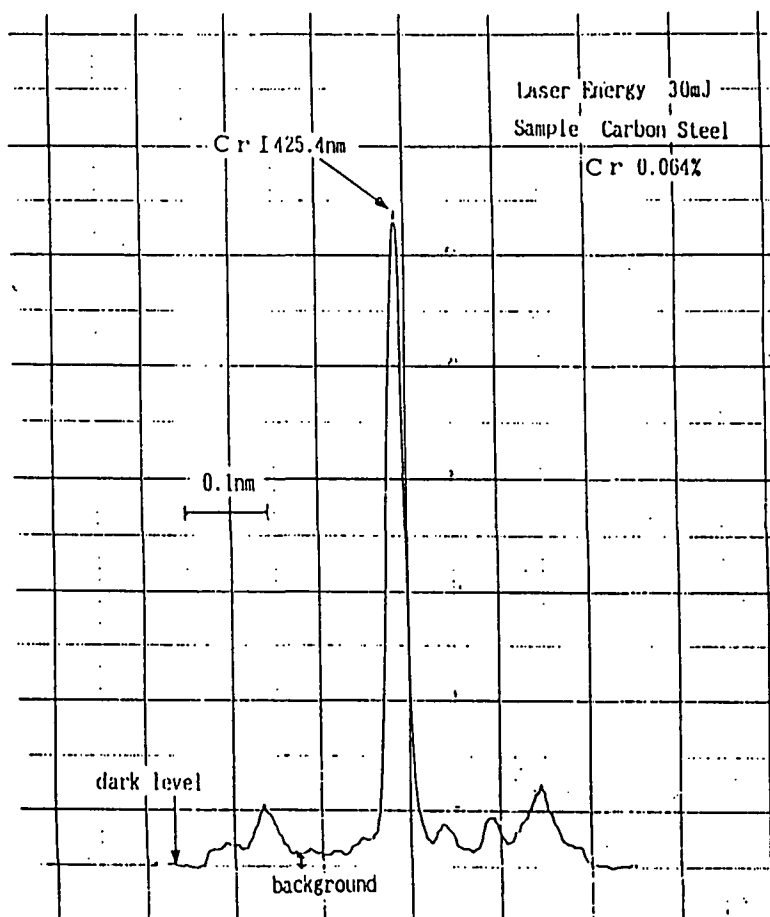


Fig. 29 Emission spectrum taken from carbon steel containing 0.064% Cr when XeCl 30 mJ pulse was focused on the target. The BEC is about 12 ppm.

wave induced plasma produced at reduced pressure gives high S/B in the measurement of analytical emission lines, and the slope of the calibration curve is near unity in a log-log plot, thus making it possible for emission spectrochemical analysis.

Also in this experiment high sensitive analysis of Li was demonstrated using silicate glass containing Li of 0.7 % as shown in Fig. 30; the background equivalent concentration for the emission of Li 670.7 nm is as low as 7 ppm.

### 5.3 Detection of Halogen atoms

Halogen atoms are usually difficult to detect by emission or absorption spectrometry methods due to the high-lying electronic energy levels. Most of the halogen resonance lines lie in the short ultraviolet region and near infra-red region. Only limited lines lie within the visible region and most of these lines are ionic lines, making it difficult to detect using ordinary plasma source, because of insufficient low temperature. Cremer et al succeeded to detect Chloride and Fluoride

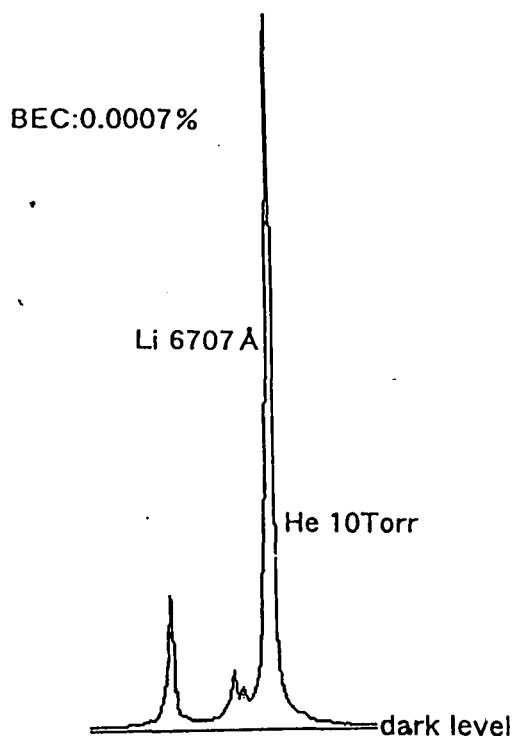


Fig.30 Emission spectrum taken from silicate glass containing Li of 0.7 % when XeCl 50 mJ pulse was focused on the target. The BEC is about 7 ppm.

spectrometrically using laser-induced breakdown method [71]. They reported that the minimum detectable concentration of Chloride (Cl 837.6 nm) and Fluoride (F I 685.6 nm) in air at 1 atm are 80 ppm and 2000 ppm, respectively, but they were unable to observe the Halogen ionic lines in the visible region. Our laser-induced shock wave plasma generates very high temperature more than 10 thousand degrees when the shock wave speed is very high by using high power TEA CO<sub>2</sub> laser [28,31,72]. In such case it can be expected that Halogen atoms is excited.

In order to prove the generation of the emission from Halogen ions chemical compound powder was used as the sample after being compressed to a pellet. Fig.31 shows the emission spectra of Cl lines in KCl samples under different surrounding

gases (He, Argon and air). It is seen that Helium gives the highest emission intensity for Cl ionic line, and air gives low emission intensity.

It was demonstrated that the plot of the Cl 479.4 nm emission intensity is proportional to Cl content in KBr pellets. In the experiment laser was focused on the target in Helium at 5 Torr. Figure 32 shows the spectra of Cl (II) 479.4 nm and Cl (II) 479.2 nm. These spectra were taken for the pellet containing 0.047 % of Chloride. From these spectra, the background equivalent concentration (B.E.C) is estimated to be 0.005%, and the detection limit of the Chloride is about 5 ppm.

#### 5.4 Analysis of food material

The quantitative analysis of food material is usually made by atomic absorption spectrometry or ICP emission spectrometry. In such cases the samples must first be ashed using environmentally harmful mineral acid and then dissolved. These methods consume a great deal of time, and error is likely to arise during the treatment. We demonstrated that food material, such as milk powder, also can be analyzed by LISPS method.

In order to make a calibration curve of Ca in milk powder and the orchard leaves, KBr powder (grain size of about 50 μm) was mixed with these materials at a weight ratio of 9 parts to 1 and compressed (300 atm for 1 minute) into a pellet (10 mm diameter and 1 mm thickness) [27]. KBr pellets containing different amounts of CaCO<sub>3</sub> were also made. These pellets were attached to a disk in the chamber, and TEA CO<sub>2</sub> laser pulse with a energy of 300 mJ was irradiated one by one. Fig. 33 shows the slope of the relative intensity of Ca I 422.6 nm to that of K I 404.4 nm as a function of Ca content in the KBr pellets. These data were taken in air at 300 Pa. It is clearly seen that there is a good linear relationship between them. At this stage of the experiment, the detection limit of Ca in milk powder is approximately 10 ppm. If we use a more improved detection system, such as OMA or polychromator, the detection limit will be reduced more.

#### 5.5 Standardization using the primary plasma

It is well known that difficulties in laser microprobe spectrochemical analysis is to make or obtain standard samples, particularly for minerals. In general, quantitative analysis is impossible without standard samples because the number of atoms vaporized from the solid target differs from sample to sample even if the power of the laser is kept constant, depending on the difference in the optical

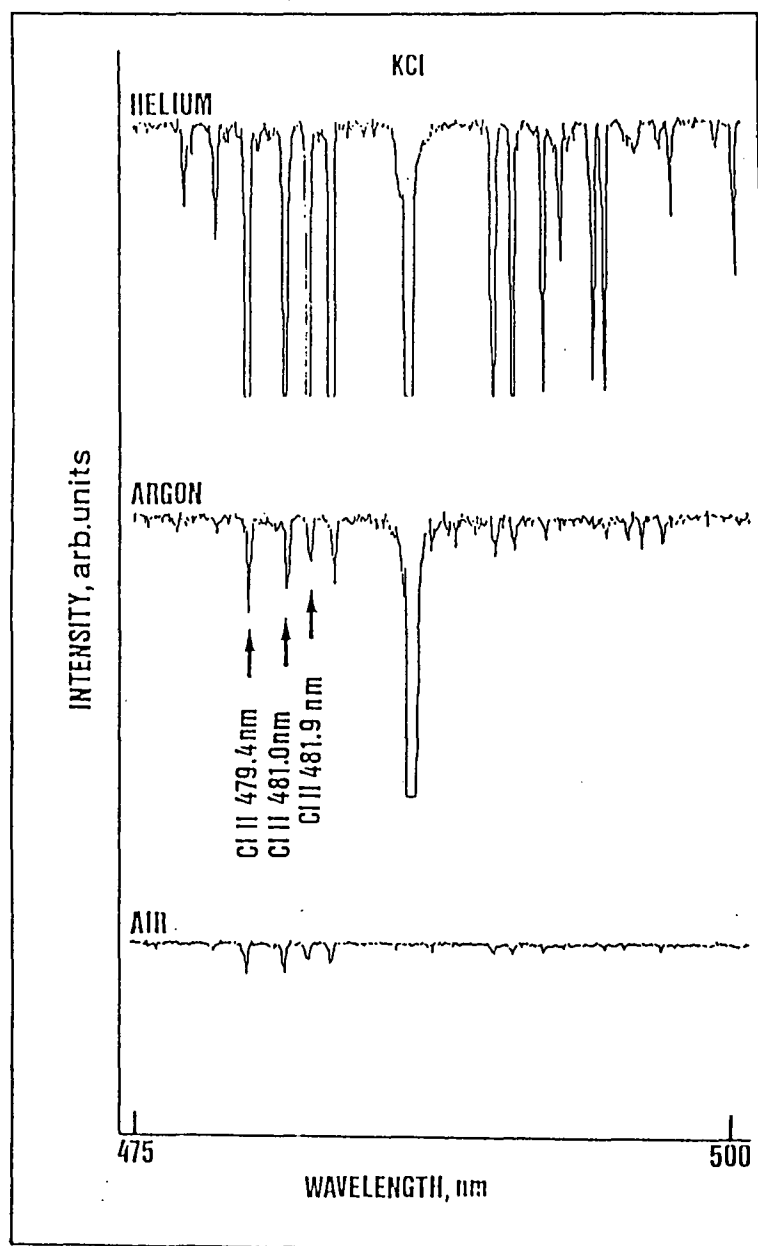


Fig. 31 Time-integrated emission spectra of Chloride in KCl, taken at 15 mm above the target surface in different surrounding gases; at 7 Torr for He, 5 Torr for argon and 7 Torr for air. TEA CO<sub>2</sub> laser (500 mJ) was focused on the target.

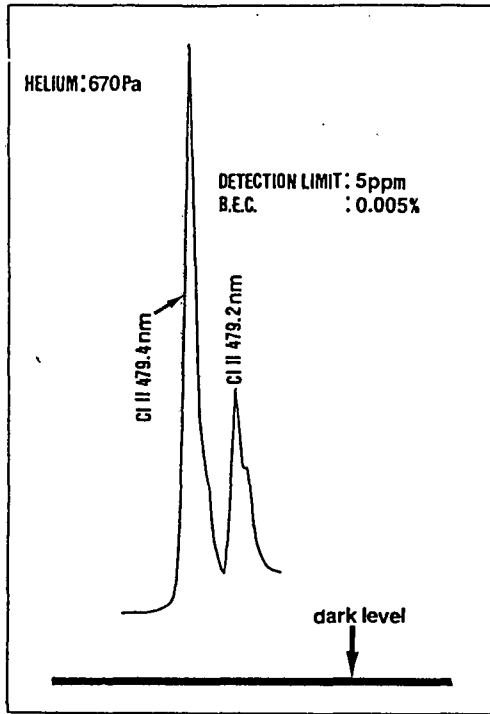


Fig.32 Emission spectra of the Cl (II) 479.4 nm and Cl(II) 479.2 nm when TEA CO<sub>2</sub> laser (500 mJ) pulse was focused on KBr pellet containing Cl in 0.047%.

and thermal properties of the targets. However, if we can extract information on the number of atoms vaporized directly, quantitative analysis may be realized even when standards samples are not available. Morton et al. have attempted to utilize the crater volume for standardizing the amount of vaporized atoms [73]. Since atoms blown off from the primary plasma, it is supposed that the intensity of the primary plasma is proportional to the number of atoms vaporized from the target [25]. As the density of the primary plasma is very high, the radiation from the primary plasma is assumed to be due to black-body radiation [74], and the emission spectrum from the primary plasma is almost independent of the type of element as shown in Fig. 4. Also it was proved experimentally that the temperature of the secondary plasma is almost constant when the laser

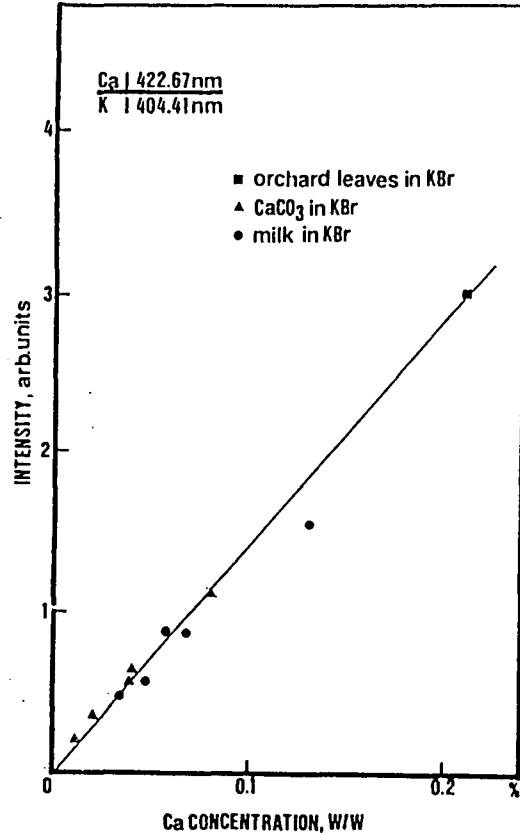


Fig.33 Plot of the relative intensity of Ca(I) 422.7 nm to that of K(I) 404.4 nm against the Ca content. TEA CO<sub>2</sub> laser (300 mJ) was focused on the pellet in air at 300 Pa.

pulse energy does not differ so much, not being dependent on either the intensity of the primary plasma nor the type of sample. Based on these facts, it was demonstrated that a normalized analytical emission line by the intensity of the primary plasma is virtually proportional to the analyte content in the host samples, regardless of the type of sample. This standardization method will be effectively used for the quantitative analysis of rock sample.

## 6. Conclusion

With the aid of unique experimental method for

time-resolved spatial distribution which was developed in our laboratory, the characteristics of laser plasma was examined with high precision. Based on the experimental results we conclude the secondary plasma is formed by the excitation resulting from the blast wave. Other evidences to prove the shock wave model were also presented in various experiments, confined plasma, reflection and diffraction of the laser plasma, selective vaporization and sub-target effect. It is surprising that the excitation process of the laser plasma produced at reduced pressure never essentially differ depending on the pulse energy of the laser ranging from a few mJ to several hundreds mJ

It was shown that the secondary plasma has characteristics quite favorable to spectrochemical analysis. Among these positive characteristics are, low background emission spectrum and good linearity between the emission intensity and the content of the element are representative. The symmetrical hemispherical shape which leads to high precision analysis and high excitation temperature which brings to high sensitive analysis are also advantages. These characteristics are closely related to the peculiar process taking place in the shock wave excitation.

There are two obvious practical applications of LISPS; one is its application to the rapid inspection of industrial products, such as steel and glass samples, and the other is the application to the field-based spectrochemical analysis of mining or geological samples.

It can be said that this LISPS method has substantially high prospect to compete with ICP spectrometry when we use this LISPS method for inspection of homogeneous samples of industrial products. In order to prove this practical quantitative experiment should be made using polychromator in the near future.

At present EPMA (Electron Probe Micro Analysis) is widely used to make micro analysis on the small minerals in rock samples. However, for this purpose the sample surface must be polished flatly with high precision, and therefore it takes time for pretreatment. In contrast to this in our method, rapid quantitative analysis can be made with more high sensitivity because in our method required flatness is not so severe and the required pressure condition can be easily obtained using air. Also in our method compact equipment can be realized by combining small pulse laser with a pulse energy of several mJ and OMA for spectrum detection system. Such compact equipment can be easily moved by a car

and quantitative analysis can be made in outdoor. It is expected that our LISPS method will be used effectively in the field of mining industry and geological science.

#### References:

- 1 Brech F. and Cross L. 1962, *Appl. Spectroscopy*, 16, 59.
- 2 Laqua K. 1979, *Analytical Laser Spectroscopy* (Omenetto N. Ed.), Wiley, New York.
- 3 Moenke H. and Moenke-Blankenburg L. 1973, *Laser Micro-Spectrochemical Analysis*, Adam Hilger, London.
- 4 Piepmeier E.H. 1986, *Analytical Applications of Lasers*, Wiley, New York, 627.
- 5 Cremers D. A. and Radziemski L. J. 1987 (R.W.Solarz and Paisner J.S. Eds.), Marcel Dekker, New York 351.
- 6 Radziemski L.J. and Cremers D.A. 1989, *Laser Induced Plasmas and Applications*, Marcel Dekker, New York.
- 7 Sabsabi M. and Cielo P. 1995, *Appl. Spectroscopy*, 49, 499.
- 8 Mao X.L., Shannon M.A., Fernandez A.J. and Russo R.E., 1995, *Appl. Spectroscopy* 49, 1054.
- 9 Multari R.A., Foster L.E., Cremers D.A. and Ferris M.J. 1996, *Appl. Spectroscopy*, 50, 1483.
- 10 Piepmeier E.H. and Osten D.E. 1971, *Appl. Spectroscopy*, 25, 642.
- 11 Dimitrov G. and Gagov V. 1979, *Spectrosc. Lett.* 10, 337.
- 12 Leis F., Sdora W., Ko J. B. and Niemax K. 1989, *Mikrochim. Acta (Wien)* 2, 185.
- 13 Iida Y. 1989, *Appl. Spectroscopy*, 43, 229.
- 14 Iida Y. 1990, *Spectrochimica Acta*, 45B, 1353.
- 15 Iida Y., Morikawa H., Tsuge A., Uwamino Y. and Ishizuka T. 1991, *Analytical Sciences* 7, 61.
- 16 Kuzuya M. and Mikami O. 1990, *Japanese J. of Applied Physics*, 29, 1568.
- 17 Kuzuya M., Takemoto T., Sakanashi H. and Mikami O., 1995, *J. Spectrosc. Soc. Japan*, 44, 17.
- 18 Lee Y.I., Terry L., Thiem, Kim G.H., Teng Y.Y. and Sneddon J. 1992, *Applied Spectroscopy* 46, 1597.
- 19 Wu J.D., Pan Q. and Chen S. C., 1997, *Applied Spectroscopy*, 51, 883.
- 20 Lee Y.I., Song K., Cha H.K., Lee J.M., Park M.C., Lee G.H. and Sneddon J., 1997, *Applied Spectroscopy* 51, 959.
- 21 Kagawa K. and Yokoi S. 1982, *Spectrochimica Acta*, 37B, 789.
- 22 Kagawa K., Yokoi S. and Nakajima S. 1983,

- Optics Communications, 45, 261.
- 23 Kagawa K., Ohtani M., Yokoi S. and Nakajima S. 1984, *Spectrochimica Acta*, 39B, 525.
  - 24 Kagawa K., Matsuda Y., Yokoi S. and Nakajima S. 1987, *J. of the Spectroscopical Society of Japan*, 36, 400.
  - 25 Kagawa K., Matsuda Y., Yokoi S. and Nakajima S. 1988, *J. of Analytical Atomic Spectrometry*, 3, 415.
  - 26 Kagawa K., Manda T., Ueda M. and Li Z. 1991, *J. of the Spectroscopical Society of Japan*, 1991, 40, 150.
  - 27 Kagawa K., Deguchi Y., Ogata A., Kurniawan H., Ikeda N. and Takagi Y. 1991, *Japanese J. of Applied Physics*, 30, L1899.
  - 28 Kurniawan H., Kobayashi T. and Kagawa K. 1992, *The Review of Laser Engineering*, 20, 31.
  - 29 Kurniawan H., Kobayashi T. and Kagawa K. 1992, *Applied Spectroscopy*, 46, 581.
  - 30 Kurniawan H., Kobayashi T., Nakajima S. and Kagawa K. 1992, *Japanese J. of Applied Physics*, 31, 1213.
  - 31 Kurniawan H., Ikeda N., Kobayashi T. and Kagawa K. 1992, *J. of the Spectroscopical Society of Japan*, 41, 21.
  - 32 Kagawa K., Tani M., Ueda H., Sasaki M. and Mizukami K. 1993, *Applied Spectroscopy*, 47, 1562.
  - 33 Tani M., Kurniawan H., Ueda H., Mizukami K., Kawai K. and Kagawa K. 1993, *Japanese J. of Applied Physics*, 32, 3838.
  - 34 Kagawa K., Kawai K., Tani M. and Kobayashi T. 1994, *Applied Spectroscopy*, 48, 198.
  - 35 Kagawa K., Hattori H., Ishikane M., Ueda M. and Kurniawan H. 1995, *Analytical Chimica Acta*, 299, 393.
  - 36 Kurniawan H., Tjia m. O., Barmawi M., Yokoi S., Kimura Y. and Kagawa K. 1995, *J. of Phys. D.* 28, 879.
  - 37 Kurniawan H., Nakajima S., Batubara J.E., Marpaung M., Okamoto M. and Kagawa K. 1995, *Applied Spectroscopy*, 49, 1072.
  - 38 Kurniawan H., Kagawa K., Okamoto M., Kobayashi T. and Nakajima S. 1996, *Applied Spectroscopy*, 50, 299.
  - 39 Kurniawan and Kagawa K. 1997, *Applied Spectroscopy*, 51, 304.
  - 40 Kurniawan H., Ishikawa Y., Nakajima S. and Kagawa K. 1997, *Applied Spectroscopy*, 51, 1769.
  - 41 Kurniawan H., Budi W. S., Suliyanti M. M., Marpaung A. M. and Kagawa K. 1998, *J. of Physics D.* in press.
  - 42 Kagawa K. and Kurniawan H. 1991, *Proceedings of the International Workshop on Strong Shock Waves (Chiba University)*, 97.
  - 43 Kagawa K., Manda T., Kurniawan H., Kobayashi T., Yokoi S. and Nakajima S. 1991, *Proceedings of the 18 th International Symposium on Shock waves*, Springer-Verlag, Tokyo, 953.
  - 44 Karlinski T. and Johnson G. 1981, *Developments in Atomic Plasma Spectrochemical Analysis*, 197, ( Barnes R.M. Ed. ), Heyden and San Ltd.
  - 45 Kagawa K., Yamamoto I. And Ueda M. 1988, *J. of Physics E.* 21, 608.
  - 46 Gibson A.F., Hughes T.P. and Ireland C.L.M. 1971, *J. Phys. D.* 4, 1527.
  - 47 Basov N.G., Krokhin O.N. and Sklizkov G.V. 1967, *JETP Lett.*, 6, 168.
  - 48 Basov N.G., Gribkov V.A., Krokhin O.N. and Sklizkov G.V. 1968, *Sov. Phys. JETP* 27, 575.
  - 49 Bobin J.L., Durand Y.A., Langer P.P and Tonon G. 1968, *J. of Applied Phys.*, 39, 4184.
  - 50 Hall R.B. 1969, *Appl. Phys.* 40, 1941.
  - 51 Emmony D.C. and Irving J.B. 1969, 2, 1186.
  - 52 Hughes T.P. 1975, *Plasma and Laser Light*, Adam Hilger, England, 435.
  - 53 Sedov I.I. 1959, *Similarity and Dimensional Methods in Mechanics*, Academic Press, New York and London, 213.
  - 54 Gregony C.E. 1960, *Modern Explosives for Engineers*, University of Queensland Press.
  - 55 Bouman P.W.J.M. 1966, *Theory of Spectrochemical Excitation*, Plenum Press New York 135.
  - 56 Bekefi G., Deutsch C. and Yaakobi B. 1976, *Principles of Laser Plasmas ( Bekeifi G. Ed.)*, 628, John Wiley and Sons, New York.
  - 57 Bockasten K. 1961, *J. Opt. Soc. Am.* 51, 943.
  - 58 Zel'dovich R. and Raizer Y.P. 1966, *Physics of Shock Waves and High Temperature Hydrodynamic Phenomena*, Academic Press, INC, Vol.1.
  - 59 Iizuka H., Honma H., Tsukamoto A. and Ohno T. 1990, *Current Topics in Shock Waves*, Y. Kim, Ed. (America Institute of Physics, New York), 856.
  - 60 Silfvast W.T. and Wood U.R. 1974, *Appl. Phys. Lett.*, 25, 274.
  - 61 Green J.M., Silfvast W.T. and Wood O.R. 1977, *J. Appl. Phys.* 48, 2753.
  - 62 Wagatsuma K. and Hirokawa K. 1985, *Anal. Chem.* 57, 2901.
  - 63 Mcwhirter R.W.P. 1965, *Plasma Diagnostic Techniques*, Huddleston R.H. and Leonard

- S.L.S. Ed., Academic Press.
- 64 Kalnicky D.J., Fassel V.A. and Kniseley F.W. 1977, *Applied Spectroscopy*, 31, 137.
- 65 Zucron M.J. and Hoffman J.D. 1976, *Gas Dynamics*, Wiley Chichester, New York, 346.
- 66 Geohegan D.B. 1992, *Appl. Phys. Lett.*, 60, 2732.
- 67 Kumuduni W.K.A., Nakayama Y., Nakata Y., Okada T. and Maeda M. 1993, *J. Appl. Phys.*, 74, 7510.
- 68 Geohegan D.B. 1994, *Pulsed Laser Depositions of Thin Films*, Chrisey D.B. and Hubler G.K. Eds., John Wiley and Sons, Inc. Chap. 5.
- 69 Kagawa K., Yanagihara S. and Yokoi S. 1985, *J. of the Spectroscopical Society of Japan*, 34, 306.
- 70 Kagawa K., Nomura H., Aoki K., Yokoi S. and Nakajima S. 1988, *J. of the Spectroscopical Society of Japan*, 37, 360.
- 71 Cremers D.A. and Radziemski L.T. 1983, *Anal. Chem.* 55, 1252.
- 72 Tani M., Mizukami K., Ueda H., Deguchi Y., Takagi Y. and Kagawa K. 1992, *J. of the Spectroscopical Society of Japan*.
- 73 Morton K., Nohe J. and Madsen B., 1972, *Applied Spectroscopy*, 27, 109.
- 74 Ready J.F. 1971, *Effect of High Power Laser radiation*, Academic Press, New York, 189.



# LASER APPLICATION IN MEDICINE

Hamdani Zain

Instrumentation and Photonic Devices Laboratory  
Graduate Study Program in Opto-Electrotechniques  
and Laser Applications, Faculty of Engineering,  
University of Indonesia

Department of Medical Physics  
Faculty of Medicine, University of Indonesia

Jakarta, July 5, 2001

Regional Workshop on Lasers and Optoelectronics

June 25 th - July 6 th, 2001

## LASER APPLICATION IN MEDICINE

### Introduction

The discovery and development of Lasers has had a significant beneficial impact on medical research and practice. One of the important area of biomedical research concerns the functions of individual components of cells. These functions are studied by damaging a particular component and observing the subsequent behavior of the cell. If the cell is unable to perform one of its normal functions, it is reasonable to attribute this function to the damaged component. Before the advent of lasers, the damaging was done with a fine needle (or microprobe). Only large cell structure could be studied in this way, and the result were sometime ambiguous. By using laser beams as a probes, this line of research has been greatly refined. A laser beam can be focused to a spot only a few microns in diameter. A beam of this size can probe cell component too small for ordinary microprobes.

Lasers also used to perform delicate surgery and to seal off bleeding areas in difficult locations. In this cases, a bundle of optical fiber is used. Light is piped through part of the bundle to illuminate the region and the surgeon views the area through another part of the bundle. When bleeding site is located, a burst of laser radiation directed toward it seals the area. The procedure is quick and the results are often permanent.

Certain types of cancers can also be controlled by laser surgery. These operations are carried out with no pain, bleeding, scars, or impairments of function.

## Laser Applications

Lasers can be extremely dangerous. The light produced by some lasers cause severe, some time permanent damage to eyes and skin. Even low power lasers are dangerous and must be treated with respect. Never look directly into laser. Even reflections can be dangerous, so be very careful when working with lasers. Become familiar with the basic safety rules provided by the manufacturers of lasers. The American National standards Institute ( ANSI ), 1430 Broadway, New York, NY, 10018, published a laser safety standard.

Lasers can be classified according to different schemes. A common system is to use the form and material of the laser (i.e, gas, solid crystal, p n junction, and so forth).

Another method of classifying lasers in according to the safety categories published by the ANSI, and the Laser Institute of America, in ANSI Z1361 – 1986.

The ANSI classes are class I, class II, class III, and class IV, A class I laser is one that is not capable of producing biological damage to the eye or skin during intended uses, by either direct or reflected exposure. These lasers may emit light in the 400 – to 1400 nm region. The class II lasers emit in the visible portion of the spectrum in the 400 – to 700 nm region. In the class II lasers, normal aversion responses such as blinking (~ 250 ms) are believed to be sufficient to afford protection against biological damage from direct or reflected light. For class II continuous wave (CW) lasers, the point source power used in exposure calculation is  $2,5 \text{ mw/cm}^2$ .

Class III laser “may be hazardous under direct and specular reflection viewing conditions but diffuse reflection is usually not hazardous”. The class III laser is typically not a fire hazard. The class IV laser is a dangerous, high powered device and may be both direct and specular reflected beam, and some times also from a diffuse reflected beam. Laser classes are determined by authorized Laser Safety Officers (LSOs), according to the criteria established in the ANSI standard or its successor.

### Biological Effects of Laser Radiation

Laser radiation striking human tissue directly, or reflected onto the tissue, is capable of inflicting varying degrees of damage. At least the following factors can play a role in causing tissue injury and influencing the degree of damage from laser beam exposures.

- Wavelength of laser radiation
- Tissue spectral absorption, reflection, and transmission
- Strength or irradiance of incident laser beam
- Size of irradiated area
- Exposure duration

Three major laser spectral bands are associated with biologic effects on tissues : visible, ultraviolet and infrared radiation wavelengths.

Frequent usage is made of spectral-band designations in discussing biologic effects.

These follows :

- Near ultraviolet : UV-A (315 – 400 nm)
- UV-B (280 – 315 nm)
- UV-C (100 – 280 nm )
- Visible : (400 – 700 nm)
- Near-infrared : IR-A (700 – 1,400 nm)
- Far-infrared : IR-B (1.4 - 3 micron )
- IR-C (3 – 1,000 micron)
- Laser beam exposure can result in tissue damage from any of the following types of mechanism :
  - Thermal effects,
  - Photochemical effects,
  - Acoustic transients,
  - Chronic exposure,

### Thermal Effects

Thermally related effects represent the major type of damage from laser beam exposure. The extent of thermal damage is principally dependent upon the tissue that is the most efficient absorber of the particular laser radiation wavelength, the strength or irradiance of the incident laser beam, the size of the irradiated area and the exposure duration. Given the vast energy ranges of lasers, effects on tissue can vary from no effect, simple tissue reddening, steam generation, charring or even explosive tearing or ripping where very high radiant exposure levels occur.

## Photochemical Effects

The photochemical effects on the eye and skin caused by ultraviolet radiation are not entirely comprehended. Nonetheless, action spectra graphs, which show the relative spectral effectiveness of actinic radiation (e.g., from the sun) in causing a skin reddening or erythema, have been experimentally defined. Skin pigmentation plays a considerable role in establishing an erythema threshold.

ANSI suggests that thereto, is probably caused by photochemical denaturization of molecules (e.g., DNA or RNA) or proteins in the cells.

## Acoustic Transients

Laser pulses striking tissues have a part of their energy changed to a mechanical compression wave or acoustic transient. This acoustic energy is capable of ripping and tearing tissue when sufficiently intense. While the retina injury mechanism is largely of thermal origin for Q-switched duration, the effect of acoustic transients caused by the rapid heating and thermal expansion in the proximity of the absorption site (e.g., each melanine granule) may play a part in the damage mechanism.

## Chronic Exposures

The damage mechanism and potential hazards to the eye or skin caused by chronic exposure to far-infrared (3 – 1,000 microns) radiation is an area requiring further study. However, corneal exposure of 0.08 to 0.4 W:cm<sup>-2</sup> in the near-infrared spectra emitted from foundry or glass furnaces are believed responsible for cataract formation. Approximately 1 mw.cm<sup>-2</sup> is the far-infrared corneal dosage received outdoors.

Chronic exposure to ultraviolet radiation is known to hasten aging of the skin, and it is believed that such exposure is responsible for causing certain skin cancer.

## Laser in Ophthalmology

The use of intense light to treat ocular diseases was first demonstrated by Prof. Meyer-Schwickerath of Germany. Meyer-schwickerath studied patients who suffered from retinal burns because of sun-gazing. Simultaneously, he noticed that some diseases developed more slowly when there were multiple retinal scars in the eyes. He developed a crude Xenon photocoagulator which produced an intense light source for the treatment of the retina through what is known as a therapeutic burns. Late, the laser was developed and the first one to be used was the Argon Laser. The Argon molecules emit blue-green light, and delivered to by fiber-optic cable to a delivery system known as the slit lamp microscope. The microscope has a precise

adjustment capabilities and the laser beam is delivered to the eye creating round burns on the retina. The power used varies between 20 to 2,000 milliwatts with a timing of about 0.1 to 0.5 seconds and the size of laser spot is between 50 to 1,000 microns.

Beside the Argon laser, other lasers have become available and they include the Krypton green, the Dye laser, carbon dioxide laser, and more recently, the Neodymium YAG laser.

#### Argon Laser

The blue green light of the Argon laser is absorbed by the pigment of the brown retina pigment epithelium and this is a very important concept because a burn of mild or moderate intensity is confined only some of the retina layers. An intense burn is therefore dangerous because it can involve the full thickness of the retina. It can then destroy the nerve fiber layers and cause severe visual field defects.

Furthermore, an intense light can cause glial tissue proliferation on the retinal surface and may also rupture Bruch's membrane. This may allow the choriocapillaries to invade subretinal space.

White tissue will not absorb the blue-green beam. It will instead reflect the light. It is therefore, impossible or extremely difficult to burn the surface of the white optic disc, white scar tissue, white hard exudates or patches of chorioretinal scars. On the other hand, areas of increased pigmentation will increase the absorption of the light and may result in intense burns.



Another concept which is important in the treatment of eye diseases with the laser is that the energy density of a particular burn is determined by the power employed and the spot size. This extremely important concept. The energy density present in a small spot size of 50 microns is greater than that of 500 microns. With a given power setting. This is very important when treating the eye with a large spot of 500 microns and then reducing it to 100 microns. The decreased spot size will increase the energy density and if the power is not adjusted downwards, an intense and sometimes explosive burn may rupture the retina and choroid. This can lead to internal bleeding and serious complications.

#### Krypton Laser

The Krypton laser works essentially in the same way as the Argon laser. However, because it emits a red beam, its absorption is different. It is useful in treating conditions very near the fovea, that is the center of the eye, because the red beam will not be absorbed by the yellow pigments found there. The red beam can pass through with very minimal absorption. It is also useful when treating areas near veins because it can create burns around the vein without damaging the latter since the Krypton laser is not absorbed by the blood in the vein. However, its advantage over Argon is minimal.

## Neodymium YAG laser

The Neodymium YAG laser has only recently been used extensively in ophthalmology. It works on a different principle. The "Q" switched YAG (Yttrium-Aluminium-Garnet) laser does not coagulate. When in focus, it cuts or disrupts tissues. Thus it has a fundamental difference from that of the Argon and Krypton laser. Because of this the YAG laser is known as a photodisrupter. It is different from the laser photocoagulators in that it does not coagulate tissues, it does not depend on pigments in order that the laser light be converted into heat energy to coagulate tissue. It is similar to the other lasers in that it needs a clear optical media in order for the beam to be focused so that reactions can take place or the sparks can occur. With an opaque media it is not possible to use either laser.

The excitement about the YAG laser is that if the beam can be focused, as in the eye, it is possible to make cuts in the eye without making an incision through the eye. Thus structures in the eye such as an opaque capsule or iris can be cut within the eye without any incision. This is very fascinating and revolutionary because we have always had a concept that for tissues to be cut there must be an incision through the surface to cut the deeper tissues. The YAG laser therefore brings a new, fascinating, futuristic approach to surgical science.

## Laser Surgery

A purpose of laser surgery in general surgery is to decrease the bleeding during operation and also achieve a curative resection of tumors. In practice, we must after need such delicate laser irradiation technique as to give little thermal damage and yet to be effective on the tissue. for example in laser treatment of hard tissue or so small or so thin tissues.

In the bloodless cutting with laser surgery, the tissue on the proposed line of cutting is coagulated by defocused beam, followed by cutting by focused beam. To facilitate cutting, the different focusing lens with the focal of 100 mm, 50 mm and 25 mm is available and a proper lens can be chosen for appropriate use.

To control bleeding with the Nd-YAG laser in the coagulation mode, irradiation is started from the surrounding tissue of the bleeding artery to achieve coagulation well and ended on the artery. To make bloodless cutting effective, cutting speed by the blade should not be faster than the speed at which coagulation layer is made by irradiation.

## CO2 Laser

The CO2 laser produces a continuous invisible beam wave length of 10.6 microns in the infrared range of the electromagnetic energy spectrum. As such it has

ionizing effect. The CO<sub>2</sub> laser beam that emits from laser head is unfocused and diameter of about 10 mm. This beam can be focused down to target areas 0.5 mm to 0.2 mm in diameter using lenses of approximate focal length. The amount of tissue destruction is predictable and can be controlled by using the appropriate amount of energy with suitable time exposure. The area of the burn is about 1 mm to 2 mm in diameter, increasing slightly with an increase in duration of exposure and with increasing power. Therefore, when only the smallest area of destruction is desired, the lasing is done at the lowest power and shortest time duration. A power setting of 5 to 10 watts combined with a time exposure of 0.2 seconds is satisfactory for precise microsurgery . but for gross dissection 10 to 15 watts of power has to be used almost continuously in the manual mode, bypassing the timer, using the footswitch to start and stop the dissection.

The CO<sub>2</sub> laser energy is practically completely absorbed by all biologic tissue, irrespective of pigmentation,. In contrast, Argon laser, for example, will pass through the cornea and be selectively absorbed by the pigmented retina. The effect the CO<sub>2</sub> laser on biologic tissue is almost entirely thermal by vapourising cells. The laser beam is totally absorbed by the water, which constitutes approximately 85% of most living tissues, wherein it is converted into heat and steam formation and causes flash vapourisation of the cellular water at 100 C. Combustion is often incomplete so that flecks of carbon may be left adjacent to the wound.

Surgery with the CO<sub>2</sub> laser offers a degree of precision that cannot be matched by conventional techniques. The laser destroy diseased tissue in sub-

millimeter target areas within a margin of 60 micrometer and to a predetermined depth. Surrounding normal cells therefore remain undamaged.

The laser has a cauterizing effect on small blood vessels of 0.5 mm or less in diameter and automatically seals them, reducing the patient's blood loss, and thereby maintains a virtually dry field of surgery, permitting an unobstructed view of the target lesions at all times. The laser has almost eliminate the need for blood transfusion in most of the cases.

#### Low Level Laser Therapy (LLLT)

Another use of laser in medicine is Low Level Laser Therapy (LLLT). In the surgical lasers, as a "light knife", a high peak power, but low energy is used, where as the low level laser use a low power, but a higher energy. When this energy is absorbed by the living cells, the applied laser energy is transformed to biochemical energy and heat. However, the induced heat is hardly measurable (0.1 C), due to the low power used. In short, induces local biochemical changes without the use of drugs.

The LLLT stimulates the Na- and K- ions pump located in the cell membrane and the generation of energy within the cells. Many of the cell activities are therefore stimulated.

The clinical effects of low laser therapy are numerous and one of very important clinical effect is the pain relieving effect. The effect is immediate and caused by a desensitization of peripheral pain receptors. To understand the effects, it is important to remember that the effect abnormal healthy tissue is not very significant. However if

cell activity somehow is depressed, the activity is very much increased by the laser stimulation. If there is an inflammation this will be suppressed.

LLLT can be used in all cases of acute or chronic pain of muscular, vascular, rheumatic, inflammatory or traumatic origin. Acute pain is treated easier and faster than chronic. All kinds of tissue damage can - and should- be treated with laser. The laser dosage is expressed in term of energy (joule).

The laser is applied locally in close contact with the skin at the following sites at points of tissue damage (e.g. wound, ulcer, rupture, sprain, etc.) at sites of inflammation (e.g. arthritis, tendinitis, etc.) at myofacial trigger points (tense and tender local points in musculature) LLLT should be the first choice of treatment in all cases of sport injuries, muscular pain, headache, tendinitis, low back pain, arthritis, and more. Other therapeutic modalities can be combined with LLLT without negative effects. There are no known side-effects and contraindications to LLLT.

#### References.

1. Terry B. Marion, William F. Hornyak : General Physics with Bioscience Essay, John Willey & Sons, Canada , 1985.
2. John R. Cameron, James G. Skofronick : Medical Physics, John Willey & Sons, Toronto, 1978.
3. P-Laser System International ApS, 9 Egendalsvej, DK-3670 Veksoe, Denmark.
4. Alex Mallow, Leon Chabot : Laser Safety Handbook, Van Nostrand Rheihold Co., Melbourne, 1978.
5. Arthur S. M. Lim and, Ang Beng Chong : Proceedings of The Inter-Faculty Symposium on Laser, National University of Singapore, 23 Oct. 1985.

6. Fumio Sano, Yoichi Kasai, Tetsuro Konno and Osamu Nishida : Extended Application of CO<sub>2</sub> Laser and Nd-YAG Laser in General Surgery, Workshop (5), The First Department of Surgery, University of Hokkaido, School of Medicine, 1984.
7. Akinori Nagasawa : Development of Practical Useful Laser Techniques. Workshop (5), Metropolitan Hiroo General Hospital. Tokyo.
8. N. Kunaratnam : CO<sub>2</sub> Laser - What it is, Proceedings of the Inter-Faculty Symposium on Lasers, National University of Singapore, 1985
9. Martin A. Mainster : Ophthalmic Laser Surgery : Principles, Technology, and Technique, Transactions of the New Orleans Academy of Ophthalmology : Toronto, Princeton , 1985. Symposium on the Laser in Ophthalmology and Glaucoma up Date, The C. V. Mosby Company, St. Louis,
10. Hugh Beckman : CO<sub>2</sub> Laser. Transactions of the New Orleans Academy of Ophthalmology : Toronto, Princeton , 1985. Symposium on the Laser in Ophthalmology and Glaucoma up Date, The C. V. Mosby Company, St. Louis,
11. Francis A. L'Esperance, Jr : New Laser System and Their Potential Clinical Usefulness. Transactions of the New Orleans Academy of Ophthalmology : Toronto, Princeton , 1985. Symposium on the Laser in Ophthalmology and Glaucoma up Date, The C. V. Mosby Company, St. Louis,
12. Francis A. L'Esperance, Jr : Current Applications of Dye Laser. Transactions of the New Orleans Academy of Ophthalmology : Toronto, Princeton , 1985. Symposium on the Laser in Ophthalmology and Glaucoma up Date, The C. V. Mosby Company, St. Louis,

BIOLOGICAL EFFECTS OF LASER LIGHT (summarized by Y. Sakurai)

thermal effect	<ol style="list-style-type: none"> <li>1. short time (ms order) temperature <sup>rise up to</sup> 200-1000 °C at the irradiated part</li> <li>2. continuance of temperature in 45-50 °C for more than a minute</li> </ol>
pressure	<ol style="list-style-type: none"> <li>1. pressure of the photon, up to the order of some decades g-force/cm<sup>2</sup>;</li> <li>2. pressure or impulse wave due to expansion, evaporation and volatilization by heat</li> </ol>
photo-chemical effect	<ol style="list-style-type: none"> <li>1. chemical change by quantum energy of light</li> <li>2. absorption by pigments</li> </ol>
electromagnetic field	ionization, generation of free radicals and destruction of molecular bonding by electric field of intensive light

Table 6-1. Ophthalmic laser sources

Name	Primary wavelengths (nm)	Active species	Pumping type	Use*	Status†
Argon	488.0 blue 514.5 green	Ar ion	Electric discharge	PC	C
Carbon dioxide	10,600 infrared (IR)	CO <sub>2</sub> molecule	Electric discharge	PC	C
Copper vapor	510 green 578 yellow	Cu atom	Electric discharge	PV, PC	I, C
Organic dye	320-970 tunable	Various dyes	Ar, Nd:YAG or other lasers	PC	P
Excimer	126-351 ultraviolet	Various excimers	Electric discharge	PR, PC	I
Erbium: YLF	1228 IR	Er ion	Flashlamp	PA	E
Gold vapor	628 red	Au atom	Electric discharge	PD	I
Helium-neon	632.8 red	Ne atom	Electric discharge	PR, PC	P
Krypton	531.0 green 568.2 yellow 647.0 red	Kr ion	Electric discharge	PD aiming, diagnosis‡	C
Nd:YAG	532 green	Nd ion	Flashlamp	PC	I
	650 red			PC	C
	1064 IR			PC	E
Ruby	1300 IR	Cr ion	Flashlamp	PD, PC	P
	694.3 red			PD	C
				PC	E

\*PA, photoablation; PC, photocoagulation; PD, photodisruption; PR, photoradiation; PV, photovaporization.

†C, clinical; E, experimental; H, historical; I, investigational; P, possible clinical use.

‡Laser retinal interferometry, laser Doppler velocimetry, and autoexposed lensometers.



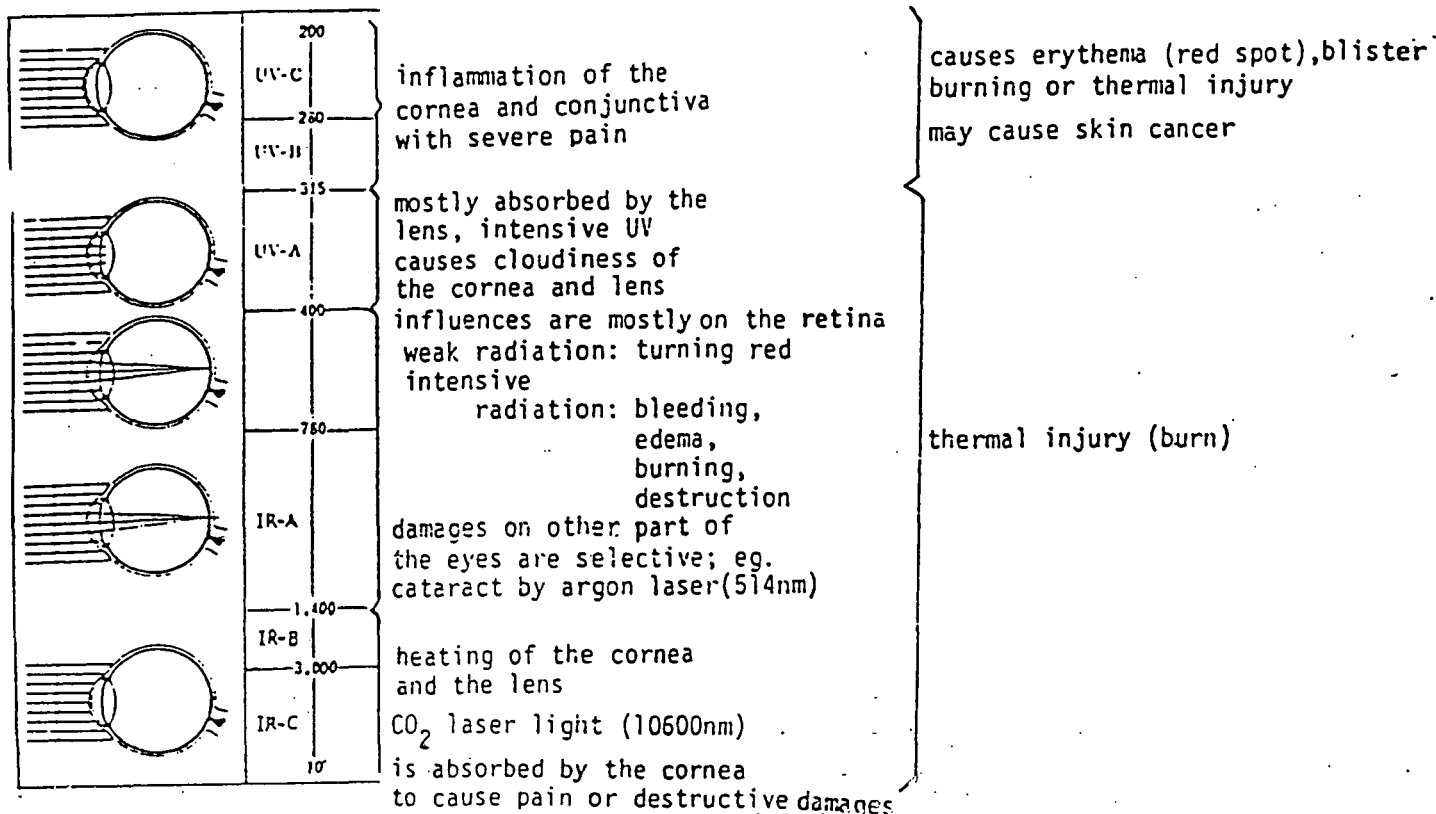
degree of danger

- (class 5): laser light perfectly shielded; no regulation required in use
- class 1: essentially safe, or can be safe by technical design
- class 2: low power, eyes can be protected by reflective blinking due to irritative feeling
- class 3A: same as class 2, however dangerous to look at the beam directly through optical apparatus
- Class 3B: dangerous to look at the beam directly
- class 4: high power, diffused reflection is dangerous

safety guide for laser equipment users

1. Avoid direct exposure to beam
2. Avoid irradiation to reflecting objects
3. Avoid use in darkness (should keep the pupil size small)
4. Wear protection glasses
5. Clearly indicate while in use
6. Test of vision, regularly

wavelength(nm)                      to the eye                      to the skin



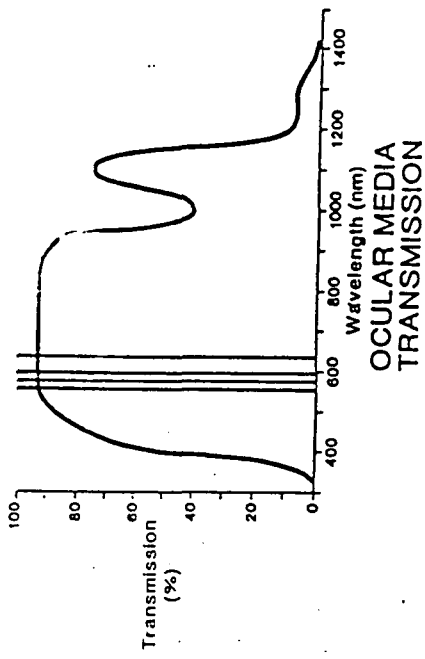


Fig. 5-24. Transmission of various wavelengths from organic dye laser (550, 570, 590, and 630 nm) through refractive ocular media.

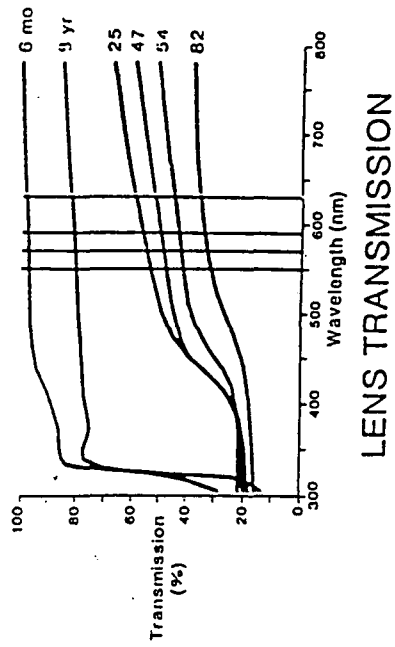


Fig. 5-28. Percentage of transmission of representative organic dye laser wavelengths through intact human lens at various ages. Percentage decreases substantially with increasing age because of filtration effect of yellow nuclear sclerotic lens.

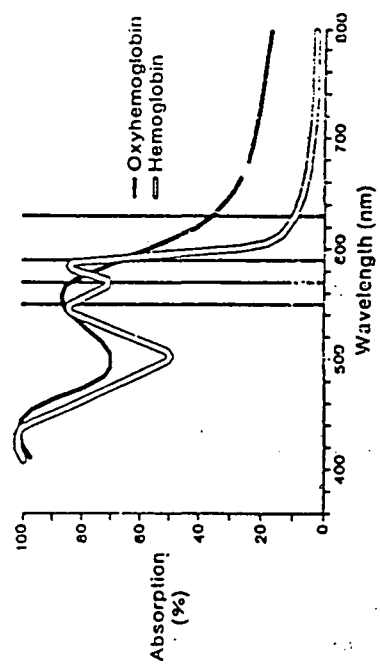


Fig. 5-25. Percentage of oxyhemoglobin and reduced hemoglobin absorption for representative wavelengths of organic dye laser in Fig. 5-24.

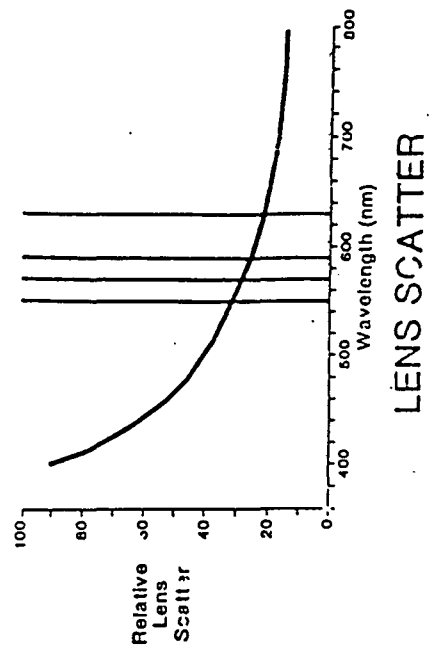


Fig. 5-29. Relative lens scatter of representative organic dye laser wavelengths. Scatter increases with shortness of wavelength.

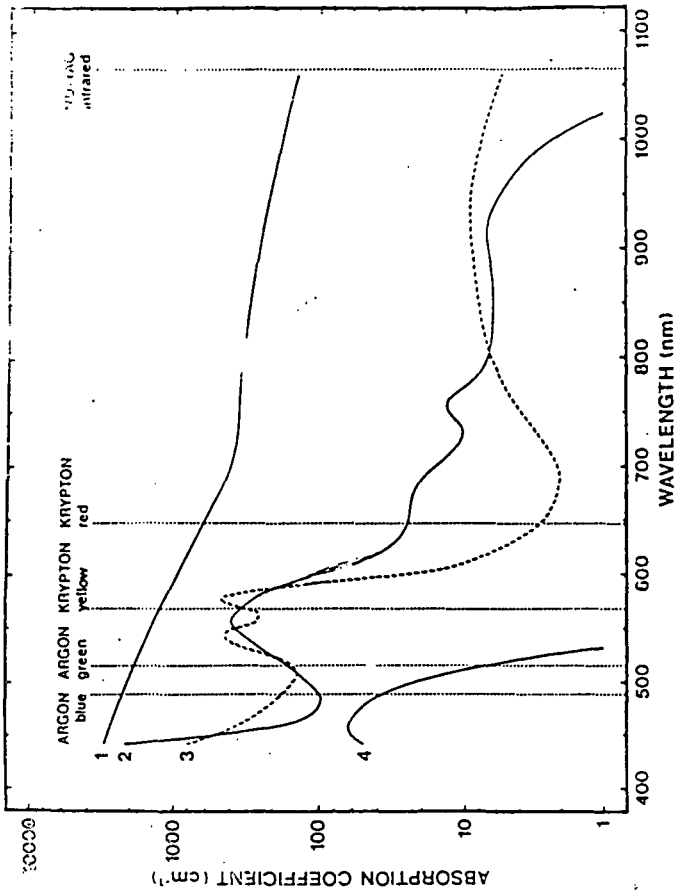


Fig. 5-3. Three primary light absorbers in ocular tissues are melanin (curve 1), hemoglobin (reduced, curve 2; oxygenated, curve 3), and macular xanthophyll (curve 4). Absorption coefficients are presented as function of wavelength, based on data from reference 12.

### ABSORPTION OF LASER ENERGY IN 1 MM OF HEMOGLOBIN AND H<sub>2</sub>O

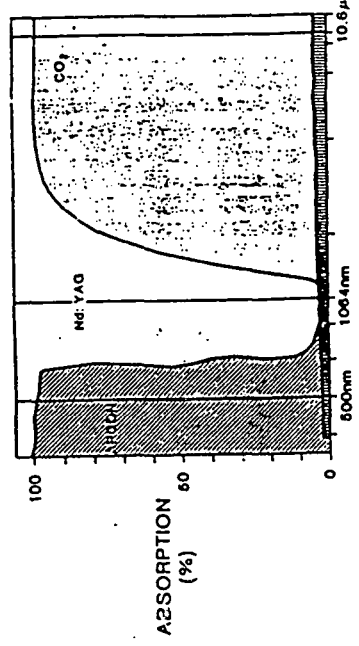


Fig. 5-5. Representative curve showing absorption characteristics of argon (500 nm), neodymium-YAG (1064 nm), and CO<sub>2</sub> (10.6 μ) lasers in hemoglobin and water.

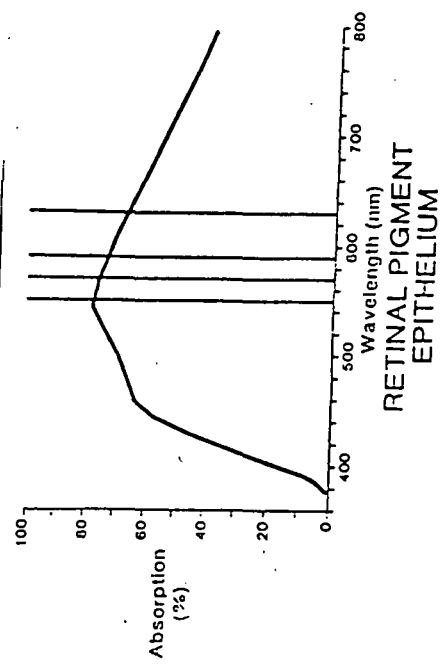


Fig. 5-26. Percentage of retinal pigment epithelium absorption for representative wavelengths of organic dye laser.

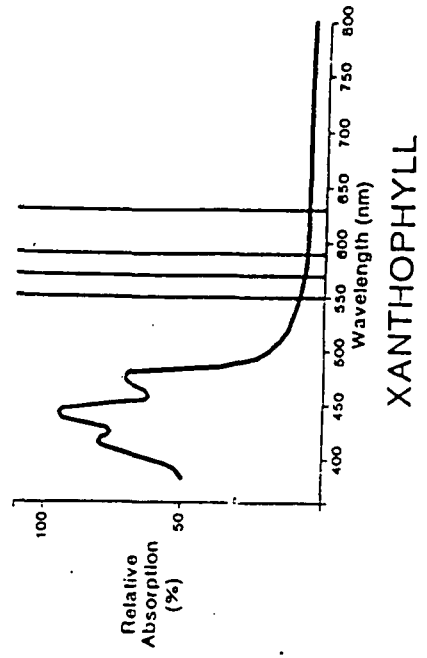


Fig. 5-27. Percentage of relative absorption of macular xanthophyll pigment for representative wavelengths. All wavelengths presently used for photocoagulation with organic dye lasers are lightly transmitted by xanthophyll pigment.

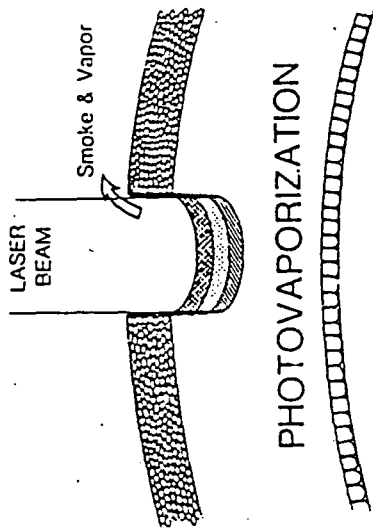


Fig. 20-10. Excellent absorption coefficient of biologic tissue allows CO<sub>2</sub> laser beam to be completely absorbed within 200 μ of tissue, causing that tissue to reach vaporization point of water and to be removed as smoke and vapor. Multiple burns with CO<sub>2</sub> laser beam result in "minishaving" and removal of multiple deeper layers at incision site.

**ABSORPTION OF LASER ENERGY  
IN PIGMENTED TISSUE**

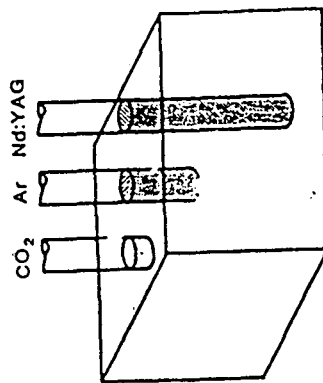
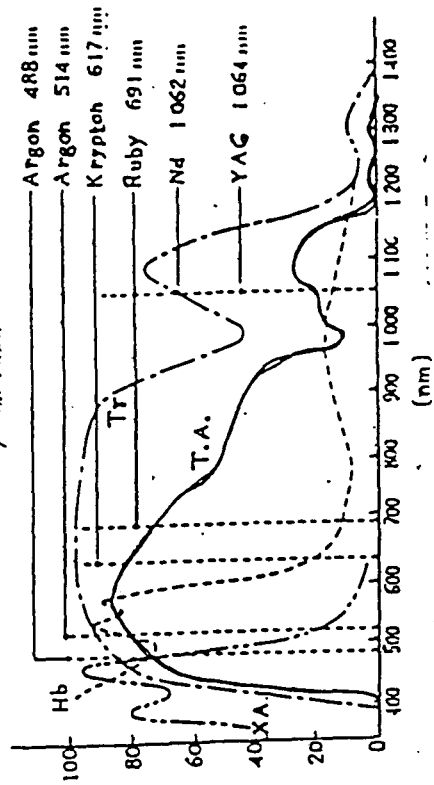


Fig. 20-11. Schematic representation of absorption and penetration characteristics of the CO<sub>2</sub> (10.6 μ), argon (500 nm), and neodymium-YAG (1064 nm) lasers in various types of pigmented tissues.

MEDIUM	NAME	WAVELENGTH (nm)	OUTPUT POWER	TOTAL EFFICIENCY (%)
GAS	N <sub>2</sub>	337	pulse 30 MW	0.02
	Argon	488, 515	CW 15 W(515nm) CW 40 W(total)	0.04
	He-Ne	633	CW 100 mW	0.01
SOLID	CO <sub>2</sub>	10600	CW 20 kW pulse 3 GW	10-20
	Ruby	694	pulse 1 GW	0.025
LIQUID	YAG(Nd <sup>3+</sup> )	1060	CW 600 W pulse 100 MW	0.7
	dye (Rh6G)	560-620	CW 1 W pulse 100 MW	0.05
Semiconductor				
	GaAs	810-900		10
	AlGaAs	720-880	CW 100 mW pulse 10 W	
	InGaAsP	1200-1600	CW 10 mW	

**LASER TREATMENT OF FUNDAL BLEEDING ( by Dr. Noyori 1983 )**  
*perforation*



Wavelength dependence of retinal coagulation efficiency  
by Noyori 1983

Tr: Transmission through the lens  
T.A.: coagulation efficiency = Tr x Absorption of the retina



Fig. 20-12. Coherent Medical Group, Inc., CO<sub>2</sub> laser micromanipulator, with surgeon controlling beam by light movement of joystick.

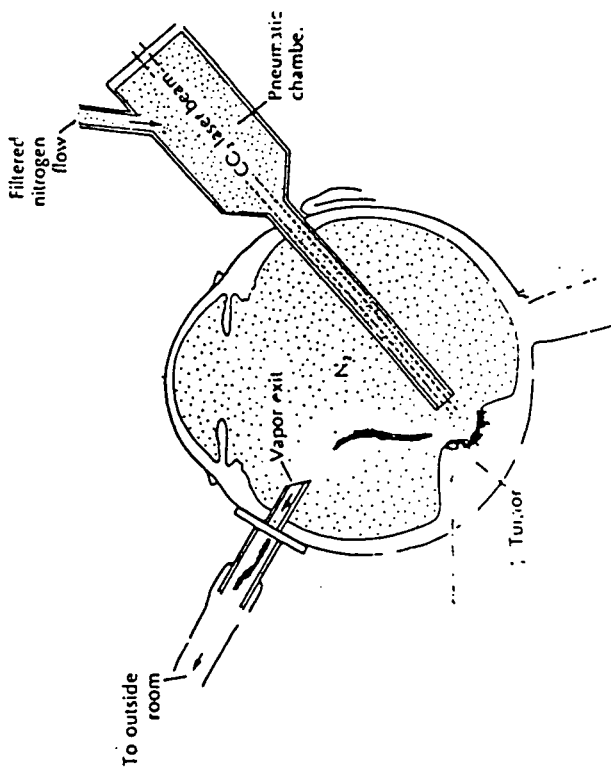
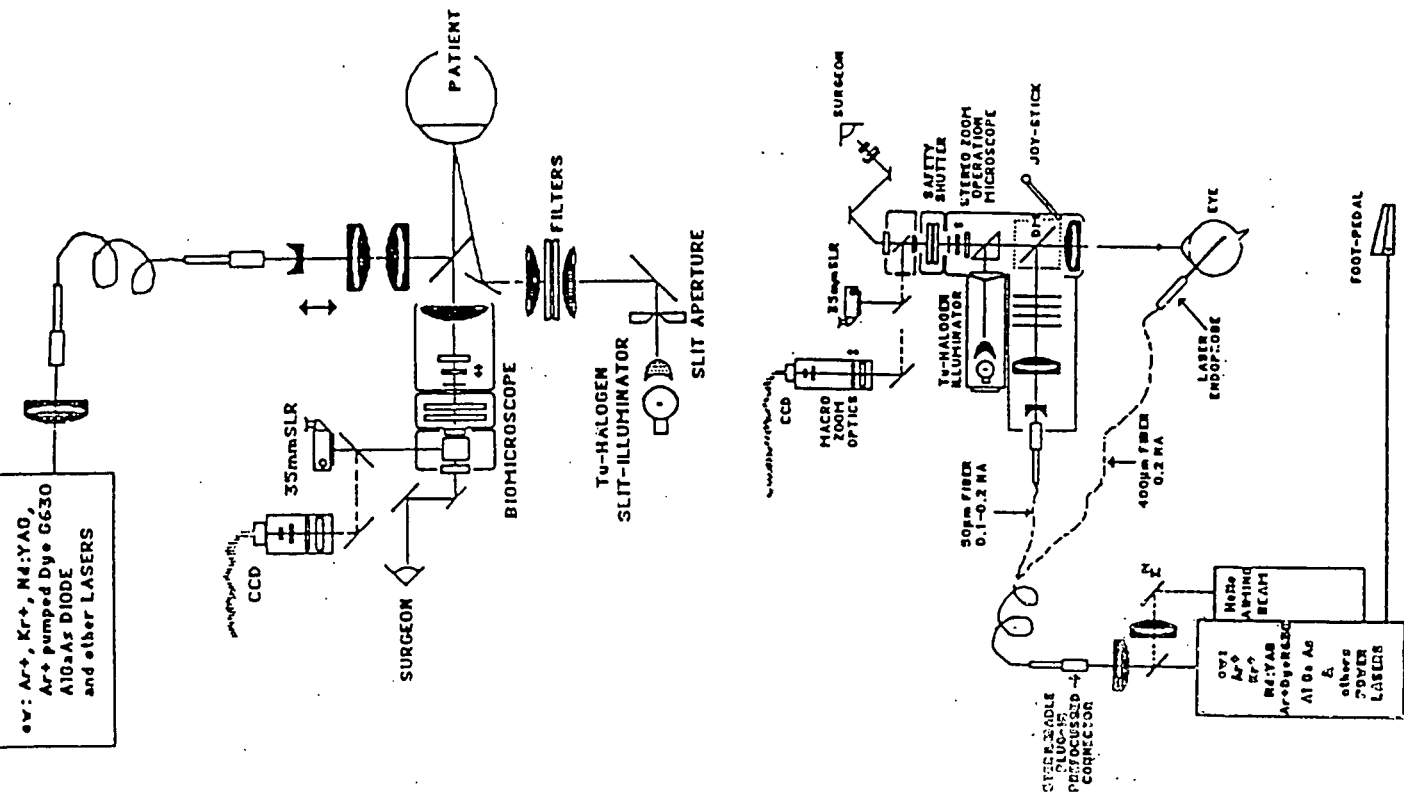
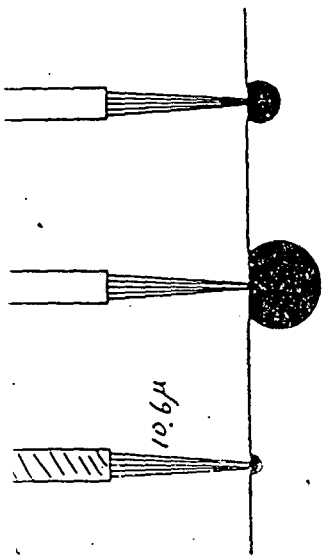


Fig. 20-13. CO<sub>2</sub> laser photovaporization of malignant choroidal or retinal tumors. Nitrogen gas is gently released through intraocular probe, after gas-vitreous exchange, to evacuate smoke and vapor from tumor





Carbon Dioxide Laser

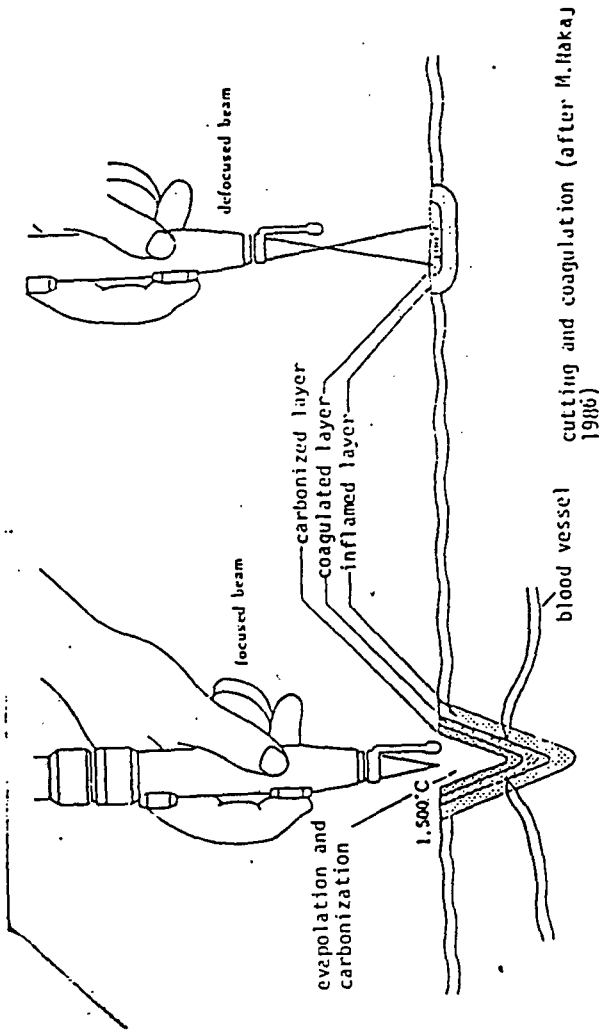
**Advantages**

- High power for tissue ablation
- No touch vaporization
- Precise microscopic control
- Minimizes brain retraction
- Decreases blood loss
- Minimizes tissue manipulation
- No electrical interference with monitors
- Protective effect of water
- Micromanipulator attachment

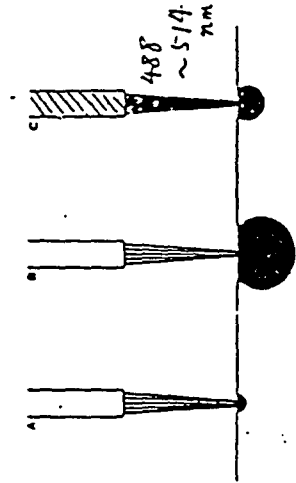
**Disadvantages**

- lack of fibre-optic cables for beam transmission
- non-transmission through water and blood
- requires co-axial pilot laser

(by J.H.Tew et al. 1986)



Argon Laser



Neodymium:YAG Laser

**Advantages**

- High power
- Potent deep tissue coagulation
- Fibre-optic transmission
- Transmission through water
- No electrical interference with monitors
- Differential absorption by blood vessels

**Disadvantages**

- precise depth of scatter is unpredictable
- poor ability to vaporize tissue
- requires co-axial pilot beam

**Advantages**

- Coagulates and vaporizes
- Fibre-optic transmission
- Small spot size
- No pilot beam required
- Transmission through water
- No interference with electrical monitors
- Precise microscopic control
- Micromanipulator

**Disadvantages**

- lower power
- inefficient

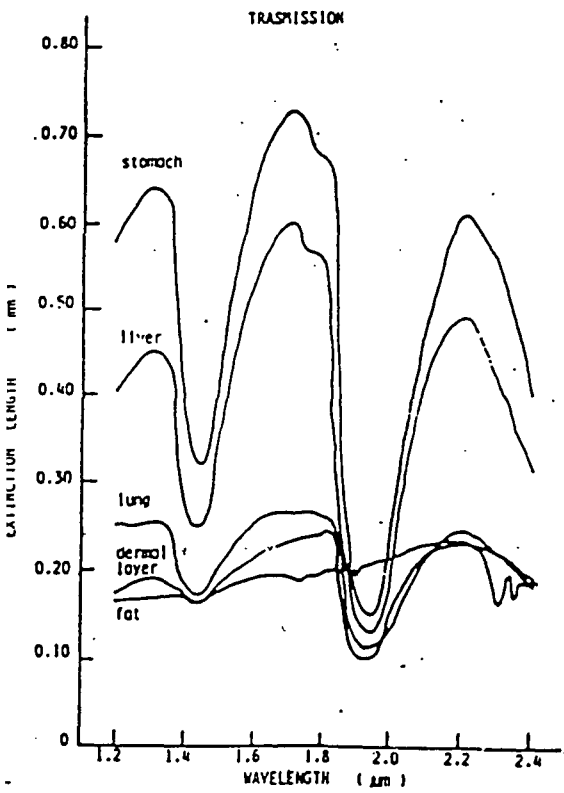


Figure 3: Typical transmittance patterns of excised animal tissues.

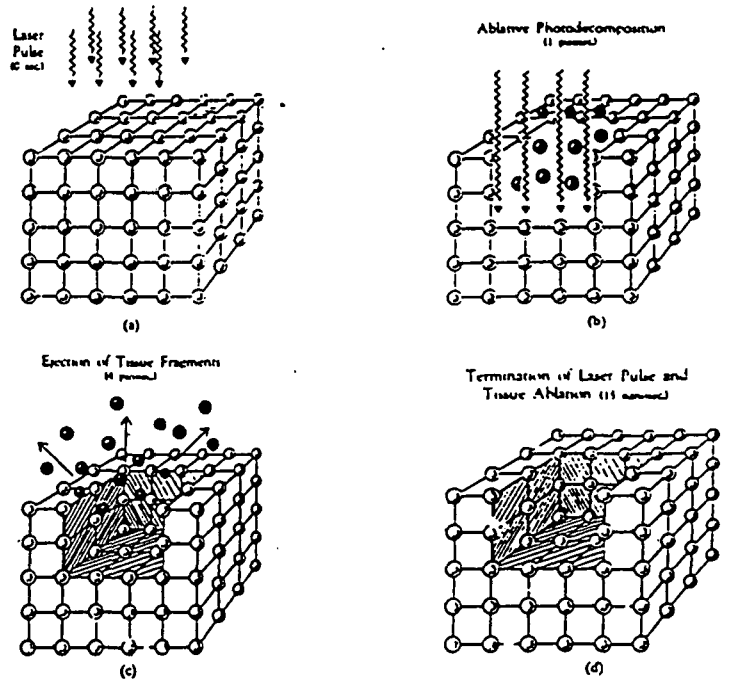


Fig. 21. 193-nm argon fluoride laser pulses result in a unique photochemical interaction with the cornea termed photoablation. The (a) laser pulse is highly absorbed in the first several microns of corneal tissue, primarily by protein chromophores (b). Since the 193-nm photons have energy in excess of the carbon-carbon intermolecular bonds of corneal tissue, the bonds are photoelectrically decoupled, resulting in (c) the ejection of many small fragments from the surface. (d) The photoablation process is completed after 15 ns, leaving clean, precise edges with only 0.3  $\mu\text{m}$  of adjacent tissue alteration.

**HOLOGRAM  
AS PROTECTION IN  
SECURITY PACKAGING**

**By Thomas Edi  
Sunarto**

**PT. PURA BARUTAMA  
KUDUS – INDONESIA**



## HOLOGRAM AS PROTECTION IN SECURITY PACKAGING

Protection refers to a very broad sense of meaning, as protection can mean, among others:

1. Protection against theft.
2. Protection against forgery.
3. Protection against copying.
4. Protection against destruction.

For each of the above-mentioned protections, specific type of protection is needed.

In this paper, what is meant by protection shall be define as “something applied to package so as to protect the package against any forgery.”

In this era good packaging has to accommodate four functions as follows:

1. As protection of the product from quality damage.
2. As a medium of product promotion.
3. As a transfer medium of information for customers dealing with the content, how to use, etc.
4. To make easy in handling and delivery.

Any how, the recent development of packaging has shown that the above functions are not enough because of counterfeiting trends. Consequently, there is one more condition

to be fulfilled: i.e. packaging must protect the product from counterfeiting effort. The condition has brought us to a term of "Security Packaging".

### **SECURITY PACKAGING**

At the moment, packaging functions as product protection from counterfeiting. Tight competition and criminal acts that increase in number has become important factors to create the counterfeiting. The loss because of the counterfeiting has been a lot, including company's reputation, money, or even death.

To anticipate counterfeiting, we need a good security system which consists of material sources, process and application technology.

### **CRITERIA OF GOOD SECURITY FEATURES IN SECURITY PACKAGING:**

What is generally accepted as good protection is that it should meet, among others, the following criteria:

- High technology.
- Easy to detect.
- Unable to be copied.
- One time use only.
- The technology can be up-graded.
- Having multi level security features.
- Having overt and covert security features.

- Not available in free market.

## **SECURITY COMPONENTS THAT CAN BE APPLIED IN PACKAGING**

There are several components that can be applied in packaging, i.e.:

### **1. Security Printing.**

It is a printing technique with a special design and method so that the result is hard to be imitated, i.e. Microtext, Relief Motif, Line Width Modulation, Rosette, Anti-copy, Guilloché, Filter Image, etc.

### **2. Security Paper.**

It is special paper which has special feature, i.e. Visible and Invisible Fiber, Planchettes, Watermarks, Color Dots, Chemical Sensitizing, etc.

### **3. Security Ink.**

It is special ink which has special feature, i.e. Fluorescence, Iridescent, Thermochromic, Phosphorescent, etc.

### **4. Hologram.**

It is a kind of security with high technology and has special security features, i.e. Microtext, Filter Image, Hidden Image, Guilloché, etc.

From the kinds of security components above, the one which mostly meet the criteria of good security feature is hologram.

In most examples of authentication, holograms are used as components added to a product or a document. This component has characteristics related to the optical effect, the transfer method and its finished shape. All are important in determining the final level of protection, because an optical security component is the combination of an optical effect and the method used for transferring the effect to a product or document requiring protection.

The use of the most suitable combination of the different elements for the item to be protected is key to the efficient protection of that item.

### WHY IS HOLOGRAM USED IN SECURITY PACKAGING.

Learning the above criteria of good security, features and considering the function of packaging as a promotional medium, security hologram can meet requirement.

It can be explained as follows:

#### **A. SECURITY REASONS.**

In order that holograms function as security device, it should meet the above mentioned criteria.

##### **1. High Technology.**

Hologram is an image made by using laser beam reflection on an object and medium because laser beam can emit monochromatic coherence light. Using high technology equipment and accurate setting up we can create good hologram.

To make hologram as protective tools needs a long and complicated process sequence. That is why the technology of hologram making is rarely mastered.

## **2. Easy to detect.**

One of the hologram unique-ness is that every hologram has its specific characteristics so that the image can be visually identified, i.e. image design, color spectrum, image depth, kinetic effect, brightness, etc.

## **3. Unable to be copied.**

The word of copy here means copying process using color photocopier or laser scanner to make illegal multiplication.

The hologram image records the amplitude and phase of the light reflected by an object completely so that it creates the real form. To produce hologram it is needed light spectrum rather than ink. Consequently if hologram is photocopied or scanned with laser, the real object can not appear or there is no image at all.

## **4. One time use only.**

Hologram can be applied in a certain technique so that it can not be used more than one time. Also security hologram with a specific design is only sold to one customer.

## **5. Hologram technology can be up-graded.**

Hologram technology always improves. The improvement is faster than the other security components, i.e. paper, printing, and ink.

## **6. Having multi level security features.**

We can place several security levels in the hologram regarding the risk level against counterfeiting. Three kinds of security level are:

- a. First level. Identification done by public.
- b. Second level. Identification done by well-trained official.

- c. **Third level. Identification done by laboratory staff, using special tools (microscope, laser pointer, etc).**
- 7. Having overt and covert security features.**
- 8. Not available in free market.**

## **B. PROMOTION REASON.**

Impact is the word that benefits graphic holographic. It is the visual impact of the medium which gives it such great power and generates so much interest.

Companies of all sizes are constantly searching for means of promotions, which will set them apart from competitors and get them noticed.

Holography adds three distinct advantages to any promotions:

### **1. Impact.**

Hologram is eye-catching. People will look at hologram for significantly longer period of time than other graphic media.

### **2. Pass-around value.**

People are often interested in good holograms and they are likely to bring them to the attention of colleagues and associates.

### **3. Retention.**

People tend to keep holograms. There are many people who have holograms on their desk which created more than ten years ago.

## **HOLOGRAM TRANSFER METHOD (APPLICATION) IN SECURITY**

### **PACKAGING**

#### **1. Hologram Security Seal.**

It is like a sticker applied to protect a product against counterfeiting. It is usually attached on the top of packaging.

It is caused of people use an original packaging and the product was changed. So to prevent this matter, we place a security seal that will be broken if is was peeled off.

Superiority of security seal hologram is once used only.

#### **2. Holographic Transparent Laminating Film.**

It is commonly applied in the lamination with packaging material.

This product generally used in the brand name of products, which the design of box has already known by people so the brand name owner did not want to give anything that damaged the original design.

To keep the originality of the design we use Transparent laminating Film beside to improve and exclusivity of packaging.

#### **3. Hologram Hot Stamping.**

It is basically to apply a hologram image on a surface by using heat. There are three kinds of the application.

- a. Individual. The image is made from an individual design.
- b. Random. The image is made from a random design.
- c. Stripe. Form of this application is a lane / stripe.

#### **4. Hologram Transfer.**

## 5. Special application.

For example: Pharmaceutical.

The hologram packaging can be described as follows:

1. Tear tape. This tear tape does not use for tear tape only but it also uses to protect. So after the outer wrapper is peeled off, this wrapper is broken too, and if it is combined with hologram it will give an effective security.
2. Top layer. Top layer of packaging combined with packaging. Usually this hologram is laminated to paper than be printed on. The printing process can use Rotogravure printing and offset printing, including UV curable ink, flexo-printing, etc. expected for folding box, it can be used to bag, Multi layer pouch, etc.
3. Holographic Aluminum for Medicine packaging.
4. At this time like a blister and stripping for pharmaceutical packaging use an ordinary printing. We give it hologram. To make a direct hologram on aluminum is very difficult.
5. Bottle cup seal. It used lamination between aluminum and sealant that we give the hologram on aluminum.
6. Shrink. It is used as a seal and usually we find a word 'don't accept if the seal is broken'. Ordinary shrink does not use any protective tools, so we can add a hologram on the shrink film. The result will be more satisfactory.



## HOLOGRAM MAKING

Technically, the making of hologram for packaging involve many different kinds of technology and undergoes many processing stages. Figure 1 show flow-chart of hologram making.

Although hologram , principally, was discovered in 1947 by Denis Gabor, hologram could come to this perfection only in 1962 as its vital component, the coherent beam (known as laser) was discovered by this year.

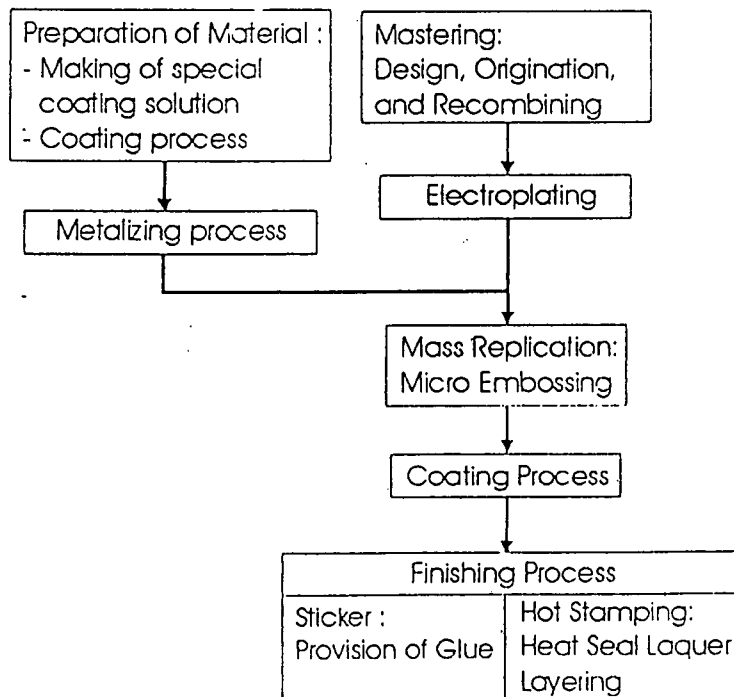


Figure 1 Flow-chart of hologram making

The process of producing the hologram can, generally be described as follows:

Hologram is an image made by using laser beam reflection on an object and medium because laser beam can emit monochromatic coherence light. Using high technology equipment and accurate setting up we can create good hologram.

To make hologram as protective tools needs a long and complicated process sequence. That is why the technology of hologram making is rarely mastered.

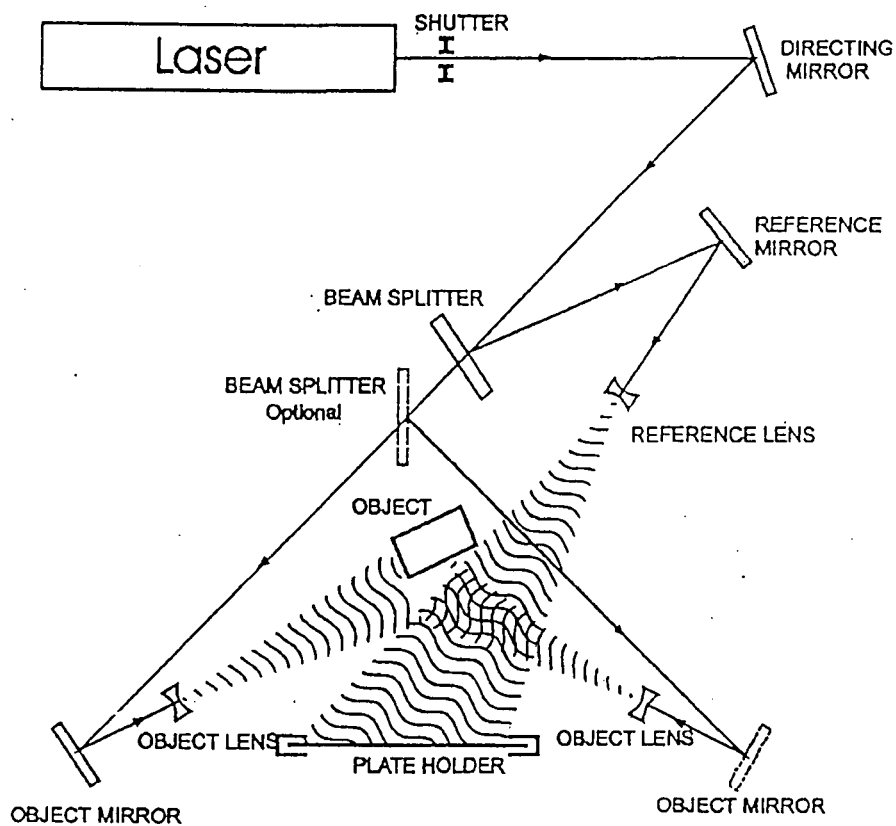


Figure 2 Basic setup for making master hologram

issues to achieve a good hologram are stability, a good light ratio, the equality of beam path distance from beam splitter to the plate, guarding against undesirable shadows on stray light and allowing enough working room for adjustment. ③

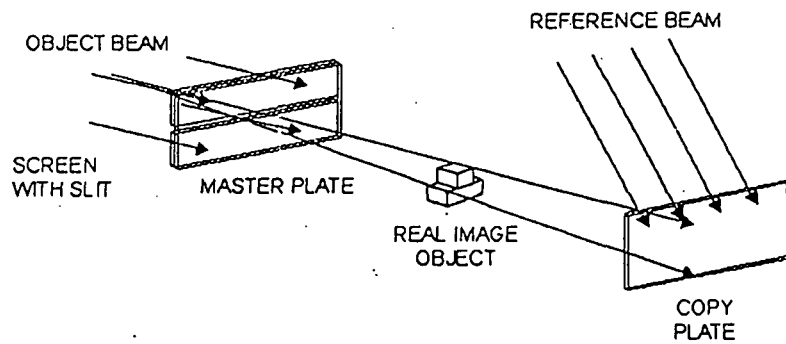


Figure 3 Basic setup for making rainbow copy hologram

If this hologram is viewed with white light, the image is seen as a smear, with spectral colors spread out across the smear. This hologram could only be seen clearly using laser light. For the hologram to be viewed with white light we have to make rainbow copy (rainbow transmission) hologram from the transmission hologram. It often to name the first transmission hologram as H1 master and the copy master hologram as H2 master. Basically the process to make the rainbow copy is illustrated in Figure 3

After the master hologram processed, the master hologram is setup with an opaque screen against it. The screen has a horizontal slit with some small vertical width of perhaps one centimeter or so in it. Then the slit hologram forms a real and a virtual image. The real image is chosen to make the copy hologram. The copy plate received light rays from the real image and forms a plane reference beam. In order to use the H2 master for embossing process, the hologram have to be a "surface relief" hologram, so it is possible to transfer the surface thickness variation of the master to transparent plastics by some combination of heat and pressure. Special materials have been developed to only produce surface relief, and they are called photoresists. Because these materials are sensitive mainly to deep-blue light, we only use Argon laser and He-Cd laser to make master holograms.

### **HOLOGRAM DESIGN (OPTICAL EFFECT)**

In order to give its outmost protection, various special hologram types and technologies could be incorporated to the design. These types included:

#### **1. CONVENTIONAL HOLOGRAPHIC AND GRATING IMAGES**

##### **Conventional holography.**

In most cases for embossed holograms, the procedure requires the exposure of a master plate and the transfer of this holograms in to photo-resist registration plate.

The resulting images can either be 2D or 3D. Animation effects can also be achieved by combining two or more masters on the same transfer hologram. Combinations of the

different rainbow colors in a transmission embossed hologram allow for the realization of multi color images and true-color images.

The ability to make conventional types of hologram and to mass-produce them as embossed holograms is now widespread so they should be considered only for low security use such as protection against 'street-crime' color photocopies.

### Grating images

'Grating Image' refer to the fact that this type of diffractive optically variable image device (DOVIDs) involved the 'writing' of very fine diffraction grating elements, each of which bends the light falling on it in a specified way. So, a specific logo, for example, may comprise hundreds or thousands of diffraction grating elements.

Because each element is a discrete surface-plane diffraction grating, these techniques allow for much brighter images than conventional holography. They can also be used to make extremely detailed images, kinetic movement effect, and some 3D effects. This also means that grating images are less susceptible to the problems that may result when hot stamped onto less suitable substrate finishes.

Several of these techniques have been developed specifically for DOVIDs for use in authentication and are not used outside security printing and authentication, which makes them appropriate for high security usage.

The first factor for the user or designer to consider is the type of holographic image to be used. Many different optical image types have evolved from the conventional holographic images used in the security field at the beginning of the 1980's, included:

- 3D hologram. An image which has the three dimension of length, breath and depth.
- 2D hologram. An image in the two dimension of length and breath.
- Multi-plane (2D/3D) hologram. Layered 2D image, in which at least one layer seems to lie behind or underneath the other.
- Multi-channel hologram. A hologram containing two or more images each in its own 'viewing channel', so that from different viewing positions a different image is seen or is super-imposed on the other image.
- Stereogram. A hologram produced by recording many individual form of sequence of images. The original sequence may be photographic film, movie footage, video or computer graphics. Stereograms are usually 3D and can show a short movement sequence.
- 2D animated grating images
- Machine-readable features. This will involved on using a machine / device which is designed to detect overt or covert feature in a specific Dovid

## 2. COMPUTER GENERATED HOLOGRAM.

Computer generated hologram or known as dot matrix hologram used a propriertery mastering system which can incorporate more security features in the production of hologram masters. The computer generated hologram is a type of 'Grating Image' which involved on writing of many of diffraction grating elements which often called as dots, controlled by computer. The computer controls the color, positions and

orientation of each diffraction elements which could lead to more complex hologram design. The high resolution feature of dot matrix mastering system could lead to creation of 3d images and incorporate effects such as dynamic and kinetic effects which give the appearance of the image moving or changing. This system could also creates multi color hologram which give a more secure and unique hologram.

### 3. LITHOGRAPHY

All holograms which are explained above are created by using laser beams, other than using laser beam, there is one extremely high security proprietary technology which used electron beam (i.e. electrical charges rather than light) to create the image. This holograms usually called e-beam holograms. This technology is both specialized and scarce and is only available in high security sector, such as for use on banknote and and other high security documents.

Factors to take into account in choosing between the different image type include:

1. The mastering complexity adapted to the security level required
2. The image control mode (lighting, training of controller, ease of identification and control automation)
3. The transfer medium and transfer method.

As in traditional security printing, the security level of the optical image can be enhanced by the design and the quality of the reproduction, For examples, if 3D imagery is selected, the image can include unique yet easily recognizable 3D elements such as a portrait of a famous person. If 2D imagery is selected, complex elements such as guilloche lines, microlettering, and animation can be integrated.

The level of security affordable by the different types of hologram is outline below.

## THE DESIGN OF A SECURITY OPTICAL IMAGE

As with all security printing, the design of holographic image for authentication purposes is an important part of the security aspects. The design must be suitable for and effective with the item on which it is to be combined. The specification will take into account..

1. The product or document to be protected
2. The role of the optical device
3. Authentication of the packaging:
  - protection of the variable information
  - tamper-proofing or evidencing
4. counterfeiting risk:
  - color photocopy
  - imitation of the hologram with holographic diffraction foil
  - re-origination
5. control conditions:
  - lighting
  - personnel
6. transfer technique for combining it with the product or document
7. graphic specifications.



Among those parameters, the designer can choose the most suitable combination between optical effect and transfer media.

### **HOLOGRAPHIC COVERT SECURITY SYSTEM**

Covert is image or part of an image which is not visible to the naked eye in standard lighting condition and which may be encoded or encrypted

Covert security holograms fall into three different categories:

1. those whose effect can be observed in white light illumination (although perhaps requiring special conditions of observation)
2. Those whose properties or data can only be detected by illuminating the surface with coherent light such as that from a laser diode or small gas laser.
3. Those with effect which are automatically detected and deciphered by some form of automatic reader device.

### **WHITE-LIGHT ILLUMINATED COVERT SECURITY FEATURE.**

Features in holograms that are visible yet covert depends on specific knowledge on the part of person authenticating the hologram, so that they know what to look for. The feature is not hidden from the untrained observer but the its exact function or viewing mode may be very distinctive and difficult to reproduce. In this way these features are akin to those on banknote and other high security printed items. They include:

- Micro-writing
- Hidden images
- Moiré patterns
- Color keys.